Quantitative thermochronology and interpretation of exhumation in the central Nepalese Himalaya

by

David Michael Whipp, Jr.

A dissertation submitted in partial fulfillment
of the requirements for the degree of
Doctor of Philosophy
(Geology)
in The University of Michigan
2008

Doctoral Committee:

Associate Professor Todd A. Ehlers, Chair
Professor Rob Van der Voo
Associate Professor Sherif El-Tawil
Associate Professor Christopher J. Poulsen
Assistant Professor Marin K. Clark
Professor Kip V. Hodges, Arizona State University

It is not the mountain we conquer, but ourselves.
-Sir Edmund Hillary

To Pokey

ACKNOWLEDGEMENTS

I am deeply thankful to my wife, Alyce, for her love, support, encouragement and patience. There is no question that this document would not exist without her. I am also grateful to my family. My mom, Mary Ann, always encouraged me to be creative, my dad, Dave Sr., showed me how hard work pays off and to have a healthy fear of corporate life, and my sister, Megan, gave me some great lessons in how to simply go for it.

I am profoundly grateful to my advisor Todd Ehlers for his mentorship. Todd helped me greatly in my growth as a scientist through his adaptive advising style, allowing me to develop and improve necessary oral and written presentation skills, refine critical thinking abilities, and make essential contacts.

I am also thankful to the other members of my dissertation committee, Marin Clark, Sherif El-Tawil, Kip Hodges, Chris Poulsen and Rob Van der Voo. Being introduced to field geology of the Himalaya by Kip was a particular pleasure. I feel fortunate, as well, to have spent time as both a GSI and student of Rob's. His tectonics of oceans and continents course was the highlight of my coursework as a graduate student. In addition, I thank Chris and Marin for their assistance in revising chapters one, four and six.

I certainly owe much of my ability to reach this point to past and present members of the Earth Surface Processes Research Group. I am particularly grateful to have shared scientific discussions, technical questions, friendship and beer with Ja-

son Barnes, Greg Stock, Matt Densmore, Nadja Insel, Rasmus Thiede and Jeff Rahl. I am fortunate to have shared friendships with other folks in the department at Michigan, including Nico de Koker, Dan Horton, John Naliboff, Shih Yu Lee, Alison Duvall, Franek Hasiuk, Erik Kneller, Sam Haines, Jim Hnat and Chris Smith.

I am fortunate to have collaborated with a number of wonderful scientists during my time at Michigan. Specifically, I thank Kate Huntington for a great field season in Nepal. I have also benefitted from discussions and time spent with Doug Burbank, Ann Blythe, Taylor Schildgen, and John Lee. Furthermore, I thank Eric Essene and Bruce Wilkinson for getting me interested in geology and for their enthusiasm and encouragement during my undergraduate studies. I would have never considered graduate school if not for them.

Lastly, I owe much of my life balance to the Ann Arbor ultimate community. In particular, I thank Sarah Stock for getting me into ultimate and the HACsters for being who they are. I am also glad to have shared the field with Richard Kollár, Katka Bodova, Juggles, Goody, Hois, Hightower, Manix, Ravin, Will Wright, Andy Holcomb, Charles Griffith, Julie Laliberté and members of the Junta.

TABLE OF CONTENTS

LIST OF FIGURES

Figure

LIST OF TABLES

Table

LIST OF APPENDICES

Appendix

CHAPTER I

Introduction

Much of Earth scientists' understanding of orogenic processes and the evolution of mountain ranges is due to rock exhumation. Exhumation exposes previously buried rock at the surface, providing insight into geodynamic, petrologic, hydrologic and other processes that occur below the Earth's surface. The term rock exhumation refers to the unroofing of rock by tectonic or surface processes, specifically normal faulting, ductile thinning and erosion (e.g., Ring et al., 1999). In contrast to extensional mountain ranges where normal faults alone can exhume rock, exhumation in active convergent orogens is driven by a combination of tectonic transport of material toward the surface and erosion of the overlying rock. Thus, an understanding of the relative contribution of both tectonic and surface processes is needed to understand the exhumation history of an active convergent orogen.

Thermochronology is a common tool for quantifying rock exhumation and erosion over millions of years. In general, mineral thermochronometers record the time since cooling below an effective closure temperature within the Earth's crust. This effective closure temperature represents the temperature below which radiogenic daughter isotopes or damage trails are retained within a mineral crystal, and above which the daughter product is lost to diffusion or annealing (e.g., Dodson, 1973). Ther-

mochronometer ages can be used to calculate average rock exhumation rates over the time since a sample cooled by estimating the paleo-depth of the effective closure temperature isotherm and dividing that depth by the thermochronometer age. By collecting rock samples from bedrock, it is therefore possible to calculate the exhumation rate of a given sample location. In addition to bedrock samples, collection of sediment samples in modern river channels or preserved basin sediment allows for the calculation of exhumation rates across an entire drainage basin upstream of a sample location.

Thermochronometer data acquisition is highly technical, but equal complexity arises in determining the depth and position of paleo-closure isotherms for exhumation rate calculations. As thermochronometer samples cool during exhumation, samples are not only affected by the surrounding rock thermal properties, but also by crustal thermal processes including erosion and sedimentation, topography, tectonics and faulting, magmatism, and groundwater circulation (e.g., Ehlers, 2005). Because of these complexities, numerical models have become increasingly common for use in forward modeling of the crustal thermal field to predict thermochronometer ages and aid in data interpretation. For instance, simple one-dimensional (1-D) thermal models have been used to show the increase and decrease in the crustal geothermal gradient resulting from erosion and sedimentation, respectively. Intuitively, these processes will affect thermochronometer ages as they will change the rate at which material is transported to the surface, as well as the geothermal gradient (Ehlers, 2005, and references therein). Two- and three-dimensional (2-D, 3-D) models have shown that topography of increasing wavelength perturbs crustal isotherms to greater depths, influencing the relationship between thermochronometer ages and sample elevation at the surface (Stüwe et al., 1994; Mancktelow and Grasemann, 1997; Braun,

2002b,a; Ehlers and Farley, 2003; Braun, 2003; Ehlers et al., 2006). Lateral rock transport and faulting have also been shown to have significant thermal effects, generating spatially variable thermochronometer cooling ages (Stüwe and Hintermüller, 2000; Ehlers et al., 2001; Batt and Brandon, 2002; Ehlers et al., 2003; Bollinger et al., 2006; Brewer and Burbank, 2006; Huntington et al., 2007). Lastly, a number of previous studies have shown that groundwater flow driven by mountain topography can modify the crustal thermal field (Smith and Chapman, 1983; Forster and Smith, 1989; Person and Garven, 1994; Person et al., 1995) and lead to further variations in thermochronometer ages.

This dissertation uses numerical models to simulate the influence of tectonic and surface processes on thermochronometer data from the central Nepalese Himalaya. Thermochronology has been widely applied in the Himalaya to better understand the tectonic and topographic evolution of the range through time (e.g., Cerveny et al., 1988; Hubbard and Harrison, 1989; Copeland and Harrison, 1990; Macfarlane et al., 1992; Sorkhabi et al., 1996; Vannay and Hodges, 1996; Harrison et al., 1997; Wobus et al., 2003; Thiede et al., 2004, 2005; Bernet et al., 2006; Szulc et al., 2006; van der Beek et al., 2006). Furthermore, geochronologic and cosmogenic nuclide studies have also sought to quantify the exhumation history of the Himalaya (e.g., Catlos et al., 2001; Vance et al., 2003; Niemi et al., 2005; Wobus et al., 2005). The models presented in this dissertation focus on the Marsyandi River valley in central Nepal because of a wealth of thermochronologic data (e.g., Edwards, 1995; Brewer et al., 2003; Burbank et al., 2003; Bollinger et al., 2004; Ruhl and Hodges, 2005; Brewer et al., 2006; Huntington et al., 2006; Blythe et al., 2007) and central location within the Himalaya. Data from the Marsyandi region is compared to predicted thermochronometer ages and age distributions to assess the sensitivity of thermochronometer ages to the

processes discussed above.

The goal of this dissertation is to quantify how tectonic, thermal and surface processes affect exhumation histories generated from bedrock and detrital thermochronometer data. In the process of addressing this goal, answers are sought to several motivating questions with respect to rock exhumation in active convergent orogens: (1) What are the dominant thermal processes affecting thermochronometer ages? (2) Which thermochronometer systems and sampling approaches are best suited for use in tectonic versus surface process studies? (3) How large is the difference in exhumation rates calculated from a 1-D versus a 3-D thermal field? (4) What is the potential impact of non-uniform sediment supply by processes like bedrock landsliding on detrital thermochronometer age distributions? (5) How much does groundwater circulation affect exhumation rates calculations? These problems are addressed in this dissertation using a 3-D tectonic, thermal, hydrologic and age prediction model to investigate the influences of rock thermal properties, exhumation, topographic evolution, faulting and groundwater flow on bedrock and detrital thermochronometers.

1.1 Dissertation outline

This work is divided into six chapters, with the primary contributions coming from chapters 2−5. This chapter (Chapter 1) is an introduction and overview and chapter 6 is a summary with the major conclusions from this work. Chapter 2 uses a 3-D tectonic and thermal numerical model and a large bedrock thermochronometer dataset to quantify the Pliocene−Quaternary exhumation history of the central Nepalese Himalaya. Data used in chapter 2 are presented in a companion paper by Blythe et al. (2007). Detrital thermochronology is the focus of both chapters 3 and 4.

Chapter 3 looks at the sensitivity of several detrital thermochronometer systems to different exhumation rates, mass transport kinematic scenarios and topographic evolution. Chapter 4 presents a tectonic model used to model detrital thermochronometer data from the Nepalese Himalaya and explore how different faulting scenarios and bedrock landslides affect predicted detrital age distributions. Lastly, chapter 5 uses a thermal and hydrologic model to investigate how the circulation of groundwater affects the crustal thermal field and exhumation rates calculated using bedrock thermochronometer data.

1.2 Publications and abstracts related to this dissertation

Publications (peer-reviewed)

Whipp, D.M., Jr., T.A. Ehlers, A.E. Blythe, K.W. Huntington, K.V. Hodges, D.W. Burbank (2007), Plio-Quaternary exhumation history of the central Nepalese Himalaya: 2. Thermo-kinematic and thermochronometer age prediction model, *Tectonics*, 26, TC3003, doi:10.1029/2006TC001991 **(Chapter 2)**

Huntington, K.W., T.A. Ehlers, K.V. Hodges, **D.M. Whipp, Jr.** (2007), Topography, exhumation pathway, age uncertainties, and the interpretation of thermochronometer data, *Tectonics*, 26, TC4012, doi:10.1029/2007TC002108

Whipp, D.M., Jr., T.A. Ehlers (in preparation), Effects of denudation, faulting and topographic evolution on detrital thermochronometer data, for submission to *Journal of Geophysical Research, Earth Surface* **(Chapter 3)**

Whipp, D.M., Jr., T.A. Ehlers (in preparation) Landsliding, faulting and the interpretation of detrital thermochronometer data from the Nepalese Himalaya, for submission to *Journal of Geophysical Research, Earth Surface* **(Chapter 4)**

Whipp, D.M., Jr., T.A. Ehlers (2007), Influence of groundwater flow on thermochronometer-

derived exhumation rates in the central Nepalese Himalaya, *Geology*: Vol. 35, No. 9, pp. 851-854, doi:10.1130/G23788A.1 **(Chapter 5)**

Conference abstracts

Whipp, D.M., T.A. Ehlers, A.E. Blythe, D.W. Burbank (2004), Constraining the Tectonic History of the Himalaya in Central Nepal with Low-Temperature Thermochronometry and Numerical Modeling, *Eos Trans. AGU*, 85(47), Fall Meet. Suppl., Abstract T31B-1308

Whipp, D.M. Jr., T.A. Ehlers, A.E. Blythe, K.W. Ruhl, K.V. Hodges, D.W. Burbank (2005), Kinematic and Erosion History of the Greater Himalayan Sequence, Central Nepal, from Integrated Thermochronology and Numerical Modeling, *Geological Society of America Abstracts with Programs*, Vol. 37, No. 7, p. 346

Huntington, K.W., T.A. Ehlers, K.V. Hodges, **D.M. Whipp, Jr.** (2006), Age Uncertainties, Topography, Exhumation Pathway, and the Interpretation of Erosion Rates and Exhumation Kinematics from Thermochronometer Age-Elevation Data, *Eos Trans. AGU*, 87(52), Fall Meet. Suppl., Abstract T11D-0464

Whipp, D.M. Jr., T.A. Ehlers (2006), Influence of groundwater flow on thermochronometer ages and exhumation rates: Insights from the Nepalese Himalaya, *Eos Trans. AGU*, 87(52), Fall Meet. Suppl., Abstract T13E-07

Whipp, D.M. Jr., T.A. Ehlers (2007), Influence of topographic evolution and faulting on detrital thermochronometer ages: Application to the Nepalese Himalaya, *Eos Trans. AGU*, 88(52), Fall Meet. Suppl., Abstract T21E-04

Publications to which I contributed

Schildgen, T., T.A. Ehlers, **D.M. Whipp, Jr.**, K. Whipple, K. Hodges, M. van Soest

(in review with co-authors), Quantifying canyon incision and Andean Plateau surface uplift, southwest Peru: A thermochronometer and numerical modeling approach

Conference abstracts to which I contributed

Schildgen, T., T. Ehlers, M. van Soest, **D. Whipp**, K. Whipple, K. Hodges (2008), Quantifying canyon incision and Andean Plateau surface uplift, southwest Peru: A thermochronometer and numerical modeling approach, *Geophysical Research Abstracts*, Vol. 10, EGU2008-A-08016

Bibliography

Batt, G. E. and Brandon, M. T. Lateral thinking; 2-D interpretation of thermochronology in convergent orogenic settings. *Tectonophysics*, 349(1-4):185–201, 2002.

Bernet, M., van der Beek, P., Pik, R., Huyghe, P., Mugnier, J.-L., Labrin, E. and Szulc, A. Miocene to Recent exhumation of the central Himalaya determined from combined detrital zircon fission-track and U/Pb analysis of Siwalik sediments, western Nepal. *Basin Research*, 18(4):393–412, 2006. doi:10.1111/j.1365-2117.2006.00303.x.

Blythe, A. E., Burbank, D. W., Carter, A., Schmidt, K. and Putkonen, J. Plio-Quaternary exhumation history of the central Nepalese Himalaya: 1. Apatite and zircon fission-track and apatite [U-Th]/He analyses. *Tectonics*, 26, 2007. doi: 10.1029/2006TC001990.

Bollinger, L., Avouac, J., Beyssac, O., Catlos, E., Harrison, T., Grove, M., Goffé, B. and Sapkota, S. Thermal structure and exhumation history of the Lesser Himalaya in central Nepal. *Tectonics*, 23(5), 2004.

Bollinger, L., Henry, P. and Avouac, J. P. Mountain building in the Nepal Himalaya: Thermal and kinematic model. *Earth and Planetary Science Letters*, 244(1-2):58–71, 2006.

Braun, J. Estimating exhumation rate and relief evolution by spectral analysis of age-elevation datasets. *Terra Nova*, 14(3):210–214, 2002a.

Braun, J. Quantifying the effect of recent relief changes on age-elevation relationships. *Earth and Planetary Science Letters*, 200(3-4):331–343, 2002b.

Braun, J. Pecube; a new finite-element code to solve the 3D heat transport equation including the effects of a time-varying, finite amplitude surface topography. *Computers & Geosciences*, 29(6):787–794, 2003.

Brewer, I. and Burbank, D. W. Thermal and kinematic modeling of bedrock and detrital cooling ages in the central Himalaya. *J. Geophys. Res.*, 111(B9):B09409, 2006.

Brewer, I. D., Burbank, D. W. and Hodges, K. V. Modelling detrital cooling-age populations; insights from two Himalayan catchments. *Basin Research*, 15(3):305–320, 2003.

Brewer, I. D., Burbank, D. W. and Hodges, K. V. Downstream development of a detrital cooling-age signal; insights from $^{40}Ar/^{39}Ar$ muscovite thermochronology in the Nepalese Himalaya. In Willett, S. D., Hovius, N., Brandon, M. T. and Fisher, D. M., editors, *Tectonics, Climate and Landscape Evolution*, volume 398 of *Penrose Conference Series*, pages 321–338. Geological Society of America, 2006.

Burbank, D. W., Blythe, A. E., Putkonen, J., Pratt-Sitaula, B., Gabet, E., Oskin, M., Barros, A. and Ojha, T. P. Decoupling of erosion and precipitation in the Himalayas. *Nature*, 426(6967):652–655, 2003.

Catlos, E. J., Harrison, T. M., Kohn, M. J., Grove, M., Ryerson, F. J., Manning, C. E. and Upreti, B. N. Geochronologic and thermobarometric constraints on the evolution of the Main Central Thrust, central Nepal Himalaya. *Journal of Geophysical Research, B, Solid Earth and Planets*, 106(8):16,177–16,204, 2001.

Cerveny, P., Naeser, N., Zeitler, P. K., Naeser, C. and Johnson, N. History of uplift and relief of the Himalaya during the past 18 million years: Evidence from

fission-track ages of detrital zircons from sandstones of the Siwalik Group. In Kleinspehn, K. and Paola, C., editors, *New Perspectives in Basin Analysis*, pages 43–61. Springer-Verlag, New York, 1988.

Copeland, P. and Harrison, T. M. Episodic rapid uplift in the Himalaya revealed by $^{40}Ar/^{39}Ar$ analysis of detrital K-feldspar and muscovite, Bengal Fan. *Geology*, 18(4):354–357, 1990.

Dodson, M. H. Closure temperature in cooling geochronological and petrological systems. *Contributions to Mineralogy and Petrology*, 40(3):259–274, 1973.

Edwards, R. M. $^{40}Ar/^{39}Ar$ geochronology of the Main Central Thrust (MCT) region; evidence for late Miocene to Pliocene disturbances along the MCT, Marsyangdi River valley, west-central Nepal Himalaya. *Journal of Nepal Geological Society*, 10:41–46, 1995.

Ehlers, T. A. Crustal Thermal Processes and the Interpretation of Thermochronometer Data. *Reviews in Mineralogy and Geochemistry*, 58:315–350, 2005.

Ehlers, T. A., Armstrong, P. A. and Chapman, D. S. Normal fault thermal regimes and the interpretation of low-temperature thermochronometers. *Physics of the Earth and Planetary Interiors*, 126:179–194, 2001.

Ehlers, T. A. and Farley, K. A. Apatite (U-Th)/He thermochronometry; methods and applications to problems in tectonic and surface processes. *Earth and Planetary Science Letters*, 206(1-2):1–14, 2003.

Ehlers, T. A., Farley, K. A., Rusmore, M. E. and Woodsworth, G. J. Apatite (U-Th)/He signal of large-magnitude accelerated glacial erosion, southwest British Columbia. *Geology*, 34(9):765–768, 2006.

Ehlers, T. A., Willett, S., Armstrong, P. A. and Chapman, D. S. Exhumation of the Central Wasatch Mountains, Utah: 2. Thermo-kinematics of exhumation and thermochronometer interpretation. *Journal of Geophysical Research*, 108(B3):2173, 2003.

Forster, C. B. and Smith, L. The influence of groundwater flow on thermal regimes in mountainous terrain; a model study. *Journal of Geophysical Research, B, Solid Earth and Planets*, 94(7):9439–9451, 1989.

Harrison, T. M., Ryerson, F. J., Le Fort, P., Yin, A., Lovera, O. M. and Catlos, E. J. A late Miocene-Pliocene origin for the central Himalayan inverted metamorphism. *Earth and Planetary Science Letters*, 146(1-2):E1–E7, 1997.

Hubbard, M. S. and Harrison, T. M. $^{40}Ar/^{39}Ar$ age constraints on deformation and metamorphism in the Main Central Thrust zone and Tibetan Slab, eastern Nepal Himalaya. *Tectonics*, 8(4):865–880, 1989.

Huntington, K. W., Blythe, A. E. and Hodges, K. V. Climate change and Late Pliocene acceleration of erosion in the Himalaya. *Earth and Planetary Science Letters*, 252(1-2):107–118, 2006.

Huntington, K. W., Ehlers, T. A., Hodges, K. V. and Whipp, Jr., D. M. Topography, exhumation pathway, age uncertainties, and the interpretation of erosion rates from thermochronometer data. *Tectonics*, 26, 2007. doi:10.1029/2007TC002108.

Macfarlane, A. M., Hodges, K. V. and Lux, D. A structural analysis of the Main Central Thrust zone, Langtang National Park, central Nepal Himalaya. *Geological Society of America Bulletin*, 104(11):1389–1402, 1992.

Mancktelow, N. S. and Grasemann, B. Time-dependent effects of heat advection and

topography on cooling histories during erosion. *Tectonophysics*, 270(3-4):167–195, 1997.

Niemi, N. A., Oskin, M., Burbank, D. W., Heimsath, A. M. and Gabet, E. J. Effects of bedrock landslides on cosmogenically determined erosion rates. *Earth and Planetary Science Letters*, 237(3-4):480–498, 2005.

Person, M. and Garven, G. A sensitivity study of the driving forces on fluid flow during continental-rift basin evolution. *Geological Society of America Bulletin*, 106(4):461–475, 1994.

Person, M., Toupin, D. and Eadington, P. One-dimensional models of groundwater flow, sediment thermal history and petroleum generation within continental rift basins. *Basin Research*, 7(1):81–96, 1995.

Ring, U., Brandon, M. T., Willett, S. D. and Lister, G. S. Exhumation processes. *Geological Society Special Publications*, 154:1–27, 1999.

Ruhl, K. W. and Hodges, K. V. The use of detrital mineral cooling ages to evaluate steady state assumptions in active orogens; an example from the central Nepalese Himalaya. *Tectonics*, 24:no.4, 14, 2005.

Smith, L. and Chapman, D. S. On the thermal effects of groundwater flow - 1. Regional scale systems. *Journal of Geophysical Research*, 88(B1):593–608, 1983.

Sorkhabi, R. B., Stump, E., Foland, K. A. and Jain, A. K. Fission-track and $^{40}Ar/^{39}Ar$ evidence for episodic denudation of the Gangotri granites in the Garhwal Higher Himalaya, India. In Burg, J.-P., editor, *Tectonophysics*, volume 260, pages 187–199. Elsevier, Amsterdam, 1996.

Stüwe, K. and Hintermüller, M. Topography and isotherms revisited: the influence of laterally migrating drainage divides. *Earth and Planetary Science Letters*, 184(1):287–303, 2000.

Stüwe, K., White, L. and Brown, R. The influence of eroding topography on steady-state isotherms; application to fission track analysis. *Earth and Planetary Science Letters*, 124(1-4):63–74, 1994.

Szulc, A. G., Najman, Y., Sinclair, H. D., Pringle, M., Bickle, M., Chapman, H., Garzanti, E., Ando, S., Huyghe, P., Mugnier, J.-L., Ojha, T. and DeCelles, P. Tectonic evolution of the Himalaya constrained by detrital ^{40}Ar-^{39}Ar, Sm-Nd and petrographic data from the Siwalik foreland basin succession, SW Nepal. *Basin Research*, 18(4):375–391, 2006. doi:10.1111/j.1365-2117.2006.00307.x.

Thiede, R. C., Arrowsmith, J. R., Bookhagen, B., McWilliams, M. O., Sobel, E. R. and Strecker, M. R. From tectonically to erosionally controlled development of the Himalayan Orogen. *Geology*, 33(8):689–692, 2005.

Thiede, R. C., Bookhagen, B., Arrowsmith, R., Sobel, E. R. and Strecker, M. R. Climatic control on rapid exhumation along the southern Himalayan Front. *Earth and Planetary Science Letters*, 222(3):791–806, 2004.

van der Beek, P., Robert, X., Mugnier, J.-L., Bernet, M., Huyghe, P. and Labrin, E. Late Miocene - Recent exhumation of the central Himalaya and recycling in the foreland basin assessed by apatite fission-track thermochronology of Siwalik sediments, Nepal. *Basin Research*, 18(4):413–434, 2006. doi:10.1111/j.1365-2117.2006.00305.x.

Vance, D., Bickle, M., Ivy-Ochs, S. and Kubik, P. W. Erosion and exhumation in

the Himalaya from cosmogenic isotope inventories of river sediments. *Earth and Planetary Science Letters*, 206(3-4):273–288, 2003.

Vannay, J. C. and Hodges, K. V. Tectonometamorphic evolution of the Himalayan metamorphic core between the Annapurna and Dhaulagiri, central Nepal. *Journal of Metamorphic Geology*, 14(5):635–656, 1996.

Wobus, C. W., Heimsath, A., Whipple, K. X. and Hodges, K. V. Active out-of-sequence thrust faulting in the central Nepalese Himalaya. *Nature*, 434:1008–1011, 2005.

Wobus, C. W., Hodges, K. V. and Whipple, K. X. Has focused denudation sustained active thrusting at the Himalayan topographic front? *Geology*, 31(20):861–864, 2003.

CHAPTER II

Plio-Quaternary exhumation history of the central Nepalese Himalaya: 2. Thermokinematic and thermochronometer age prediction model

2.1 Abstract

In the Himalaya and other active convergent orogens, linear relationships between thermochronometer sample age and elevation are often used to estimate long-term exhumation rates. In these regions, high-relief topography and nonvertical exhumation pathways may invalidate such one-dimensional (1-D) interpretations and lead to significant errors. To quantify these errors, we integrate apatite fission track (AFT) ages from the central Himalaya with a 3-D coupled thermokinematic model, from which sample cooling ages are predicted using a cooling-rate-dependent algorithm. By changing the slip partitioning between faults near the Main Central thrust and the Main Frontal thrust system at the Himalayan range front, we are able to explore the significance of different tectonic scenarios on predicted thermochronometer ages. We find that the predicted AFT cooling ages are not sensitive to the different slip partitioning scenarios but depend strongly on erosion rate: Predicted ages are most

Official citation:
Whipp, D.M., Jr., T.A. Ehlers, A.E. Blythe, K.W. Huntington, K.V. Hodges, D.W. Burbank, Plio-Quaternary exhumation history of the central Nepalese Himalaya: 2. Thermo-kinematic and thermochronometer age prediction model, *Tectonics*, 26, TC3003, doi:10.1029/2006TC001991, 2007

consistent with kinematic models that produce erosion rates of 1.8−5.0 mm/yr. This range is considerably smaller than that derived from regression lines through the data (−2.6−12.2 mm/yr). The pattern of observed AFT ages shows more complexity than our models predict. None of the kinematic scenarios are able to fit >80% of all of the AFT data, most likely because erosion is spatially variable. Such complexities notwithstanding, we conclude that the use of thermokinematic modeling and thermochronologic data sets to explore detailed fault kinematics in rapidly eroding active orogens has great promise but requires integration of higher-temperature (>∼350°C) data sets to maximize effectiveness.

2.2 Introduction

Climate-driven erosion has been hypothesized to drive deformation along the Himalayan front (Beaumont et al., 2001; Hodges et al., 2001, 2004; Thiede et al., 2004). Detailed studies that quantify long-term erosion rates are therefore needed as a first step toward calibrating geodynamic and landform evolution models where erosional processes are coupled with deformation (e.g., Beaumont et al., 1992; Willett, 1999). In some orogens, zones of high precipitation have been suggested to correspond with regions of enhanced long-term erosion rates (e.g., Reiners et al., 2003); however, in the Himalaya, increased erosion rates have also been argued to be decoupled from climate forcing (e.g., Burbank et al., 2003) and the extent of climate-erosion coupling has been shown to vary temporally (e.g., Thiede et al., 2004, 2005). An ideal location to address some of these issues is the central Nepalese Himalaya (Figure 2.1a), where the late Cenozoic uplift of the Tibetan Plateau may have significantly increased the strength of the Indian Monsoon. This strengthening could have increased precipitation and potentially focused erosion on the southern margin of the plateau

(Molnar et al., 1993; Ruddiman et al., 1997). When combined with evidence of late Miocene−Quaternary renewal of faulting within the interior of the Himalayan orogenic wedge (Seeber and Gornitz, 1983; Macfarlane et al., 1992; Harrison et al., 1997; Catlos et al., 2001; Hodges et al., 2004; Wobus et al., 2005), the timing of the hypothesized increase in erosion suggests that climate-driven erosion may have induced tectonic activity through modification of gravitational body forces. The objective of this study is to take an initial step toward testing the previous hypothesis by quantifying the rates and spatial variations in erosion across a drainage basin within the Himalayan front.

In general, the major south vergent structures in the Himalaya developed through sequential activation of faults south of the previous deformation front (e.g., Hodges, 2000). As a new fault in a more distal position is initiated, slip along more hinterland faults is commonly thought to have ceased. Lavé and Avouac (2000) suggest that nearly all of the Holocene convergence between India and southern Tibet has been accommodated by the young range-bounding fault, the Main Frontal thrust (MFT): an observation that could be consistent with slip solely on the most distal fault. However, thermochronologic, geomorphic, and cosmogenic isotope evidence support the idea that faulting may occur out of sequence near the Main Central thrust (MCT) and within its proximal footwall (1−30 km). For example, within the interior of the Himalayan wedge, faults near the MCT trace may have been active during the late Miocene and Pliocene, and could be active today (Wobus et al., 2003; Hodges et al., 2004; Wobus et al., 2005). Very young cooling ages and cosmogenic nuclide data for samples collected from within the MCT hanging wall suggest erosion at average rates of ∼1−3 mm/yr since the Pliocene (Burbank et al., 2003; Vance et al., 2003; Thiede et al., 2004; Niemi et al., 2005). Burbank et al. (2003) reported uniformly

young apatite fission track (AFT) cooling ages in the hanging wall of the MCT in the Annapurna Himalaya of central Nepal, a region in which precipitation is spatially variable from $\sim$0.5$-$4.0 m/yr. As a consequence, they found no evidence of a close coupling of precipitation with rapid exhumation in central Nepal. However, the mean annual precipitation records and average exhumation rates differ in timescale by several orders of magnitude, so direct a comparison may have limited utility. In NW India, Thiede et al. (2004, 2005) found their youngest white mica $^{40}Ar/^{39}Ar$ cooling ages within the hanging wall of the Munsiari thrust. The Munsiari thrust is generally not recognized in Nepal, but occupies a structural position beneath the Vaikrita thrust, a fault that most researchers correlate with the MCT in central Nepal (Valdiya, 1980). Conversely, the AFT data of Thiede et al. (2004, 2005) were youngest within areas of locally heavy precipitation, suggesting a coupling of climate and erosion over the time during which their AFT samples cooled. Hodges et al. (2004) found that not only were young AFT cooling ages correlated with locally heavy precipitation, but they observed evidence of Quaternary faulting near the MCT in central Nepal. Their observations support theory-based models involving a coupling between erosion along the Himalayan range front and southward extrusion of middle to lower crustal material (Beaumont et al., 2001; Hodges et al., 2001).

Thermochronometer data used by Burbank et al. (2003), Thiede et al. (2004, 2005) and Hodges et al. (2004) record the cooling history of exhumed samples, but the interpretation of cooling ages from an active orogen is not simple. For example, the apparent exhumation rates derived from the slope of AFT cooling ages versus sample elevation (Thiede et al., 2004; Blythe et al., 2007) rely on simplifying assumptions about the subsurface thermal field and exhumation history. In some cases, these assumptions can introduce large (20$-$200%) errors in the interpreted ex-

humation rates (Stüwe et al., 1994; Mancktelow and Grasemann, 1997; Ehlers, 2005). True exhumation rates can be better constrained using thermokinematic modeling to simulate more realistic subsurface thermal fields and thermal histories of the thermochronometer samples (Batt and Brandon, 2002; Ehlers et al., 2003; Braun and Robert, 2005). Previous thermal and kinematic modeling studies of the Himalaya have approximated the exhumation pathways and the resulting thermal field as two-dimensional with slip on only one fault (Henry et al., 1997; Bollinger et al., 2006; Brewer and Burbank, 2006). Using a two-dimensional (2-D) approximation neglects the three-dimensional (3-D) influence of topography and fault geometry, which can be significant at high slip rates.

In this study, we use a 3-D thermokinematic model of the central Nepalese Himalaya (Figure 2.1) to predict thermochronometer cooling ages that are compared to a large data set of AFT ages (Figure 2.2). The AFT data are presented and discussed in detail in the companion paper by Blythe et al. (2007). The primary goal of this study is to use the model to quantify average erosion rates over the time span of AFT ages. A secondary goal is to determine whether the cooling age data can be used to differentiate among various tectonic models. We explore four tectonic scenarios in which Indo- Tibetan convergence is partitioned between the MFT and MCT (Figures 2.1c and 2.1d). The model uses fault kinematics and geometries that vary in three dimensions and accounts for the first-order influence of topography (e.g., valley and ridge positions), which will influence the predicted sample cooling ages. We investigate exhumation and faulting histories of the late Pliocene to Quaternary times, the age range of available AFT data (Blythe et al., 2007). By comparing the ages predicted from the 3-D thermal model to the data, we are able to quantify potential errors in exhumation rates derived from regression line slopes of sample

age versus elevation and infer spatial variations in the erosion history of the central Nepalese Himalaya. Also, by varying overthrusting rates on the MCT and MFT, we address the utility (or lack thereof) of low-temperature thermochronometer data for determining the magnitude of out-of-sequence thrusting in a rapidly eroding region.

2.3 Geologic Setting

The spectacular peaks of the Himalaya mark the southern margin of a broad region of deformation developed in response to the collision and continued convergence between India and Eurasia since the early Paleogene ($\sim$65$-$50 Ma) (see reviews by Gansser (1964), Le Fort (1975), and Hodges (2000)). The range is typically divided into four tectonostratigraphic zones: the Tibetan zone, Greater Himalayan zone, the Lesser Himalayan zone and the Subhimalayan zone (terminology of Hodges (2000)). Zone contacts correspond to major fault zones that can be traced along strike for much of the length of the orogen. The Paleozoic to Paleogene primarily marine sedimentary rocks of the Tibetan sequence (TS) are bounded on the north by the Indus-Tsangpo suture zone and on the south by lowangle, predominantly normal faults of the South Tibetan fault system (STF). Structurally beneath the TS are metamorphic and igneous rocks of the Greater Himalayan sequence (GHS), which are bounded by the MCT to the south. The dominantly clastic metasedimentary rocks of the Lesser Himalayan sequence (LHS) are bounded to the south by the Main Boundary thrust (MBT). The Subhimalayan zone comprises Neogene and younger foreland basin sediments in the hanging wall of the MFT.

Since the early Miocene, much of the postcollisional convergence between India and Eurasia has been accommodated by a series of southward vergent, southward younging thrust systems. The oldest of these, the Main Central thrust system, devel-

oped and experienced its principal movement in latest Oligocene−early Miocene time (Hubbard and Harrison, 1989; Hodges et al., 1996; Coleman, 1998). The structurally highest portions of the Lesser Himalayan zone, directly beneath the main splay of the MCT zone, have experienced a complex deformation history related to post-early Miocene southward thrusting. Some of this structure is likely to be related to MCT slip, but other studies (e.g., DeCelles et al., 2001; Robinson et al., 2003; Pearson and DeCelles, 2005) have argued convincingly that most slip can be attributed to Middle Miocene development of the Ramgarh thrust and a Lesser Himalayan duplex system as deformation stepped progressively southward into the Lesser Himalayan zone. The principal locus of surface shortening is generally thought to have shifted to the MBT and, eventually, to the MFT zones in late Miocene−Pliocene time (e.g., Hodges, 2000, and references therein). Most researchers regard the MFT as projecting downdip, across a buried ramp beneath the Lesser Himalayan−Greater Himalayan zone transition, to connect with a master décollement referred to as the Main Himalayan thrust (MHT) (e.g., Lyon-Caen and Molnar, 1983; Schelling and Arita, 1991; Pandey et al., 1995).

Despite this general southward progression of thrust deformation, several studies have yielded convincing evidence of significant out-of-sequence thrusting over the early Miocene−Recent interval (Brun et al., 1985; Grujic et al., 1996; Hodges et al., 1996; Searle, 1999). Of particular interest to our study is the evidence for very young out-of-sequence thrusting near the trace of the MCT system and within the northernmost Lesser Himalayan zone. Seeber and Gornitz (1983) first suggested the possibility of out-of-sequence thrusting along the MCT trace based on an analysis of river profiles as they crossed the Greater Himalayan−Lesser Himalayan zone boundary. Subsequently, very young $^{40}Ar/^{39}Ar$ cooling ages from rocks at this structural level

were attributed to late stage reactivation of the MCT system by Macfarlane (1993), although both Copeland et al. (1991) and Edwards (1995) suggested an alternative interpretation based on the possibility of hydrothermal resetting. The documentation by Harrison et al. (1997) and Catlos et al. (2001) of late Miocene−Pliocene metamorphic monazite growth during deformation at this level renewed the argument for out-of-sequence thrusting, but some of the strongest evidence in favor of this process comes from integrated structural, geomorphic, and thermochronologic studies in central Nepal (Wobus et al., 2003; Hodges et al., 2004; Wobus et al., 2005; Huntington and Hodges, 2006). These findings show that brittle thrust structures within a few kilometers of the outcrop trace of the principal strand of the MCT system have experienced slip in late Pliocene−Quaternary time and, as a consequence, separate domains with distinctive patterns of mineral cooling ages and Quaternary exhumation histories. Evidence for Quaternary out-of-sequence faulting, however, conflicts with the work of Lavé and Avouac (2000) who suggest little to no out-of-sequence thrusting has occurred during the Holocene. This conflict shows that the magnitude of post-late Miocene out-of-sequence thrusting is unclear. If there has been a significant amount of out-of-sequence thrusting, presumably this shortening is transferred downdip to the MHT where the out-of-sequence structures splay off of that master décollement (Hodges et al., 2001).

2.4 Thermochronometer Data Set

Thermochronometer ages yield the time since samples cooled below their effective closure temperature (Dodson, 1973). When combined with estimates of the distance traveled from the closure temperature isotherm to the surface, the data provide a means for determining long-term ($>10^5$ years) exhumation rates. Higher-

temperature thermochronometers have closure temperatures at greater depths, thus the exhumation rates calculated from those systems integrate over longer time periods and greater distances. Lower-temperature AFT data are used here to quantify rock exhumation histories. For comparison to other data sets, higher-temperature muscovite $^{40}Ar/^{39}Ar$ ages are predicted from the thermokinematic model discussed below. AFT cooling ages are calculated using the density of damage trails created by spontaneous fission of ^{238}U at a known rate that are preserved within the crystal lattice of apatite in a rock sample (see reviews by Donelick et al. (2005) and Tagami and O'Sullivan (2005)). Muscovite $^{40}Ar/^{39}Ar$ cooling ages are based on measuring the retention of ^{40}Ar derived from the natural decay of ^{40}K in muscovite (see review by Harrison and Zeitler (2005)). Apatite fission-track and muscovite $^{40}Ar/^{39}Ar$ cooling ages have cooling-rate-dependent closure temperatures of $\sim$100$-$140°C and $\sim$350$-$425°C, respectively, for cooling rates of 2$-$100°C/Myr (Robbins, 1972; Hames and Bowring, 1994; Donelick et al., 2005; Ehlers et al., 2005; Tagami and O'Sullivan, 2005).

Blythe et al. (2007) provide bedrock AFT cooling ages that present a detailed exhumation history for the Marsyandi River catchment in central Nepal. We use 82 AFT ages reported by Blythe et al. (2007) to compare to ages predicted from a thermokinematic model. The AFT data are divided into ten transects to aid in observing any spatial variations in exhumation (Figure 2.2). We briefly summarize the data used here, and the reader is referred to Blythe et al. (2007) for a more thorough discussion.

The AFT sample ages range from <0.4 (95% confidence interval) to 3.8 $\pm$ 1.0 Ma (2σ uncertainty) across the study region and samples span an elevation range of 474$-$4621 m. There is no clear trend in the spatial distribution of ages across

the study area, although very young ages (<0.5 Ma) tend to occur at low elevation, near the rivers. The simplest way to get an estimate of exhumation rates from data collected in vertical transects is to plot the sample ages as a function of elevation (Wagner and Reimer, 1972; Wagner et al., 1977), where the slope of a regression line through the data is the apparent exhumation rate. Although these transects are not strictly vertical, age-elevation regressions can be carried out and the range of apparent exhumation rates from the slope of a weighted least squares regression of each transect are highly variable. The apparent rates range between −12.1 and 12.2 mm/yr, where negative rates are from transects with inverted age-elevation trends.

2.5 The Model

Although calculating exhumation rates from regression lines on age-elevation plots is a common way to interpret data, large uncertainties are possible when samples are collected over a horizontal distance that is greater than the wavelength over which topography affects the subsurface closure isotherm geometry. Additional problems are possible if the samples are carried in a thrust sheet with a large lateral component of motion, where nonvertical transport can lead to additional uncertainty. To avoid these uncertainties, it is useful to estimate the distance a sample has traveled since passing through the closure temperature for that system. In the simplest case, that distance can be determined by calculating a steady state one-dimensional (1-D) vertical thermal profile or using a constant geothermal gradient. Assuming vertical sample exhumation, the exhumation rate is calculated by measuring the distance from the surface to the closure temperature isotherm and dividing that distance by the sample age. In active orogens, however, the thermal field is multidimensional and

commonly transient with rock exhumation paths that have significant lateral and vertical components (e.g., Stüwe et al., 1994; Mancktelow and Grasemann, 1997; Ehlers et al., 2001; Batt and Brandon, 2002; Ehlers et al., 2003). The interpretation of thermochronometer data from such settings is more complex and benefits from the use of thermal models to generate realistic subsurface thermal fields. The model we use consists of three components: (1) a kinematic model (Figures 2.1c and 2.1d) that prescribes nodal advection velocities for (2) a thermal finite element model (Figure 2.3), which calculates temperature as a function of location and kinematic field, and (3) a thermochronometer age prediction model that generates sample ages at the surface as a function of their cooling rate. The following three sections detail the three model components. Table 2.1 lists the physical dimensions of the model and free parameters explored.

2.5.1 Kinematic Model

In this study the fault kinematics of the Himalayan front are considered by partitioning slip between the MCT and MFT, assuming a constant convergence rate between India and Tibet of 20 mm/yr. We also take into account subduction of the Indian Shield and underplating of material from the Indian plate into the overriding wedge (Figures 2.1b−2.1d). Potential slip on the STF is not considered because the displacement history of the STF over the range of ages covered by the AFT data is unclear and poorly constrained in comparison with activity on the MFT or MCT (e.g., Hodges, 2000). Furthermore, one model was run with the STF active at the same rate as the MCT and we saw no difference in the model predicted AFT ages within the sample uncertainties. We assume a shortening direction of 198° across thrust faults and that the Indian Shield moves north at 018°. The shortening direction is subparallel to the transport direction inferred from measured stretching

lineations in the MCT shear zone (Brunel, 1986) and consistent with the present-day convergence direction between the Tibetan Plateau and India as measured by GPS (Bilham et al., 1997; Larson et al., 1999; Wang et al., 2001; Jouanne et al., 2004; Zhang et al., 2004).

Faults in the model are approximated as planar surfaces based on the geologic cross section of Lavé and Avouac (2000) (Figures 2.1b−2.1d) and tectonic map of Searle and Godin (2003) (Figure 2.2). The MFT splays off of the MHT and strikes perpendicular to the shortening direction at 288°. The MFT-MHT system dip angle varies with depth as shown in Figures 2.1c and 2.1d. The shallow southern section dips gently at 7°, the middle ramp section dips at 20° and the deep northern section dips at 8°, consistent with surface observations and microseismicity (Lavé and Avouac, 2000). The strike of the MCT is a linear approximation of the mapped MCT II trace of Searle and Godin (2003) (Figure 2.2) and it dips 28° NNE. The STF is not active in the kinematic models, but is included in the model geometry because it separates two model rock types with significantly different material properties: the GHS and TS. The STF is approximated as three linear segments with dip angles parallel to the MCT at 28° (Macfarlane et al., 1992; Hodges et al., 1996; Searle and Godin, 2003). The structural geometry does not vary with time because most of our cooling ages are very young (<3 Ma). Although the structural geometry is likely to have changed over longer timescales, we suggest that this is the simplest scenario that still captures the plausible kinematic scenarios for Plio-Quaternary faulting. Comparison to the data later in the paper allows us to evaluate whether this degree of complexity is sufficient.

Slip across faults is prescribed to honor the present-day geodetic convergence rate between India and Tibet of ∼20 mm/yr (Bilham et al., 1997; Larson et al., 1999;

Wang et al., 2001; Jouanne et al., 2004). Convergence is partitioned between overthrusting on the MFT and MCT and underthrusting of the Indian Shield beneath the Himalaya. It is important to note that in our model, overthrusting and underthrusting refer to the horizontal component of motion, and should not be confused with the fault slip rate. The rate of underthrusting, $v_{underthrusting}$, is adjusted to honor the 20 mm/yr convergence rate depending on the overthrusting rate:

$$v_{\text{underthrusting}} = v_{\text{obs}} - (v_{\text{MFT}} + v_{\text{MCT}}) \tag{2.1}$$

where v_{obs} is the Indo-Tibetan convergence rate and v_{MFT} and v_{MCT} are the overthrusting velocities of the MFT and MCT.

The model uses the kink-band, fault-bend folding method of the thrust sheets (Suppe, 1983) and slip occurs parallel to the model fault planes. Mass is conserved in the model. The slip rate on an individual structure is a function of the dip angle of the structure and the convergence rate across that structure. For each fault, the slip rate is calculated as

$$v_{\text{slip,MFT}} = (|v_{\text{MFT}}| + |v_{\text{underthrusting}}|) \,/\, \cos\theta_{i,\text{MFT}} \tag{2.2a}$$

$$v_{\text{slip,MCT}} = |v_{\text{MCT}}| / \cos\theta_{\text{MCT}} \tag{2.2b}$$

where $\theta_{i,MFT}$ is the dip angle of the ith dip plane of the MFT and θ_{MCT} is the dip angle of the MCT. Note that because the convergence rates are fixed in the model, the fault slip rate on different dip sections of the MFT will vary. Because of this, slip on individual structures will be referred to by the overthrusting rate across that structure. The ranges of overthrusting rates explored in the model are 1−15 mm/yr across the MFT and 0−8 mm/yr across the MCT, as shown in Table 2.1.

One objective of this study is to quantify the range of possible erosion rates over the last ∼3 Myr, the time covered by the AFT data. Rock exhumation in

this region of the Himalaya occurs by erosion, and because the model geometry and topography are static, the exhumation and erosion rates are dictated by the kinematic model. In this paper, we define the model exhumation rate to be the rate at which material approaches the model surface from depth parallel to the transport direction because the exhumation pathways have a significant component of lateral motion. This definition is slightly different than that used in many studies, where the exhumation rate is strictly related to vertical transport (e.g., Ring et al., 1999). In contrast, we define the model erosion rate to be the vertical component of the exhumation rate prescribed in the kinematic model. Thus the erosion rate at a given position (x, y, z) in the model, $v_z(x, y, z)$, is a function of the orientation of underlying structures and rate of overthrusting. The erosion rate $v_z(x, y, z)$ is

$$v_z(x,y,z) = \begin{cases} v_{\mathrm{MFT}} \tan\theta_{i,\mathrm{MFT}} & \text{if } \{y_{\mathrm{MFT}} < y < y_{\mathrm{MCT}}\} \\ v_{\mathrm{MFT}} \tan\theta_{i,\mathrm{MFT}} + v_{\mathrm{MCT}} \tan\theta_{\mathrm{MCT}} & \text{if } \{y > y_{MCT}\} \end{cases} \tag{2.3}$$

where y_{MFT} and y_{MCT} are the y coordinates of the MFT and MCT, at the x coordinate and z coordinate of the point of interest. The coordinate system has the x coordinate increasing to the east, y coordinate increasing to the north and z coordinate positive upward, as shown in Figure 2.3.

Previous work has estimated long-term erosion rates in the Greater Himalayan zone to be several millimeters per year (e.g., Burbank et al., 2003; Thiede et al., 2004). Using these results as a starting point, we chose combinations of fault kinematics that generate erosion rates between $\sim$1$-$6 mm/yr in the Greater Himalayan zone. The kinematic simulations were divided into four subsets: (1) the MFT is the only active structure, (2) the MFT and MCT have equal overthrusting rates, (3) the MFT has a larger overthrusting rate than the MCT, and (4) the MCT has a larger overthrusting rate than the MFT. We did not simulate cases where the MCT was the only active

structure because those models would not exhume samples south of the model MCT to the surface.

We assume an incompressible material and conservation of mass. We also assume that the fault locations are fixed in the model, such that the MCT does not move with respect to the MFT when the MFT is active. Because of the steady state topography and the above assumptions, in kinematic scenarios b−d (e.g., Figure 2.1d), some of the subducting Indian Shield material is incorporated into the base of the LHS via underplating. This underplating balances the erosional removal of material south of the MCT.

2.5.2 Thermal Model

The background thermal state of continental crust depends on heat flow into the base of the crust and material properties (e.g., thermal conductivity, radiogenic heat production). Deviations from this background state can occur in regions of active faulting, erosion, sedimentation, and/or with significant topographic relief (Stüwe et al., 1994; Mancktelow and Grasemann, 1997; Braun, 2005; Ehlers, 2005). Furthermore, in regions of rapid faulting such as the Himalaya, shear heating along faults can be significant (Graham and England, 1976; Barton and England, 1979; Arita, 1983; England et al., 1992; Henry et al., 1997). We calculate the 3-D thermal field of a 140 × 84 × 50 km (L × W × D) region within the Himalayan front. Processes accounted for in the model include rock uplift due to faulting, erosion, topography, basal heat flow variations, and thermophysical material properties.

The subsurface thermal field is calculated using the steady state advection-diffusion equation:

$$\frac{\nabla(K\nabla T)}{\rho c} - \bar{v}\nabla T = -\frac{A}{\rho c} \tag{2.4}$$

where T is temperature and $\bar{v}$ is the material velocity. K, A, r and c are the thermal conductivity, radiogenic heat production per unit volume, density and heat capacity, respectively. The reasons for using the steady state advection-diffusion equation are discussed in section 2.5.3. Our modeling approach is similar to that of Ehlers and Farley (2003) and uses the finite element program FRACTure (Kohl and Hopkirk, 1995). The thermal model is coupled to the kinematic model detailed in section 2.5.1 and used to solve Equation (2.4) in 3-D in an Eulerian (spatial) reference frame. By using a 3-D solution to Equation (2.4), we are able to account for the effects of advection in three dimensions, short-wavelength (valley-ridge) and long-wavelength (Tibetan Plateau−Gangetic Plains) topography, and the effects of various material properties.

We minimized the N-S spatial extent of the model, but kept it large enough to prevent the lateral boundary conditions from generating an unrealistic thermal influence because of the long-wavelength topography (Table 2.1). The upper surface of the model is derived from a 250-m digital elevation model of the region and has a constant temperature boundary condition. Upper surface temperatures were fixed at 14°C at sea level and decreased at an atmospheric lapse rate of 7°C per kilometer elevation increase. The basal boundary condition in the model is a constant flux, which is varied from 20 to 50 mW/m^2. These basal heat fluxes are in agreement with the values calculated from measurements of surface heat flow out of the Indian Shield (Roy and Rao, 2000). Radiogenic heat production is set to 0.8 μmW/m^3 for the Indian Shield and LHS which also yields surface heat flow values similar to the observations (Roy and Rao, 2000). For the TS an average sedimentary rock heat production of 0.5 μW/m^3 is used (Rybach, 1976). Heat production in the GHS is varied from 0.8 to 3.0 μW/m^3, similar to the range represented by previous

measurements (England et al., 1992). Thermal conductivity measurements from rocks sampled in the study area average 3.35 ± 0.85 W/m K at room temperature (Table A.1). Thermal conductivity for the model domain is fixed at either 2.5 or 3.0 W/m K, similar to the temperature-corrected measured values (Sass et al., 1992; Clauser and Huenges, 1995). The ranges of material properties investigated are summarized in Table 2.1.

2.5.3 Model Assumptions

We make several simplifying assumptions in an effort to capture the important thermal influences, but not overcomplicate the model.

Assumption 1: Topographic Steady State

The assumption of topographic steady state was used here for several reasons. First, at this point we have no clear way of constraining how topography has changed over the last >3 Ma. The additional free parameters required to simulate evolving topography would not be well constrained and we have chosen instead to work with the smallest set of assumptions possible in the modeling. Second, several lines of evidence suggest that major changes in the position of fluvial systems have not occurred recently. If relief changes occurred, they may have happened over relatively short timescales (<10 kyr) (Gabet et al., 2004), and the magnitude of relief change is likely smaller than the average AFT sample age uncertainties. Although little evidence of the paleoriver locations exists, the south flowing rivers draining the southern margin of the Tibetan Plateau are suggested to have flowed along similar paths for several million years (e.g., Gupta, 1997). Work in progress is testing our assumption of topographic steady state over the time period samples cooled. More specifically, we are evaluating what data and modeling approaches are required to quantify changes

in relief and drainage locations in the Marsyandi valley (e.g., approach of van der Beek et al. (2002) and Braun and van der Beek (2004)).

Stüwe et al. (1994) showed from a 2-D thermal model that, at increasingly high erosion rates, the AFT closure isotherm will move to shallower levels in the crust and more closely mimic the overlying topography. Assuming a horizontal AFT closure isotherm beneath 5 km high topography, the difference in distance from the isotherm to surface under peaks versus valleys is 5 km. At an erosion rate of 5 mm/yr, the depth to the isotherm becomes shallower and the difference in isothermal depth between peaks and valleys decreases to ∼1 km (Stüwe et al., 1994). Although the shorter-wavelength relief between valleys and ridges in our study area may have changed over the time interval to which our samples are sensitive (average AFT cooling age of 1.0 Ma), we have no reason to doubt that the major topographic influences were likely in place for the time during which most samples cooled.

Braun (2002) showed that longer-wavelength topography will cause the subsurface isotherms to be disturbed to greater depths than shorter-wavelength topography. Thus lower-temperature thermochronometers will be more sensitive to shorter-wavelength topography than higher-temperature systems. For example, the largest topographic influences on subsurface thermal gradients are the long-wavelength, north-south elevation changes across the Himalayan front and shorter-wavelength, east-west oriented topography across the Marsyandi drainage. Predicted $^{40}Ar/^{39}Ar$ cooling ages are more likely sensitive to the long-wavelength topography (Brewer et al., 2003), whereas the shorter-wavelength, valley-ridge topography is likely to influence the AFT ages. The first-order, valley-ridge topographic features are at least as old as most of the AFT cooling ages (∼1.0 Ma) and the Tibetan Plateau, the major north-south topographic influence, is thought to have been at high elevation since

at least the late Miocene (Harrison et al., 1992; Tapponnier et al., 2001). Second-order variations in the topography through time, such as several hundred meters of changing relief across the Marsyandi drainage or variations in shorter-wavelength topography, are possible in this area, but are not constrainable with the data due to large uncertainties in sample ages. For additional discussion of how the wavelength of topography can influence thermochronometer ages, see Braun (2002).

AFT sample locations where steady state topography is clearly unrealistic have been excluded from our analysis (Bagarchhap, Chame, Dharapani transects; A−C in Figure 2.2). For these transects, the sampled ridges are oriented such that they have steeper slopes than the fault transporting those samples to the surface in the model. When particles coincident with the sample locations are tracked back in time to generate thermal histories, those samples exit the model domain, travel through the air above the model surface and later reenter the model. This generates unrealistic predicted cooling ages. We instead focus on samples that have had the simplest exhumation history, where particle tracking generates simple thermal histories (Khudi, Jagat, Nagi Lek, Syange, Tal transects; D−J in Figure 2.2). Although significant topographic change has likely occurred in this area, we have minimized its effect on our interpretation by focusing on the vertical transects sensitive to the dominant topographic features in the region. The remaining transect locations (Bagarchhap, Chame, Dharapani transects; A−C in Figure 2.2) are the focus of work in progress interpreting the topographic evolution of subsidiary drainages in the region.

Assumption 2: Thermal Steady State

Stüwe et al. (1994) showed that a transient thermal field will approach steady state more quickly at higher erosion rates. For example, at erosion rates of 1 to 5 mm/yr, thermal equilibration within 20% of steady state is achieved in 20 to

4 Myr, respectively. If the Himalayan front has been present and eroding since at least the late Miocene (Harrison et al., 1992; Tapponnier et al., 2001), then subsurface thermal field has likely approximated a steady state within the uncertainties in the data.

Assumption 3: Significant Shear Heating

Shear heating is included to account for frictional heating on the fault planes using the methods of Henry et al. (1997). We follow the moderate friction case of Hansen and Carter (1982), where the fault zone is assumed to be 1 km wide and the strain rate is equal to the slip rate across the fault. The maximum allowed shear stress is 50 MPa and calculated as the minimum of either a brittle, pressure-dependent law or ductile, temperature-dependent power law. The additional heat produced is added to the nodal radiogenic heat production within the shear zone. The slip rates on the faults are fairly high (e.g., Table 2.1) and produce significant shear heating.

Assumption 4: Negligible Heat Transfer by Fluid Flow

Recent work by Evans et al. (2004) suggests advective heat transfer by fluids may be significant in the Greater Himalayan zone. Although the effect of heat transfer by fluids may be important, its significance relative to rapid advective heat transfer by rock exhumation is unknown (e.g., Ehlers, 2005). For this study we make the same assumption as all other thermochronometer studies to date and assume conductive heat transfer and advective heat transfer by rock exhumation are the dominant thermal processes. Simulating heat transfer by fluid flow is beyond the scope of this study, largely due to the additional unconstrained parameters in the model. Additional work in progress by the authors is evaluating the influence of fluid flow on thermochronometer ages.

2.5.4 Thermochronometer Age Prediction

Thermochronometer ages are calculated using model-derived cooling histories for particles coincident with the sample locations. Cooling histories were generated by tracking samples from the surface back to different depths in the steady state thermal model for the last 20 Myr. Note however that only the last ∼3 Myr of the cooling history is important because most of the AFT samples cooled at this time. Predicted AFT ages were calculated using the Laslett et al. (1987) kinetic annealing algorithm as implemented by Ehlers et al. (2003). Muscovite $^{40}Ar/^{39}Ar$ ages are also predicted from the sample cooling histories, but the kinetics of argon diffusion in muscovite are not understood in detail. Because of this, we report the predicted ages as the time since the rock cooled below 350°C, but we regard this as a minimum estimate for the closure temperature and use it only for illustrative purposes of how a higher-temperature thermochronometer responds to different kinematic scenarios.

2.6 Results

In our modeling approach, we evaluated discrete combinations of model parameters from the range of plausible values (Table 2.1). This approach evaluates the parameter space and identifies the range of geologically possible scenarios (e.g., slip partitioning, material properties, basal heat flux) that produce the observed cooling ages. In total, this required 397 simulations. In the following sections, we discuss the influence of each of these parameters and test the sensitivity of the predicted ages to these variables. The parameter of interest in each section is varied across the chosen range of values, while all the other free parameters are fixed at average values. Ages predicted from the Nagi Lek transect sample locations (transect J in Figure 2.2) are shown because this transect is oriented such that the predicted ages

are least likely to be affected by the steady state topography, and the transect has a large elevation range and number of samples. The dominant effects on cooling ages discussed below are similar for the other transects. We plot model predicted ages using nominal AFT and $^{40}Ar/^{39}Ar$ uncertainties of 20% and 10% of the sample age, respectively, to highlight which processes are significant within typical sample uncertainties.

2.6.1 Effect of Basal Heat Flux on Predicted Ages

Increasing the heat flux into the base of the thermal model increases the maximum temperature within the model domain and steepens the thermal gradient near the surface. As a result, the distance traveled from a given closure isotherm to the surface decreases. Thus ages predicted from models with higher basal heat flux are younger than those from models with lower basal heat flux (Figure 2.4). We model varying basal heat fluxes of 20, 35 and 50 mW/m^2, while thermal conductivity is set to 2.5 W/m K, heat production in the GHS is specified as 1.9 $\mu W/m^3$, and shear heating is included. The kinematic model has 4 mm/yr of overthrusting for the MFT and 2 mm/yr for the MCT.

A 2.5-fold increase in the basal heat flux leads to predicted AFT ages that are younger by $\sim$10%, whereas the muscovite $^{40}Ar/^{39}Ar$ ages become $\sim$15$-$20% younger (Figure 2.4). When the uncertainties are considered for both sets of predicted ages, they are statistically indistinguishable for all three heat flux values, although if age uncertainties were $<$10% for the predicted $^{40}Ar/^{39}Ar$ ages, the effect of a threefold change in basal heat flux would be statistically discernable. Because the AFT data lack sensitivity to the basal heat flux, they cannot be used to constrain the range of tested values. Considering the measured surface heat flux data in India, the most likely basal heat flux values are 20$-$35 mW/m^2 (Roy and Rao, 2000). In addition,

although the influence of basal heat flux variations is not significant in this study, we note that at slower erosion rates typical of other mountain ranges the influence of basal heat flow on near-surface thermal gradients can be significantly larger.

2.6.2 Effect of Heat Production on Predicted Ages

Increasing the radiogenic heat production in the GHS is predicted to have a major impact on exhumed thermochronometer sample ages (Figure 2.5). The three models shown here have heat production values of 0.8, 1.9 and 3.0 μW/m^3, basal heat flux of 35 mW/m^2, thermal conductivity of 2.5 W/m K, and include shear heating. The kinematic model has a rate of overthrusting of 4 mm/yr for the MFT and 2 mm/yr for the MCT.

Similar to the case for varying basal heat flux, higher heat production values steepen the thermal gradient near the model surface, leading to younger predicted ages. For an heat production variations, we are unable to eliminate any of the range of tested values using the model (Table 2.1). Muscovite ^{40}Ar/^{39}Ar data should be able to constrain the range of tested values. Measurements of heat-producing element concentrations yield an average volumetric heat production value of 2.1 μW/m^3 (Table A). Thus our preferred heat production values are 1.9 and 3.0 μW/m^3, due to the high concentration of heat-producing elements in the GHS (England et al., 1992).

2.6.3 Effect of Shear Heating on Predicted Ages

The magnitude of heat contributed to the thermal field from shear heating depends on the fault slip rate, temperature and pressure at a location within the shear zone (Henry et al., 1997; Bollinger et al., 2006). We assess two models: one that includes shear heating; the other not (Figure 2.6). Both models have basal heat flux values of

35 mW/m^2, heat production of 1.9 μW/m^3 and thermal conductivity of 2.5 W/m K. The prescribed kinematics are 4 mm/yr of overthrusting for the MFT and 2 mm/yr for the MCT.

With the given kinematic field, predicted AFT ages are ∼0.2 Myr younger and predicted ^{40}Ar/^{39}Ar ages are ∼0.8 Myr younger with the addition of shear heating. Despite this ∼15% decrease in predicted ages, neither the AFT ages nor the ^{40}Ar/^{39}Ar ages are statistically different within error bars. Because our AFT data show insufficient sensitivity to shear heating, we are unable to rule out shear heating. However, the difference in lower crustal temperatures between models with and without shear heating is significant (∼50−100°C). Thus we include shear heating in the model simulations in the event that it becomes more significant when predicting ^{40}Ar/^{39}Ar ages at slower exhumation rates, when advective heat transfer processes are less dominant in the thermal field.

2.6.4 Effect of Thermal Conductivity on Predicted Ages

Increasing the thermal conductivity in the thermal model decreases the maximum temperature and causes the thermal gradient to be less steep (Figure 2.7). This decrease in temperature leads to comparatively older predicted ages. In the example shown, the thermal conductivity is varied between 2.5 and 3.0 W/m K and the kinematic field has overthrusting of 4 mm/yr for the MFT and 2 mm/yr for the MCT. The models each have basal heat flux values of 35 mW/m^2, heat production of 1.9 μW/m^3 and include shear heating.

AFT and ^{40}Ar/^{39}Ar ages predicted from the thermal model with a thermal conductivity of 3.0 W/m K average ∼0.2−0.3 and ∼0.9−1.0 Myr older, respectively, than those from the model with lower thermal conductivity. With the error bars, the AFT ages for both scenarios cannot be distinguished, but muscovite ^{40}Ar/^{39}Ar

data should be sensitive to thermal conductivity variations. Because the AFT data are likely not sufficiently sensitive to variations in thermal conductivity, we cannot exclude any of the values used in this sensitivity test. Measurements of the thermal conductivity in rocks from the GHS show a temperature-corrected average value of 2.75 W/m K that is intermediate to the tested values of 2.5 and 3.0 W/m K (Table A.1).

2.6.5 Effect of Fault Kinematics on Predicted Ages

The kinematic field that drives advection in the thermal model has a strong influence on predicted samples ages. In the previous sections, the effects of different model parameters were shown by the variations in predicted ages within a given parameter space. In this section, we test 22 different kinematic fields and find the kinematic influence tends to dominate the variations in other model parameters. Because of this, the data are plotted in a manner that shows which kinematic models best fit the observed ages. However, rather than show the overthrusting rates for each fault, the plots list the different kinematic models by their erosion rate (v_z, Equation (2.3)) in subplots for the different tectonic scenarios (Figure 2.8). The listed erosion rates are for the Greater Himalayan zone in the model, the region where most of the samples were collected. Thus, for a given kinematic model, nearly all of the samples should be vertically exhumed at the same rate. The other velocity components (v_x and v_y) can be calculated using Equation (2.3) and the structural geometry, as discussed in section 2.5.1. The quality of fit of the predicted ages to the observed is quantified using the square root of a modified, reduced chi-square misfit,

$$\chi^2 = \sqrt{\frac{\sum_{i=1}^{N} \left(\frac{\mathrm{Age}_{p_i} - \mathrm{Age}_{o_i}}{U_i} \right)^2}{N}} \tag{2.5}$$

where Age_{p_i} is the ith predicted age, Age_{o_i} is the ith observed age, U_i is the one sigma uncertainty in the ith age, and N is the number of samples in the summation. χ^2 values are always greater than or equal to zero, with zero representing a perfect fit to the data and increasing values representing greater misfit.

Because erosion rates are linked directly to predicted cooling ages and are dictated by fault slip rates in the context of a fixed topographic surface, minimizing the misfit between predicted and observed cooling ages yields the erosion rates that best fit the data (Figure 2.8). The χ^2 misfit values were calculated for ages predicted from the Nagi Lek transect (J in Figure 2.2) for each of the kinematic models shown. The GHS heat production was fixed at 3.0 μW/m^3, shear heating was included and the thermal conductivity was 2.5 W/m K. The χ^2 minima in the subplots (Figure 2.8) show the kinematic fields that provide the best fit to the data (shaded region). The data are best fit by χ^2 values that are $\sim$2, which generally represent models where the predicted ages are within the 2σ uncertainties of the data. In all of the plots, the initial decrease in misfit to a minima and subsequent increase at higher erosion rates reflects predicted ages that are too old at slow rates and too young at higher rates. The χ^2 misfit values for the AFT data in the Nagi Lek transect show they are best fit with average erosion rates between $\sim$2.0 and 4.5 mm/yr. Thus these data are sensitive to the erosion rate, but not to the partitioning of slip on to different thrusts. This result is discussed in more detail in section 2.7.2.

2.7 Discussion

The previous results demonstrate the sensitivity of predicted AFT and muscovite ^{40}Ar/^{39}Ar ages to different thermophysical processes and material properties in the crust. The dominant message conveyed by these results is an acute sensitivity of

predicted ages to the erosion rate generated by different kinematic fields. Simply put, in a rapidly eroding region such as the Himalayan front, the thermal field is dominated by advective heat transfer from rock exhumation. Whereas for the other processes and material properties considered (e.g., basal heat flow, heat production, conductivity, etc.) a twofold to threefold increase causes a noticeable change in exhumed sample ages, the difference in predicted ages is generally within sample age uncertainties. In contrast, a similar change in erosion rates produces a readily documentable variation in predicted ages.

It should be noted that the insensitivity of sample AFT ages to most thermal model parameters (Figures 2.4−2.7) will not apply to other active orogens if the exhumation rates are slower ($<\sim$1 mm/yr) and the thermal field more conductive than the simulations shown here. Moreover, much of this insensitivity emerges from the relatively large uncertainties assigned to the AFT ages (20%). For thermochronometer samples with smaller uncertainties, the sensitivity to all parameters would increase. In the following sections, we revisit the influence of the kinematic field on thermochronometer ages and evaluate the erosion and kinematic history of the Greater Himalayan zone.

Despite the previously highlighted dominance of advective heat transfer on the Greater Himalayan zone, it is important to note that nonuniqueness exists in the model results and trade-offs between different model parameters can produce nearly identical thermochronometer ages. The ages predicted from the thermokinematic model depend on the basal heat flux into the model, radiogenic heat production and thermal conductivity within the model, and the prescribed kinematic field and resultant shear heating. With five free parameters in the models, several combinations of variables provide an equal quality of fit to the thermochronometer data. This is not

surprising, given the possible trade-offs in thermal influences between, for example, increasing heat production while decreasing basal heat flux. Our goal in evaluating which variables provide the best fit to the data is to constrain the range of free parameters and create a preferred parameter space.

Another important point is that the erosion rates calculated from the models are average erosion rates and may mask shorter-timescale variations in exhumation. For instance, ages generated by slow exhumation followed by a pulse of rapid exhumation may be fit by a model that has an intermediate exhumation rate. One sign of such a misfit is when model-predicted ages match the average age of the observed ages, but do not follow the age-elevation trend of those data. Models that include transient variations in the thermal field would be required to fit such a trend and are beyond the scope of this paper.

2.7.1 Fit of Predicted Ages to Data

In general, the predicted AFT ages from the best fit models fall within the 2σ uncertainties of the data for a given transect, yet predicted ages for some transects do not. We compare observed ages and their apparent erosion rates with predicted ages and the model-derived erosion rates for most transects (Figure 2.9). The Bagarchhap, Chame and Dharapani transects (A−C in Figure 2.2) are not shown because the assumption of steady state topography in the model is clearly violated when predicting cooling ages for samples collected on hillslopes that are parallel to or steeper than the rock exhumation trajectory prescribed by the kinematic model, as discussed in section 2.5.3.

The predicted ages shown for each transect are from the best fit kinematic models for each tectonic scenario, with a basal heat flow of 20 mW/m^2, GHS heat production of 3.0 μW/m^3 and thermal conductivity of 2.5 W/m K. With the exception of the

two Khudi transects, nearly all of the ages predicted from the best fit kinematic models are within the 2σ uncertainties of the data. This suggests that the model realistically simulates the major thermal and kinematic influences. This also implies that there have been no major changes in the topographic relief since the samples cooled, because the model topography is in a strict steady state and the model yields predicted ages that fit the data. It is worth noting, though, that much of the data have large uncertainties, which may mask signs of relief change or other factors affecting the cooling ages.

The predicted ages do not fit the data well for the two Khudi transects (Figures 2.9b and 2.9c). For the Khudi East transect (F in Figure 2.2), the misfit reflects the limited number of kinematic models that were run. Best fit predicted ages from Kinematic scenarios b and d (erosion rates of 2.7 and 2.5 mm/yr) are generally too young to fit the data. For those scenarios, a kinematic model that generates a slightly slower erosion rate ($\sim$2 mm/yr) would likely provide a better fit. For the Khudi West transect (E in Figure 2.2), it appears that the data cannot be fit simply by using models with different erosion rates. For the models with slip on the MCT, the predicted ages are too old at low elevations and too young at high elevations. This is because the lowest two samples in the Khudi West transect are in the footwall of the MCT in the model, rather than the hanging wall (Figure 2.2). The lowest two samples are not likely to be strongly affected by slip on the MCT in the model and require fairly high overthrusting rates on the MFT to generate predicted ages that fit the observations. Because the MCT is riding atop the material moved along the MFT, any additional slip on the MCT leads to predicted ages in the model hanging wall that are too young to fit the data.

Notably, the data-derived apparent exhumation rates can differ significantly from

the model erosion rates (Figure 2.9). For a majority of transects, the apparent exhumation rate is greater than the model-derived erosion rate. Commonly, a nearly 50% difference separates these two rates. At least two factors affect the data-derived rates. First, because the regressions are error-weighted, a single age with a small error near the top or base of a transect can exert a strong influence on the regression line slope. Hence a young age high in the section can produce a negative slope. Second, overestimated erosion rates likely reflect a violation of one or more of the assumptions required to interpret regression line slopes as erosion rates on age-elevation plots of thermochronometer data, i.e., the samples must follow vertical exhumation paths and either be collected in a strictly vertical profile or the closure isotherm geometry must not be perturbed by the overlying topography. Low-temperature thermochronometer isotherms are likely to be perturbed by the overlying topography because of their shallow crustal depth. An exception to previous discussion is evident for the Syange transects (Figures 2.9d and 2.9e), where the apparent erosion rate is lower than the model-predicted rate. On these transects the slope of the regression line through the data is less than the trend in the predicted ages. One possible explanation for this trend is an acceleration in post-closure erosion. If the AFT samples pass through their closure isotherm at a slow rate and are subsequently brought to the surface at a slightly higher rate, the ages would be young, but the slope of the ages on an age-elevation plot would be shallow. The trend could also be explained by the effects of changing relief or groundwater flow, which are discussed in detail in section 2.7.3. Work in progress is exploring these ideas.

In addition to predicting AFT ages for the data transects, we predicted muscovite $^{40}Ar/^{39}Ar$ ages to compare to ages from elsewhere in the Himalaya (Figure 2.10). The $^{40}Ar/^{39}Ar$ ages were predicted for the same transects and using the same models as

the AFT predicted ages shown in Figure 2.9. The predicted $^{40}Ar/^{39}Ar$ ages are very young, no older than 5.5 Ma, with an average age of ∼3.5 Ma. These ages are generally younger than those seen at similar structural positions within the Himalaya. Detrital muscovite $^{40}Ar/^{39}Ar$ ages in the GHS from two studies in the Marsyandi drainage have average ages of ∼5 and ∼7 Ma (Ruhl and Hodges, 2005; Brewer et al., 2006). This suggests that our $^{40}Ar/^{39}Ar$ ages were predicted using a model with an erosion rate that was too fast, leading to predicted ages that are too young. Because we are able to fit the AFT data with those erosion rates, however, this implies that erosion rates were slower prior to the time covered by the AFT data. The cause of the acceleration in erosion could either reflect a change in the tectonic forcing or regional/global climate. As noted by Huntington et al. (2006) and Huntington and Hodges (2006), little evidence exists to support a large-scale tectonic change, so climate is the more likely driver of accelerated exhumation. Timing of this inferred acceleration in erosion coincides with an intensification of northern hemisphere glaciation (Raymo, 1994), establishment of the modern-day summer and winter monsoon system (Gupta and Thomas, 2003) and a global increase in sedimentation rates and grain sizes (Zhang et al., 2001). More bedrock muscovite $^{40}Ar/^{39}Ar$ data from the model region would be necessary to quantify this apparent acceleration.

2.7.2 Is Out-Of-Sequence Faulting Significant?

One of the uncertainties in the evolution of the Himalaya in central Nepal is whether or not there has there been large-magnitude out-of-sequence displacement near the trace of the MCT system subsequent to early Miocene time. The AFT cooling ages range from ∼0 to 4 Ma, allowing us to investigate the history of activity on the MCT using kinematic models with and without slip on the MCT during this time period.

We have explored various kinematic models in terms of quality of fit to the AFT data (Figure 2.8). If the AFT data are sensitive to the different tectonic scenarios, we should expect to see a better fit for one of those scenarios, as expressed by the χ^2 misfit values. What we observe in the AFT data, however, is that an equal fit ($\chi^2 < 2$) to the data can be attained by kinematic models with or without activity on the MCT. Furthermore, the fit of the predicted ages to the observed ages (Figure 2.9) shows that the predicted ages depend more on the erosion rate generated by the kinematic models than the kinematic scenario. In Figures 2.9f and 2.9g this is particularly clear, with the predicted ages plotting nearly atop each other for the different kinematic scenarios with similar erosion rates.

The similar χ^2 misfit values for the AFT data in the best fit simulations are likely the result of models that produce similar thermal fields. At high vertical exhumation rates, the closure isotherm for the AFT system is advected to within several kilometers of the model surface and the near-surface (<5 km) thermal field differs less between different kinematic scenarios. In addition, the trajectories of particles transported along the MCT or MFT are different by only 8° in our model. We infer that the similarities in near-surface thermal fields and rock exhumation trajectories generate χ^2 misfit values for the AFT data in the best fit models that are comparable for all of the tectonic scenarios. In rapidly eroding regions, higher-temperature chronometers (e.g., muscovite or hornblende $^{40}Ar/^{39}Ar$) may be more sensitive to the fault kinematics because their age will be a function of a longer thermal history. In other words, higher-temperature data will integrate information over a greater distance and potentially be more sensitive to slight differences in rock exhumation trajectory. The model-predicted $^{40}Ar/^{39}Ar$ ages (Figure 2.10) support this idea, and several transects show sensitivity to the different kinematic scenarios. Slower erosion

rates would increase the sensitivity to the kinematics, with ages that are statistically different including the assigned 10% error bars for several transects. On the other hand, using thermochronometers representing higher-temperature data puts more demands on the model assumptions. The assumed kinematic and topographic geometries have to remain constant through longer intervals of time; assumptions that become less likely with increasing age.

2.7.3 Spatial Variations in Erosion

In the kinematic model, most of the sample locations are within the same thrust sheet and above planar faults dipping at constant angles, so the majority of samples are exhumed at the same rate for a given tectonic scenario. Despite spatially uniform exhumation histories, predicted sample ages at similar elevations vary across the model domain because of the thermal influences of the overlying topography, proximity to the faults and material properties. If the model geometry, material properties and assumption of steady state topography are realistic, at least one kinematic model should provide a good fit to all of the AFT data.

Within the range of erosion rates that produces predicted ages that fit at least 80% of the observed ages on individual transects, none of our models can fit the data for all transects. Across our data set, erosion rates vary by about twofold (Figure 2.11), as calculated from the data transects where at least 80% of the predicted AFT ages fit within the 2σ uncertainties of the observed ages. The range of erosion rates listed is from all kinematic scenarios and thermal models with a 20 mW/m^2 basal heat flux, 2.5 W/m K thermal conductivity and shear heating. The range of rates for models with GHS heat production values of 3.0 μW/m^3 and 0.8 μW/m^3 are shown beside the transects on top and bottom, respectively. The AFT data are best fit by kinematic models that produce erosion rates of 1.8−5.0 mm/yr. However, no

single kinematic model can fit all of the data transects. For example, the Khudi East transect (F in Figure 2.2) requires erosion rates of no greater than 2.0 mm/yr for the high heat production models, while the Tal transect (D in Figure 2.2) requires an erosion rate of at least 3.3 mm/yr. This suggests that the erosion rate across the Marsyandi River drainage is not only rapid, but also spatially variable.

One possible explanation for the inability of the model to fit all the AFT data equally well is smaller-scale faulting within the MCT sheet. Hodges et al. (2004) found evidence of several faults between the MCT and STF within the Marsyandi River valley with tectonically significant Quaternary displacement on them. These smaller-scale features were shown to offset the cooling ages of AFT samples from Burbank et al. (2003) by $\sim$1 Ma. The simplified the tectonic scenario in model does not reproduce the effects of displacement on the smaller-scale faults because we do not know enough about their geometry to include them. Rather, we evaluated the effects of the primary structures. Because there may be many unmapped smaller-scale faults, we contend that it is reasonable to focus on the larger-scale tectonic elements, which should have more influence on the regional cooling age patterns.

Another potential explanation for the difference in rates required to fit the data transects is changes in topographic relief. A local weather network in the study area (Barros et al., 2000; Burbank et al., 2003) shows that annual monsoon precipitation varies from $\sim$0.5 to 4.0 m/yr across the Greater Himalayan zone over a 6-year period of observations. Although not observed in the data used by Burbank et al. (2003), it is possible that, if present-day precipitation patterns are representative of long-term precipitation patterns, precipitation could influence the spatial distribution of erosion, as suggested by numerical models (e.g., Willett, 1999). Gabet et al. (2004) found a strong correlation between mean hillslope angles and mean annual rainfall

in the Himalaya, where landsliding controls the maximum hillslope angles and relief within unglaciated valleys. They concluded that precipitation may control relief in the Himalaya and that the response time to changes in precipitation may be rapid (<10 kyr). Hodges et al. (2004) looked at river channel morphologies from the region spanning the southern Tibetan zone to the northern Lesser Himalayan zone and argued that deformation is coupled to precipitation in the Himalaya. They suggest that the focused precipitation along the southernmost edge of the Greater Himalayan zone has led to reactivation of the MCT, presumably driving rock uplift across the entire Greater Himalayan zone. Notably, however, our modeled erosion rates are at least as rapid for the northern transects as in the southern transects, despite a reduction of precipitation by >50%. This absence of a north-south trend in erosion rates also appears in the samples collected at river level across the study area (see Blythe et al. (2007, Figure 3) for sample ages and locations). A comparison of the best fit erosion rates constrained by the χ^2 misfit for the northern versus southern river bottom samples shows that the rates are statistically indistinguishable. A rate of ∼2.8 mm/yr provides the best statistical match to the entire river bottom data set, but rates as high as 4−5 mm/yr are admissible. Hence, with the exception of three more slowly eroding (and wetter) transects in the south (Khudi East, Syange South, Syange North transects; F, G, H in Figure 2.2), no discernable gradient in erosion rates emerges from this study.

Without any change in tectonic uplift, spatial variations in erosion could lead to relatively short-lived changes in topographic relief. For example, if relief increases, cooling ages near the valley would be younger (from river incision) and ages near ridges would be older (from increased distance traveled since closure) (Braun, 2002). Although relief changes can affect cooling ages, our model is unable to simulate

changes in relief. All we can conclude at this time is that relief change is one possible mechanism for some of the smaller misfits observed between predicted and observed ages.

It is also possible that topographically driven fluid flow may have modified the subsurface thermal field and affected the AFT ages. Groundwater can carry thermal energy from ridges to valleys as it flows, which would decrease the thermal gradient beneath peaks and increase it beneath valleys. The effect on cooling ages would be to produce older ages on ridges and younger ages in the valleys, rendering the age-elevations trends less steep. Evans et al. (2004) mapped several hot springs within the Marsyandi valley, showing that the groundwater may be heated by the surrounding ridges. The magnitude of this effect depends on many other factors (such as rock permeability, hillslope geometry and precipitation) and is currently unknown. Overall, we consider temporal variations in topographic relief, hydrothermal heating, slip on faults that were not modeled and unknown spatial variations in heat production and thermal conductivity to be the important possibilities for explaining the misfit of the model-predicted ages to the data. Further modeling is underway to quantify these effects.

2.8 Conclusions

We used a 3-D coupled thermokinematic model to generate subsurface thermal fields for the Marsyandi River valley in central Nepal, from which thermochronometer ages were predicted and compared to collected data. The model is parameterized by the 3-D variability in overlying topography, fault geometry, fault kinematics, boundary conditions and material properties. The primary results of this study are as follows:

1. In regions that are rapidly exhumed, the kinematic field and associated thermal advection dominate over the influences of material properties and basal heat flux in affecting the thermal history. For example, the difference in misfit due to the different basal heat flux values is trivial compared to the kinematic influence (Figure 2.8). In comparing the misfits among the other material properties, we find that kinematics always dominates. Across the variation expected in natural rock samples, the influence of varying material properties is concealed by the advective heat transfer from the kinematic field.

2. The range of apparent exhumation rates derived from the slope of regression lines through sample ages versus elevation is -2.6 to 12.2 mm/yr. The range of erosion rates in the model that provide a good fit between predicted and observed AFT ages is less than half as large ($1.8-5.0$ mm/yr). This >200% difference between the simple 1-D interpretation using regression lines and the model-constrained rates illustrates the utility thermokinematic models for reducing the variance in calculated erosion rates. Rapid erosion, nonvertical exhumation and high-relief topography will likely invalidate the assumptions required to accurately calculate exhumation rates using the slope of regression lines through vertical transect data potentially leading to large errors.

3. The AFT data do not allow us to rule out any of the modeled kinematic scenarios and we are not able to say whether the MCT has had tectonically significant displacement since 3 Ma.

4. Differentiating between possible thrust belt kinematic models requires (1) rock exhumation pathways that are considerably different and (2) either slower exhumation rates or a thermochronometer data set that covers higher temperatures. The kinematic scenarios tested differed by only 8° in rock exhumation trajectory

and the AFT data were not sensitive to this difference. We suggest that the possible rock exhumation trajectories must be considerably larger than 8° in order to have sensitivity with low-temperature thermochronometers. In areas that are exhumed at rates of less that 1 mm/yr, distances to the closure temperature for low-temperature thermochronometers may be greater and larger differences in the subsurface thermal field should exist. At these slower rates, it may be possible to differentiate more subtle differences in rock exhumation trajectories. Smaller differences in rock exhumation pathways might also be detected using higher-temperature thermochronometers (such as muscovite $^{40}Ar/^{39}Ar$) because the difference in distance traveled from the closure temperature should be larger at higher temperatures. Future studies in rapidly eroding collisional orogens may benefit from the use of these higher-temperature systems when attempting to constrain thermal and kinematic scenarios.

5. No single kinematic model can fit at least 80% of the AFT ages for all transects. This suggests that erosion in the study area is nonuniform. Possible explanations for the spatial variability are unmapped small-scale faults, relief change from differential erosion within the basin or groundwater flow affecting the cooling ages.

6. Samples should be collected on hillslopes that face the same direction as the thrust vergence when using steady state model topography. Samples collected on hillslopes that face opposite to the thrust vergence and have slope angles similar to or greater than the fault dip angle present problems when generating predicted rock thermal histories. For slope angles that are greater than the fault dip angle, particles may be tracked out of the model domain as they move back in time parallel to the fault. Ages predicted from these thermal histories are meaningless as the thermal history is clearly unrealistic. However, samples collected in this type of orientation

likely contain valuable information about the timing and rate of valley formation (e.g., Bagarchhap, Chame transects; B, A in Figure 2.10) and are well suited for evaluating landscape evolution models of valley incision.

2.9 Acknowledgements

P. Glanis, C. Williams (USGS), J. Kaste, and A. Heimsath (Dartmouth College) provided the thermal property measurements presented in Appendix A. Reviews by P. van der Beek and R. Thiede greatly improved the paper. This manuscript benefited from thoughtful discussions with A. Heimsath, J. Barnes, and M. Densmore. This work was supported by NSF grant EAR-9909647 to T. Ehlers. This work is part of the NSF Continental Dynamics project "Geomorphic-Geodynamic Coupling at the Orogen Scale."

Table 2.1: Numerical Model Parameters

Property/Parameter	Model Input Value
Material Properties	
GHS heat production	0.8−3.0 μW/m^3
LHS/Indian Shield heat production	0.8 μW/m^3
TS heat production	0.5 μW/m^3
Thermal conductivity	2.5−3.0 W/m K
Specific heat	800 J/kg K
Density	2750 km/m^3
Numerical Parameters	
MFT overthrusting rate	1−15 mm/yr
MCT overthrusting rate	0−8 mm/yr
STF extension rate	0 mm/yr
Model time step	10^5 years
Horizontal node spacing	700 m
Average vertical node spacing	∼1500 m
Surface temperature	14−7°C/km times elevation
Basal heat flow	20−50 mW/m^2
Model domain	84 × 140 × 58 km

Figure 2.1: (a) Shaded relief digital elevation model (DEM) of the Himalaya showing the central Nepal study area (rectangle) and the location of (b) a geologic cross section (thick line), modified from Figure 2 of Lavé and Avouac (2000). STF, South Tibetan fault; MCT, Main Central thrust; MBT, Main Boundary thrust; MFT, Main Frontal thrust. (c) Three-dimensional schematic block diagram for tectonic scenario a, where slip occurs only on the MFT (arrows show sense of motion on fault). The exhumation pathway (thick dashed line) would parallel the fault and transport rock through closure temperatures ($Tc_1 - Tc_3$) for several isotopic systems (thin dashed lines). Example exhumation pathway for a thermochronometer sample sensitive to closure temperatures $Tc_1 - Tc_3$ (white circles). (d) Tectonic scenarios bd, where slip is partitioned between the MCT and MFT. In these scenarios, sample exhumation parallels the MCT and material is transferred into the overriding wedge via underplating (small vertical arrows).

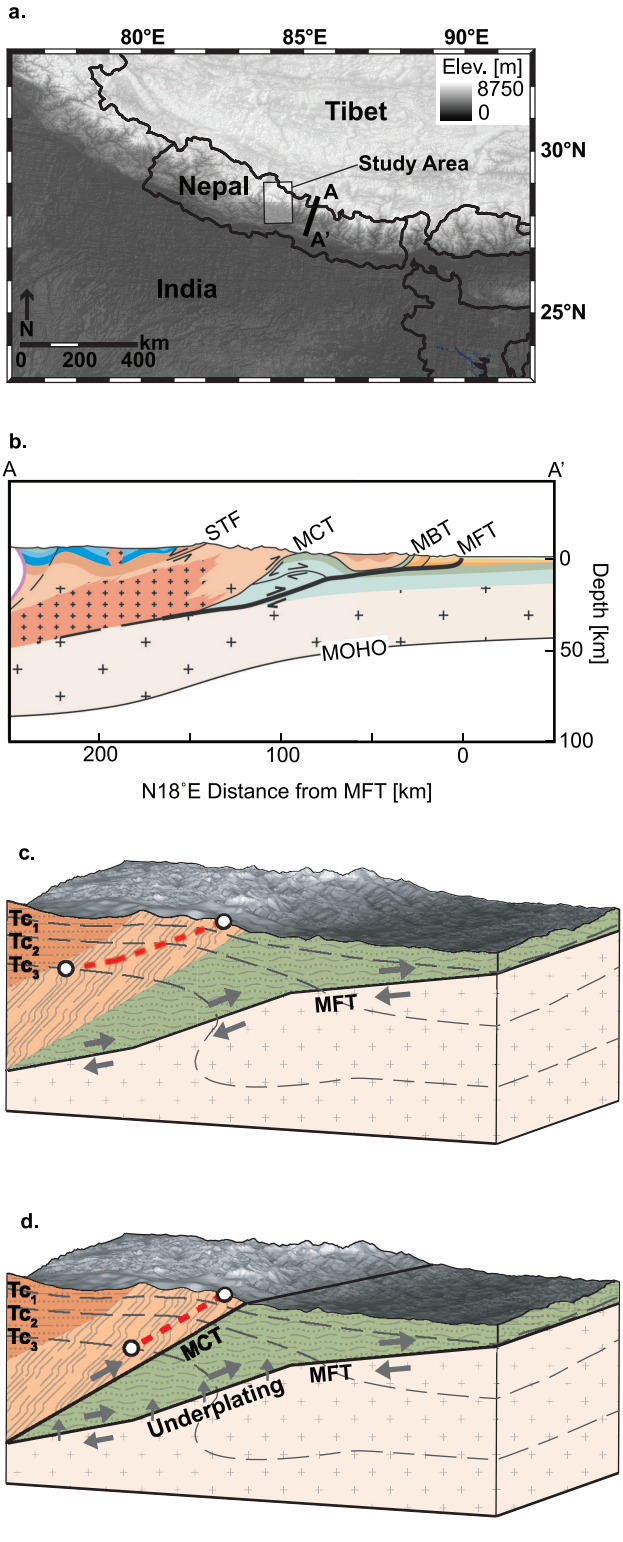
a.
80°E
85°E
90°E
Elev. [m]
8750
0
Tibet
30°N
Study Area
Nepal
A
A'
India
25°N
N
km
0 200 400
b.
A
A'
STF
MCT
MBT
MFT
0
Depth [km]
MOHO
50
100
200
100
0
N18°E Distance from MFT [km]
c.
Tc1
Tc2
Tc3
MFT
d.
Tc1
Tc2
Tc3
MCT
MFT
Underplating

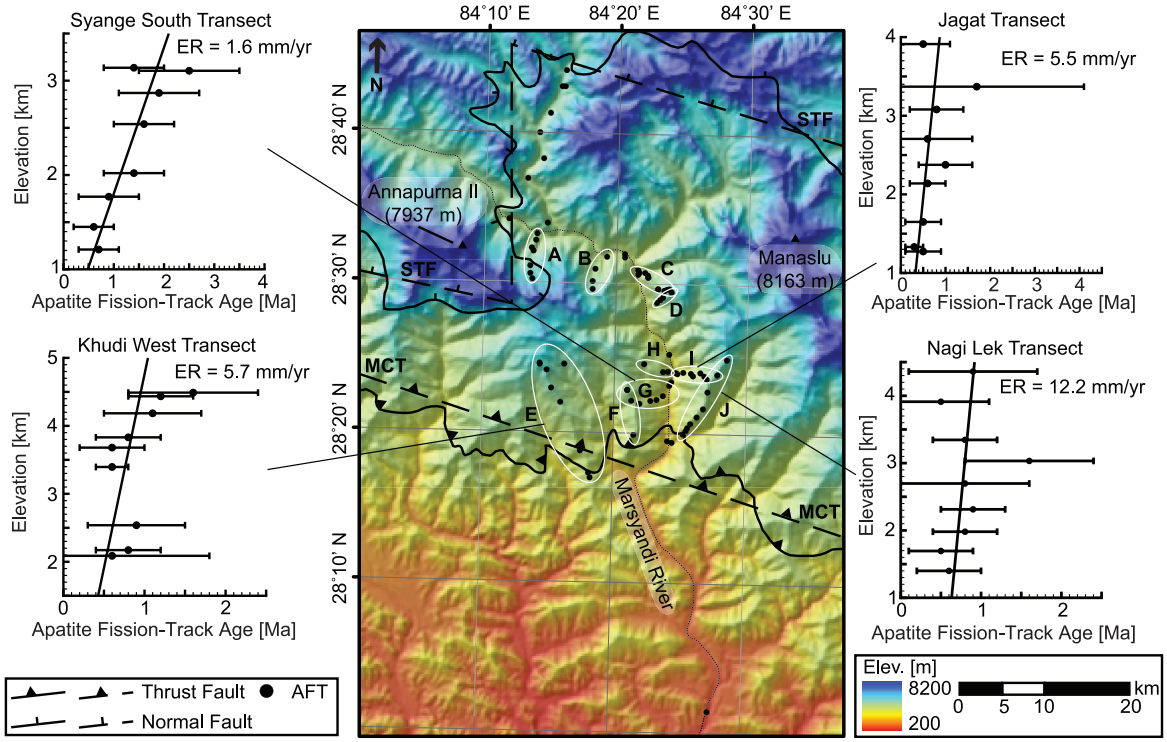

Figure 2.2: Shaded relief DEM of the Marsyandi River valley, central Nepal showing the surface traces of the STF and MCT II from Searle and Godin (2003) (thick solid lines) with the model approximations of those faults (thick dashed lines). Abbreviations are as in Figure 2.1. Apatite fission track (AFT) sample locations (black circles) are divided into transects (white ovals), where A, Chame; B, Bagarchhap; C, Dharapani; D, Tal; E, Khudi West; F, Khudi East; G, Syange South; H, Syange North; I, Jagat; and J, Nagi Lek. Age-elevation plots are shown for several transects with weighted least squares regression lines showing the range of apparent exhumation rates (ER; 1.6−12.2 mm/yr).

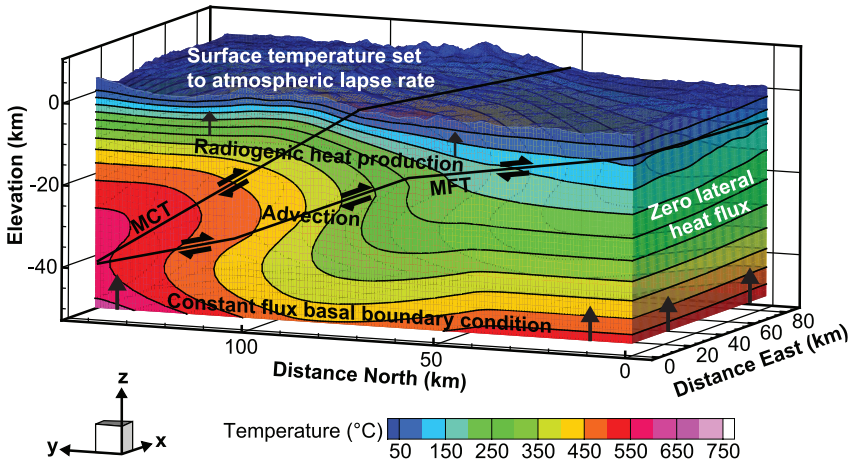

Figure 2.3: Three-dimensional block diagram of the thermokinematic model illustrating the boundary conditions and thermal model components. The kinematic model has the MFT and MCT active (thick lines). Abbreviations are as in Figure 2.1. Contoured temperatures (thin lines) show significant perturbation to the subsurface thermal field from the kinematic model and other thermal influences.

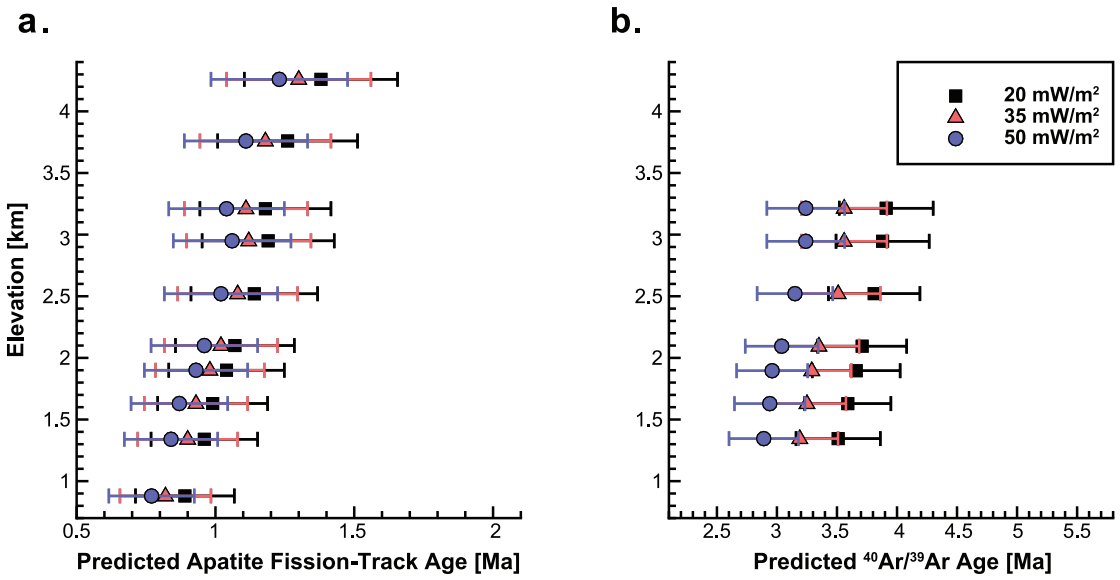

Figure 2.4: Effect of varying basal heat flux on predicted sample ages for the Nagi Lek transect. Predicted (a) apatite fission track (AFT) and (b) muscovite ^{40}Ar/^{39}Ar ages versus sample elevation for models with basal heat flux values of 20, 35, and 50 mW/m^2 (squares, triangles, and circles). Age error bars are 20% and 10% for the AFT and ^{40}Ar/^{39}Ar, respectively.

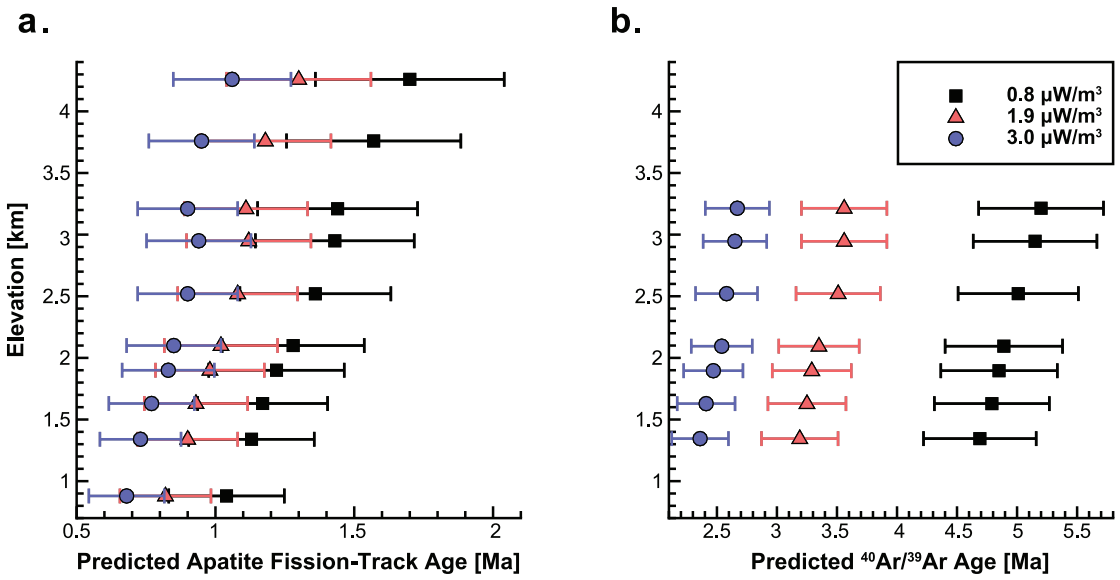

Figure 2.5: Effect of varying Greater Himalayan sequence heat production on predicted sample ages. Predicted (a) apatite fission track (AFT) and (b) muscovite $^{40}Ar/^{39}Ar$ sample ages versus sample elevation for models with heat production values of 0.8, 1.9 and 3.0 $\mu W/m^3$ (squares, triangles, circles). Age error bars are 20% and 10% for the AFT and $^{40}Ar/^{39}Ar$, respectively.

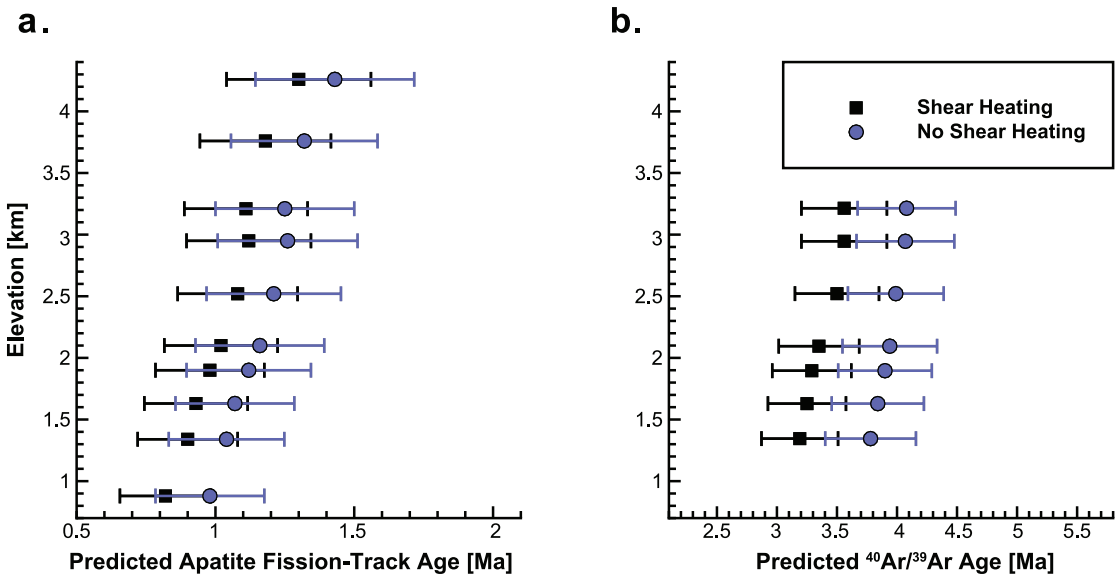

Figure 2.6: Effect of shear heating on predicted sample ages. Predicted (a) apatite fission track (AFT) and (b) muscovite $^{40}Ar/^{39}Ar$ sample ages versus sample elevation for models with and without shear heating (squares, circles). Age error bars are 20% and 10% for the AFT and $^{40}Ar/^{39}Ar$, respectively.

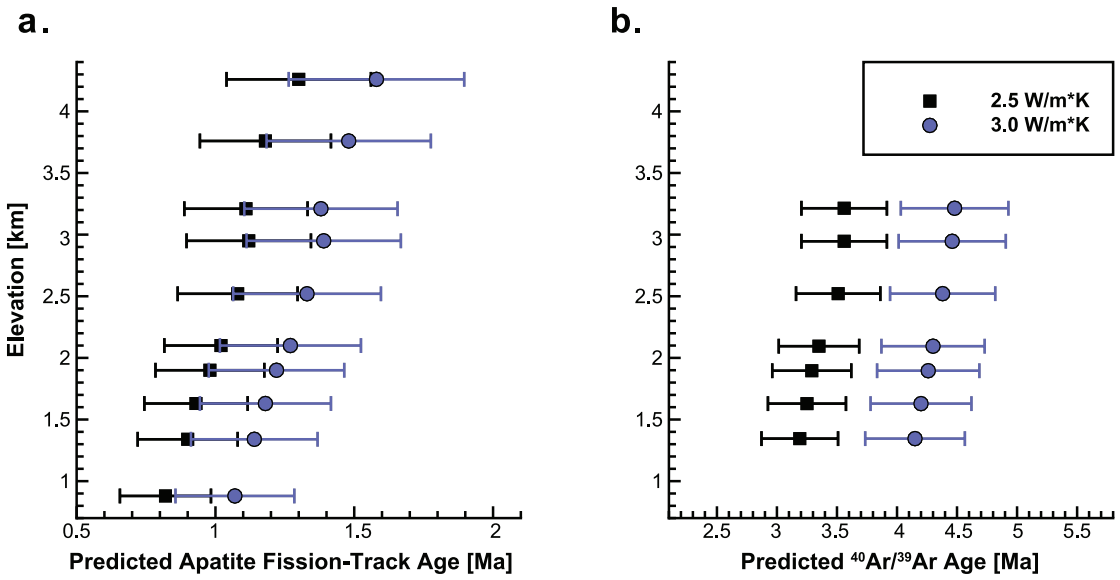

Figure 2.7: Effect of varying thermal conductivity on predicted sample ages. Predicted (a) apatite fission track (AFT) and (b) muscovite $^{40}Ar/^{39}Ar$ sample ages versus sample elevation for models with thermal conductivity values of 2.5 and 3.0 W/m K (squares, circles). Age error bars are 20% and 10% for the AFT and $^{40}Ar/^{39}Ar$, respectively.

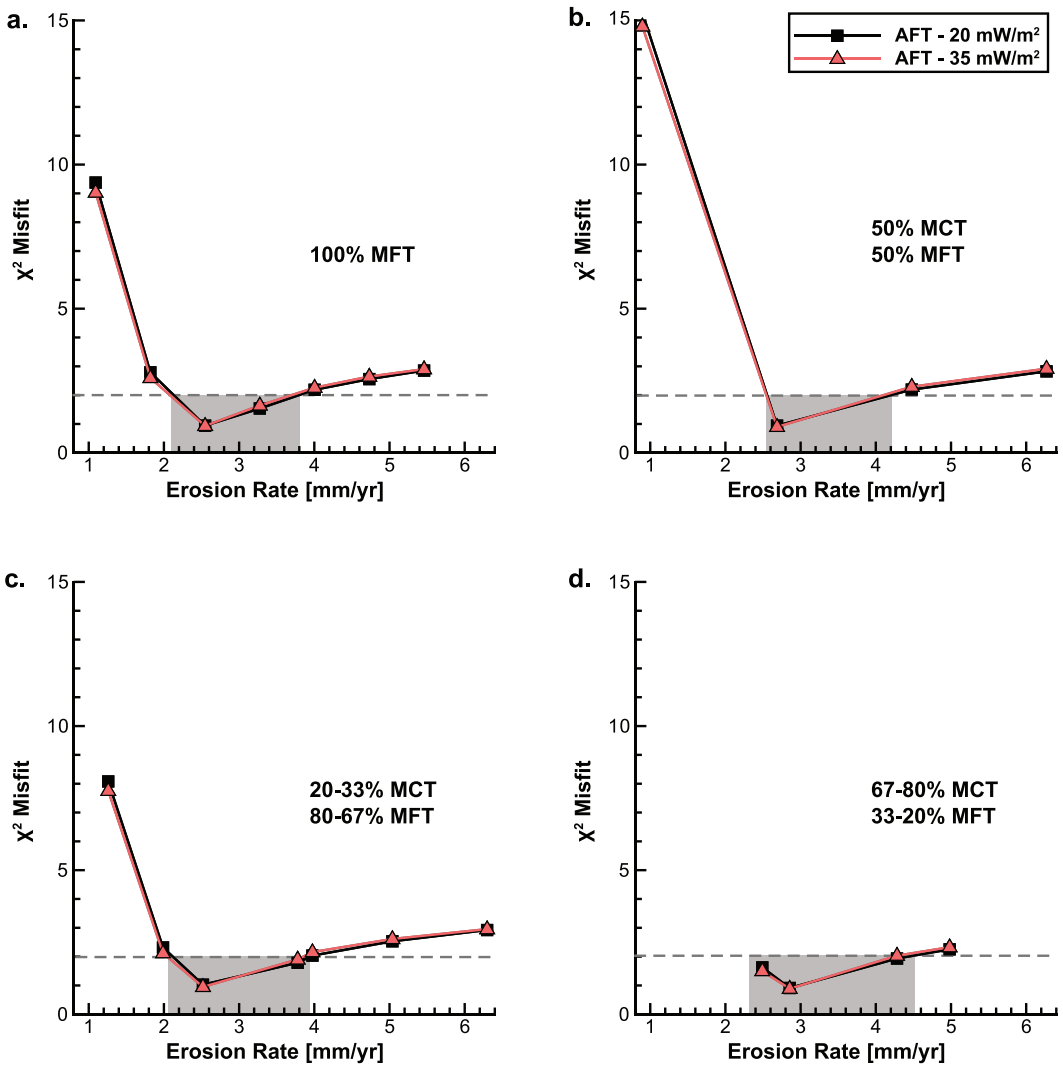

Figure 2.8: Effect of varying fault kinematics on predicted sample ages. The χ^2 misfit values for predicted and observed AFT ages versus erosion rates derived from various thermokinematic models with basal heat flux values of 20 and 35 mW/m^2 (squares, circles). Four different tectonic scenarios are shown: (a) slip only on the MFT, (b) equal overthrusting rate on the MFT and MCT, (c) larger overthrusting rate on the MFT than the MCT, and (d) larger overthrusting rate on the MCT than the MFT. The range of model-derived erosion rates that provide a good fit to the AFT data (shaded region) is constrained by χ^2 misfit values of <2 (dashed line). Abbreviations are as in Figures 2.1 and 2.2.

Figure 2.9: Fit of AFT predicted ages to observed ages in transects for different kinematic scenarios. Observed AFT ages (circles) are shown with their 2σ uncertainties and apparent exhumation rate from the slope of the weighted regression line. Predicted ages are shown with their model-derived erosion rate for the four tectonic scenarios: Slip only on the MFT (squares), equal overthrusting rate on the MFT and MCT (triangles), larger overthrusting rate on the MFT than the MCT (inverted triangles), and larger overthrusting rate on the MCT than MFT (diamonds). Abbreviations are as in Figures 2.1 and 2.2.

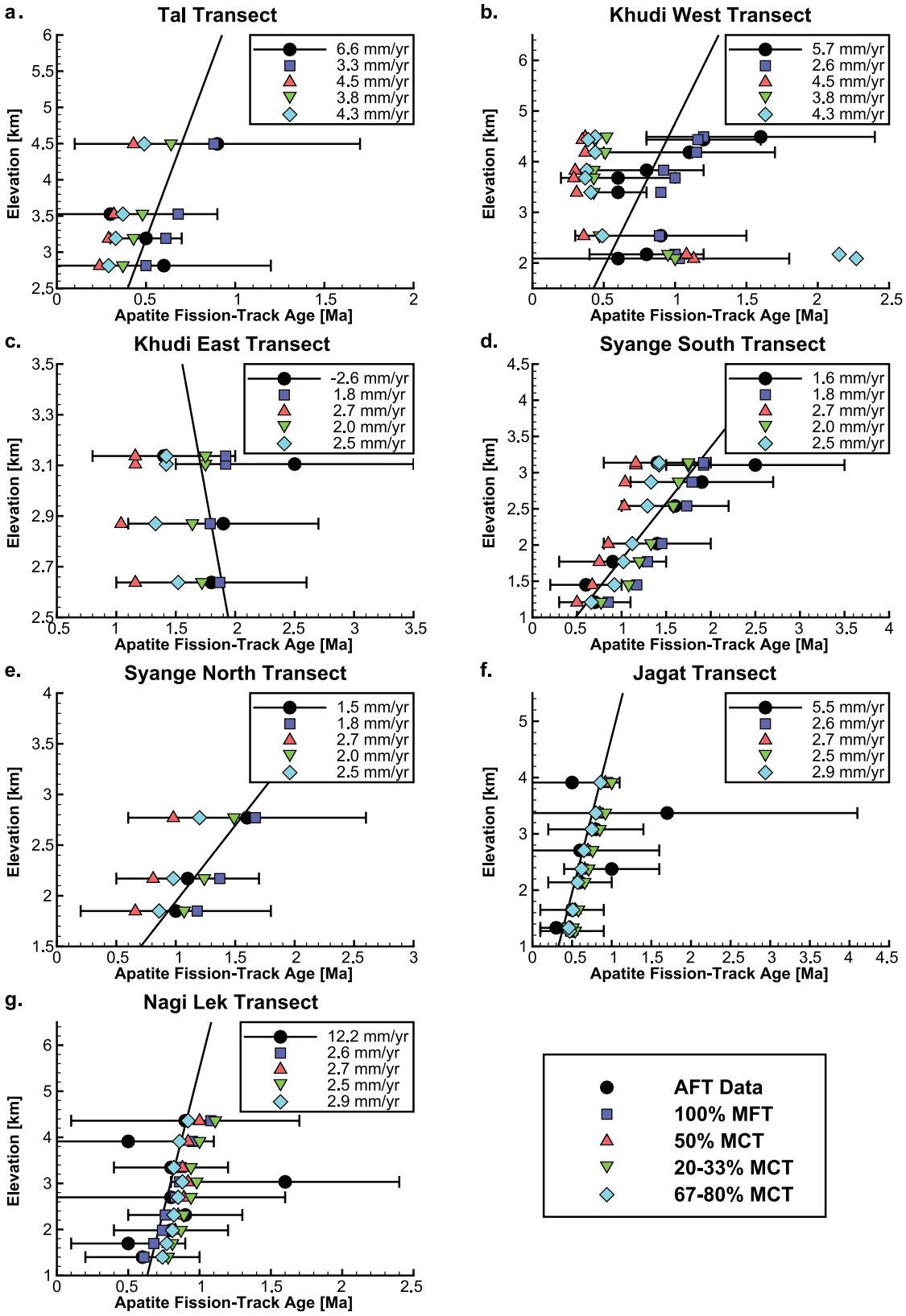
a.
Tal Transect
6.6 mm/yr
3.3 mm/yr
4.5 mm/yr
3.8 mm/yr
4.3 mm/yr
Elevation [km]
Apatite Fission-Track Age [Ma]
b.
Khudi West Transect
5.7 mm/yr
2.6 mm/yr
4.5 mm/yr
3.8 mm/yr
4.3 mm/yr
Elevation [km]
Apatite Fission-Track Age [Ma]
c.
Khudi East Transect
-2.6 mm/yr
1.8 mm/yr
2.7 mm/yr
2.0 mm/yr
2.5 mm/yr
Elevation [km]
Apatite Fission-Track Age [Ma]
d.
Syange South Transect
1.6 mm/yr
1.8 mm/yr
2.7 mm/yr
2.0 mm/yr
2.5 mm/yr
Elevation [km]
Apatite Fission-Track Age [Ma]
e.
Syange North Transect
1.5 mm/yr
1.8 mm/yr
2.7 mm/yr
2.0 mm/yr
2.5 mm/yr
Elevation [km]
Apatite Fission-Track Age [Ma]
f.
Jagat Transect
5.5 mm/yr
2.6 mm/yr
2.7 mm/yr
2.5 mm/yr
2.9 mm/yr
Elevation [km]
Apatite Fission-Track Age [Ma]
g.
Nagi Lek Transect
12.2 mm/yr
2.6 mm/yr
2.7 mm/yr
2.5 mm/yr
2.9 mm/yr
Elevation [km]
Apatite Fission-Track Age [Ma]
AFT Data
100% MFT
50% MCT
20-33% MCT
67-80% MCT

Figure 2.10: Predicted muscovite $^{40}Ar/^{39}Ar$ ages in transects for different kinematic scenarios. Ages are shown with 10% age uncertainties and their model-derived erosion rate for the four tectonic scenarios: Slip only on the MFT (squares), equal overthrusting rate on the MFT and MCT (triangles), larger overthrusting rate on the MFT than the MCT (inverted triangles), and larger overthrusting rate on the MCT than the MFT (diamonds). Abbreviations are as in Figure 2.1.

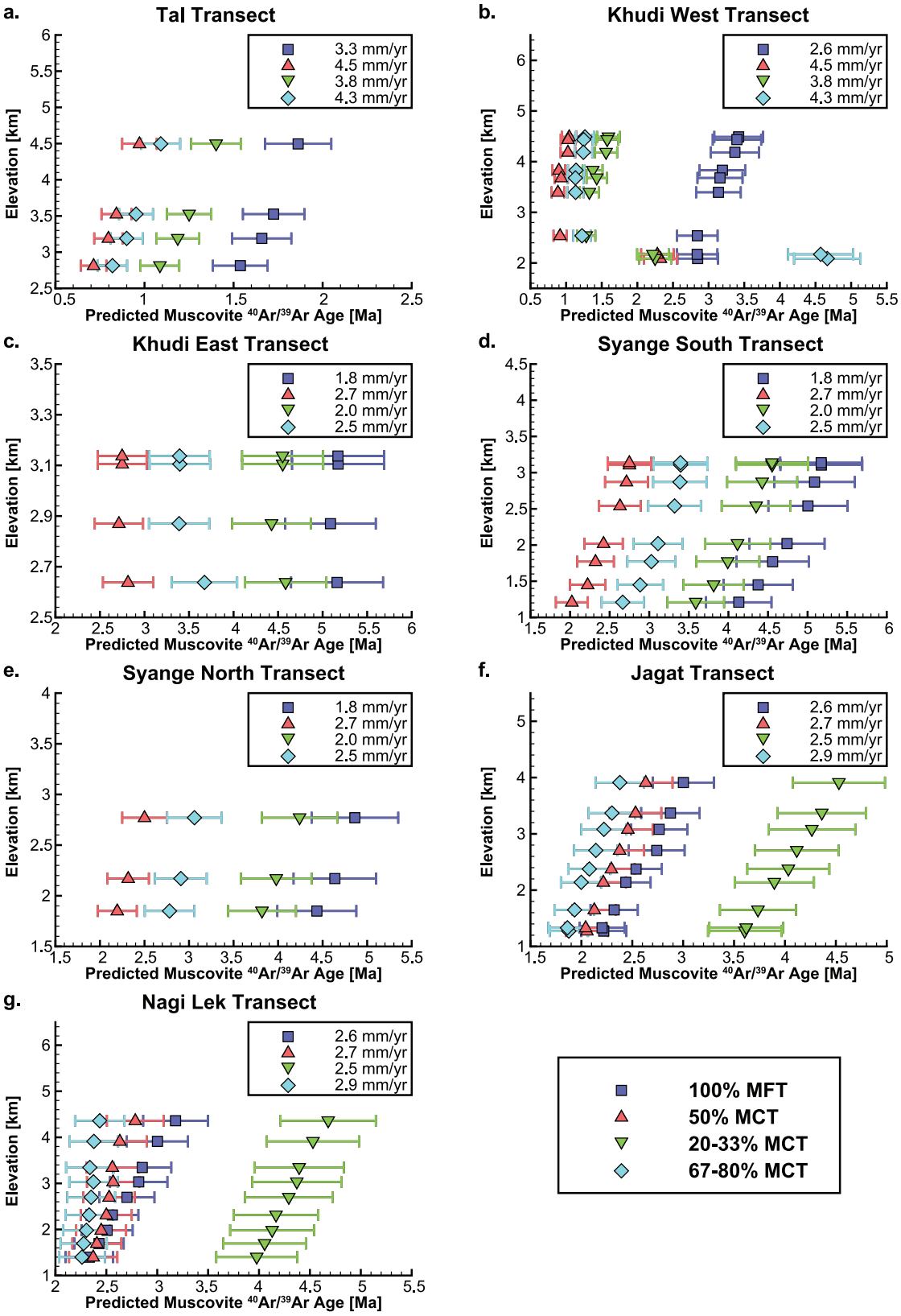
a.
Tal Transect
3.3 mm/yr
4.5 mm/yr
3.8 mm/yr
4.3 mm/yr
Elevation [km]
Predicted Muscovite 40Ar/39Ar Age [Ma]
b.
Khudi West Transect
2.6 mm/yr
4.5 mm/yr
3.8 mm/yr
4.3 mm/yr
Elevation [km]
Predicted Muscovite 40Ar/39Ar Age [Ma]
c.
Khudi East Transect
1.8 mm/yr
2.7 mm/yr
2.0 mm/yr
2.5 mm/yr
Elevation [km]
Predicted Muscovite 40Ar/39Ar Age [Ma]
d.
Syange South Transect
1.8 mm/yr
2.7 mm/yr
2.0 mm/yr
2.5 mm/yr
Elevation [km]
Predicted Muscovite 40Ar/39Ar Age [Ma]
e.
Syange North Transect
1.8 mm/yr
2.7 mm/yr
2.0 mm/yr
2.5 mm/yr
Elevation [km]
Predicted Muscovite 40Ar/39Ar Age [Ma]
f.
Jagat Transect
2.6 mm/yr
2.7 mm/yr
2.5 mm/yr
2.9 mm/yr
Elevation [km]
Predicted Muscovite 40Ar/39Ar Age [Ma]
g.
Nagi Lek Transect
2.6 mm/yr
2.7 mm/yr
2.5 mm/yr
2.9 mm/yr
Elevation [km]
Predicted Muscovite 40Ar/39Ar Age [Ma]
100% MFT
50% MCT
20-33% MCT
67-80% MCT

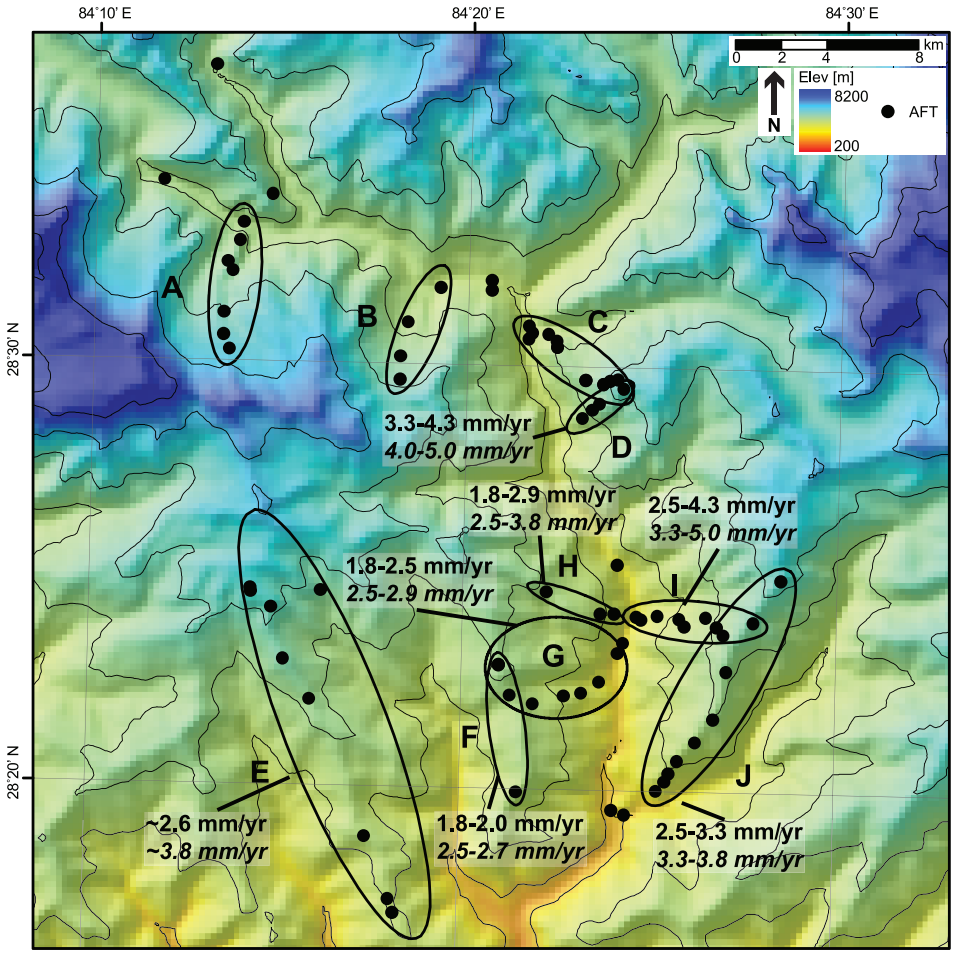

Figure 2.11: Model-constrained range of erosion rates for the data transects (ovals) shown on a shaded relief DEM of the study area with sample locations for AFT data (circles). Ranges are listed where at least 80% of the predicted ages are within the 2σ uncertainties of the observed ages. The upper range is for a model with a Greater Himalayan sequence heat production of 3.0 μW/m^3 and the lower, italicized range is for a heat production of 0.8 μW/m^3. Abbreviations are as in Figures 2.1 and 2.2, and transect names are as in Figure 2.2.

Bibliography

Arita, K. Origin of the inverted metamorphism of the Lower Himalayas, central Nepal. *Tectonophysics*, 95(1-2):43–60, 1983.

Barros, A. P., Joshi, M., Putkonen, J. and Burbank, D. W. A study of the 1999 monsoon rainfall in a mountainous region in central Nepal using TRMM products and rain gauge observations. *Geophysical Research Letters*, 27(22):3683–3686, 2000.

Barton, C. M. and England, P. C. Shear heating at the Olympos (Greece) thrust and the deformation properties of carbonates at geological strain rates. *Geological Society of America Bulletin*, 90(5):483–492, 1979.

Batt, G. E. and Brandon, M. T. Lateral thinking; 2-D interpretation of thermochronology in convergent orogenic settings. *Tectonophysics*, 349(1-4):185–201, 2002.

Beaumont, C., Fullsack, P. and Hamilton, J. Erosional control of active compressional orogens. In McClay, K., editor, *Thrust Tectonics*, pages 1–18. Chapman and Hall, New York, 1992.

Beaumont, C., Jamieson, R. A., Nguyen, M. H. and Lee, B. Himalayan tectonics explained by extrusion of a low-viscosity crustal channel coupled to focused surface denudation. *Nature*, 414(6865):738–742, 2001.

Bilham, R., Larson, K. M., Freymueller, J. T., Jouanne, F., Le Fort, P., Leturmy, P., Mugnier, J. L., Gamond, J. F., Glot, J. P., Martinod, J., Chaudury, N. L., Chitrakar, G. R., Gautam, U. P., Koirala, B. P., Pandey, M. R., Ranabhat, R., Sapkota, S. N., Shrestha, P. L., Thakuri, M. C., Timilsina, U. R., Tiwari, D. R.,

Vidal, G., Vigny, C., Galy, A. and de Voogd, B. GPS measurements of present-day convergence across the Nepal Himalaya. *Nature*, 386(6620):61–64, 1997.

Blythe, A. E., Burbank, D. W., Carter, A., Schmidt, K. and Putkonen, J. Plio-Quaternary exhumation history of the central Nepalese Himalaya: 1. Apatite and zircon fission-track and apatite [U-Th]/He analyses. *Tectonics*, 26, 2007. doi: 10.1029/2006TC001990.

Bollinger, L., Henry, P. and Avouac, J. P. Mountain building in the Nepal Himalaya: Thermal and kinematic model. *Earth and Planetary Science Letters*, 244(1-2):58–71, 2006.

Braun, J. Quantifying the effect of recent relief changes on age-elevation relationships. *Earth and Planetary Science Letters*, 200(3-4):331–343, 2002.

Braun, J. Quantitative Constraints on the Rate of Landform Evolution Derived from Low-Temperature Thermochronology. *Reviews in Mineralogy and Geochemistry*, 58:351–374, 2005.

Braun, J. and Robert, X. Constraints on the rate of post-orogenic erosional decay from low-temperature thermochronological data; application to the Dabie Shan, China. *Earth Surface Processes and Landforms*, 30(9):1203–1225, 2005.

Braun, J. and van der Beek, P. Evolution of passive margin escarpments; what can we learn from low-temperature thermochronology? *Journal of Geophysical Research*, 109(F4):F04009, 2004.

Brewer, I. and Burbank, D. W. Thermal and kinematic modeling of bedrock and detrital cooling ages in the central Himalaya. *J. Geophys. Res.*, 111(B9):B09409, 2006.

Brewer, I. D., Burbank, D. W. and Hodges, K. V. Modelling detrital cooling-age populations; insights from two Himalayan catchments. *Basin Research*, 15(3):305–320, 2003.

Brewer, I. D., Burbank, D. W. and Hodges, K. V. Downstream development of a detrital cooling-age signal; insights from $^{40}Ar/^{39}Ar$ muscovite thermochronology in the Nepalese Himalaya. In Willett, S. D., Hovius, N., Brandon, M. T. and Fisher, D. M., editors, *Tectonics, Climate and Landscape Evolution*, volume 398 of *Penrose Conference Series*, pages 321–338. Geological Society of America, 2006.

Brun, J.-P., Burg, J.-P. and Chen Guo, M. Strain trajectories above the Main Central Thrust (Himalaya) in southern Tibet. *Nature*, 313(6001):388–390, 1985.

Brunel, M. Ductile thrusting in the Himalayas; shear sense criteria and stretching lineations. *Tectonics*, 5(2):247–265, 1986.

Burbank, D. W., Blythe, A. E., Putkonen, J., Pratt-Sitaula, B., Gabet, E., Oskin, M., Barros, A. and Ojha, T. P. Decoupling of erosion and precipitation in the Himalayas. *Nature*, 426(6967):652–655, 2003.

Catlos, E. J., Harrison, T. M., Kohn, M. J., Grove, M., Ryerson, F. J., Manning, C. E. and Upreti, B. N. Geochronologic and thermobarometric constraints on the evolution of the Main Central Thrust, central Nepal Himalaya. *Journal of Geophysical Research, B, Solid Earth and Planets*, 106(8):16,177–16,204, 2001.

Clauser, C. and Huenges, E. Thermal conductivity of rocks and minerals. *AGU Reference Shelf*, 3:105–126, 1995.

Coleman, M. E. U-Pb constraints on Oligocene-Miocene deformation and anatexis

within the central Himalaya, Marsyandi Valley, Nepal. *American Journal of Science*, 298(7):553–571, 1998.

Copeland, P., Harrison, T. M., Hodges, K. V., Maruejol, P., Le Fort, P. and Pecher, A. An early Pliocene thermal disturbance of the Main Central Thrust, central Nepal; implications for Himalayan tectonics. *Journal of Geophysical Research, B, Solid Earth and Planets*, 96(5):8475–8500, 1991.

DeCelles, P. G., Robinson, D. M., Quade, J., Ojha, T. P., Garzione, C. N., Copeland, P. and Upreti, B. N. Stratigraphy, structure, and tectonic evolution of the Himalayan fold-thrust belt in western Nepal. *Tectonics*, 20(4):487–509, 2001.

Dodson, M. H. Closure temperature in cooling geochronological and petrological systems. *Contributions to Mineralogy and Petrology*, 40(3):259–274, 1973.

Donelick, R. A., O'Sullivan, P. B. and Ketcham, R. A. Apatite Fission-Track Analysis. *Reviews in Mineralogy and Geochemistry*, 58:49–94, 2005.

Edwards, R. M. $^{40}Ar/^{39}Ar$ geochronology of the Main Central Thrust (MCT) region; evidence for late Miocene to Pliocene disturbances along the MCT, Marsyangdi River valley, west-central Nepal Himalaya. *Journal of Nepal Geological Society*, 10:41–46, 1995.

Ehlers, T. A. Crustal Thermal Processes and the Interpretation of Thermochronometer Data. *Reviews in Mineralogy and Geochemistry*, 58:315–350, 2005.

Ehlers, T. A., Armstrong, P. A. and Chapman, D. S. Normal fault thermal regimes and the interpretation of low-temperature thermochronometers. *Physics of the Earth and Planetary Interiors*, 126:179–194, 2001.

Ehlers, T. A., Chaudhri, T., Kumar, S., Fuller, C. W., Willett, S. D., Ketcham, R. A., Brandon, M. T., Belton, D. X., Kohn, B. P., Gleadow, A. J., Dunai, T. J. and Fu, F. Q. Computational Tools for Low-Temperature Thremochronometer Interpretation. *Reviews in Mineralogy and Geochemistry*, 58:589–622, 2005.

Ehlers, T. A. and Farley, K. A. Apatite (U-Th)/He thermochronometry; methods and applications to problems in tectonic and surface processes. *Earth and Planetary Science Letters*, 206(1-2):1–14, 2003.

Ehlers, T. A., Willett, S., Armstrong, P. A. and Chapman, D. S. Exhumation of the Central Wasatch Mountains, Utah: 2. Thermo-kinematics of exhumation and thermochronometer interpretation. *Journal of Geophysical Research*, 108(B3):2173, 2003.

England, P., Le Fort, P., Molnar, P. and Pecher, A. Heat sources for Tertiary metamorphism and anatexis in the Annapurna-Manaslu region, central Nepal. *Journal of Geophysical Research, B, Solid Earth and Planets*, 97(2):2107–2128, 1992.

Evans, M. J., Derry, L. A. and France-Lanord, C. Geothermal fluxes of alkalinity in the Narayani river system of central Nepal. *Geochemistry, Geophysics, Geosystems - G (super 3)*, 5:no.8, 21, 2004.

Gabet, E. J., Pratt-Sitaula, B. A. and Burbank, D. W. Climatic controls on hillslope angle and relief in the Himalayas. *Geology*, 32(7):629–632, 2004.

Gansser, A. *Geology of the Himalayas*. Wiley Interscience, London, 1964.

Graham, C. M. and England, P. C. Thermal regimes and regional metamorphism in the vicinity of overthrust faults; an example of shear heating and inverted meta-

morphic zonation from southern California. *Earth and Planetary Science Letters*, 31(1):142–152, 1976.

Grujic, D., Casey, M., Davidson, C., Hollister, L. S., Kuendig, R., Pavlis, T. L. and Schmid, S. M. Ductile extrusion of the Higher Himalayan Crystalline in Bhutan; evidence from quartz microfabrics. *Tectonophysics*, 260(1-3):21–43, 1996.

Gupta, A. K. and Thomas, E. Initiation of Northern Hemisphere glaciation and strengthening of the Northeast Indian monsoon; Ocean Drilling Program Site 758, eastern equatorial Indian Ocean. *Geology*, 31(1):47–50, 2003.

Gupta, S. Himalayan drainage patterns and the origin of fluvial megafans in the Ganges foreland basin. *Geology*, 25(1):11–14, 1997.

Hames, W. E. and Bowring, S. A. An empirical evaluation of the argon diffusion geometry in muscovite. *Earth and Planetary Science Letters*, 124(1-4):161–169, 1994.

Hansen, F. D. and Carter, N. L. Creep of selected crustal rocks at 1000 MPa. *Eos, Transactions, American Geophysical Union*, 63(18):437, 1982.

Harrison, T. M., Copeland, P., Kidd, W. S. F. and Yin, A. Raising Tibet. *Science*, 255(5052):1663–1670, 1992.

Harrison, T. M., Ryerson, F. J., Le Fort, P., Yin, A., Lovera, O. M. and Catlos, E. J. A late Miocene-Pliocene origin for the central Himalayan inverted metamorphism. *Earth and Planetary Science Letters*, 146(1-2):E1–E7, 1997.

Harrison, T. M. and Zeitler, P. K. Fundamentals of Noble Gas Thermochronometry. *Reviews in Mineralogy and Geochemistry*, 58:123–149, 2005.

Henry, P., Le Pichon, X. and Goffe, B. Kinematic, thermal and petrological model of the Himalayas; constraints related to metamorphism within the underthrust Indian crust and topographic elevation. *Tectonophysics*, 273(1-2):31–56, 1997.

Hodges, K. V. Tectonics of the Himalaya and southern Tibet from two perspectives. *Geological Society of America Bulletin*, 112(3):324–350, 2000.

Hodges, K. V., Hurtado, J. M. and Whipple, K. X. Southward extrusion of Tibetan crust and its effect on Himalayan tectonics. *Tectonics*, 20(6):799–809, 2001.

Hodges, K. V., Parrish, R. R. and Searle, M. P. Tectonic evolution of the central Annapurna Range, Nepalese Himalayas. *Tectonics*, 15(6):1264–1291, 1996.

Hodges, K. V., Wobus, C. W., Ruhl, K., Schildgen, T. and Whipple, K. X. Quaternary deformation, river steepening, and heavy precipitation at the front of the Higher Himalayan ranges. *Earth and Planetary Science Letters*, 220:379–389, 2004.

Hubbard, M. S. and Harrison, T. M. $^{40}Ar/^{39}Ar$ age constraints on deformation and metamorphism in the Main Central Thrust zone and Tibetan Slab, eastern Nepal Himalaya. *Tectonics*, 8(4):865–880, 1989.

Huntington, K. W., Blythe, A. E. and Hodges, K. V. Climate change and Late Pliocene acceleration of erosion in the Himalaya. *Earth and Planetary Science Letters*, 252(1-2):107–118, 2006.

Huntington, K. W. and Hodges, K. V. A comparative study of detrital mineral and bedrock age-elevation methods of estimating erosion rates. *Journal of Geophysical Research, F, Earth Surface*, 111(F03011):doi:10.1029/2005JF000454, 2006.

Jouanne, F., Mugnier, J. L., Gamond, J. F., Le Fort, P., Pandey, M. R., Bollinger,

L., Flouzat, M. and Avouac, J. P. Current shortening across the Himalayas of Nepal. *Geophysical Journal International*, 157(1):1–14, 2004.

Kohl, T. and Hopkirk, R. J. "FRACTure" a simulation code for forced fluid flow and transport in fractured, porous rock. *Geothermics*, 24(3):333–343, 1995.

Larson, K. M., Buergmann, R., Bilham, R. and Freymueller, J. T. Kinematics of the India-Eurasia collision zone from GPS measurements. *Journal of Geophysical Research, B, Solid Earth and Planets*, 104(1):1077–1093, 1999.

Laslett, G. M., Green, P. F., Duddy, I. R. and Gleadow, A. J. W. Thermal annealing of fission tracks in apatite. *Chemical Geology; Isotope Geoscience Section*, 65(1):1–13, 1987.

Lavé, J. and Avouac, J. P. Active folding of fluvial terraces across the Siwaliks Hills, Himalayas of central Nepal. *Journal of Geophysical Research, B, Solid Earth and Planets*, 105(3):5735–5770, 2000.

Le Fort, P. Himalayas; the collided range; present knowledge of the continental arc. *American Journal of Science*, Vol. 275-A, Tectonics and mountain ranges:1–44, 1975.

Lyon-Caen, H. and Molnar, P. Constraints on the structure of the Himalaya from an analysis of gravity anomalies and a flexural model of the lithosphere. *JGR. Journal of Geophysical Research. B*, 88(10):8171–8191, 1983.

Macfarlane, A. M. Chronology of Tectonic Events in the Crystalline Core of the Himalaya, Langtang National Park, Central Nepal. *Tectonics*, 12(4):1004–1025, 1993.

Macfarlane, A. M., Hodges, K. V. and Lux, D. A structural analysis of the Main Central Thrust zone, Langtang National Park, central Nepal Himalaya. *Geological Society of America Bulletin*, 104(11):1389–1402, 1992.

Mancktelow, N. S. and Grasemann, B. Time-dependent effects of heat advection and topography on cooling histories during erosion. *Tectonophysics*, 270(3-4):167–195, 1997.

Molnar, P., England, P. and Martinod, J. Mantle dynamics, uplift of the Tibetan Plateau, and the Indian monsoon. *Reviews of Geophysics*, 31(4):357–396, 1993.

Niemi, N. A., Oskin, M., Burbank, D. W., Heimsath, A. M. and Gabet, E. J. Effects of bedrock landslides on cosmogenically determined erosion rates. *Earth and Planetary Science Letters*, 237(3-4):480–498, 2005.

Pandey, M. R., Tandukar, R. P., Avouac, J. P., Lave, J. and Massot, J. P. Interseismic strain accumulation on the Himalayan crustal ramp (Nepal). *Geophysical Research Letters*, 22(7):751–754, 1995.

Pearson, O. N. and DeCelles, P. G. Structural geology and regional tectonic significance of the Ramgarh Thrust, Himalayan fold-thrust belt of Nepal. *Tectonics*, 24:no.4, 26, 2005.

Raymo, M. E. The initiation of Northern Hemisphere glaciation. *Annual Review of Earth and Planetary Sciences*, 22:353–383, 1994.

Reiners, P. W., Ehlers, T. A., Mitchell, S. G. and Montgomery, D. R. Coupled spatial variations in precipitation and long-term erosion rates across the Washington Cascades. *Nature*, 426(6967):645–647, 2003.

Ring, U., Brandon, M. T., Willett, S. D. and Lister, G. S. Exhumation processes. *Geological Society Special Publications*, 154:1–27, 1999.

Robbins, G. A. *Radiogenic argon diffusion in muscovite under hydrothermal conditions*. Thesis or dissertation; master's; monographic, Brown University, 1972.

Robinson, D. M., DeCelles, P. G., Garzione, C. N., Pearson, O. N., Harrison, T. M. and Catlos, E. J. Kinematic model for the Main Central Thrust in Nepal. *Geology*, 31(4):359–362, 2003.

Roy, S. and Rao, R. U. M. Heat flow in the Indian Shield. *Journal of Geophysical Research, B, Solid Earth and Planets*, 105(11):25,587–25,604, 2000.

Ruddiman, W. F., Raymo, M. E., Prell, W. L. and Kutzbach, J. E. The uplift-climate connection; a synthesis. In Ruddiman, W. F., editor, *Tectonic Uplift and Climate Change*, page 535. Springer, 1997.

Ruhl, K. W. and Hodges, K. V. The use of detrital mineral cooling ages to evaluate steady state assumptions in active orogens; an example from the central Nepalese Himalaya. *Tectonics*, 24:no.4, 14, 2005.

Rybach, L. Radioactive heat production; a physical property determined by the chemistry of rocks. In Strens, R., editor, *The physics and chemistry of minerals and rocks*. John Wiley and Sons, London, United Kingdom, 1976.

Sass, J. H., Lachenbruch, A. H., Moses, T. H., J., Morgan, P., Zoback, M. D. and Lachenbruch, A. H. Heat flow from a scientific research well at Cajon Pass, California. *Journal of Geophysical Research, B, Solid Earth and Planets*, 97(4):5017–5030, 1992.

Schelling, D. and Arita, K. Thrust tectonics, crustal shortening, and the structure of the far-eastern Nepal Himalaya. *Tectonics*, 10(5):851–862, 1991.

Searle, M. P. Extensional and compressional faults in the Everest-Lhotse Massif, Khumbu Himalaya, Nepal. *Journal of the Geological Society of London*, 156(2):227–240, 1999.

Searle, M. P. and Godin, L. The South Tibetan detachment and the Manaslu Leucogranite; a structural reinterpretation and restoration of the Annapurna-Manaslu Himalaya, Nepal. *Journal of Geology*, 111(5):505–523, 2003.

Seeber, L. and Gornitz, V. River profiles along the Himalayan Arc as indicators of active tectonics. *Tectonophysics*, 92(4):335–367, 1983.

Stüwe, K., White, L. and Brown, R. The influence of eroding topography on steady-state isotherms; application to fission track analysis. *Earth and Planetary Science Letters*, 124(1-4):63–74, 1994.

Suppe, J. Geometry and kinematics of fault-bend folding. *American Journal of Science*, 283(7):684–721, 1983.

Tagami, T. and O'Sullivan, P. B. Fundamentals of Fission-Track Thermochronology. *Reviews in Mineralogy and Geochemistry*, 58:19–47, 2005.

Tapponnier, P., Xu, Z., Roger, F., Meyer, B., Arnaud, N., Wittlinger, G. and Yang, J. Oblique stepwise rise and growth of the Tibet Plateau. *Science*, 294(5547):1671–1677, 2001.

Thiede, R. C., Arrowsmith, J. R., Bookhagen, B., McWilliams, M. O., Sobel, E. R. and Strecker, M. R. From tectonically to erosionally controlled development of the Himalayan Orogen. *Geology*, 33(8):689–692, 2005.

Thiede, R. C., Bookhagen, B., Arrowsmith, R., Sobel, E. R. and Strecker, M. R. Climatic control on rapid exhumation along the southern Himalayan Front. *Earth and Planetary Science Letters*, 222(3):791–806, 2004.

Valdiya, K. S. The two intracrustal boundary thrusts of the Himalaya. *Tectonophysics*, 66(4):323–348, 1980.

van der Beek, P., Summerfield, M. A., Braun, J., Brown, R. W. and Fleming, A. Modeling postbreakup landscape development and denudational history across the southeast African (Drakensberg Escarpment) margin. *Journal of Geophysical Research, B, Solid Earth and Planets*, 107:no.12, 18, 2002.

Vance, D., Bickle, M., Ivy-Ochs, S. and Kubik, P. W. Erosion and exhumation in the Himalaya from cosmogenic isotope inventories of river sediments. *Earth and Planetary Science Letters*, 206(3-4):273–288, 2003.

Wagner, G., Reimer, G. and Jager, E. Cooling ages derived by apatite fission-track, mica Rb-Sr and K-Ar dating: the uplift and cooling history of the Central Alps. *Mem. Ist. Geol. Min. Univ. Padova*, XXX, 1977.

Wagner, G. A. and Reimer, G. M. Fission track tectonics; the tectonic interpretation of fission track apatite ages. *Earth and Planetary Science Letters*, 14(2):263–268, 1972.

Wang, Q., Zhang, P., Freymueller, J. T., Bilham, R., Larson, K. M., Lai, X., You, X., Niu, Z., Wu, J., Li, Y., Liu, J., Yang, Z. and Chen, Q. Present-day crustal deformation in China constrained by Global Positioning System measurements. *Science*, 294(5542):574–577, 2001.

Willett, S. D. Orogeny and orography; the effects of erosion on the structure of

mountain belts. *Journal of Geophysical Research, B, Solid Earth and Planets*, 104(12):28,957–28,982, 1999.

Wobus, C. W., Heimsath, A., Whipple, K. X. and Hodges, K. V. Active out-of-sequence thrust faulting in the central Nepalese Himalaya. *Nature*, 434:1008–1011, 2005.

Wobus, C. W., Hodges, K. V. and Whipple, K. X. Has focused denudation sustained active thrusting at the Himalayan topographic front? *Geology*, 31(20):861–864, 2003.

Zhang, P., Molnar, P. and Downs, W. R. Increased sedimentation rates and grain sizes 2-4 Myr ago due to the influence of climate change on erosion rates. *Nature*, 410(6831):891–897, 2001.

Zhang, P., Shen, Z., Wang, M., Gan, W., Buergmann, R., Molnar, P., Wang, Q., Niu, Z., Sun, J., Wu, J., Sun, H. and You, X. Continuous deformation of the Tibetan Plateau from Global Positioning System data. *Geology*, 32(9):809–812, 2004.

CHAPTER III

Effects of denudation, faulting and topographic evolution on detrital thermochronometer data

3.1 Abstract

Detrital thermochronometer data collected from modern rivers or sedimentary basins have potential to record drainage basin-wide changes in topographic relief, fault kinematics, and spatial and temporal variations in erosion. However, few studies have addressed the effects of these different factors on detrital thermochronometer age distributions. Here we use transient 3-D thermokinematic and landform evolution models to simulate the effects of drainage basin evolution and fault kinematics on the thermal field through which detrital samples cool. Cooling-rate-dependent apatite (U-Th)/He (AHe), zircon fission-track and muscovite $^{40}Ar/^{39}Ar$ (MAr) grain-age distributions are predicted for samples collected from river and basin sediments. These distributions are interpreted to determine the sensitivity of different thermochronometer systems to denudation and deformation histories in drainage basins of varying size. We find that detrital thermochronometer data in rapidly eroding regions have a strong sensitivity to the kinematics of exhumation, but lack sensitivity to changes in topographic relief under most conditions. In addition, a comparison of the

Official citation:
Whipp, D.M., Jr., and T.A. Ehlers, Effects of denudation, faulting and topographic evolution on detrital thermochronometer data, for submission to *Journal of Geophysical Research, Earth Surface*

denudation rates estimated using conventional 1-D age-elevation relationships and the prescribed model rate reveals significant overestimation. At rapid ($\sim$2.5 mm/y) denudation rates, we see rate overestimates of >300% and $\sim$90% for the AHe and MAr systems between the two approaches. In models that explore possible age distributions in foreland basin sediments, we confirm that the lag time concept is useful and a reliable means for identifying denudation rate changes as no significant change in lag time occurs for changing topographic relief scenarios. Furthermore, we find that for drainage basins with erosion rates between 0.5$-$2.5 mm/y, the AHe system is best for detecting very recent ($\leq$2 Ma) rate changes, while the MAr system is better for the last 5$-$20 Ma.

3.2 Introduction

Geodynamic models predict a strong coupling between climate-driven erosion and tectonic deformation in active mountain ranges (e.g., Beaumont et al., 1992; Willett, 1999; Beaumont et al., 2001). To assess the strength of this coupling in natural settings, it is necessary to first quantify the long-term (>1 My) denudation and topographic history of an orogen. Detrital geochronology techniques can provide catchment-wide denudation histories (e.g., Cerveny et al., 1988; Copeland and Harrison, 1990; Renne et al., 1990; Brandon and Vance, 1992; Garver and Brandon, 1994a; Spiegel et al., 2000; Bernet et al., 2001; Schaller et al., 2001; Ruhl and Hodges, 2005; Hodges et al., 2005; Brewer et al., 2006; van der Beek et al., 2006; Schaller and Ehlers, 2006; Stock et al., 2006; Vermeesch, 2007) and have the potential to record temporal variations in both tectonics and landscape evolution (e.g., Stock and Montgomery, 1996; Brewer et al., 2003; Bernet et al., 2006; Szulc et al., 2006; Rahl et al., 2007; Reiners, 2007). However, similar to bedrock thermochronometer data, the in-

terpretation of detrital thermochronometer data can be complicated by a number of factors, such as evolving topography, erosion, faulting, groundwater flow, rock thermophysical properties and paleo-wildfires (e.g., Ehlers et al., 2001; Ehlers and Farley, 2003; Ehlers, 2005; Brewer and Burbank, 2006; Reiners et al., 2007; Whipp et al., 2007; Whipp and Ehlers, 2007). At present, their relative influence is unclear, limiting the potential power of detrital thermochronometer data. The goal of this paper is to quantify the impact of variable exhumation histories, faulting scenarios and topographic evolution on predicted detrital thermochronometer age distributions to determine the expected sensitivity of detrital datasets to these factors.

Previous studies explored the effects of crustal thermal processes on bedrock thermochronometer ages and the impact of various processes on detrital thermochronometer ages. Denudation and steady-state surface topography were shown to significantly affect the subsurface thermal field and low-temperature thermochronometers in mountainous regions using time-independent (Stüwe et al., 1994) and time-dependent (Mancktelow and Grasemann, 1997) two-dimensional (2-D) thermal models. Improving on the strictly vertical rock advection simulated in those studies, Henry et al. (1997), Stüwe and Hintermüller (2000) and Batt and Brandon (2002) showed how a lateral velocity component to particle transport changes predicted bedrock thermochronometer ages. Braun (2002) also used 2-D thermal modeling to show that changes in topographic relief in orogens can have a strong influence on the relationship between thermochronometer age and sample elevation, in some cases even inverting that relationship. In addition, a number of recent studies have further extended our understanding of how bedrock thermochronometers are affected by two- and three-dimensional (3-D) variations in exhumation kinematics, topographic evolution and rock thermal properties (e.g., Ehlers et al., 2001; Braun, 2003; Ehlers

and Farley, 2003; Bollinger et al., 2006; Brewer and Burbank, 2006; Whipp et al., 2007; Huntington et al., 2007).

The extension of the above methods into detrital applications that simulate grain-age distributions in modern rivers or sedimentary basins has lagged behind the bedrock equivalents. In one of the first modeling applications, Brewer et al. (2003) used a 2-D thermal model to predict a relationship between bedrock cooling ages and elevation that was convolved with the elevation hypsometry of drainage basins to generate predicted catchment age distributions from modern river sediments (Figure 3.1A−D). Using a similar approach, Ruhl and Hodges (2005) replaced the model-generated bedrock age-elevation relationship with an observed relationship and applied their model to determine catchment-wide denudation rates and test assumptions about spatial variations in catchment erosion. Brewer and Burbank (2006) improved on the use of a linear bedrock age-elevation relationship by implementing a more complex 2-D thrust fault kinematic model. Their model was extended laterally across the area of interest to allow for catchment sub-sampling and comparison to data from modern river sediment. Most recently, Rahl et al. (2007) used a simple one-dimensional (1-D) transient thermal model to predict age distributions in both modern river sediment and foreland basin deposits resulting in a variety of temporally variable denudation histories. The power of their model is the ability to better quantify temporal trends in denudation generated from cooling age distributions preserved in foreland basins.

Although the approaches used in previous studies (e.g., Figure 3.1A−D) have advanced our understanding of detrital thermochronometer data, it remains unclear how sensitive detrital data are to long-term variations in erosion or tectonics at the scale of an individual drainage basin (e.g., Figure 3.1A,E−G). The utility of

previous techniques is limited by the requirements that topography and the thermal field be in steady state, and the catchment denudation rates are spatially invariant (Figure 3.1F). We complement previous studies by modeling the detrital record of various processes both in modern river and foreland basin sediment. We modified a 3-D thermokinematic numerical model (Braun, 2003) to predict grain-age distributions from drainage basins as a function of topographic evolution, exhumation kinematics and rock thermophysical properties. The primary goal of this study is to characterize the effects of rock transport kinematics and evolving topography on predicted age distributions. In the companion paper to this by Whipp and Ehlers (2008), we apply this model to quantify the tectonic and erosional history of the central Nepalese Himalaya using available detrital thermochronometer datasets. In the models used in this study, we clarify the potential processes that can be detected in detrital thermochronometer datasets with and without the use of numerical models to aid in data interpretation. Our secondary goal is to assess the magnitude of error in basin-wide denudation rate estimates calculated using 1-D age-elevation relationships.

3.3 Numerical Modeling Approach

We utilize a modified version of the thermokinematic numerical model Pecube (Braun, 2003) to simulate a number of processes potentially recorded in detrital thermochronometer data. The model was modified to predict grain-age distributions for various thermochronometer systems in drainage basins across a landscape (Figure 3.1A,E−G). The model consists of three components: (1) A kinematic and erosion model, (2) a thermal model and (3) an age prediction model (Figure 3.2). The kinematic model is coupled to the thermal model and used to track the exhumation and cooling history for thermochronometer age prediction. Below, we provide

detail on the numerical model setup and free parameters. Discussion of the numerical model results can be found in Section 3.4.

3.3.1 Kinematic Model

The kinematic model is used to simulate rock transport resulting from processes such as erosional exhumation and faulting. In addressing the sensitivity to these processes in detrital thermochronometer data, we focus on three different kinematic scenarios. The first scenario is that of vertical transport of rock as the overlying material is eroded. The second case is similar to the vertical case, but with an additional lateral component to the velocity field. This scenario, although somewhat simplified, is designed to incorporate the first order thermal effects of lateral transport of rock, such as in an active convergent orogen. The final scenario is referred to as the thrust scenario and uses the most complicated kinematics. In this scenario, the velocity field is intended to simulate the effects rock transport within a fold and thrust belt would have on the thermal field (e.g., Figure 3.3). This scenario includes multiple active thrust faults, frictional shear heating on those faults and partitioning of zones of varying thermophysical material properties by the faults. Although relevant information on the thrust scenario is provided below, a detailed discussion can be found in the companion paper to this by Whipp and Ehlers (2008).

Vertical Kinematic Scenario

In the cases where the model topography does not change with time, the vertical kinematic scenario yields a spatially uniform denudation rate. In this study, we focus on kinematic model variants that produce denudation rates typical of those observed in active orogens (0.5−2.5 mm/y). For this kinematic scenario, the prescribed magnitude of the vertical velocity is the only free parameter and is exactly balanced by

the denudation rate such that the topography is in steady state. Thus, the range of input velocities in the vertical kinematic scenario is 0.5−2.5 mm/y.

Lateral Kinematic Scenario

Similar to the vertical kinematic scenario, denudation in the lateral kinematic scenario is spatially uniform when the model topography does not evolve. In this case, the denudation rate exactly compensates the vertical component of the velocity field. Thus, the desired range of denudation rates is generated by varying two free parameters: The lateral component of the velocity field and the angle of material transport with respect to horizontal. We assume a uniform angle with respect to horizontal of 40°, which generates denudation rates of 0.5−2.5 mm/y with an input convergence rate range of ∼0.8−3.9 mm/y.

Thrust Kinematic Scenario

The thrust model features several active faults with variable dip angle near the surface and at depth, leading to spatially variable denudation rates (e.g., Figure 3.1F). This model features three thrust faults, one normal fault and was constructed to simulate the structure in the central Nepalese Himalaya. In the model region relevant to this study, there are two important structures: A thrust fault that intersects the model upper surface and the basal décollement from which that fault splays (Figure 3.3). The thrust fault has a dip angle of 40° and splays off the basal décollement dipping at 10° at a depth of ∼25 km. The resulting geometry is such that most of the basin area for basins used in this study is within the steeply dipping portion of the hanging wall and a small fraction is within the more shallow section. The result of this geometry is that denudation rates within the steeply dipping section of the hanging wall are ∼3.7 times faster than rates in the shallowly dipping section

(e.g., Figure 3.1F). To generate the desired range of denudation rates, the thrust model requires input convergence rates of $\sim$0.6$-$3.0 mm/y.

Another important difference with the thrust kinematic scenario is that the reference frame has the topography fixed with the faults migrating laterally (e.g., Figures 3.3, 3.6A). This approach is similar to the horizontal landscape advection case of Herman et al. (2007). Rocks above the basal décollement move strictly vertically toward the model surface. The rate of vertical motion is controlled by the dip angle of a given fault hanging wall section as the faults move laterally into their present day positions at time 0 Ma. The rate of lateral motion is set by the convergence rate across the faults and the number of faults that are active inboard of the structure of interest.

3.3.2 Erosion model

One of the unique and powerful features of Pecube is the simple implementation of complicated geometries including input of digital elevation models (DEMs) for surface topography and the ability to include temporal variations surface topography. Topographic modification in Pecube is driven by two terms: A scaling factor that is multiplied by the surface elevations to scale the topographic relief, and an offset factor that shifts all of the surface elevations by a constant value. Both values are input at each time step specified in the model and the combination of the two terms will morph the topography between the previous values and the current values over the time difference between the given time steps. For example, consider the case of model topography with a 4 km peak elevation and 4 km of topographic relief. To maintain a constant peak elevation while decreasing the topographic relief by 50%, the scaling factor would change from 1 to 0.5, while the offset factor would increase from 0 to 2 km. The scaling factor alone would decrease the maximum elevation from

4 km to 2 km, but the offset factor shifts all elevations in the topography up 2 km, maintaining the peak elevation of 4 km. In section 3, we discuss model results using the combination of the two parameters to simulate both a 50% increase and 50% decrease in topographic relief while maintaining a constant valley-bottom, constant mean or constant peak elevation.

The various relief change scenarios discussed above generate spatial variations in the denudation rate. For example, when the topography is fixed, a parcel of rock traveling vertically toward the model surface at 1 mm/y would experience a denudation rate of 1 mm/y. However, in a case where the topographic relief is decreasing and the upper surface of the model is moving with time, the denudation rate for parcels of rock beneath a high peak and a valley would be greater and less than 1 mm/y, respectively (Figure 3.7A). Therefore, the effective denudation rate is simply the combination of the input background rate and the rate of change of the surface elevations, where lowering of the surface topography increases the effective denudation rate and raising the surface elevations has the opposite effect.

3.3.3 Thermal Model

The kinematic and erosion model above is coupled to the thermal model through the advection velocity in the transient advection-diffusion equation solved using Pecube (Carslaw and Jaeger, 1959; Braun, 2003),

$$\rho c\left(\frac{\partial T}{\partial t}+v_x\frac{\partial T}{\partial x}+v_y\frac{\partial T}{\partial y}+v_z\frac{\partial T}{\partial z}\right)=\frac{\partial}{\partial x}k\frac{\partial T}{\partial x}+\frac{\partial}{\partial y}k\frac{\partial T}{\partial y}+\frac{\partial}{\partial z}k\frac{\partial T}{\partial z}+\rho A \tag{3.1}$$

where ρ is rock density, c is rock specific heat capacity, T is temperature, t is time, x, y and z are spatial coordinates, v_x, v_y, and v_z are the advection velocity components from the kinematic model, k is thermal conductivity and A is volumetric

radiogenic heat production. Equation 1 is formulated in the finite element method using the streamline-upwind Petrov-Galerkin method for numerical stability (Brooks and Hughes, 1982). The resulting equations are solved using constant temperature (Dirichlet) upper and lower boundary conditions and zero flux (Neumann) boundaries on the model sides and a Gauss-Seidel iterative method with over-relaxation (Bathe, 1982). The calculation output is the full 3-D thermal field for the given input model region (Figure 3.3).

For the simulations presented here, we use a geometry of a lithospheric block that is 150 × 310 × 130 km (L × W × D) in size (Figure 3.3). The average x-y node spacing in the finite element mesh is ∼950 m. Although this study does not focus specifically on the Himalaya, we utilize a DEM from central Nepal for the surface topography as this region features high-relief topography typical of active orogens. The DEM-derived surface topography is from a Shuttle Radar Topography Mission DEM from central Nepal with a resolution of ∼90 m (Farr et al., 2007).

In addition to the input kinematic scenario and topographic evolution, there are several other parameters in Pecube that affect the thermal calculation, but were not varied between simulations. As mentioned above, the finite element solution of Equation 1 uses constant temperature boundary conditions at the base and upper surface of the model. We use a basal temperature of 1350°C at 130 km depth. The upper surface temperature is 24°C at sea level and follows an atmospheric lapse rate of 6°C per km elevation increase. Thermophysical material properties, such as thermal conductivity and specific heat capacity are spatially invariant in models using the vertical and lateral kinematic models. In the thrust model, the faults separate regions of distinct material properties, and thus the material properties listed above vary spatially depending on the location of the material relative to the

faults. In addition, there is another heat source in the thrust models resulting from frictional shear heating on the fault surfaces. Details on the spatial partitioning of material properties and shear heating in the thrust model can be found in the companion paper to this by Whipp and Ehlers (2008). In all of the models, the radiogenic heat production is constant from the surface down to 50 km depth and there is no radiogenic heat production below that depth. It should be noted that the model setup does not include the effects of groundwater flow on the crustal thermal field (e.g., Smith and Chapman, 1983; Forster and Smith, 1989; Person et al., 1995; Whipp and Ehlers, 2007), however, it is expected that the sensitivity to the model free parameters would not change. Lastly, all of the transient thermal models have a simulation time of 50 My. A summary of the material property values can be found in Table 1.

3.3.4 Bedrock Thermochronometer Age Prediction Model

Cooling-rate-dependent thermochronometer ages are calculated in the model by tracking the exhumation pathway and cooling history of rocks exposed at the surface of the model. Model-predicted thermal histories are used to calculate apatite (U-Th)/He (AHe), apatite fission-track (AFT), zircon (U-Th)/He (ZHe), zircon fission-track (ZFT) and muscovite $^{40}Ar/^{39}Ar$ (MAr) thermochronometer ages as implemented in Braun et al. (2006). Kinetic parameters used for (U-Th)/He age prediction include: (1) Durango apatite (Farley, 2000), (2) the apatite alpha-radiation damage model of Shuster et al. (2006) and (3) the average zircon kinetics from Reiners et al. (2004). AFT ages are predicted using the Crowley et al. (1991) kinetic parameters. ZFT and MAr ages are calculated based on the concepts of Dodson (1973) as implemented in Braun et al. (2006), with the kinetic parameters of Brandon et al. (1998) for ZFT, and Robbins (1972) and Hames and Bowring (1994) for MAr. For

simplicity in the presentation of results, we focus on three systems that span a wide range of temperature sensitivities: Durango AHe, ZFT and MAr. These systems have effective closure temperatures (Dodson, 1973) of ∼67−83°C, ∼232−256°C and ∼381−426°C, respectively, for cooling rates of 10−100°C/My (e.g., Ehlers et al., 2005; Reiners and Brandon, 2006). As mentioned above, the total model run time is 50 My, so reset cooling ages will have an age of <50 Ma.

3.3.5 Generation of Detrital Age Distributions

Bedrock thermochronometer ages at the model surface are used to calculate grain-age distributions produced upstream of user-defined sample locations (e.g., Figure 3.2). The drainage basin area located upstream of detrital sample locations is determined using the D8 algorithm with imposed gradients flat resolution (Garbrecht and Martz, 1997) that identifies the contributing points on the landscape. After extracting ages from the landscape, an age histogram is created, forming the raw age distribution. This raw age distribution assumes: (1) Every point in the catchment contributes sediment, and (2) transport time and sediment storage are negligible. We assess the validity of the former assumption in the companion paper to this, where predicted and observed ages are compared (Whipp and Ehlers, 2008), whereas the later assumption is reasonable in high-relief active orogens. Following age extraction from the landscape, the same points are probed in the model to generate the corresponding distribution of denudation rates. The individual denudation rates and matching raw ages are then convolved to generate a model probability density function (PDF_m) of age (t) using an approach similar to that of Ruhl and Hodges (2005),

$$\mathrm{PDF}_m = \frac{1}{\sigma_{t_m}\sqrt{2\pi}} \exp\left[-\frac{1}{2}\left(\frac{t-t_m}{\sigma_{t_m}}\right)^2\right] \times v_z \tag{3.2}$$

where σ_{t_m} is the model one sigma age uncertainty, t is the range of ages over which PDF_m is defined, t_m is the predicted age and v_z is the corresponding denudation rate. In the cases we consider, the sample uncertainty (σ_{t_m}) is a function of the model-predicted cooling ages and assumed to be 5% for AHe, 10% for ZFT and 4% for MAr to represent typical errors associated with grain-age reproducibility and analytical uncertainties. A basin wide age distribution is created by summing the individual age PDFs to form a model synoptic probability density function (SPDF_m),

$$\mathrm{SPDF}_m = \left[\frac{1}{n}\sum_{i=1}^{n}\mathrm{PDF}_m(i)\right] \times \left(\frac{1}{\bar{v_z}}\right) \tag{3.3}$$

where n is the number of ages extracted from the river catchment and $\bar{v_z}$ is the mean denudation rate in that catchment. This approach is slightly different than the method used by Ruhl and Hodges (2005) because of the denudation rate scaling. Thus, the detrital grain-age prediction component of this study produces synthetic distributions for user-defined locations on the landscape. Next, we address the sensitivity of these distributions to variations in exhumation kinematics and topography.

3.4 Results

In the following, we identify possible diagnostic signatures in thermochronometer grain-age distributions of processes such as changes in denudation rate, fault activity, and topographic relief. Our results focus on the AHe, ZFT and MAr thermochronometer system response to each of these processes. With the exception of Section 3.4.4, that explores the effect of varying the drainage basin size, all results in this section are from a single drainage basin in the Nepalese Himalaya with a drainage area of $\sim$2775 km^2 and 7164 m of topographic relief.

3.4.1 Effects of changing denudation rates

Time-invariant denudation rates

The simplest scenario that we explore is the effect of time-invariant denudation rates on detrital thermochronometer ages. For each of the models discussed here, the vertical kinematic scenario is used and the input vertical velocity magnitude is the only free parameter. Denudation rates of 0.5, 1.0 or 2.5 mm/y are explored (Figure 3.4A). These rates encompass the range of values typical of active orogens.In these models, the surface topography does not change with time such that the vertical velocity is equivalent to the denudation rate.

The primary effect of increasing the model denudation rate from 0.5 to 2.5 mm/y is a well-known shift towards younger peak ages in the age distributions for each thermochronometer system (e.g., Garver et al., 1999). This result is not surprising as increasing the denudation rate at the surface not only increases the rate at which material approaches the surface, but also advects the effective closure temperature isotherms to shallower depths, both serving to decrease the predicted thermochronometer ages. In the case of the AHe system, peak ages decrease ∼91% for rates of 0.5 to 2.5 mm/y (Figure 3.4B). This trend persists for both the ZFT and MAr systems, with a ∼90% and ∼91% decrease in peak age, respectively (Figure 3.4C,D).

Another important change across the range of explored denudation rates is the decrease in age range (i.e., width of each age distribution) with increasing denudation rate. Again, this is not an unexpected result as more rapid exhumation would increase the slope of the relationship between sample age and elevation, thus decreasing the age range across a fixed range of elevations (e.g., one drainage basin). For the discussion of age ranges here and in subsequent sections, note that we define the age range to be that which encompasses 99% of the area beneath the predicted SPDF_m

curves, similar to Ruhl and Hodges (2005). For the AHe thermochronometer, an increase in denudation rate from 0.5 to 2.5 mm/y decreases the age range within the catchment age distribution by ∼89%. Similarly, the ZFT and MAr age ranges show decreases of ∼89% and ∼87% (Figure 3.4C,D).

Transient variations in denudation rate

The effect of an acceleration in denudation rate was explored using a vertical kinematic field and input denudation rates of either 0.5 or 2.5 mm/y. The free parameter in this case is the time at which an instantaneous acceleration in denudation rate occurs, either at 10 or 2 Ma. For comparison, we also examine models with time invariant rates of either 0.5 or 2.5 mm/y (Figure 3.5A). The surface topography does not change with time.

As was the case for time invariant denudation rates, the largest signal of an acceleration in denudation is a shift toward a younger peak age. Furthermore, the earlier (10 Ma) acceleration leads to a larger shift in peak age relative to the peak resulting from denudation that is constant at the initial rate. For example, with the AHe system, the peak ages are ∼88% and ∼83% younger for denudation rate changes at 10 and 2 Ma, respectively (Figure 3.5B). The higher temperature thermochronometer systems also show this trend with the ZFT peak ages decreasing from the fixed slow rate peak age of 14.2 Ma by ∼87% and ∼67% for the acceleration at 10 and 2 Ma, respectively (Figure 3.5C). The MAr peak ages decrease from 29.2 Ma at a constant denudation rate of 0.5 mm/y by ∼87% and ∼27% when the denudation rate increases to 2.5 mm/y at 10 and 2 Ma (Figure 3.5D). Furthermore, as seen in the previous section, an increase in denudation rate tends to generate a decrease in the age range of the corresponding distribution.

Another interesting behavior among the various thermochronometer age distribu-

tions is the decrease in response time to changes in denudation rate as the effective closure temperature for the given system decreases. In other words, the peak age for a lower temperature thermochronometer system (e.g., AHe) will show a denudation rate change by way of a larger shift in peak age relative to that change appearing in the age distribution for a higher temperature system (e.g., MAr). Consider the case where the denudation rate increases from 0.5 to 2.5 mm/y at 2 Ma. The AHe peak age decreases by ∼83% relative to the peak age when the denudation rate is fixed at 0.5 mm/y. Compared to the peak age with a constant denudation rate of 2.5 mm/y, which generates a peak age that is ∼91% lower than that at the slow fixed rate, the peak age difference is only ∼8%. However, for the MAr system, the difference in peak age for those same scenarios is ∼64% (Figure 3.5B,D). This behavior is also shown well in the age ranges for the AHe and MAr thermochronometers. The age range for the AHe system with a 5-fold increase in denudation rate at 2 Ma is ∼81% smaller than the range at a constant slow rate (0.5 mm/y). This is similar to the difference seen between the fixed slow and fixed fast denudation rates (∼89%), differing by only ∼8%. Again, for the same scenarios, the MAr age ranges differ by ∼80%, as the age range with an acceleration at 2 Ma is only ∼7% smaller than the range with a constant slow rate. Effectively, this is showing that the higher temperature systems have a greater response time to perturbations in denudation rate (e.g., Reiners and Brandon, 2006; Rahl et al., 2007). This would be expected, given the need to remove greater amounts of overlying material to expose material that has passed through the effective closure temperature isotherm subsequent to a change in denudation rate.

3.4.2 Effects of exhumation kinematics and faulting

The kinematics of rock exhumation are an important influence on grain-age distributions. Here we consider the effects of lateral transport of rock and faulting on age

distributions. The only model free parameter in this section is the exhumation kinematics and, as above, we compare the results from the lateral and thrust kinematic scenarios to models using the vertical kinematic scenario (Figure 3.6A). For the vertical and lateral kinematic models used here, the denudation rate is 1 mm/y. For the thrust model, most of the basin investigated has a denudation rate of 1 mm/y, and a small section has a denudation rate of 0.27 mm/y due to the ramp-flat geometry of the underlying thrust fault (Figure 3.6A). The denudation rates are constant with time, with the exception of the thrust model as explained below, and the surface topography does not change.

The peak ages and age range of the vertical and lateral kinematic scenarios are quite similar, with a general trend of younger peak ages and larger age ranges in the lateral scenario. As mentioned above, both scenarios have denudation rates of 1 mm/y, but in order to generate the 1 mm/y denudation rate with the lateral model, the magnitude of the advection velocity vectors parallel to the prescribed 40° dip must be larger than those in the vertical model. The net effect of the lateral model velocity vectors is advection of heat from the northern margin of the model into the center of the model domain (Figure 3.3), slightly warming the region beneath the basin of interest. The increased warmth in that area generates the slightly younger peak ages, while the lateral velocity component generates a slightly broader age range. In the AHe system, this can be seen by a ∼13% decrease in the peak age for the lateral kinematic model. For the same kinematics, the age range increases by ∼32% (Figure 3.6B). This age trend is also present in the higher temperature thermochronometer systems. For the ZFT system, the peak age decreases by ∼15% while the age range increases only ∼7% for the lateral model (Figure 3.6C). The decrease in peak age and increase in age range for ZFT is fairly similar to the ∼9%

peak age decrease and ∼7% age range increase seen in the MAr thermochronometer (Figure 3.6D).

As opposed to the vertical and lateral kinematic scenarios, the thrust scenario exhibits notably different age distributions. First, although the majority of the basin area of interest has a surface denudation rate of 1 mm/y by the end of the model run at 0 Ma, lateral advection of the faults in that model generates temporal changes in the denudation rate (Figure 3.6A). For the majority of the basin, the background denudation rate for the early portion of the model run is 0.27 mm/y as the hanging wall of the model thrust sheet is moving over a fault with a 10° dip angle. As material moves into the more steeply dipping section, the denudation rate increases to 1 mm/y. Second, subduction of material beneath the thrust belt leads to an overall cooling of the near surface. As relatively cool material near the surface is advected below the thrust belt, the geothermal gradient near the surface decreases leading to a general trend of older ages. With these two points in mind, consider the AHe thermochronometer system. As Figure 3.6B shows, the peak age from the thrust model is ∼75% older than the vertical model peak. In this case, the age difference reflects earlier cooling below the effective AHe closure isotherm in the cooler thermal field. In addition, although somewhat difficult to see in Figure 3.6B, the age range for the thrust model is 13.1 My, significantly larger than the range for either the vertical or lateral models. Again, this range reflects the fact that a small portion of the drainage basin has a slower background denudation rate and that the rate has varied spatially through time. The ZFT thermochronometer has a similar trend to the AHe system, with an older peak age and much larger age range. In this case, the peak age is ∼56% older than the vertical model peak age and the age range is also ∼1100% larger. The increase in offset of the peak ages reflects the fact that a

larger portion of the ZFT cooling history occurs with the slower denudation rate and the large age range is the result of unreset ZFT ages due to insufficient exhumation. The MAr system peak age is ∼56% older that the age from the vertical kinematic model and the age range is ∼760% larger. The large age range again reflects the presence of unreset MAr ages because there has not been enough overlying material removed.

3.4.3 Effects of evolving topography

Increasing and decreasing topographic relief

In contrast to the sections above that explored how variations in exhumation rate and pathway affect cooling ages, this section looks at how detrital age distributions change in response to evolution of surface topography. To illustrate this effect, we highlight several models that feature either a 50% increase or a 50% decrease in topographic relief across the model region as the only model free parameter (Figure 3.7A). The changes in topography occur linearly through time over the last 10 My of the model run. Furthermore in this section, the 50% change in topographic relief occurs around the mean elevation of the landscape. In other words, a decrease in relief would occur as an increase in elevation within the low-elevation valleys and lowering of the peaks. In addition to evolving surface topography, models in this section use the vertical kinematic scenario with a temporally constant prescribed denudation rate of 1 mm/y. Thus, a relief decrease over 10 My generates a range of effective denudation rates of 0.87−1.25 mm/y and increasing relief yields a range of 0.75−1.13 mm/y. The effects of changing relief around different elevations (e.g., ridge or valley, Figure 3.8) in the landscape are discussed later.

The primary effects of topographic relief changes are variations in the effective denudation rate that generate younger peak ages when relief decreases and older

peak ages when relief increases. For the 50% decrease in relief models, the peak age of the AHe thermochronometer decreases by ∼21% (Figure 3.7B). In contrast, the peak age of the AHe distribution for the 50% relief increase model shows an increase by ∼11%. Again, as was the case in the previous sections, the ZFT and MAr systems behave in a similar manner; in the 50% relief decrease models the peak ages decrease by ∼9% for both ZFT and MAr, whereas peak ages increase by ∼6% in the increasing relief case (Figure 3.7C,D). An interesting trend shown by the changes in peak age is that low-temperature thermochronometers (e.g., AHe) have greater sensitivity to relief changes. This is perhaps not unexpected as the effective closure temperature isotherm for the AHe system resides much closer to the surface. As before, increased denudation rates also generate narrower age ranges. For the decreasing relief model, the ranges decrease by ∼60%, ∼33% and ∼37% for AHe, ZFT and MAr, respectively. For the increasing relief scenarios, the age ranges increase by ∼13%, ∼12% and ∼14% for the three systems. Similar to the changes in peak ages, it appears that the AHe system is most sensitive to relief changes and there is greater sensitivity to relief decreases in all three thermochronometers.

Landscape reference points for relief change

In addition to the effects from increasing or decreasing topographic relief, the fixed point in the landscape about which relief changes can influence age distributions. For instance, the age distribution resulting from an increase in topographic relief with a constant minimum elevation (river level) would be different than that generated with a constant maximum elevation (mountain peak). In this section, we consider topographic relief change scenarios where relief increases by 50% over 10 My about either a fixed minimum, mean or maximum elevation (Figure 3.8A). The vertical kinematic scenario is used and the background denudation rate (1 mm/y)

does not change with time. The combination of the background denudation rate and topographic change yields an effective denudation rate range of 0.61−1.0 mm/y for increasing relief about a fixed minimum elevation. When the maximum elevation is fixed, the effective denudation rate range increases to 1.0−1.39 mm/y. As before, the effective denudation rate range is 0.75−1.13 mm/y with a fixed mean elevation.

Similar to the case in the previous section, relief change scenarios that generate higher effective denudation rates yield younger peak ages and lower denudation rates generate older peak ages. For instance, the AHe age peak decreases by ∼24% relative to the fixed mean peak age for the fixed maximum elevation scenario. In addition, a 50% relief increase with a fixed maximum elevation leads to a ∼24% age range decrease. With a fixed minimum elevation, the AHe peak age increases by ∼18% and the age range increases similarly by ∼20% (Figure 3.8B). The ZFT thermochronometer shows slightly less sensitivity to the fixed elevation point about which relief changes. With a fixed maximum elevation, the ZFT peak age decreases by ∼19% whereas a fixed minimum elevation increases the peak age by ∼14%, both relative to the fixed mean scenario. In addition, relative to the fixed mean elevation scenario, the age range decreases by ∼21% and increases by ∼17% for the fixed maximum and fixed minimum elevation scenarios, respectively (Figure 3.8C). The MAr system shows a slight decrease in sensitivity to the point about which elevation changes with the fixed maximum scenario generating peak ages that are ∼20% younger and the fixed minimum ∼10% older than the constant mean elevation scenario peak age. Furthermore, the age range for the fixed maximum scenario decreases by ∼15% while the fixed minimum range increases by only ∼2% relative to the fixed mean age range (Figure 3.8D).

3.4.4 Effects of basin size

The final factor expected to affect detrital age distributions is the size of the basin used to extract cooling ages from the model. As opposed to the previous sections that looked at how various model inputs affected the predicted cooling age distribution, the only free parameter in this section is the area from which cooling ages are extracted. In addition to the catchment that has been used for all of the previous sections, we examine age distributions from two tributary catchments of varying size (Figure 3.9A). The largest catchment and focus thus far has a drainage area of ∼2775 km^2 with 7164 m of relief. The intermediate catchment is only ∼59% of the size of the large catchment with 5315 m of relief. The smallest catchment has a drainage area that is ∼30% of the large catchment and 4097 m of topographic relief. For the comparison of age distributions in this section, models use the vertical kinematic scenario with a background denudation rate of 1 mm/y and no change in the surface topography.

Results indicate that the peak ages generated from the three catchments of differing basin area and relief do not vary appreciably (Figure 3.9B−D). The AHe peak age for the largest basin is 1.6 Ma and the peak ages for the medium and small catchments both only increase by <2%. The trend is the same for the ZFT and MAr age distributions with ages increasing by only 1−2% for both the medium and small catchments. The age ranges are more strongly affected by the catchment size. The predicted range for the AHe system decreases by ∼9% and ∼27% for the medium and small catchments, respectively. Similarly, the ZFT age range decreases by ∼5% for the medium catchment and ∼16% for the smallest. The MAr age distributions are also significantly affected by the basin size with an age range decrease of ∼9% for the medium catchment area and ∼24% for the small catchment.

3.5 Discussion

We now turn our focus to specific applications of detrital thermochronometers and the implications of the previous results on them. We start by addressing the question of when interpretations of detrital thermochronometer data are affected by 1-D techniques and when a 3-D model could improve on those results. Next, we extend our results to discuss temporal trends that might be observed in detrital thermochronometer data collected in sedimentary basins. We then look at the response time of various thermochronometer systems to changes in denudation rate and which systems would be expected to record changes of different magnitude at different times. Lastly, we conclude with a discussion of the issue of non-uniqueness in detrital thermochronology and what numerical models can provide in terms of reducing interpretation uncertainties.

3.5.1 Is a 3-D thermal model really necessary?

A common application of detrital thermochronometer data from modern river sediments is the estimation of basin-wide denudation rates. One of the simplest methods for this calculation involves needing to know only the range of elevation and cooling ages within the catchment. The catchment elevation range can be attained from a DEM, and although data collection can be tedious, once collected, the basin-wide denudation rate can be calculated by simply dividing the catchment elevation range by the age range (e.g., Ruhl and Hodges, 2005). In essence, this 1-D interpretation is the same as using a linear relationship between sample age and elevation (e.g., Figure 3.1A−D). Because that is the case, the true denudation rate will only be recovered if the effective closure isotherm of interest resides at a constant depth relative to sea level. In other words, the closure isotherm is assumed horizontal

and not significantly perturbed by the surface topography, groundwater circulation, faulting, variability in thermophysical rock properties, or other similar influences (e.g., Whipp and Ehlers, 2007; Whipp et al., 2007). If the isotherm is not flat, but perturbed by the overlying topography, as is commonly the case in high-relief mountain ranges, then estimates of the denudation rate based on the methodology above will tend to overestimate the true denudation rate. However, it should also be noted that there can be unknown model parameters in 3-D models that can limit their accuracy as well. For example, if spatial variations in rock thermophysical properties are not captured in a 3-D model, large errors could be introduced. For the purpose of this section, we analyze how 1-D and 3-D methods differ in their predicted age distributions to assess if the addition of extra dimensions in the calculations makes an appreciable difference.

Comparison of the prescribed model denudation rate to that predicted using the catchment elevation range divided by the model-predicted age range shows consistent overestimation, particularly for low-temperature thermochronometers and high denudation rates. The comparison was performed on the models discussed in Section 3.3.1, where the vertical kinematic scenario was used with time invariant denudation rates and topography. For the AHe system, even at the relatively slow prescribed denudation rate of 0.5 mm/y, the denudation rate estimate using the methods of Ruhl and Hodges (2005) is 1.4 mm/y, 180% higher than the 3-D model-prescribed rate. As the prescribed rate increases, the overestimate also climbs, with a rate difference of 380% at a prescribed rate of 2.5 mm/y. For higher-temperature thermochronometers, such as MAr, there is significant improvement to the overestimation problem, with the overestimate decreasing to 40% at a model input rate of 0.5 mm/y. However, at a rate of 2.5 mm/y, the overestimate again increases to

104%. Further comparison using additional rates and thermochronometer systems can be found in Table 2.

Overall, the comparison between 3-D and 1-D models shows potential for significant overestimation of denudation rates. For a 1-D interpretation, estimates can be improved by use of higher-temperature thermochronometers or application in regions thought to be eroding at slower rates. It is also important to note that overestimation of denudation rates would be expected to decrease using other model-based techniques. For example, the 2-D approach of Brewer et al. (2003) used a prescribed denudation rate to generate the predicted age-elevation relationship that is convolved with the basin hypsometry to generate a predicted PDF. Assuming insignificant lateral variations in the subsurface thermal field in the region of interest, the input denudation rate should provide a good estimate of the true denudation rate when the predicted and observed age PDFs are similar. Caution should still be used, though, with low-temperature thermochronometers as those systems will be more sensitive to the 3-D variability in the surface topography. 1-D models, such as that utilized by Rahl et al. (2007), may also be used for estimating denudation rates, but the applications are more limited. Because a 1-D model does not generate an age-elevation relationship, and thus does not utilize the basin hypsometry, those models should only be used in areas with relatively simple basin hypsometries, with unimodal elevation distributions and an elevation frequency peak that falls near the middle of the elevation range. In those cases, the predicted 1-D age peak should coincide with the observed age peak for an input denudation rate similar to the true denudation rate. Detrital thermochronometer data from regions with highly skewed or multimodal hypsometries are better interpreted using 2-D or 3-D models. Thus, given the inherent complexities in the crustal thermal field of active, high-relief oro-

gens, caution should be used when applying more simple estimates for denudation rates.

3.5.2 Transient record in basin stratigraphy

One of the potentially most powerful applications of detrital thermochronology is the analysis of foreland basin sediment sequences to generate temporal records of denudation in the adjacent hinterland (e.g. Copeland and Harrison, 1990; Renne et al., 1990; Cerveny et al., 1988; Brandon and Vance, 1992; Garver and Brandon, 1994a). A number of recent studies have taken advantage of the longer-term denudation record preserved in basin sediment to better understand the magnitude and timing of exhumation as driven by hinterland tectonic or climatic variability (e.g., Szulc et al., 2006; Bernet et al., 2006; van der Beek et al., 2006; Carrapa et al., 2006; Sobel et al., 2006; Coutand et al., 2006; Kuhlemann et al., 2006). Although much can be learned from basic observations of age distributions in foreland basin sediments, such as variations in lag time (e.g., Bernet and Garver, 2005, and references therein), it remains unclear how various processes affect the temporal record of denudation driven by tectonic or topographic changes. Below, we explore two examples of 15 My records that would be generated in a foreland basin. The first model explores the record of a 5-fold increase in denudation rate at 10 Ma with fixed topography. The second model features a uniform background exhumation rate of 1 mm/y and simulates a 50% increase in topographic relief from $10-0$ Ma. Both models use the vertical kinematic scenario and are compared to models the do not change the parameter of interest with time. For this analysis, we assume that sample burial depth is sufficiently small such that cooling ages will not be reset after deposition.

The foreland basin record of a 5-fold increase in denudation rate shows an initial

shift in peak age, followed by a narrowing of the catchment age range. As shown in Figure 3.10A, there is virtually no difference between the age distributions of the model with a fixed denudation rate of 0.5 mm/y and the acceleration model prior to 10 Ma. Both models show peak ages of ∼44 Ma and age ranges of ∼13 Ma, with the age range reflecting the 4% 1σ error used in generating the model SPDF_m. As both models utilize a denudation rate of 0.5 mm/y up until 10 Ma, this result is to be expected. By 5 Ma, with 5 My of denudation at the higher rate of 2.5 mm/y, the age distribution for the acceleration model begins to diverge from the constant 0.5 mm/y model. The peak age of the acceleration model decreases to ∼15 Ma relative to the ∼34 Ma peak age of the slow denudation rate model. In spite of this decrease in peak age, the ∼10 My age range of the acceleration model is similar to both the range of ∼12 My at 10 Ma and the ∼11 My range in the constant 0.5 mm/y model at 5 Ma. This shift to a younger peak age without a significant change in age range reflects the onset of the more rapid denudation rate without exhumation of samples that cooled below their effective closure temperature at the more rapid rate. As expected, the majority of samples in the ∼9−19 Ma age range would have passed through their effective closure temperature at the slower rate of 0.5 mm/y. By 0 Ma, the peak age of the acceleration model has decreased to ∼5 Ma, only ∼2 My older than the peak age of the constant fast (2.5 mm/y) denudation rate model. In this case, the age range has also decreased to ∼2 My and is quite similar to the ∼1.4 My age range of the high denudation rate model. Thus, the overall trend for a 5-fold acceleration in denudation rate is an initial decrease in peak age with no appreciable change in age range, followed by further decrease in the peak age and a decrease in the age range as the samples that cooled below their effective closure temperature at the higher rate are exhumed.

Denudation rate changes in detrital thermochronometers are often detected using the concept of changing lag time. As defined in Garver and Brandon (1994b), the lag time is the age difference between the measured thermochronometer age and the depositional age of the sampled sedimentary unit. Thus, the lag time is a measure of the time required for the thermochronometer sample ages that form the peak age to travel from the depth of their effective closure temperature isotherm to the surface and then to their depositional basin. In general, for active orogens, the transport time at the surface is considered negligible. With this in mind, an increase in lag time would represent a decrease in denudation rate within the source region and a decrease would reflect a rate increase. For example, in the denudation rate change model in Figure 3.10A, the lag time rapidly decreases from ∼29 My at 10 Ma to ∼4 My at 0 Ma. In contrast, the lag time for the constant 0.5 and 2.5 mm/y denudation rate models are ∼29 and ∼2.6 My at all times (15−0 Ma). These trends are easily seen in plots of cooling age versus depositional age (e.g., Figure 3.11), where lines of constant lag time can help accentuate changes in denudation rate. In this case, the constant denudation rate models will plot along lines of constant lag time, while the acceleration model crosses the lag time contours (squares within shaded region, Figure 3.11). The acceleration model lag times would also be expected to fall within the region delineated by the 0.5 and 2.5 mm/y constant rate models, diverging from the 0.5 mm/y at 10 Ma and merging with the 2.5 mm/y model lag times once thermal steady state has been reached. As visible in Figure 3.11, after 10 My of denudation at the higher rate, the lag time difference shows that the thermal field is nearing a new steady state.

A less pronounced detrital grain-age signal is visible in basin sediments where the upstream area has experienced relief change. Increasing relief by 50% at 10 Ma shows

very little change in the resulting age distributions. As Figure 3.10B shows, the age distributions prior to any topographic change at 15 and 10 Ma are almost identical, in spite of a 50% difference in topographic relief. The slight differences are peak ages that are ∼1% younger and age ranges that are ∼18% smaller in the topographic evolution model. The small peak age difference reflects the fact that the cooling ages are older in the fixed topography model because of the increased distance from the effective closure temperature isotherm to the model surface. The majority of the basin elevations are above the mean elevation and thus higher than the same point in the variable topography model. By 5 Ma, as the relief begins to increase in the changing relief model, the peak age increases by ∼1.3% relative to the fixed topography model, but the age range still exceeds that of the fixed topography model by ∼10%. In this case, the shift is reflecting slightly lower effective denudation rates within the catchment as relief is increasing, but doing so by increases in the surface elevation for points above the mean elevation. By 0 Ma, however, both the peak age and age range show a more significant difference relative to the fixed topography model with values that are ∼6% and ∼15% higher, respectively. Again, the older peak age and larger age range are the result of slower background denudation rates as the majority of the basin elevations increase.

All told, however, the observed differences in the peak age and age range of the changing relief model relative to the fixed topography model are likely not detectable in real data. The age distributions in Figure 3.10B are too similar at each sampled time and would not yield statistically different age distributions using common statistical tests such as the two-sample Kolmogorov-Smirnov or Kuiper's tests (e.g., Press et al., 1992; Amidon et al., 2005; Ruhl and Hodges, 2005, and references therein) without dating an unusually high number of sample grains ($\gg$100). Because of the

similarity in the age distributions, it is not surprising that there is very little difference in the lag time of the two distributions as well (Figure 3.11). Both distributions plot along a lag time contour line, showing no significant change in the background denudation rate with time. This is quite reasonable as the denudation rate variations in the relief change model are small (<0.25 mm/y). The offset in the peaks is visible in Figure 3.11, showing a slight decrease in the denudation rate of the relief change model, but again this is highly unlikely to be detectable without dating very large numbers of grains. It is worth noting, however, that topographic evolution scenarios with more rapid changes in relief, fixed peak or valley elevations or slower background denudation rates may increase the difference in age distributions, allowing detection of relief changes.

3.5.3 Detrital response time for changes in denudation rate

As discussed above, changes in the denudation rate cause a shift in the peak age of a detrital thermochronometer sample, but the magnitude of that shift depends on the magnitude of the rate change, the time elapsed since the rate change and the closure temperature of the thermochronometer system (e.g., Rahl et al., 2007). In general, larger changes in denudation rate will generate larger shifts in the peak age. The peak age shift will also be greater if the rate change occurs further in the past. In other words, one might expect a larger peak shift for a 5-fold increase in denudation rate at 10 Ma than for a 2-fold increase at 2 Ma. Furthermore, because lower closure temperature thermochronometers record cooling through a more shallow portion of the crust than higher temperature systems, we might expect increased sensitivity to denudation rate changes. As larger changes in peak age would be more easily detected, it is useful to have a general sense of the predicted peak age shift for a rate change at various magnitudes and times, and for thermochronometer systems with

different effective closure temperatures.

Both the AHe and MAr thermochronometer systems respond similarly to changes in denudation rate, with a more rapid response and larger relative peak age shift in the AHe system. As predicted above, both thermochronometers show larger peak age shifts for greater magnitudes of rate change and earlier rate changes (Figure 3.12). For example, an increase in denudation rate from 0.5 to 1.5 mm/y at 10 Ma generates a peak age that is ∼74% younger than a constant 0.5 mm/y model in the AHe system (a in Figure 3.12). If the rate change magnitude is increased such that the rate changes from 0.5 to 2.5 mm/y, the resulting peak age is ∼88% younger than the constant 0.5 mm/y peak age. The MAr system behaves much like the AHe system, with peak age decreases of ∼70% and ∼87% for denudation rate increases of 1.0 and 2.0 mm/y, respectively (e,f in Figure 3.12). Also important is the timing of the rate change, with an increase in denudation rate of 1.0 mm/y in the AHe system generating peak ages that are ∼69% and ∼74% younger for changes at 2 and 10 Ma (c,a in Figure 3.12). Again, the MAr system follows the same trend with peak ages that are ∼14% and ∼70% younger with denudation rate changes at 2 and 10 Ma (g,e in Figure 3.12). Of interest is the fact that the AHe thermochronometer shows much less sensitivity to the timing of denudation rate change than the MAr system, provided there has been at least 2 My since the rate change. Comparing the magnitude of peak age shift for both systems, a 1 mm/y acceleration at 10 Ma decreases the peak age by ∼74% for AHe and ∼70% for MAr (a,e in Figure 3.12). However, a rate change at 2 Ma only decreases the MAr peak age by ∼14%, whereas the AHe peak would have decreased by ∼69% (g,c in Figure 3.12). Even with a more substantial rate change of 2 mm/y at 2 Ma, the MAr age peak only decreases by ∼34%, as opposed to the AHe peak age decrease of ∼83% (h,d in Figure 3.12). With

this in mind, it is easy to see that the AHe thermochronometer would be superior to MAr in detecting recent denudation rate changes ($\leq$2 Ma), while MAr would be better suited for addressing rate changes over the last 5$-$20 Ma. Clearly this range would vary with the magnitude of expected rate change, but this should serve as a guideline for studies designed to detect changes in denudation rate over the last 20 My.

3.5.4 Non-uniqueness

One of the potential problems with the interpretation of both bedrock and detrital thermochronometer data is non-uniqueness. This issue has been discussed by a number of authors (e.g., van der Beek et al., 1999; Gunnell, 2000; Ehlers, 2005; Reiners et al., 2005; Bollinger et al., 2006; Rahl et al., 2007; Whipp et al., 2007, and many others) and arises from uncertainty in the large number of factors that can affect the cooling history of a given thermochronometer sample. For instance, the thermal effects of a slightly higher denudation rate might be similar to that of higher volumetric heat production. All other things equal, predicted thermochronometer ages from either of those model variants might be statistically equal. If nothing else is known about the material properties or denudation history of a given region from other data and the model predictions fit a dataset equally well, then one must conclude that either of the model options is plausible. Clearly, this highlights the need to constrain as many model free parameters as possible using material thermal property measurements and other proxy data. In addition, unknown model parameters should be assigned a range of values that encompasses the potential parameter space in order to ensure that conclusions from the applied model are robust.

There are some model parameters, however, that will tend to have a larger impact on the thermal field and predicted thermochronometer ages than others. In

our detrital modeling study, is it clear that the denudation rate has a large impact on the predicted thermochronometer age distributions (Figure 3.4). The timing of denudation rate changes can also significantly affect the age distributions, but the timing of a rate change may be difficult to constrain depending on the thermochronometer system (Figures 3.5B,D and 3.12). The exhumation kinematics may also have a strong effect on age distributions, but similar to the conclusions of Whipp et al. (2007), it appears that the denudation rate dominates the effect of kinematics with low-temperature thermochronometers (Figure 3.6B). Both topographic change and basin size had smaller impacts on the predicted age distributions in the model parameter space we explored. This suggests that relief change would likely be difficult to detect and that basin size is not as important as the location of the basin with respect to spatial variations in denudation. Thus, in rapidly eroding, active orogens we expect the denudation rate to be the most dominant factor affecting thermochronometer age distributions with the kinematics being of significant concern with higher temperature systems. This implies that although uncertainty in other model parameters may exist, significant conclusions can be drawn using low-temperature thermochronometer datasets and more simple numerical models that only consider the effects of variable denudation rate and timing of rate changes. It should be noted, however, that this may not be the case in more slowly eroding orogens and interpreting data from regions with large magnitude, recent topographic changes may require the use of more sophisticated models.

3.6 Conclusions

In this study we used a 3-D thermokinematic and erosion numerical model to explore the response of detrital thermochronometer age distributions to changes in

denudation rate, exhumation kinematics, topographic evolution and basin size. The major conclusions of this work are:

1. Denudation rate estimates made using 1-D assumptions about the thermal field show a significant overestimate compared to 3-D thermal models, particularly for low-temperature thermochronometers. At a background denudation rate of 2.5 mm/y, the AHe predicted denudation rate using a 1-D technique exceeded the 3-D model-prescribed rate by >300%. With the MAr thermochronometer, that same rate reduced the overestimate to ∼90%. Although these rates may be quite high, they are typical of active orogens (such as the Himalaya, Southern Alps and Taiwan) and we urge caution in using such techniques to calculate denudation rates. In more slowly eroding regions, use of 1-D techniques may be justifiable.

2. Low-temperature thermochronometers may be of greater utility than higher temperature systems in trying to interpret recent ($\leq$2 Ma) changes in denudation rate. However, as the response time of the low-temperature systems is shorter, higher temperature systems may be of greater use for rate change detection further in the past ($\sim$5$-$20 Ma).

3. An acceleration in denudation rate that could be potentially observed in foreland basin sediments is characterized by an initial decrease in peak age with a fairly constant age range, followed by a further decrease in peak age and age range. The overall rate change can easily be observed by calculating the changes in lag time, however a substantial time may pass before the age range in a given sample decreases following the rate change.

4. Variations in the background denudation rate dominate the influence of other

explored parameters with low-temperature thermochronometers. The observed peak age shifts and age range changes resulting from changing denudation rates would be expected to mask the effects of other potential forcings.

5. The exhumation kinematics can also have a strong influence on the predicted age distributions, particularly with higher temperature thermochronometer systems. Although no significant difference in age distributions for the lateral versus vertical kinematic scenarios was observed, the thrust faulting model showed substantial difference in the cooling ages. As suggested by Whipp et al. (2007), thermochronometer studies that seek to constrain the faulting history of rapidly eroding, active orogens would be best served using systems such as MAr, which will integrate their cooling over a larger distance and have increased sensitivity to the exhumation kinematics. An application using detrital thermochronometer modeling can be found in the companion paper by Whipp and Ehlers (2008).

6. The AHe system showed a slight sensitivity to changes in topographic relief, but in general, there was very little sensitivity in detrital age distributions to changing relief in the models we explored. There is potential for an increased response in cases where the relief change occurs over a very short time interval or within regions with a slower background denudation rate. In addition for the case where topography changes about a fixed mean elevation, basins that sample sediment near equally from areas that reside on either side of the mean elevation may show a greater response, as would be predicted by Braun (2003).

7. Over the range of basin areas sampled, basin size did not appear to have a significant effect on the predicted age distributions. This may not true for very small basins, but for the basin sizes typically sampled in active orogens, we saw

no effect. It should be noted, however, that the location of the basin relative to regions of variable denudation rate would be very important. In other words, the age distribution for a basin in the immediate hanging wall of a steep thrust fault would be very different from that of a basin far from a thrust and above a gentle ramp, even if the basins are of similar size.

3.7 Acknowledgements

We are most grateful to J. Braun for providing the source code for Pecube and to C. Spath for his assistance in modifying the code. This manuscript benefited from thoughtful discussions with J. Barnes, M. Densmore, K. Hodges, K. Huntington, F. Herman and P. van der Beek. This work was supported by NSF grants EAR-0544954 and EAR-0724656 to T. Ehlers.

Table 3.1: Numerical Model Parameters

Property/Parameter	Model Input Value
Material Properties	
Vertical model heat production	0.8 μW/m^3
Lateral model heat production	0.8 μW/m^3
Thrust model heat production[a]	0.5−1.9 μW/m^3
Heat production e-folding depth	−10 km
Thermal conductivity	2.75 W/m K
Specific heat	1000 J/kg K
Density	2700 kg/m^3
Numerical Parameters	
Vertical model denudation rate	0.5−2.5 mm/y
Lateral model dip angle	40°
Lateral model convergence rate	0.8−3.9 mm/y
Thrust model convergence rate[a]	0.6−3.0 mm/y
Topographic scaling factor	0.5−1
Topographic offset factor	0.068−4.061 km
Horizontal node spacing	∼0.95 km
Vertical node spacing (0−5 km)	∼0.95 km
Vertical node spacing (5−15 km)	∼2.85 km
Vertical node spacing (15−130 km)	∼8.55 km
Surface temperature at sea level	24°C
Atmospheric lapse rate	−6°C/km
Basal temperature	1350°
Model domain	150 × 310 × 130 km

[a] Additional detail about this model available in Whipp and Ehlers (2008)

Table 3.2: Comparison to denudation rates predicted using method of Ruhl and Hodges (2005)

System	Input rate [mm/y]	Age range [Ma]	Estimated rate[a] [mm/y]	Overestimate
AHe	0.5	5.3	1.4	180%
AHe	1.0	2.2	3.3	230%
AHe	2.5	0.6	12.0	380%
ZFT	0.5	10.5	0.7	40%
ZFT	1.0	4.3	1.7	70%
ZFT	2.5	1.2	6.0	140%
MAr	0.5	10.5	0.7	40%
MAr	1.0	4.6	1.6	60%
MAr	2.5	1.4	5.1	104%

[a]Calculated using catchment relief of 7.164 km

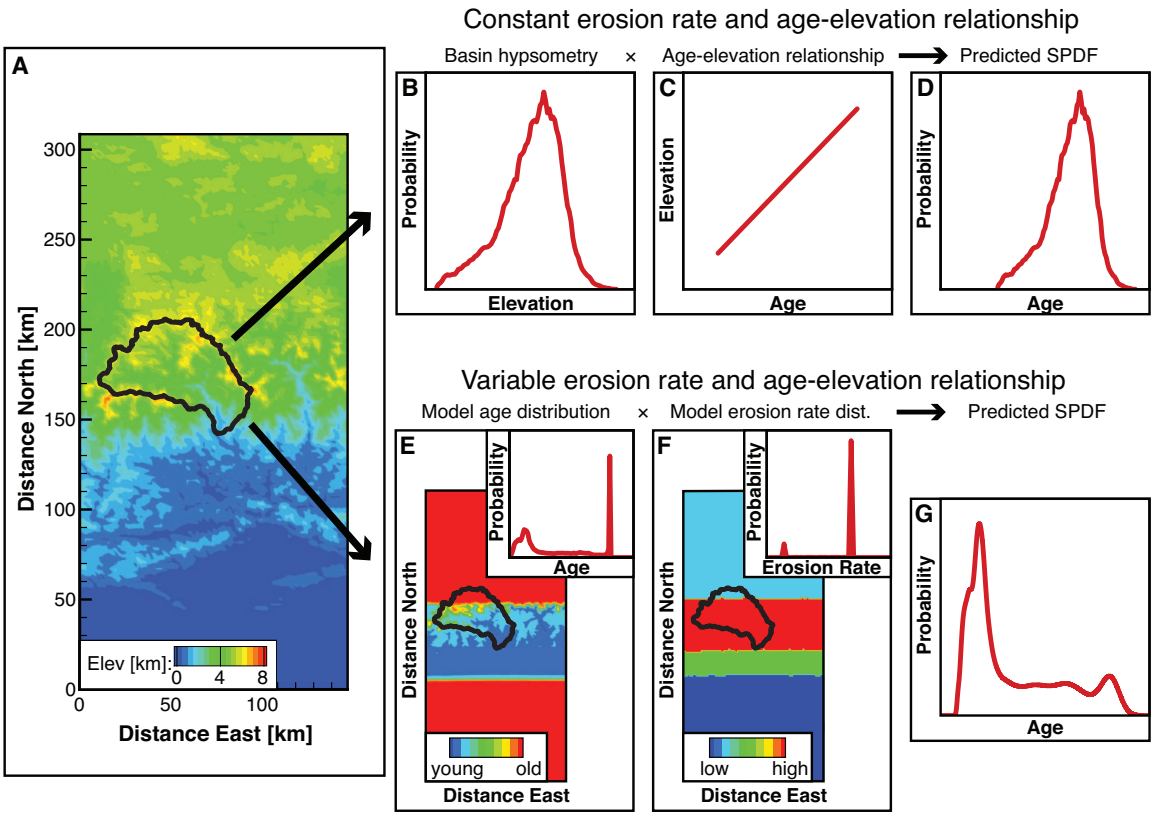

Figure 3.1: Comparison of methods used to produce predicted detrital age distributions in previous works (B−D) and in this study (E−G). (A) Contoured model topography from the central Nepalese Himalaya with the catchment boundary (black outline) used for age distribution prediction. (B−D) Summary of previous detrital thermochronology modeling studies (e.g., Brewer et al., 2003; Ruhl and Hodges, 2005; Stock et al., 2006; Vermeesch, 2007), where a basin hypsometry (B) was convolved with a fixed bedrock age-elevation relationship (C) to generate a predicted age distribution assuming spatially uniform erosion. This is referred to as the 1-D approach in the text. (E−G) The methodology used in this study where the contoured predicted ages (E), surface denudation rates (F) and their distributions (E,F inset plots) are spatially variable in 3-D. The age and denudation rate distributions are combined to generate the predicted age distribution (G).

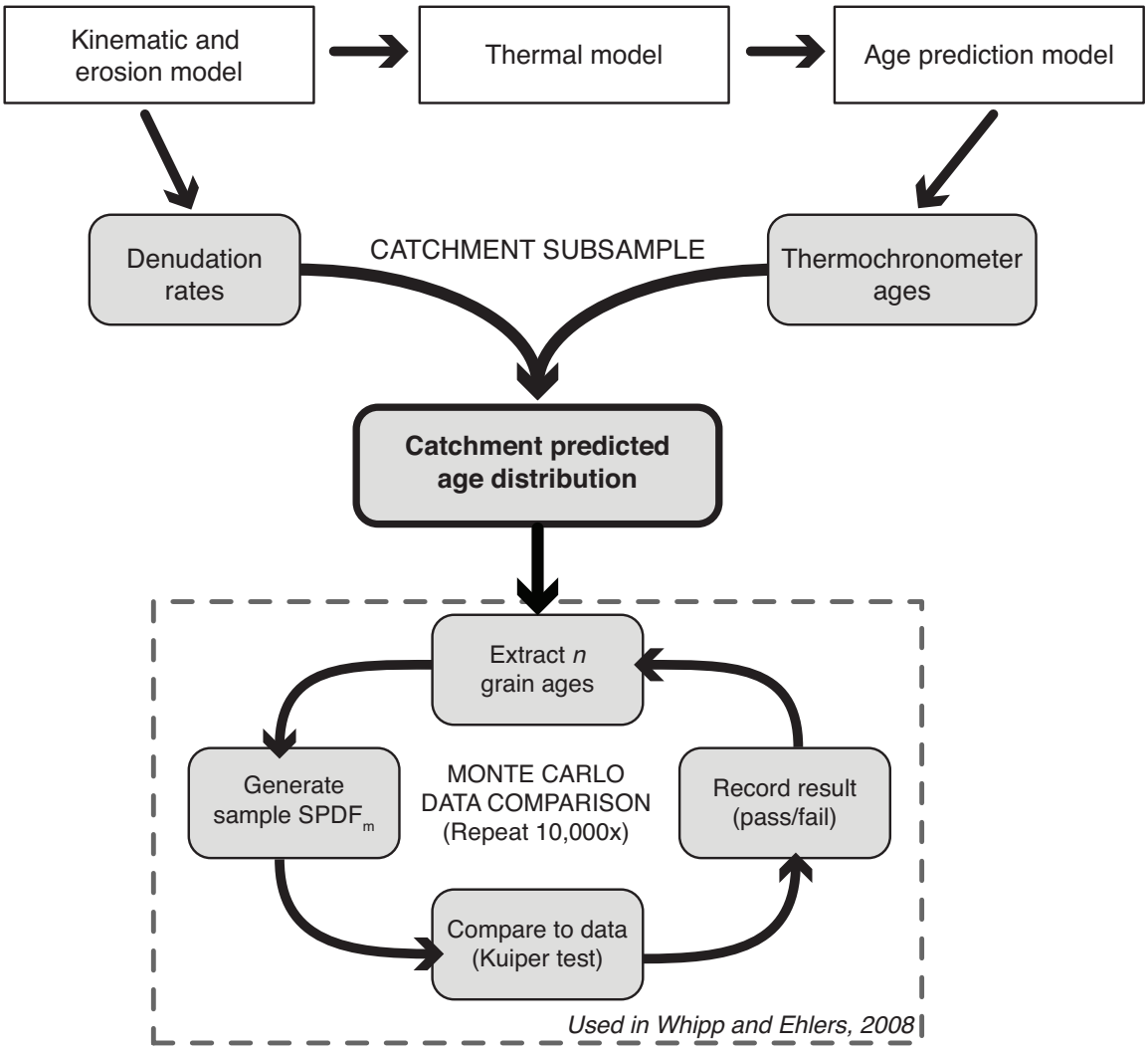

Figure 3.2: Flow diagram showing the modeling procedure used in this study and chapter four. The coupled thermokinematic model controls the predicted ages at the model surface. Denudation rates and ages within the catchment of interest are sub-sampled and combined to produce the model-predicted age distribution. If a data comparison is desired, n ages are randomly extracted from catchment age distribution, where n is the number of ages contributing to the observed age distribution. The observed and predicted age distributions are then compared and the results are recorded. This process is repeated 10,000x to ensure results are robust.

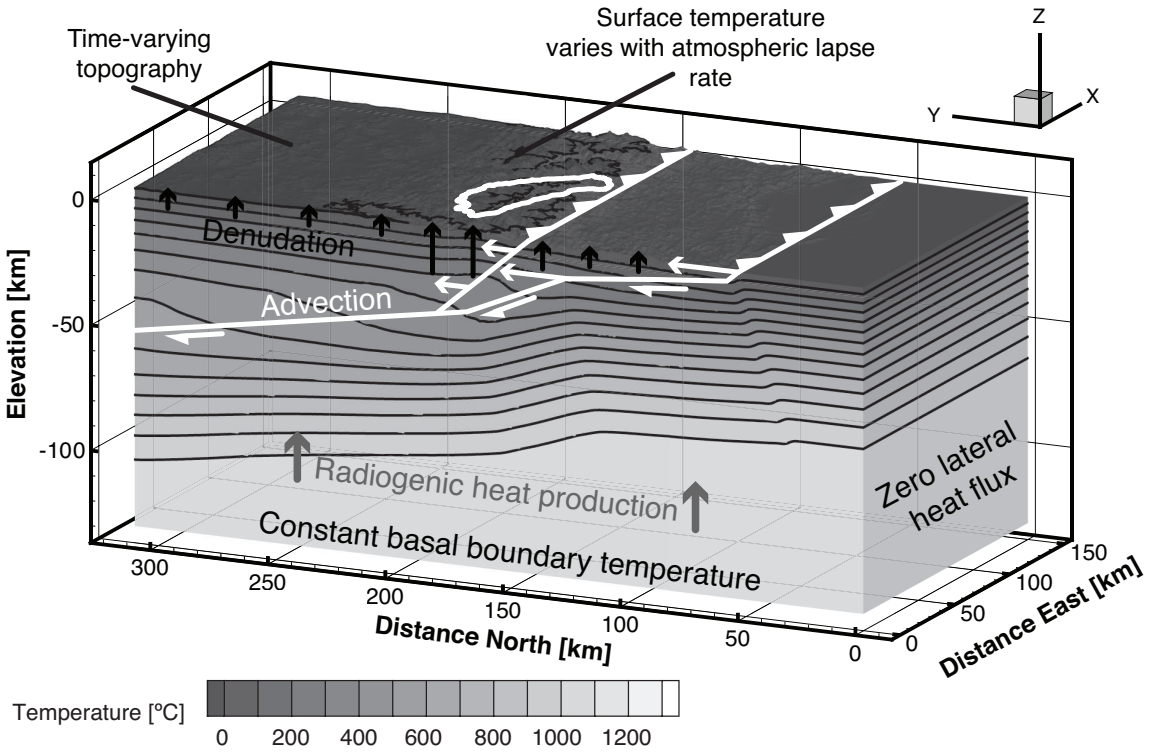

Figure 3.3: Example 3-D thermal model showing thermal model components and boundary conditions. The thrust kinematic model is illustrated here, where the faults (white lines) are advected in the positive y-direction with time as subduction occurs beneath the basal thrust. Temperature contours (thin black lines) show the thermal perturbation resulting from the thrust kinematics. Denudation (black arrows) balances the flux of material through the model surface and is spatially variable as controlled by the kinematic model. Fault positions with time dictate the denudation rates within the catchment of interest (white outline).

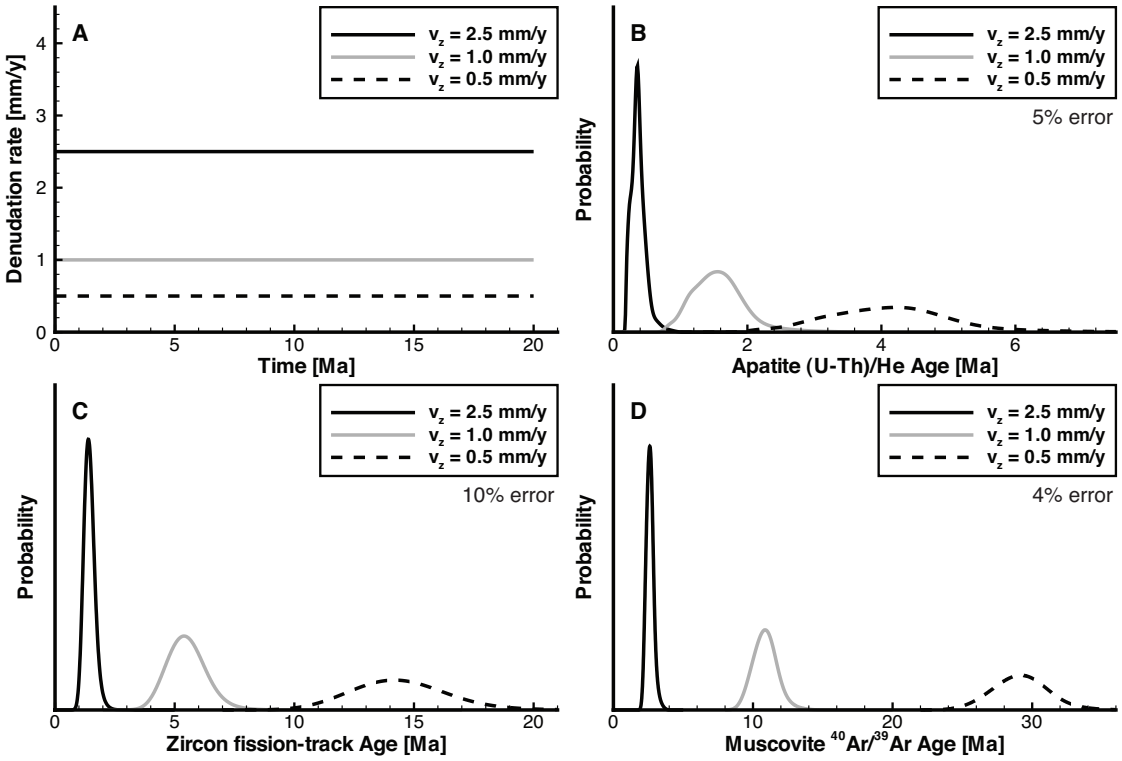

Figure 3.4: Effect of variable magnitude denudation rates on predicted age distributions. (A) Time-invariant denudation rates of 2.5 (solid black), 1.0 (gray) and 0.5 mm/y (dashed black) are used with the vertical kinematic scenario to predict AHe (B), ZFT (C) and MAr (D) age distributions. The listed percent error is the 1σ uncertainty used in generating the predicted SPDF_m curves.

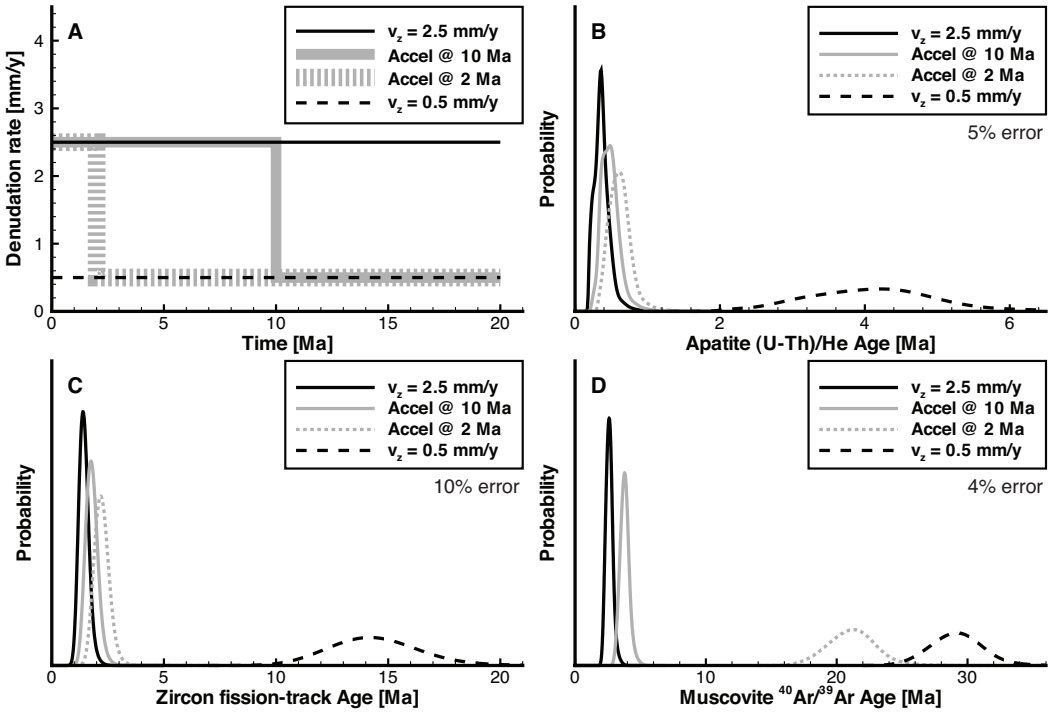

Figure 3.5: Effect of temporal variations in denudation rate on predicted age distributions. (A) Time-invariant denudation rates of 2.5 (solid black) and 0.5 mm/y (dashed black) are shown with rates that increase from 0.5 to 2.5 mm/y at either 10 Ma (solid gray) or 2 Ma (dashed gray). These models use the vertical kinematic scenario to predict AHe (B), ZFT (C) and MAr (D) age distributions. The listed percent error is the 1σ uncertainty used in generating the predicted SPDF$_m$ curves.

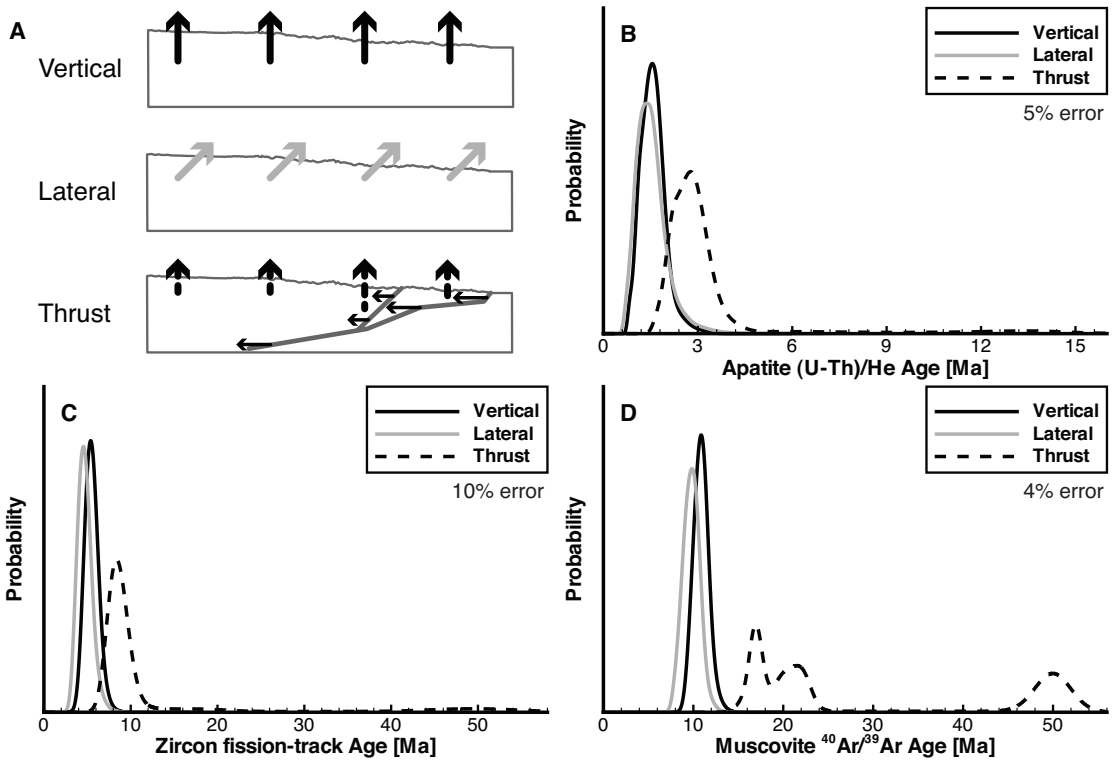

Figure 3.6: Effect of different kinematic scenarios on predicted age distributions. (A) Schematic cross-section showing velocity vectors in the vertical (solid black), lateral (solid gray) and thrust (dashed black) kinematic scenarios. These models generally have a denudation rate of 1 mm/y (see text for details) and are used predict AHe (B), ZFT (C) and MAr (D) age distributions. The listed percent error is the 1σ uncertainty used in generating the predicted SPDF_m curves.

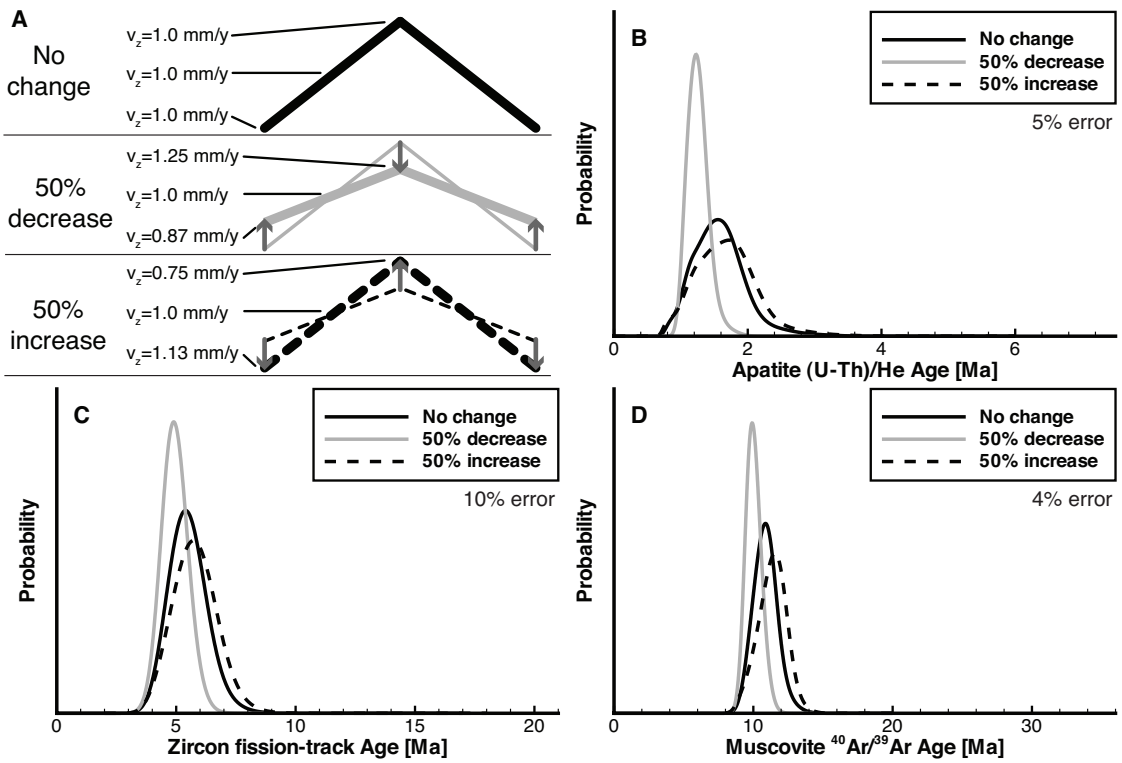

Figure 3.7: Effect of topographic evolution on predicted age distributions. (A) Schematic cross-section of time-invariant surface topography (solid black) shown with that resulting from a 50% decrease (solid gray) and 50% increase (dashed black) in topographic relief with a fixed mean elevation. These models are used to predict AHe (B), ZFT (C) and MAr (D) age distributions. The listed percent error is the 1σ uncertainty used in generating the predicted SPDF_m curves.

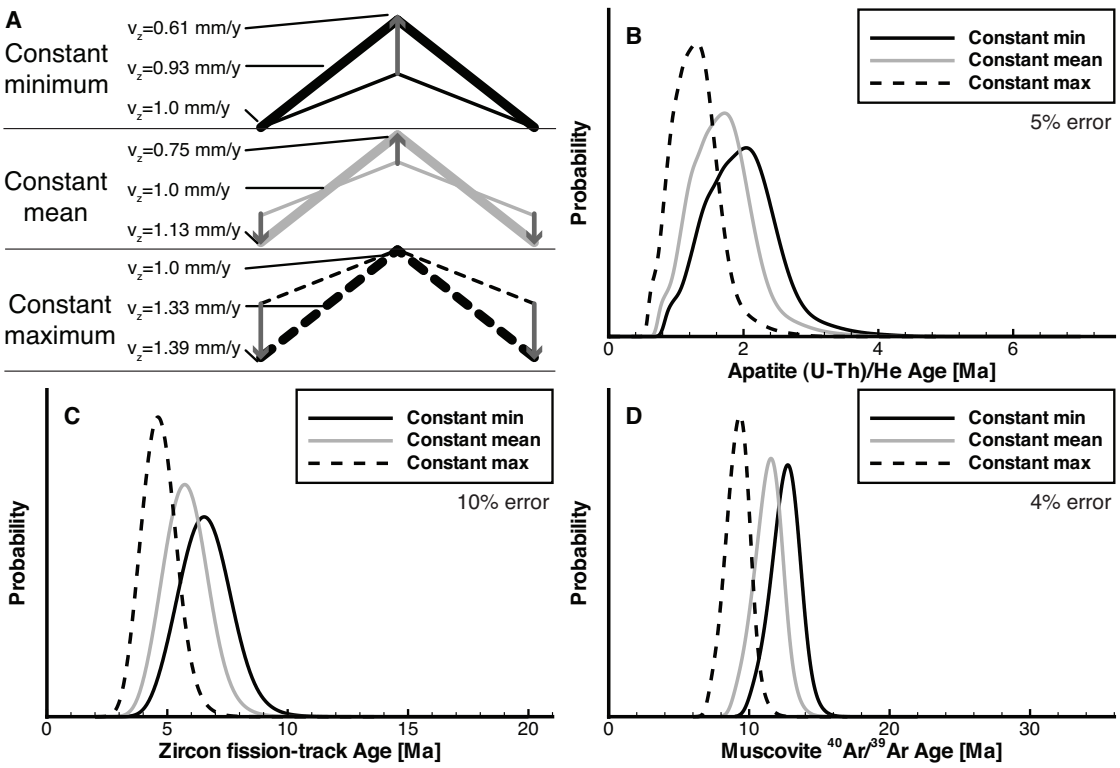

Figure 3.8: Effect of topographic evolution fixed elevation point on predicted age distributions. (A) Schematic cross-section of scenarios with a 50% increase in topographic relief with either a fixed minimum (solid black), fixed mean (solid gray) or fixed maximum (dashed black) elevation. These models are used to predict AHe (B), ZFT (C) and MAr (D) age distributions. The listed percent error is the 1σ uncertainty used in generating the predicted SPDF_m curves.

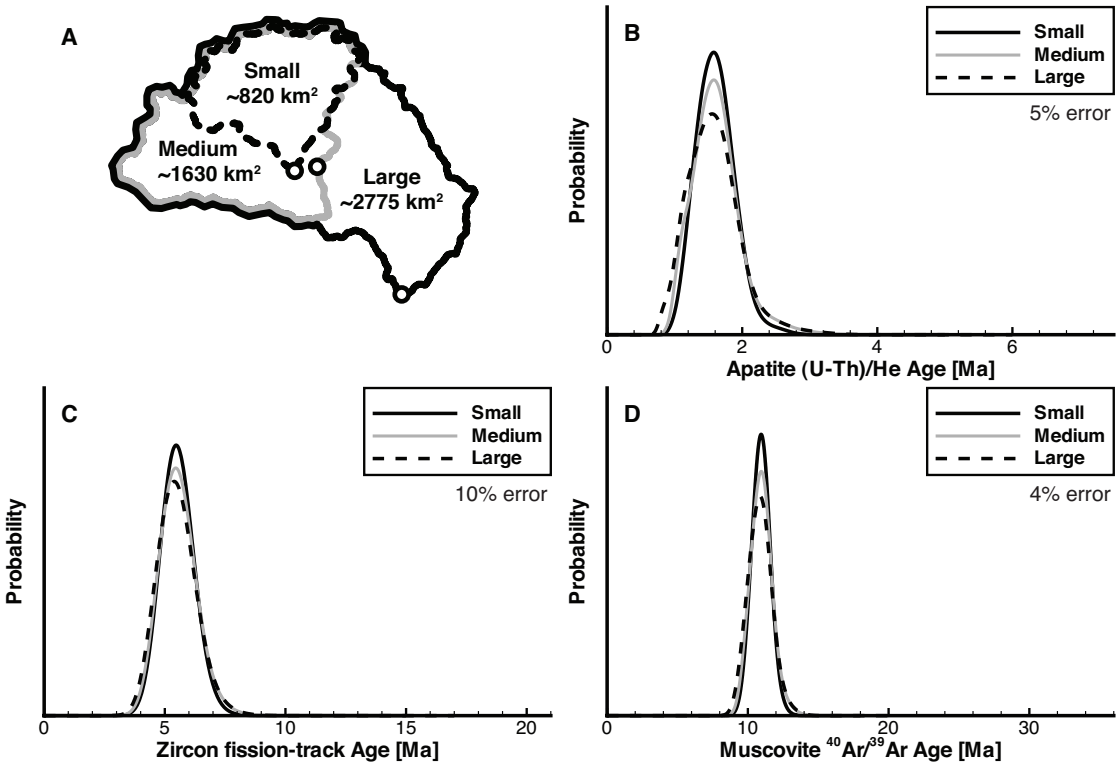

Figure 3.9: Effect of basin size on predicted age distributions. (A) Different basin sizes used for age prediction where the large basin (solid black) is the basin used in all previous age distributions and the medium (solid gray) and small (dashed black) basins are tributary catchments to the large basin. For each basin, AHe (B), ZFT (C) and MAr (D) age distributions are predicted. The listed percent error is the 1σ uncertainty used in generating the predicted SPDF_m curves.

Figure 3.10: Temporal response to changes in denudation rate and topographic relief at 10 Ma that may be recorded in foreland basin sediments. Schematic stratigraphic column represents sediment preserved from 15−0 Ma and sampled at 5 My intervals. (A) Predicted MAr age distributions for a 5x acceleration in denudation rate (solid black) shown with distributions generated with time-invariant denudation rates of 2.5 (solid gray) and 0.5 mm/y (dashed gray) using the vertical kinematic scenario. (B) Predicted MAr age distributions for a 50% increase in topographic relief (solid black) and that predicted for time-invariant topography (dashed gray). Both models use the vertical kinematic scenario with a background denudation rate of 1 mm/y. All vertical axes are at the same scale.

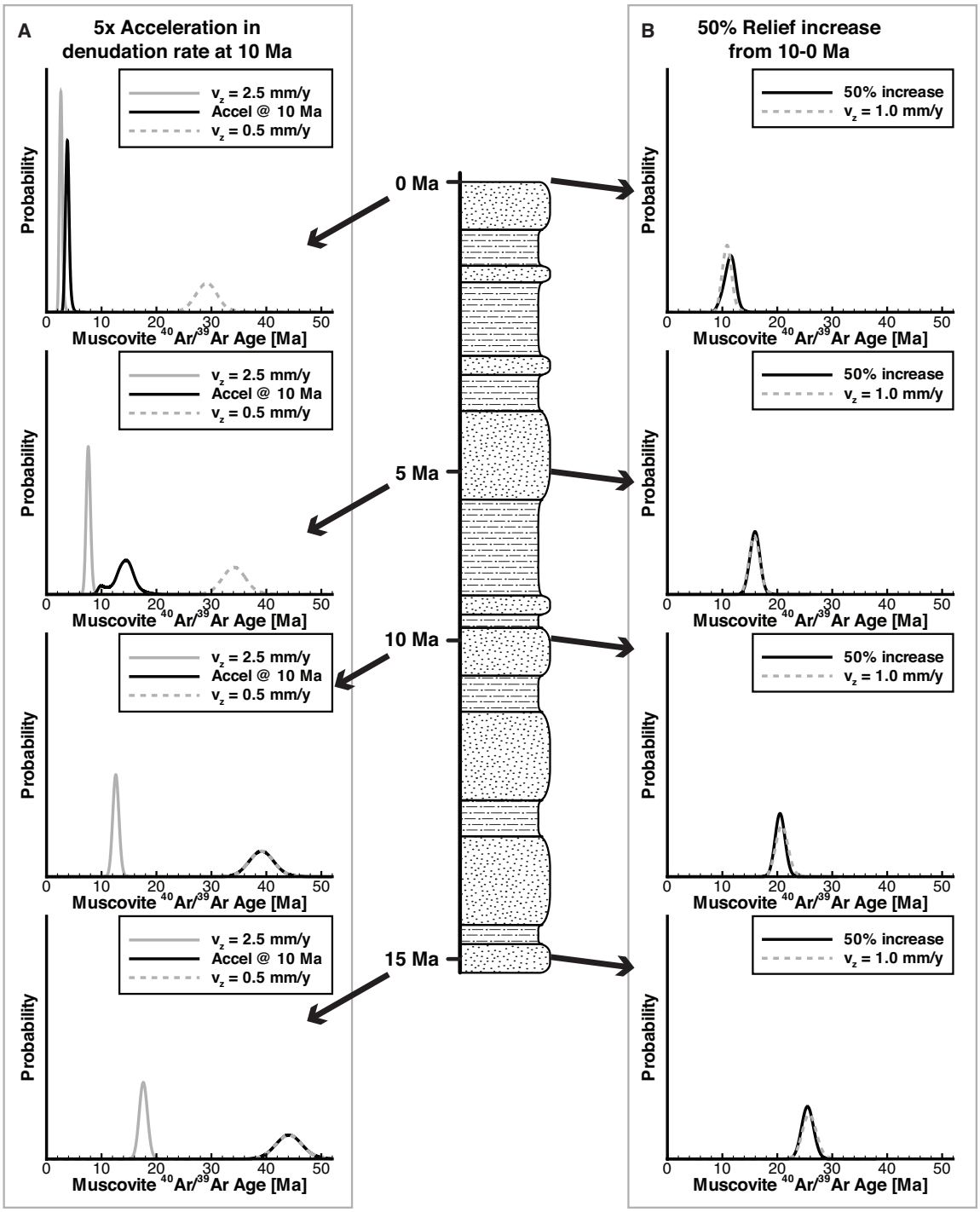
A
5x Acceleration in denudation rate at 10 Ma
B
50% Relief increase from 10-0 Ma
0 Ma
5 Ma
10 Ma
15 Ma
v_z = 2.5 mm/y
Accel @ 10 Ma
v_z = 0.5 mm/y
50% increase
v_z = 1.0 mm/y
Probability
Muscovite 40Ar/39Ar Age [Ma]
0
10
20
30
40
50

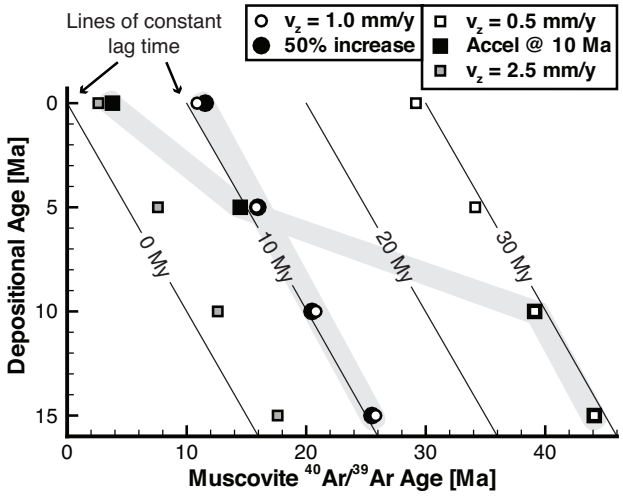

Figure 3.11: Changes in lag time for variations in denudation rate and topographic relief predicted in foreland basin deposits. Peak ages are plotted for the denudation rate and topographic change scenarios shown in Figure 3.10 (within light gray zones). Symbols that plot along the lines of constant lag time (thin gray lines) show no change in lag time in the hypothetical deposits.

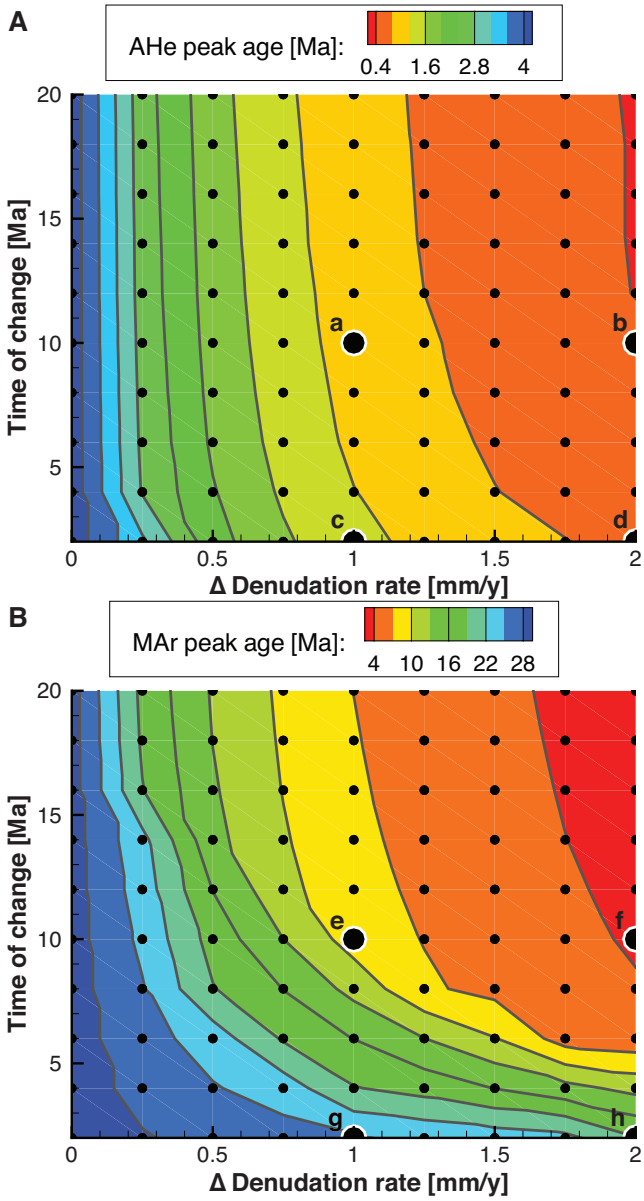

Figure 3.12: Changes in peak ages resulting from an acceleration in denudation rate at various times. The background denudation rate of 0.5 mm/y is accelerated by 0−2 mm/y at 2−20 Ma. Each small black circle represents an individual model run from which the contoured AHe (A) and MAr (B) peak ages were derived. The larger black circles are discussed in the text.

Bibliography

Amidon, W. H., Burbank, D. W. and Gehrels, G. E. Construction of detrital mineral populations: insights from mixing of U-Pb zircon ages in Himalayan rivers. *Basin Research*, 17(4):463–485, 2005.

Bathe, K.-J. *Finite Element Procedures in Engineering Analysis*. Prentice-Hall civil engineering and engineering mechanics series. Prentice-Hall, Inc., 1st edition, 1982.

Batt, G. E. and Brandon, M. T. Lateral thinking; 2-D interpretation of thermochronology in convergent orogenic settings. *Tectonophysics*, 349(1-4):185–201, 2002.

Beaumont, C., Fullsack, P. and Hamilton, J. Erosional control of active compressional orogens. In McClay, K., editor, *Thrust Tectonics*, pages 1–18. Chapman and Hall, New York, 1992.

Beaumont, C., Jamieson, R. A., Nguyen, M. H. and Lee, B. Himalayan tectonics explained by extrusion of a low-viscosity crustal channel coupled to focused surface denudation. *Nature*, 414(6865):738–742, 2001.

Bernet, M. and Garver, J. I. Fission-track Analysis of Detrital Zircon. *Reviews in Mineralogy and Geochemistry*, 58(1):205–237, 2005.

Bernet, M., van der Beek, P., Pik, R., Huyghe, P., Mugnier, J.-L., Labrin, E. and Szulc, A. Miocene to Recent exhumation of the central Himalaya determined from combined detrital zircon fission-track and U/Pb analysis of Siwalik sediments, western Nepal. *Basin Research*, 18(4):393–412, 2006. doi:10.1111/j.1365-2117.2006.00303.x.

Bernet, M., Zattin, M., Garver, J. I., Brandon, M. T. and Vance, J. A. Steady-state exhumation of the European Alps. *Geology*, 29(1):35–38, 2001.

Bollinger, L., Henry, P. and Avouac, J. P. Mountain building in the Nepal Himalaya: Thermal and kinematic model. *Earth and Planetary Science Letters*, 244(1-2):58–71, 2006.

Brandon, M., Roden-Tice, M. and Garver, J. Late Cenozoic exhumation of the Cascadia accretionary wedge in the Olympic Mountains, northwest Washington State. *Geological Society of America Bulletin*, 110(8):985–1009, 1998. ISSN 0016-7606.

Brandon, M. T. and Vance, J. A. Tectonic evolution of the Cenozoic Olympic subduction complex, Washington State, as deduced from fission track ages for detrital zircons. *American Journal of Science*, 292(8):565–636, 1992.

Braun, J. Quantifying the effect of recent relief changes on age-elevation relationships. *Earth and Planetary Science Letters*, 200(3-4):331–343, 2002.

Braun, J. Pecube; a new finite-element code to solve the 3D heat transport equation including the effects of a time-varying, finite amplitude surface topography. *Computers & Geosciences*, 29(6):787–794, 2003.

Braun, J., van der Beek, P. and Batt, G. E. *Quantitative Thermochronology*. Cambridge University Press, 1 edition, 2006.

Brewer, I. and Burbank, D. W. Thermal and kinematic modeling of bedrock and detrital cooling ages in the central Himalaya. *J. Geophys. Res.*, 111(B9):B09409, 2006.

Brewer, I. D., Burbank, D. W. and Hodges, K. V. Modelling detrital cooling-age populations; insights from two Himalayan catchments. *Basin Research*, 15(3):305–320, 2003.

Brewer, I. D., Burbank, D. W. and Hodges, K. V. Downstream development of a detrital cooling-age signal; insights from $^{40}Ar/^{39}Ar$ muscovite thermochronology in the Nepalese Himalaya. In Willett, S. D., Hovius, N., Brandon, M. T. and Fisher, D. M., editors, *Tectonics, Climate and Landscape Evolution*, volume 398 of *Penrose Conference Series*, pages 321–338. Geological Society of America, 2006.

Brooks, A. and Hughes, T. Streamline Upwind / Petrov-Galerkin formulations for convective dominated flows with particular emphasis on the incompressible Navier-Stokes Equations. *Computer Methods in Applied Mechanics and Engineering*, 32:199–259, 1982.

Carrapa, B., Strecker, M. R. and Sobel, E. R. Cenozoic orogenic growth in the Central Andes: Evidence from sedimentary rock provenance and apatite fission track thermochronology in the FiambalBasin, southernmost Puna Plateau margin (NW Argentina). *Earth and Planetary Science Letters*, 247(1-2):82–100, 2006.

Carslaw, H. S. and Jaeger, J. C. *Conduction of Heat in Solids*. Clarendon Press, Oxford, 3rd edition, 1959.

Cerveny, P., Naeser, N., Zeitler, P. K., Naeser, C. and Johnson, N. History of uplift and relief of the Himalaya during the past 18 million years: Evidence from fission-track ages of detrital zircons from sandstones of the Siwalik Group. In Kleinspehn, K. and Paola, C., editors, *New Perspectives in Basin Analysis*, pages 43–61. Springer-Verlag, New York, 1988.

Copeland, P. and Harrison, T. M. Episodic rapid uplift in the Himalaya revealed by $^{40}Ar/^{39}Ar$ analysis of detrital K-feldspar and muscovite, Bengal Fan. *Geology*, 18(4):354–357, 1990.

Coutand, I., Carrapa, B., Deeken, A., Schmitt, A. K., Sobel, E. R. and Strecker, M. R. Propagation of orographic barriers along an active range front: insights from sandstone petrography and detrital apatite fission-track thermochronology in the intramontane Angastaco basin, NW Argentina. *Basin Research*, 18(1):1–26, 2006.

Crowley, K. D., Cameron, M. and Schaefer, R. l. Experimental studies of annealing of etched fission tracks in fluorapatite. *Geochimica et Cosmochimica Acta*, 55(5):1449–1465, 1991.

Dodson, M. H. Closure temperature in cooling geochronological and petrological systems. *Contributions to Mineralogy and Petrology*, 40(3):259–274, 1973.

Ehlers, T. A. Crustal Thermal Processes and the Interpretation of Thermochronometer Data. *Reviews in Mineralogy and Geochemistry*, 58:315–350, 2005.

Ehlers, T. A., Armstrong, P. A. and Chapman, D. S. Normal fault thermal regimes and the interpretation of low-temperature thermochronometers. *Physics of the Earth and Planetary Interiors*, 126:179–194, 2001.

Ehlers, T. A., Chaudhri, T., Kumar, S., Fuller, C. W., Willett, S. D., Ketcham, R. A., Brandon, M. T., Belton, D. X., Kohn, B. P., Gleadow, A. J., Dunai, T. J. and Fu, F. Q. Computational Tools for Low-Temperature Thremochronometer Interpretation. *Reviews in Mineralogy and Geochemistry*, 58:589–622, 2005.

Ehlers, T. A. and Farley, K. A. Apatite (U-Th)/He thermochronometry; methods

and applications to problems in tectonic and surface processes. *Earth and Planetary Science Letters*, 206(1-2):1–14, 2003.

Farley, K. Helium diffusion from apatite: General behavior as illustrated by Durango fluorapatite. *Journal of Geophysical Research, B, Solid Earth and Planets*, 105(B2):2903–2914, 2000. ISSN 0148-0227.

Farr, T. G., Rosen, P. A., Caro, E., Crippen, R., Duren, R., Hensley, S., Kobrick, M., Paller, M., Rodriguez, E., Roth, L., Seal, D., Shaffer, S., Shimada, J., Umland, J., Werner, M., Oskin, M., Burbank, D. and Alsdorf, D. The shuttle radar topography mission. *Reviews of Geophysics*, 45(2), 2007. ISSN 8755-1209. doi: 10.1029/2005RG000183.

Forster, C. B. and Smith, L. The influence of groundwater flow on thermal regimes in mountainous terrain; a model study. *Journal of Geophysical Research, B, Solid Earth and Planets*, 94(7):9439–9451, 1989.

Garbrecht, J. and Martz, L. W. The assignment of drainage direction over flat surfaces in raster digital elevation models. *Journal of Hydrology*, 193(1-4):204–213, 1997.

Garver, J. I. and Brandon, M. T. Erosional denudation of the British Columbia Coast Ranges as determined from fission-track ages of detrital zircon from the Tofino basin, Olympic Peninsula, Washington. *Geological Society of America Bulletin*, 106(11):1398–1412, 1994a.

Garver, J. I. and Brandon, M. T. Fission-track ages of detrital zircons from Cretaceous strata, southern British Columbia: Implications for the Baja BC hypothesis. *Tectonics*, 13(2):401–420, 1994b.

Garver, J. I., Brandon, M. T., Roden-Tice, M. K. and Kamp, P. J. J. Exhumation history of orogenic highlands determined by detrital fission-track thermochronology . In Ring, U., Brandon, M. T., Lister, G. S. and Willett, S. D., editors, *Exhumation processes; normal faulting, ductile flow and erosion*, volume 154 of *Geological Society Special Publications*, pages 283–304. Geological Society of London, 1999.

Gunnell, Y. Apatite fission track thermochronology: an overview of its potential and limitations in geomorphology. *Basin Research*, 12(2):115–132, 2000.

Hames, W. E. and Bowring, S. A. An empirical evaluation of the argon diffusion geometry in muscovite. *Earth and Planetary Science Letters*, 124(1-4):161–169, 1994.

Henry, P., Le Pichon, X. and Goffe, B. Kinematic, thermal and petrological model of the Himalayas; constraints related to metamorphism within the underthrust Indian crust and topographic elevation. *Tectonophysics*, 273(1-2):31–56, 1997.

Herman, F., Braun, J. and Dunlap, W. J. Tectonomorphic scenarios in the Southern Alps of New Zealand. *Journal of Geophysical Research*, 112:no. B4, 25, 2007.

Hodges, K., Ruhl, K., Wobus, C. and Pringle, M. $^{40}Ar/^{39}Ar$ Thermochronology of Detrital Minerals. *Reviews in Mineralogy and Geochemistry*, 58(1):239–257, 2005. doi:10.2138/rmg.2005.58.9.

Huntington, K. W., Ehlers, T. A., Hodges, K. V. and Whipp, Jr., D. M. Topography, exhumation pathway, age uncertainties, and the interpretation of erosion rates from thermochronometer data. *Tectonics*, 26, 2007. doi:10.1029/2007TC002108.

Kuhlemann, J., Dunkl, I., Brügel, A., Spiegel, C. and Frisch, W. From source

terrains of the Eastern Alps to the Molasse Basin: Detrital record of non-steady-state exhumation. *Tectonophysics*, 413(3-4):301–316, 2006.

Mancktelow, N. S. and Grasemann, B. Time-dependent effects of heat advection and topography on cooling histories during erosion. *Tectonophysics*, 270(3-4):167–195, 1997.

Person, M., Toupin, D. and Eadington, P. One-dimensional models of groundwater flow, sediment thermal history and petroleum generation within continental rift basins. *Basin Research*, 7(1):81–96, 1995.

Press, W. H., Teukolsky, S. A., Vetterling, W. T. and Flannery, B. P. *Numerical Recipes in C: The Art of Scientific Computing*. Cambridge University Press, 2 edition, 1992.

Rahl, J. M., Ehlers, T. A. and van der Pluijm, B. A. Quantifying transient erosion of orogens with detrital thermochronology from syntectonic basin deposits. *Earth and Planetary Science Letters*, 256(1-2):147–161, 2007.

Reiners, P., Thomson, S., McPhillips, D., Donelick, R. and Roering, J. Wildfire thermochronology and the fate and transport of apatite in hillslope and fluvial environments. *Journal of Geophysical Research, F, Earth Surface*, 112, 2007. doi: 10.1029/2007JF000759.

Reiners, P. W. Thermochronologic Approaches to Paleotopography. *Reviews in Mineralogy and Geochemistry*, 66(1):243–267, 2007.

Reiners, P. W. and Brandon, M. T. Using Thermochronology to Understand Orogenic Erosion. *Annual Review of Earth and Planetary Sciences*, 34:419–466, 2006.

Reiners, P. W., Ehlers, T. A. and Zeitler, P. K. Past, Present, and Future of Thermochronology. *Reviews in Mineralogy and Geochemistry*, 58(1):1–18, 2005.

Reiners, P. W., Spell, T. L., Nicolescu, S. and Zanetti, K. A. Zircon (U-Th)/He thermochronometry: He diffusion and comparisons with $^{40}Ar/^{39}Ar$ dating. *Geochimica et Cosmochimica Acta*, 68(8):1857–1887, 2004.

Renne, P. R., Becker, T. A. and Swapp, S. M. $^{40}Ar/^{39}$ Ar laser-probe dating of detrital micas from the Montgomery Creek Formation, Northern California; clues to provenance, tectonics, and weathering processes. *Geology*, 18(6):563–566, 1990.

Robbins, G. A. *Radiogenic argon diffusion in muscovite under hydrothermal conditions.* Thesis or dissertation; master's; monographic, Brown University, 1972.

Ruhl, K. W. and Hodges, K. V. The use of detrital mineral cooling ages to evaluate steady state assumptions in active orogens; an example from the central Nepalese Himalaya. *Tectonics*, 24:no.4, 14, 2005.

Schaller, M. and Ehlers, T. A. Limits to quantifying climate driven changes in denudation rates with cosmogenic radionuclides. *Earth and Planetary Science Letters*, 248(1-2):153–167, 2006.

Schaller, M., von Blanckenburg, F., Hovius, N. and Kubik, P. W. Large-scale erosion rates from in situ-produced cosmogenic nuclides in European river sediments. *Earth and Planetary Science Letters*, 188(3-4):441–458, 2001.

Shuster, D. L., Flowers, R. M. and Farley, K. A. The influence of natural radiation damage on helium diffusion kinetics in apatite. *Earth and Planetary Science Letters*, 249(3-4):148–161, 2006.

Smith, L. and Chapman, D. S. On the thermal effects of groundwater flow - 1. Regional scale systems. *Journal of Geophysical Research*, 88(B1):593–608, 1983.

Sobel, E. R., Chen, J. and Heermance, R. V. Late Oligocene-Early Miocene initiation of shortening in the Southwestern Chinese Tian Shan: Implications for Neogene shortening rate variations. *Earth and Planetary Science Letters*, 247(1-2):70–81, 2006.

Spiegel, C., Kuhlemann, J., Dunkl, I., Frisch, W., von Eynatten, H. and Balogh, K. The erosion history of the Central Alps: evidence from zircon fission track data of the foreland basin sediments. *Terra Nova*, 12(4):163–170, 2000. doi:10.1046/j.1365-3121.2000.00289.x.

Stock, G. M., Ehlers, T. A. and Farley, K. A. Where does sediment come from? Quantifying catchment erosion with detrital apatite (U-Th)/He thermochronometry. *Geology*, 34(9):725–728, 2006.

Stock, J. D. and Montgomery, D. R. Estimating palaeorelief from detrital mineral age ranges. *Basin Research*, 8(3):317–327, 1996. doi:10.1046/j.1365-2117.1996.00177.x.

Stüwe, K. and Hintermüller, M. Topography and isotherms revisited: the influence of laterally migrating drainage divides. *Earth and Planetary Science Letters*, 184(1):287–303, 2000.

Stüwe, K., White, L. and Brown, R. The influence of eroding topography on steady-state isotherms; application to fission track analysis. *Earth and Planetary Science Letters*, 124(1-4):63–74, 1994.

Szulc, A. G., Najman, Y., Sinclair, H. D., Pringle, M., Bickle, M., Chapman, H., Garzanti, E., Ando, S., Huyghe, P., Mugnier, J.-L., Ojha, T. and DeCelles, P.

Tectonic evolution of the Himalaya constrained by detrital ^{40}Ar-^{39}Ar, Sm-Nd and petrographic data from the Siwalik foreland basin succession, SW Nepal. *Basin Research*, 18(4):375–391, 2006. doi:10.1111/j.1365-2117.2006.00307.x.

van der Beek, P., Braun, J. and Lambeck, K. Post-Palaeozoic uplift history of southeastern Australia revisited: results from a process-based model of landscape evolution. *Australian Journal of Earth Sciences*, 46(2):157–172, 1999. doi: doi:10.1046/j.1440-0952.1999.00701.x.

van der Beek, P., Robert, X., Mugnier, J.-L., Bernet, M., Huyghe, P. and Labrin, E. Late Miocene - Recent exhumation of the central Himalaya and recycling in the foreland basin assessed by apatite fission-track thermochronology of Siwalik sediments, Nepal. *Basin Research*, 18(4):413–434, 2006. doi:10.1111/j.1365-2117.2006.00305.x.

Vermeesch, P. Quantitative geomorphology of the White Mountains (California) using detrital apatite fission track thermochronology. *Journal of Geophysical Research, F, Earth Surface*, 112(F3):F03004, 2007. doi:10.1029/2006JF000671.

Whipp, Jr., D. M. and Ehlers, T. A. Influence of groundwater flow on thermochronometer-derived exhumation rates in the central Nepalese Himalaya. *Geology*, 35(9):851–854, 2007. doi:10.1130/G23788A.1.

Whipp, Jr., D. M. and Ehlers, T. A. Landsliding, faulting and the interpretation of detrtial thermochronometer data. *Chapter 4 (this volume)*, 2008.

Whipp, Jr., D. M., Ehlers, T. A., Blythe, A. E., Huntington, K. W., Hodges, K. V. and Burbank, D. W. Plio-Quaternary exhumation history of the central Nepalese Himalaya: 2. Thermo-kinematic and thermochronometer age prediction model. *Tectonics*, 26, 2007. doi:10.1029/2006TC001991.

Willett, S. D. Orogeny and orography; the effects of erosion on the structure of mountain belts. *Journal of Geophysical Research, B, Solid Earth and Planets*, 104(12):28,957–28,982, 1999.

CHAPTER IV

Landsliding, faulting and the interpretation of detrital thermochronometer data from the Nepalese Himalaya

4.1 Abstract

Recent studies have highlighted the utility of detrital thermochronometer samples from modern river and basin sediments in quantifying temporal and spatial variations in drainage basin erosion, as well as the deformation and exhumation history of orogens. Less well known are the influence and sensitivity of detrital thermochronometers to different surface processes or individual faults within catchments. In this study, we address these issues using a 3-D transient thermokinematic, landform evolution and age prediction model to simulate the effects faulting and landsliding on predicted detrital muscovite $^{40}Ar/^{39}Ar$ age distributions. Model results are compared to observed age distributions collected from modern river sands in the Nepalese Himalaya to determine the geomorphic and tectonic processes that provide a good fit to the data. Preliminary results suggest variations in the faulting and deformation history of the region alone do not provide an adequate fit to the data, suggesting sampled basin sediment may not have been contributed from all regions in the basin as predicted from balanced tectonic uplift and erosion, or the explored

Official citation:
Whipp, D.M., Jr., and T.A. Ehlers, Landsliding, faulting and the interpretation of detrital thermochronometer data from the Nepalese Himalaya, for submission to *Journal of Geophysical Research, Earth Surface*

tectonic model parameter space may be too small. Non-uniform sediment sampling is addressed by exploring the effects of randomly placed bedrock landslides on predicted age distributions. We find that ages are quite sensitive to landsliding and sediment residence times within the catchment. Furthermore, landslide-generated sediment sampled in modern river samples from areas with short ($\sim$1 year) sediment residence times can under-sample the catchment age range and influence calculated exhumation histories.

4.2 Introduction

Topography in convergent orogens is the result of the combination of tectonic deformation and erosion at the surface. Detrital thermochronology is an increasingly popular tool for quantifying orogen tectonic and erosion histories over millions of years. A number of recent studies have used detrital thermochronometers to address paleotopography (Stock and Montgomery, 1996; Reiners, 2007), spatial variations in basin erosion (Ruhl and Hodges, 2005; Brewer et al., 2006; Stock et al., 2006) and orogen faulting evolution (Wobus et al., 2003; Bernet et al., 2006; Carrapa et al., 2006; Sobel et al., 2006; Szulc et al., 2006; van der Beek et al., 2006). However, the calculation of long-term erosion rates in high-relief, active convergent orogens from detrital thermochronometer data is complicated by the thermal effects of thrust faulting, spatially variable uplift rates and non-uniform sediment contribution within the sampled upstream drainage basin area from surface processes such as bedrock landsliding (Figures 4.1, 4.6). In this study we investigate the influence of landsliding and faulting scenarios on detrital grain-age distributions from modern river samples. General principles are discussed and model predictions are applied to published samples from rivers in the Nepalese Himalaya.

Previous detrital modeling studies have addressed rates and spatial variations in basin erosion and the effects of faulting on detrital thermochronometer data. As one of the first detrital thermochronometer modeling studies, Brewer et al. (2003) used a 2-D numerical model to predict relationships between bedrock thermochronometer ages and sample elevation that were combined with basin hypsometries to predict detrital age distributions. Predicted age distributions were further compared to thermochronometer data from two drainage basins in central Nepal to quantify basin erosion rates. Ruhl and Hodges (2005) and Stock et al. (2006) combined observed bedrock thermochronometer age-elevation relationships with basin elevation distributions to address rates and spatial variations in erosion in the Nepalese Himalaya and Sierra Nevada. Brewer and Burbank (2006) extrapolated 2-D thermal model results along strike of a simplified Himalayan tectonic model to predict a quasi-3-D crustal thermal field with the effects of thrust faulting. Model results were further combined with an age prediction model to yield predicted bedrock and detrital thermochronometer ages that were compared to data.

Previous work has advanced our understanding of detrital thermochronometer data, but was limited by several restrictive assumptions. The studies of Brewer et al. (2003), Ruhl and Hodges (2005) and Stock et al. (2006) used linear relationships between bedrock thermochronometer age and elevation, which may be unrealistic for high-relief orogens. Furthermore, by convolving basin hypsometry with predicted or observed linear age-elevation relationships, it is assumed that there are no spatial variations in erosion within the catchment. Brewer and Burbank (2006) modeled thermal advection and rock exhumation in the Himalaya using a single fault. This simplified geometry does not consider the potential effects of other significant mapped thrust faults, including the Main Central Thrust (MCT) which is thought to have

had significant out-of-sequence activity during the Late Miocene−Recent time period (e.g., Seeber and Gornitz, 1983; Harrison et al., 1997; Catlos et al., 2001; Wobus et al., 2003; Hodges et al., 2004; Wobus et al., 2005; Huntington and Hodges, 2006). In addition, the study of Brewer and Burbank (2006) extrapolated a 2-D thermal model across the study region to generate predicted cooling ages within the model catchments. This approach is certainly more justifiable for the white mica $^{40}Ar/^{39}Ar$ data they model than it would be for lower temperature thermochronometers. However, it still neglects 3-D topographic effects and fault geometry variations that could influence the distributions of predicted cooling ages.

This study utilizes a transient 3-D thermokinematic and age prediction model of the Nepalese Himalaya to explore how different tectonic evolution scenarios, denudation rates and bedrock landsliding affect detrital thermochronometer age distributions. Model results are compared to detrital data from central Nepal to determine the range of geomorphic and faulting scenarios that provide a good fit to the observations. The primary goal of this study is to help improve the interpretation of detrital thermochronometer data by illustrating their sensitivity to various tectonic and surface processes, such as bedrock landsliding.

4.3 Geologic Setting

The most recent phase of deformation in the Himalaya is thought to have begun in the Early Miocene with sequential activation of several orogen-scale thrust faults (e.g., Gansser, 1964; Le Fort, 1975; Hodges, 2000). The oldest and most interior of those structures, the Main Central Thrust (MCT), was first active in the Early Miocene, potentially coeval with passive roof extension on the South Tibetan Detachment (STD) (e.g., Burchfiel and Royden, 1985; Searle, 1989; Harris, 2007).

These two structures allowed for extrusion of the igneous and upper-amphibolite-facies metamorphic rocks of the Greater Himalayan Sequence (GHS) as large thrust nappes. By the Middle Miocene, deformation propagated south to the Main Boundary Thrust (MBT) (e.g., Meigs et al., 1995) driving erosional exhumation of the lower-greenschist to lower-amphibolite-facies rocks within the Lesser Himalayan Sequence (LHS). In addition, the Middle−Late Miocene onset of underplating and duplex formation within the Lesser Himalaya likely enhanced uplift (e.g., DeCelles et al., 2001; Pearson and DeCelles, 2005). By the Middle to Late Pliocene, the MBT became inactive and deformation again shifted south, in favor of thrusting on the Main Frontal Thrust (MFT), the modern day deformation front of the range. Estimates of Holocene Indo-Tibetan convergence show that nearly all of the ∼20 mm/y of convergence was accommodated by the MFT (Lavé and Avouac, 2000) and are consistent with present-day geodetic measurements (Bilham et al., 1997; Larson et al., 1999; Bettinelli et al., 2006). In contrast to this simple notion of southward-propagating thrusts, however, there have been a number of recent studies suggesting intermittent out-of-sequence activity on the MCT (e.g., Seeber and Gornitz, 1983; Hodges et al., 1996; Harrison et al., 1997; Catlos et al., 2001; Wobus et al., 2003; Hodges et al., 2004; Wobus et al., 2005; Huntington and Hodges, 2006). Because of this controversy, we use the model described below to consider both tectonic scenarios.

4.4 Numerical Modeling Approach

This study utilizes a modified version of the thermokinematic numerical model Pecube (Braun, 2003) to solve the 3-D transient advection-diffusion equation. The program was adapted to predict detrital muscovite $^{40}Ar/^{39}Ar$ (MAr) thermochronometer ages at the surface. Below, we discuss details about the model relevant to our

application in the Himalaya, whereas a general discussion about the modified code can be found in Whipp and Ehlers (2008).

4.4.1 Thrust Kinematic Model

Advective heat transport from thrust faulting is one of the primary heat transfer processes in active convergent orogens. This study uses a thrust kinematic model geometry based on geologic cross-sections (Lavé and Avouac, 2000, and references therein) and tectonic maps (Searle and Godin, 2003; Bollinger et al., 2004) from central Nepal. Fault surfaces in the model are approximated as planar and kink-band, fault-bend folding (Suppe, 1983) is used between fault segments of differing dip angle.

The model features three thrust faults and one normal fault with variable dip angles at the surface and at depth: The MFT, MBT, MCT and STD (Figure 4.3). The southernmost thrust (MFT) is the distal expression of the basal detachment beneath the Himalaya. Although rarely exposed at the surface, a surface dip angle of 40° is assumed for the MFT down to where it joins the detachment fault with a gentle dip of 4°. The MFT and detachment dip angles are similar to those inferred from bedding in fault-bend folds in the MFT hanging wall and plate flexure models (e.g., Lavé and Avouac, 2000). Approximately 25 km north of the MFT, the MBT intersects the model surface with a dip angle of 40° and splays from the basal detachment at a point where the detachment dip angle is 7°. North of the MBT, the detachment features a mid-crustal ramp dipping at 19°, prior to shallowing to 10°. The mid-crustal ramp and detachment position north of it are constrained from foliation plane dip angles (Schelling and Arita, 1991), seismic events (Pandey et al., 1995), and reflections from the INDEPTH seismic survey (Zhao et al., 1993; Brown et al., 1996). At the surface, the MCT has a dip angle of 40° down to where it

splays from the basal décollement with a dip angle of 10°. The MCT dip angle is consistent with the range of foliations measured in rocks of the GHS from western Nepal (Valdiya, 1980; DeCelles et al., 2001) and slightly steeper than measured dip of the MCT shear zone in central Nepal (Valdiya, 1980; Macfarlane et al., 1992; Hodges et al., 1996; Searle and Godin, 2003). Along with the position of the basal décollement, these faults generate a zone of relatively rapid uplift that is coincident with the location of the highest topographic relief. Structurally above the MCT, the STD parallels the MCT with a surface dip angle of 40°, again slightly steeper than the observed surface dip angle (Searle and Godin, 2003). At depth, the dip shallows to parallel the basal detachment.

Transport of material by the thrust faults occurs perpendicular to modeled fault traces assuming a constant convergence rate. The model domain is oriented such that the model y-axis is parallel to the thrust vergence direction of 198°. The vergence direction is subparallel to observed stretching lineations (Brunel, 1986) and also aligned with modern-day geodetic measurements of Indo-Tibetan convergence (Bilham et al., 1997; Larson et al., 1999; Jouanne et al., 2004; Bettinelli et al., 2006). Surface fault traces are approximated as linear features from the tectonic maps of Searle and Godin (2003) and Bollinger et al. (2004) with the exception of the STD, which has three segments to follow the mapped trace. Other than the strike-slip section of the STD, faults strike perpendicular to vergence, parallel to the model x-axis. Slip is partitioned among the different structures such that a constant convergence rate of 20 mm/y is maintained between India (south of MFT) and Tibet (north of STD). This convergence rate is based on both present-day geodetic measurements from central and eastern Nepal (19 ± 2.5 mm/y) (Bettinelli et al., 2006) and estimates of shortening over the Holocene (21 ± 1.5 mm/y) (Lavé and Avouac,

2000).

This study uses a tectonic model with the above kinematics that is based on the general evolution of faulting in the central Nepalese Himalaya. This model is designed to replicate the major tectonic events in the Himalaya since the early Miocene and maintain denudation rates within the GHS of 1−2.5 mm/y over the last ∼3 Ma. The tectonic model has no active faults from 50−23 Ma. At 23 Ma both the MCT and STD become active with equal convergence/extension rates of 0.6−7.3 mm/y, simulating extrusion of the GHS (e.g., Grujic et al., 1996; Beaumont et al., 2001; Hodges et al., 2001; Searle et al., 2006; Jessup et al., 2006). At 13 Ma the MCT and STD become inactive and the MBT becomes the only active structure, slightly earlier than suggested by (Meigs et al., 1995), but coincident with the suggested cessation of thrusting on the MCT (Hodges, 2000, and references therein). At 9 Ma duplex formation within the Lesser Himalaya is enabled (DeCelles et al., 2001; Robinson et al., 2001) via underplating of subducted material between the mid-crustal ramp and the point from which the MCT splays off the basal décollement. Finally, at 3 Ma the MBT becomes inactive and the MFT is activated (e.g., DeCelles et al., 2001; Robinson et al., 2003). To explore the potential for out-of-sequence thrusting on the MCT, several models were run with a reactivation of the MCT along with the MFT at 3 Ma.

Another important aspect of the tectonic model is that the faults in the model are advected laterally with time such that material above the basal décollement has purely vertical movement (e.g., Figures 4.3; 3.6A of Whipp and Ehlers (2008)). This kinematic model setup is similar to the horizontal advection of the landscape scenario used by Herman et al. (2007) and is utilized to ensure vertical mass transport and particle pathways for predicting thermochronometer ages. Because the model

topography is in steady state, vertical particle pathways are important to ensure that particles do not track outside of the model volume. It should be noted that although vertical particle pathways are used for generating predicted ages, the lateral velocity components are included in the calculation of the thermal field to ensure that the thermal effects of overthrusting are reproduced.

4.4.2 Thermal Model

The faults in the kinematic model described above divide the model into zones of varying exhumation rate and rock material properties. The topography in the model is derived from a 90 m Shuttle Radar Topography Mission digital elevation model (Farr et al., 2007) and does not change with time. Because of this, all material that fluxed through the upper surface of the model by the active faults is instantaneously eroded. Thus, the denudation rate in any portion of the model is equal to the vertical component of the kinematic velocity vectors in the tectonic model. The faults also divide the model material properties into five regions: (1) the Indian Shield subducted beneath the Himalaya and basal décollement, (2) the Sub-Himalaya in the MFT hanging wall, (3) the LHS in the MBT/décollement hanging wall, (4) the GHS in the MCT hanging wall and (5) the Tethyan Himalaya (TH) in the STD hanging wall. Rock thermophysical properties for the GHS are based on average values for measured rock thermal conductivity and radiogenic heat production (Whipp et al., 2007). Radiogenic heat production in the TH is set to an average sedimentary heat production of 0.5 μW/m^3. For the other units, heat production values consistent with observed surface heat flow measurements (Roy and Rao, 2000) are used, as is an average rock thermal conductivity. The model uses constant temperature boundary conditions for the base and top of the model. The basal temperature is fixed at 1350°C at 130 km depth, while the surface temperature varies with elevation, as-

suming a sea level temperature of 24°C and atmospheric lapse rate of 6°C/km. The thermal solution is calculated from a conductive steady state with no advection. A summary of the thermal model parameters can be found in Table 1.

An additional heat source within the model is provided by frictional heating along the active fault surfaces. Frictional shear heating is calculated at all points within the model domain following the moderate friction case of Hansen and Carter (1982). The shear stress at any point is defined as the minimum of either the pressure-dependent brittle stress or the ductile, temperature-dependent power law stress. The maximum shear stress is not allowed to exceed 50 MPa. Frictional heating becomes important in any portion of the model with significant differential velocities (i.e., fault zones) and can provide a significant amount of volumetric heat production at high slip rates. Because frictional heating is a volumetric heat source, it is combined with the radiogenic heat production of a given unit.

4.4.3 Quantifying Model Fits

The range of model free parameters explored in this study is evaluated by quantifying the misfit between the model-predicted and observed thermochronometer grain-age probability density functions (PDFs). Misfits are computed using a Monte Carlo technique that consists of four steps (Figure 3.2 of Whipp and Ehlers, 2008): (1) n grains are extracted from the raw grain-age distribution within the catchment of interest, where n is the number of grain-ages used in calculating the data PDF. (2) A predicted PDF (PDF_m) of age (t) is generated for each grain-age (e.g., Ruhl and Hodges, 2005),

$$\mathrm{PDF}_m = \frac{1}{\sigma_{t_m}\sqrt{2\pi}} \exp\left[-\frac{1}{2}\left(\frac{t-t_m}{\sigma_{t_m}}\right)^2\right] \times v_z \tag{4.1}$$

where σ_{t_m} is the median one sigma age uncertainty in the observed grain-ages, t is the range of ages over which PDF_m is defined, t_m is the predicted age and v_z is the corresponding denudation rate. Basin-wide age distributions are created by summing the individual age PDFs to generate a model synoptic probability density function (SPDF_m),

$$\mathrm{SPDF}_m = \left[\frac{1}{n}\sum_{i=1}^{n}\mathrm{PDF}_m(i)\right] \times \left(\frac{1}{\bar{v_z}}\right) \tag{4.2}$$

where n is the number of measured ages in the catchment of interest and $\bar{v_z}$ is the mean denudation rate in that catchment. (3) The observed and predicted age SPDFs are compared using a two-sample Kuiper's statistic test (e.g., Press et al., 1992; Ruhl and Hodges, 2005; Stock et al., 2006) to determine whether or not they differ at the 95% confidence level. Kuiper's statistic (V) is defined as the sum of the maximum distance (D) of the cumulative model-predicted SPDF above and below the the cumulative data SPDF,

$$V = D_+ + D_- = \max_{-\infty<x<\infty}[S_N(x) - P(x)] + \max_{-\infty<x<\infty}[P(x) - S_N(x)] \tag{4.3}$$

where $S_N(x)$ is the model predicted SPDF and $P(x)$ is the data SPDF. The significance (Q) is defined as,

$$Q(\lambda) = 2\sum_{j=1}^{\infty}(4j^2\lambda^2 - 1)e^{-2j^2\lambda^2} \tag{4.4}$$

where λ is defined as,

$$\lambda = \left[\sqrt{N_e} + 0.155 + 0.24/\sqrt{N_e}\right] V \tag{4.5}$$

and N_e is the effective number of samples, defined as,

$$N_e = \frac{N_1 N_2}{N_1 + N_2} \tag{4.6}$$

where N_1 and N_2 are the number of contributing to the predicted and data SPDFs. Note that in this case, $N_1 = N_2$ because an equal number of grain ages are used to calculate the observed and predicted SPDFs. Using Equations 3−6, Kuiper's test states that two distributions are statistically identical at the significance level α if $Q > \alpha$. A significance level α=0.05 is used, corresponding to a confidence interval of 95%. (4) Lastly, results are recorded. The above procedure is repeated 10,000 times to generate the percentage of predicted age PDFs that are statistically similar to the observed PDF for a given basin.

4.5 Results

In this section, the sensitivity of predicted MAr grain-age PDFs to different faulting scenarios, denudation rates and bedrock landsliding is explored in three drainage basins. Three catchments were selected that drain three different tectonostratigraphic regions: The LHS, GHS and TH. With the largest drainage fraction south of the MCT, the Darondi catchment was selected as the catchment in the LHS (Figure 4.2). The Darondi catchment has a drainage basin area of 608 km^2 and is a tributary to the Marsyandi River. The data PDF in this catchment is generated from 25 dated detrital muscovite grains (Brewer et al., 2006). In the MCT hanging wall, the Nyadi River is another tributary to the Marsyandi River and it exclusively drains the GHS (Figure 4.1). The Nyadi catchment has a drainage area of 182 km^2 and the data PDF was constructed from 111 muscovite grains (Ruhl and Hodges, 2005). Although not draining the TH exclusively, data are used from a trunk stream sample in the Marsyandi River just downstream from the STD that includes the Nar and Khansar tributaries (Figure 4.2). This basin is the largest of the three selected with a drainage area of 1631 km^2 and the data PDF in this catchment is based on

25 dated muscovite grain ages (Brewer et al., 2006).

4.5.1 Effects of different faulting scenarios

As discussed above, there is controversy surrounding the Plio-Quaternary faulting history in the Nepalese Himalaya and models in this section are used to explore the sensitivity of detrital MAr data to a potential thrust reactivation in the Pliocene and their fit to observed MAr data. The timing of activation of faults in both tectonic models is identical except during the last 3 My of the model run, where the MCT is or is not reactivated out of sequence. Thus, faulting is the only free parameter varied in this section. Both models maintain constant convergence rates that generate denudation rates of ∼2.5 mm/y within the GHS during the last 3 My of the model run, consistent with rates calculated from apatite fission-track data in the model region (Blythe et al., 2007; Whipp et al., 2007). The surface topography does not change with time.

The predicted MAr age PDFs for the two faulting scenarios are quite different, with older peak ages and larger age ranges for the MCT reactivation scenario. Peak ages in the MCT reactivation scenario are at least 5 My older than the scenario where the MCT is not reactivated (Figure 4.4). The main reason for this peak age difference is a slower denudation rate prior to MCT reactivation. One of our assumptions in the model setup is that there have been no major changes in the Indo-Tibetan convergence rate since 23 Ma. In combination with having denudation rates of ∼2.5 mm/y within the GHS over the last 3 My of the model run, the rate of overthrusting is higher for the models without any out-of-sequence thrusting. The reason for the higher overthrusting rate is that in the MCT reactivation case, material in the GHS is in the MCT hanging wall with a dip angle of 40°, whereas exhumation of GHS material is driven by thrusting over the mid-crustal ramp with a dip angle of

19° when the MCT is not reactivated. Thus, the overthrusting rate must be higher for the no reactivation case to maintain an equal exhumation rate. This results in both increased geothermal gradients from higher advection velocities and more rapid exhumation of material in regions other than the GHS, reducing the MAr peak ages for all three basins (Figure 4.4). This difference in denudation history also affects the age ranges for the three basins. Although the age range difference is largely the result of unreset MAr ages in the LHS and TH (Figure 4.4A,C), even the Nyadi catchment in the GHS has a larger age range for the MCT reactivation model (Figure 4.4B).

For the scenarios explored above, the general quality of fit of the predicted age PDFs from the two tectonic models the data is poor. Only 160 of the 10,000 predicted age PDFs (1.6%) in the Darondi catchment pass Kuiper's test for the model without reactivation of the MCT. This can be seen in Figure 4.4A as the small overlap between the swath of predicted age PDFs (dark gray lines) and the observed data PDF (black line). For the case where the MCT is reactivated, 0.0% of the predicted age PDFs pass Kuiper's test. For the Nyadi catchment, 97.1% of the predicted PDFs pass Kuiper's test and the quality of fit is quite clear in Figure 4.4B. However, for the MCT reactivation scenario, 0.0% of the predicted PDFs pass. The quality of fit for both model variants in the Nar/Khansar basin is poor with 0.0% of the predicted age PDFs passing Kuiper's test (Figure 4.4C). Furthermore, comparison of the predicted and observed PDF age ranges shows little similarity.

4.5.2 Effects of variable denudation rates

Variable maximum denudation rate

In this section, the effects of time-invariant denudation rates of different magnitude are investigated. In each model, the only free parameter is the overthrusting rate, which is constant over time to generate denudation rates in the GHS of either

1.0 or 2.5 mm/y during the last 3 My of the model run. As above, the choice of rates here is similar to observed rates in the GHS within the Marsyandi River valley. The MAr data of Ruhl and Hodges (2005) and Huntington et al. (2006) suggest average erosion rates of $\sim$0.6$-$0.7 mm/y in the Miocene and Pliocene, while the 2.5 mm/y rate is consistent bedrock apatite fission-track derived erosion rates over the Plio-Quaternary (Blythe et al., 2007; Whipp et al., 2007). The tectonic model without any out-of-sequence thrusting is used and there are no changes in the surface topography.

Both the peak ages and age range increase at the slower denudation rate and the goodness of fit does not improve (Figure 4.5A-C). The observed increase in peak age and age range are expected as discussed in Whipp and Ehlers (2008). The slower denudation rate increases the age range not only by decreasing the slope of the relationship between MAr age and elevation, but also because portions of the catchments contain unreset MAr ages. For example, the age range is 8 times larger in the Darondi catchment at the slow denudation rate (Figure 4.5A). Furthermore, although the peak age at the 2.5 mm/y denudation rate is younger than the data age peak, the peak age using the slower denudation rate is too old to fit the observed data (0.0% pass). The Nyadi and Nar/Khansar catchments behave the same was as the Darondi, with larger age ranges and peak ages that are too old to match the observed age peaks when the slower denudation rate is used (0.0% pass).

Acceleration in denudation rate

As opposed to the previous section where the overthrusting rate was constant through time, here the overthrusting rate is varied with time to accelerate between maximum denudation rates within the GHS of 1.0 mm/y and 2.5 mm/y. In other words, the model begins with an overthrusting rate that is equal to that of the

1.0 mm/y denudation rate model from the previous section and increases the overthrusting rate at various times to generate denudation rates equal to those of the 2.5 mm/y model. Thus, the only free parameter in this section is the time at which an instantaneous rate increase occurs: 13, 9 or 3 Ma. In this case, the timing of the rate increases corresponds approximately with the onset of thrusting on the MBT (∼13 Ma) (e.g., Meigs et al., 1995), the onset of underplating and duplex formation in the LHS (∼9 Ma) (e.g., DeCelles et al., 2001; Robinson et al., 2001) or the onset of thrusting on the MFT (∼3 Ma) (e.g., Hodges, 2000, and references therein). It should be noted that the acceleration in denudation at 3 Ma may also be related to climate change as suggested by Huntington et al. (2006). The model topography is held constant throughout the model run and the tectonic model with no out-of-sequence thrusting is used.

The peak age and age range trends are similar to those observed in the previous section, with increasingly young peak ages for earlier shifts to the 2.5 mm/y denudation rate. As observed in Whipp and Ehlers (2008), an earlier increase to a faster denudation rate shifts the age peak to be more similar to that of a constant fast rate. For instance, in the Darondi catchment, peak ages of ∼2.2 Ma and ∼2.1 Ma for an increase from 1.0 to 2.5 mm/y at 9 and 13 Ma, respectively, are similar to the 2.0 Ma peak age for the constant 2.5 mm/y model (Figure 4.5A,D). The peak age for an acceleration at 3 Ma, however, is unreset at ∼50 Ma. This trend is also observed in the Nar/Khansar catchment, where the peak ages from the accelerations at 9 and 13 Ma (∼13.6 and ∼10.4 Ma, respectively) are similar to the constant fast denudation rate model peak age (∼13 Ma), while the age PDFs for the acceleration at 3 Ma model show an unreset peak age (Figure 4.5C,F). Peak ages in the Nyadi catchment are all reset, with the accelerations at 9 and 13 Ma yielding peak ages of

∼8.0 and ∼6.1 Ma, similar to the constant 2.5 mm/y denudation rate model peak age of ∼5.3 Ma. In this case, the acceleration at 3 Ma model has a ∼14.0 Ma peak age that is quite similar to that of the constant 1.0 mm/y denudation rate model peak age (∼15.4 Ma). It is worth noting that the age ranges for the acceleration models have little utility. With the exception of the Nyadi catchment, the age PDFs all have some fraction of unreset grains within the model age distribution. The effect of this is larger age ranges for the models with earlier increases in denudation rate because the peak ages are younger in those models (e.g., Figure 4.5D,F). This behavior would make interpretations of changes in denudation rate difficult using the age range alone.

An acceleration in denudation rate at different times increases the goodness of fit of the predicted age PDFs to the data in some catchments, but no clear trend emerges for the best-fit time for an acceleration in all three catchments. In the Darondi basin, a constant denudation rate of 2.5 mm/y in the GHS provided a marginal fit to the observed PDF with only 1.6% of the predicted PDFs passing Kuiper's test (Figure 4.5A). That fit is improved by an acceleration from 1.0 to 2.5 mm/y at 13 Ma, with 14.3% of the model PDFs passing (Figure 4.5D). However, an acceleration at 9 or 3 Ma decreases the goodness of fit. Furthermore, although more predicted PDFs pass Kuiper's test with an acceleration at 13 Ma, the overall percentage that pass is still low. In the Nyadi catchment, the fit at a constant rate of 2.5 mm/y was good, with 97.1% passing Kuiper's test (Figure 4.5B). With an increase in denudation rate from 1.0 to 2.5 mm/y at any of the modeled times, the goodness of fit is effectively zero. Much like the Darondi, the Nar/Khansar catchment shows an improvement in fit for an increase in denudation rate from 1.0 to 2.5 mm/y. At best, 13.9% of the predicted PDFs pass Kuiper's test for the increase at 9 Ma. Again, however, the

overall fit to the data is poor.

4.5.3 Effects of bedrock landsliding

The focus of the previous results sections was on exploring the sensitivity of detrital MAr data to various faulting and denudation histories. In this section, the influence of surface processes on the distribution of detrital grain ages collected in river channels is discussed. The focus is on the role of bedrock landsliding as that is the dominant erosional mechanism within much of the glacier-free portion of the Himalaya (e.g., Shroder and Bishop, 1998; Shroder, 1998).

Landslides can provide non-uniform sediment contribution from within drainage basins and lead to detrital thermochronometer age distributions with grain-ages sourced from specific points within the catchment (e.g., Figure 4.6; Stock et al., 2006; Vermeesch, 2007). As opposed to the assumption in the model discussion thus far that the contribution of grain-ages is proportional to tectonic flux of material through the model surface, landslides may not sample the entire catchment area (Figure 4.6A). Thus, depending on the location and number of landslides over the sediment residence time in the channel, a given detrital sample PDF may cover a similar age range with a very different overall form (Figure 4.6B).

Landslide-scaled detrital MAr PDFs are generated by extracting grain-ages from basin age distributions that include landslide-derived sediment contributed over a given time period. An initial distribution of landslide areas is generated for a 10,000 y time period using the power-law frequency-area relationship of Hovius et al. (1997). To ensure an appropriate number of larger landslides, that relationship was extrapolated to allow for landslides of up to 38.5 km^2, where the maximum landslide area is based on the average minimum distance between ridges and valleys in the upper portions of the catchments. After the correct number of landslides have been gen-

erated for the given basin area, either one or ten years of landslides are randomly drawn from the power-law-scaled distribution. The landslides are randomly placed within the drainage basin of interest such that the entire landslide area falls within the basin boundary. The landslide depths scale with landslide width according to an empirical relationship such that the maximum landslide depth is equal to 5% of the landslide width (Hovius et al., 1997) and the landslides have a hemispheroidal form. Assuming that the predicted thermochronometer ages do not vary with depth, ages are extracted from the landslide regions and added to the basin raw age distribution. Then, as done for the non-landslide models, n grain ages are taken at random from the total age distribution, where n is the number of observed grain ages in the data for the basin of interest. From those n grains, a predicted age PDF is generated, the predicted and observed PDFs are compared using Kuiper's test and the process is repeated 10,000 times in a Monte Carlo model (e.g., Figure 3.2B of Whipp and Ehlers, 2008).

Age distributions from one year of landslides

In this section, the effect of bedrock landsliding on predicted MAr PDFs is considered by sampling accumulated basin sediment from one year of landslides. One year of landslides are randomly distributed within the three drainage basins and PDFs are generated for landslide sediment residence times of one and ten years. The tectonic model with no out-of-sequence thrusting and a maximum denudation rate in the GHS of 2.5 mm/y is used. The model topography does not change with time.

A shorter landslide sediment residence time and smaller basin size tend to generate predicted age PDFs that differ significantly from those without landslides. The Nyadi catchment is the smallest of the three catchments and predicted PDFs show a large impact of landsliding on the peak age of the one-year landslide sediment

residence time model, with a significant offset from the non-landslide model PDFs (Figure 4.7A,B). The two sets of PDFs sample a similar age range, but the peak age is ∼2 My older for the landslide model. In the ten-year residence time landslide model the PDFs are similar to those from the no-landslide model, with comparable peak ages and age ranges (Figure 4.7A,C). In the Darondi catchment, the range of predicted PDFs for a one-year residence time shows the effect of randomly placed landslides that occurred primarily at low-elevation. These low-elevation slides increase the young peak age probability, but do not shift the peak age (Figure 4.8A,B). However, because the sampled grain-ages come almost exclusively from the landslides, the age range observed in the PDFs is smaller than that generated without landsliding and there is a smaller older age peak. With a ten-year residence time, landslides sample a much larger portion of the catchment and the predicted age PDFs are similar to those generated without landslides (Figure 4.8A,C). The Nar/Khansar drainage basin is the largest of the three catchments and shows slightly less of an effect of landsliding than the Darondi catchment. The peak age of the one-year residence time landslide model is nearly identical to the no-landslide PDF age peak, and similar to the Darondi catchment, the age range in the landslide model is relatively small (Figure 4.9A,B). In the same trend as the other two catchments, the predicted age PDFs for the ten-year residence time landslide model are similar to the no-landslide model (Figure 4.9A,C).

Although some of the landslide models fit the observed MAr PDFs better than no-landslide models, the majority of the PDFs from one year of landsliding do not improve the fit to the data. In the Nyadi basin, where the no-landslide model has a good fit to the data, one year of landsliding with a one-year residence time yields no PDFs that pass Kuiper's test. With a ten-year residence time, the fit improves,

but is still only about half as good as the no-landslide model (Figure 4.7). In the Darondi catchment, only 1.6% of the predicted PDFs passed Kuiper's test for the model without landsliding. For this catchment, the overall fit to the data did not improve for the one year of sampled landslides, with 0.0% passing Kuiper's test for either residence time (Figure 4.8). None of the model-predicted PDFs from the no-landslide model passed Kuiper's test and one year of landsliding with a one-year sediment residence time does not improve this result. However, 5% of the predicted PDFs for the landslide model with a ten-year residence time pass Kuiper's test showing a slight improvement (Figure 4.9).

One hundred year landslide variability

The focus is now turned to annual samples from one of the catchments over a one hundred year period to provide a sense of the variability of the PDFs in landslide-dominated regions. This section is in contrast to the previous, where the grain-ages were randomly extracted to create PDFs from the same age distribution and compared to the data. In this case, the landslide age distribution generation process is repeated 100 times to look at the range of PDFs that would be expected from randomly sampling channel sediments for various sediment residence times. The same tectonic model, GHS denudation rate and fixed topography are used. One key difference is that the predicted PDF plots show only one PDF for each landslide age distribution (100 total; Figure 4.10B,C) in contrast to 100 predicted PDFs from the same age distributuion (e.g., Figures 4.7−4.9).

Predicted age PDFs in the Nyadi catchment show considerable variability in peak age, particularly with a short sediment residence time. Peak ages for random sampling of the no-landslide models have very little variation in peak age, with all of the peaks falling within one uniform zone. In contrast, the landslide model with a

one-year sediment residence time shows a broad swath of predicted age PDFs (Figure 4.10A,B). As expected, the age range covered by the landslide models is nearly identical to that of the no-landslide model, but the peak ages range over ∼3.3 My, with peak ages as old as ∼8.3 Ma. At the longer sediment residence time of ten years, the range of possible PDFs is smaller with a better defined central age peak (Figure 4.10C). The distribution of PDFs shows less definition than without landsliding, but the peak ages span a narrow range and are <0.5 My different between the two.

The range of predicted age PDFs for both landslide models do not fit the data as well as those predicted without landsliding, but the fit does improve with increased residence time. In the Nyadi catchment, the previous section showed 0.0% of the age PDFs predicted from the landslide model with a one-year residence time passed Kuiper's test (Figure 4.7B). In this case, 1.9% of the predicted PDFs pass (Figure 4.10B), indicating that although the vast majority of predicted PDFs are statistically different than the data, there is potential for similar PDFs to be generated with the shorter residence time. In other words, there is much variability in the predicted PDFs with this landslide model, but there are some PDFs generated with landslides that are indistinguishable from the data. It is relatively simple to see why so few predicted PDFs pass Kuiper's test with such a large peak age range (∼3.3 My) for a fairly young range of age peaks (∼5.0−8.3 Ma). With a longer landslide sediment residence time of ten years, both the range of peak ages and the overall data fit improve. For this model, 24.1% of the predicted age PDFs pass Kuiper's test and the peak ages predominantly match the data peak.

4.6 Discussion

4.6.1 Implications for detrital dataset interpretation

Even though the model fits to the data generally do not improve with the use of the landslide model, these preliminary model results are important in that they show the potential for landslides to generate very different PDFs depending on the location of the slides and the sediment residence time (e.g., Figures 4.7A,B, 4.10A-C). This result implies that there is potential for detrital datasets collected in regions where landsliding is the dominant erosion process to be affected by non-uniform sampling of the upstream drainage. Thus, data interpretations that assume steady-state denudation of the catchment may be invalid in those areas. This leads to three potential concerns for studies in areas with bedrock landslides: (1) There is potential for techniques that use the PDF age range and catchment relief to calculate paleo-erosion rates in the catchment (e.g., Brewer et al., 2003; Ruhl and Hodges, 2005; Huntington and Hodges, 2006; Stock et al., 2006; Vermeesch, 2007) to overestimate the true catchment denudation rate. This overestimate is possible because sampled sediment would be expected to be sourced from the entire basin elevation range, but may have been contributed from a much smaller elevation range. The narrow elevation range would provide a smaller age range in the sample, such as was observed in some of the landslide models with residence times of one year (e.g., Figures 4.8B,4.9B). (2) There may be problems with detrital data interpretation using numerical models because of variations in the dataset peak ages. For example, in areas with short sediment residence times and a large thermochronometer age range within the catchment detritus, a landslide at high elevation could shift the detrital age distribution toward old ages. The resulting denudation rate calculation could be biased towards underestimating the true catchment denudation rate. (3) The narrow age range from a high-elevation

landslide could lead to the interpretation that a large denudation rate deceleration occurred following cooling of this sample.

4.6.2 Future directions

The tectonic model scenarios without landsliding showed that no single model variant provided a good fit to all three of the drainage basins. It might be expected that if the input kinematic model and various other model setup assumptions are correct then there is potential for a small range of model input parameters to provide a good fit to the data for all three catchments. There are several potential reasons for the observed misfit between the predicted age PDFs and the data. First, we explored a fairly small range of tectonic model free parameters to understand the effects of various faulting histories on detrital thermochronometer data. It is possible that some of the fault dip angles, activation times and slip rates may have been significantly different than what were used. Future work is needed to address the uncertainties in fault dip angles at depth, as well as explore a larger range of fault convergence velocities and timing of rate changes.

Future studies using detrital thermochronometer data collected from modern river channels should utilize available data on landslide sediment residence time from the field area. A key factor in addressing the potential impact of landslides on detrital grain-age PDFs is the amount of time that landslide-derived sediment is available to be sampled in the channel. As shown, residence times as short as ten years provide reasonable security that basin sediments are not being heavily biased by bedrock landsliding. As many field regions may have basins with residence times in excess of ten years, our preliminary findings may not affect data interpreted from those areas. However, small, steep tributary catchments may have significantly shorter residence times and landsliding may impact the interpretation of data from those

basins. When available, bedrock samples from nearby basins may be of use to ensure the entire age range is covered by the detrital samples. Furthermore, in basins with variable bedrock crystallization age or lithology, analysis of mineral provenance could reveal possible biases in sampled sediment (e.g., Amidon et al., 2005; Brewer et al., 2006).

4.7 Conclusions

This study utilized a thermokinematic and age prediction numerical model of the Nepalese Himalaya to explore the effects of the major tectonic and erosional factors in active convergent orogens: Thrust faulting and bedrock landsliding. Model predicted MAr age PDFs were compared to data in three catchments in the Marsyandi River drainage basin, leading to the following preliminary, conclusions:

1. Comparison of model-predicted MAr PDFs from models with and without re-activation of the MCT show a better fit to detrital MAr data without out-of-sequence activity on the MCT. In addition, MAr data from the GHS are best fit with a model with a constant convergence and overthrusting rate. However, additional tectonic model parameters need to be explored to further support this result.

2. None of the models in Section 4.5 were able to fit the data from all three catchments. It is possible that bedrock landsliding may bias the data to which the model results are compared and could explain the inability of the model to fit the data.

3. Bedrock landsliding in regions with short ($\sim$1 y) sediment residence times can lead to undersampling of catchment age ranges (e.g., Vermeesch, 2007). Undersampling can lead to smaller age ranges and overestimation of true catchment

denudation rates.

4. Sampling of preserved basin sediments may help offer a better-mixed sample incorporating grains over a longer time range. As shown, an increased sediment residence time provides a better representation of the grain-age variations within the basin.

5. When possible, detrital sample collection in areas with previous bedrock samples (e.g., Ruhl and Hodges, 2005; Huntington and Hodges, 2006; Stock et al., 2006; Vermeesch, 2007) offers potential for identifying detrital datasets that have not been affected by bedrock landslides.

4.8 Acknowledgements

We are most grateful to J. Braun for providing the source code for Pecube and to C. Spath for his assistance in modifying the code. This manuscript benefited from thoughtful discussions with J. Barnes, M. Densmore, K. Hodges, K. Huntington, F. Herman and P. van der Beek. This work was supported by NSF grant EAR-0724656 to T. Ehlers.

Table 4.1: Numerical Model Parameters

Property/Parameter	Model Input Value
Material Properties	
GHS heat production	1.9 μW/m^3
TH heat production	0.5 μW/m^3
IS/SH/LHS heat production	0.8 μW/m^3
Heat production e-folding depth	$-$10 km
Thermal conductivity	2.75 W/m K
Specific heat	1000 J/kg K
Density	2700 kg/m^3
Numerical Parameters	
Thrust model convergence rate	0.6$-$7.3 mm/y
Horizontal node spacing	$\sim$0.95 km
Vertical node spacing (0$-$5 km)	$\sim$0.95 km
Vertical node spacing (5$-$15 km)	$\sim$2.85 km
Vertical node spacing (15$-$130 km)	$\sim$8.55 km
Surface temperature at sea level	24°C
Atmospheric lapse rate	$-$6°C/km
Basal temperature	1350°
Model domain	150 $\times$ 310 $\times$ 130 km

GHS=Greater Himalayan Sequence, TH=Tethyan Himalaya, IS=Indian Shield, SH=Sub-Himalaya, LHS=Lesser Himalayan Sequence

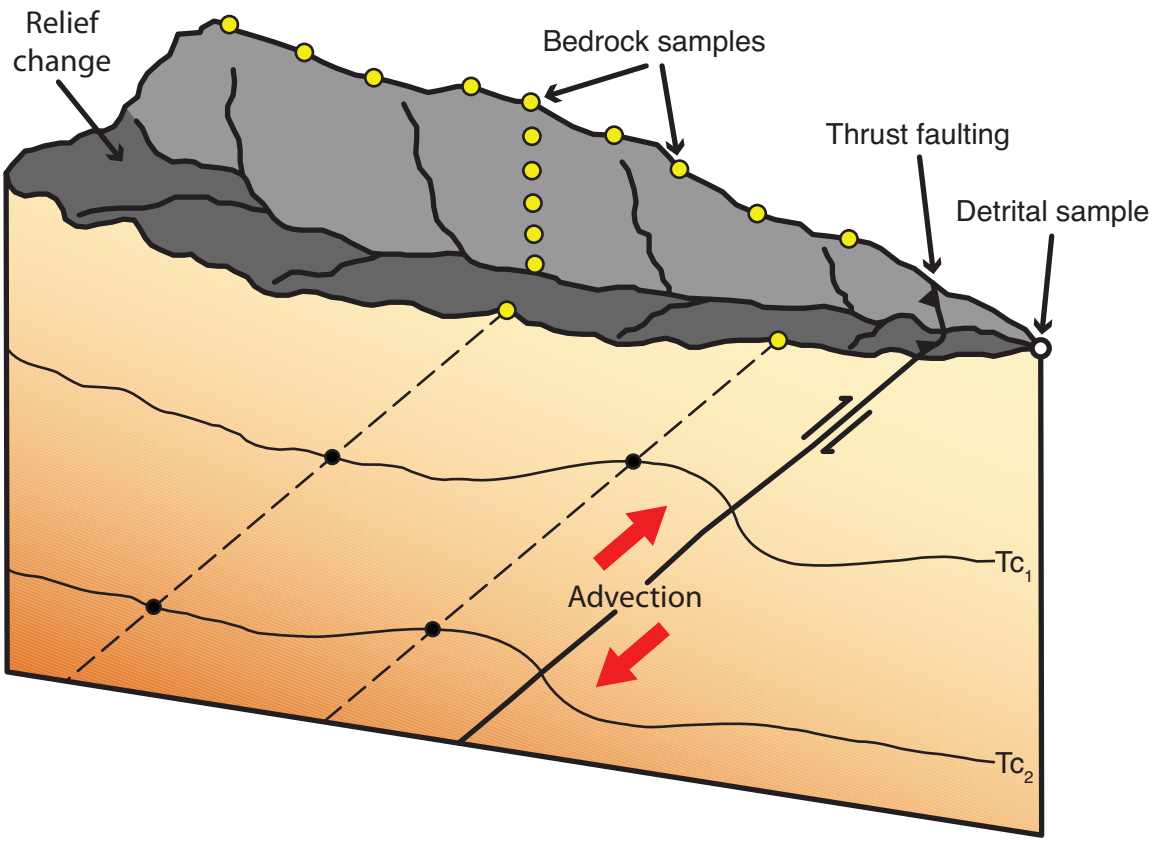

Figure 4.1: 3-D schematic model of the crust beneath a drainage basin. Bedrock (yellow circles) and detrital (white circle) thermochronometer data can be used to constrain the exhumation history of the basin. As thermochronometers follow an exhumation pathway (dashed line) they are sensitive to the thermal effects of numerous tectonic and surface processes, including thrust faulting and topographic relief change, which affect the position of their effective closure temperature isotherms (thin black lines).

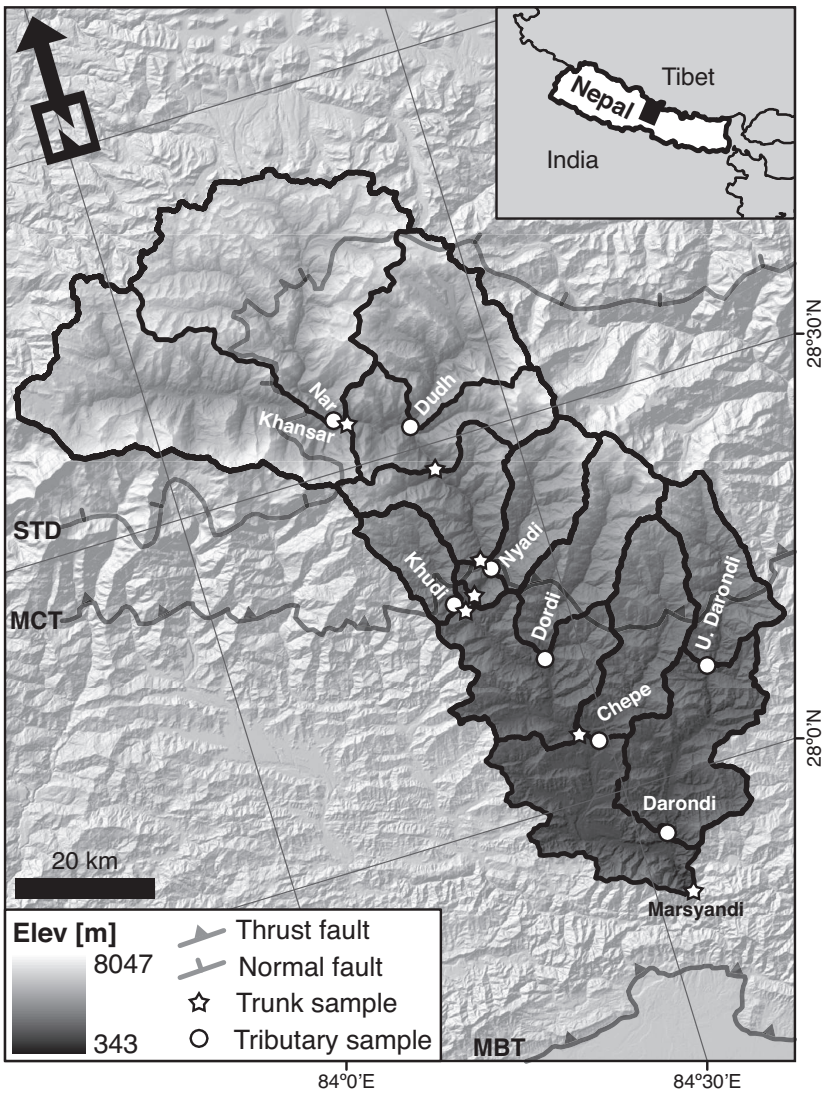

Figure 4.2: Summary map of detrital thermochronometer data in the Marsyandi River drainage basin. Tributary (white circle) and trunk stream (white star) MAr detrital thermochronometer sample locations from Brewer et al. (2006) and Ruhl and Hodges (2005) with mapped fault locations from Searle and Godin (2003) and Bollinger et al. (2004). Black rectangle in inset map shows detailed map area. Abbreviations as follows: MCT=Main Central Thrust, STD=South Tibetan Detachment, AHe=Apatite (U-Th)/He, AFT=Apatite fission-track, ZFT=Zircon fission-track, MAr=Muscovite $^{40}Ar/^{39}Ar$.

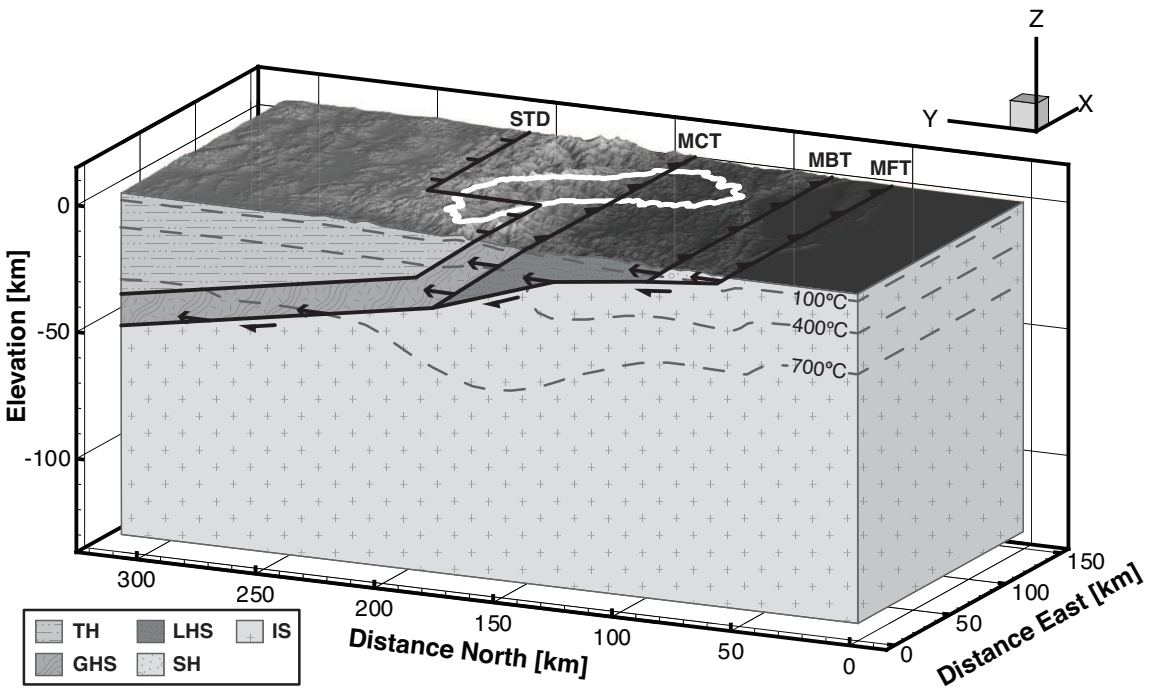

Figure 4.3: 3-D tectonic model block. When active, faults (thick lines) are advected laterally with time, moving material in the hanging wall up vertically. Rock advection warps the subsurface isotherms (dashed lines) that affect predicted thermochronometer ages in the Marsyandi River catchment (bounded in white). In addition to tectonic motion, the predicted ages are sensitive to rock thermophysical physical properties that vary with lithostratigraphic unit. Abbreviations as in Figure 2 and as follows: MFT=Main Frontal Thrust, MBT=Main Boundary Thrust, IS=Indian Shield, SH=Sub Himalaya, LHS=Lesser Himalayan Sequence, GHS=Greater Himalayan Sequence, TH=Tethyan Himalaya.

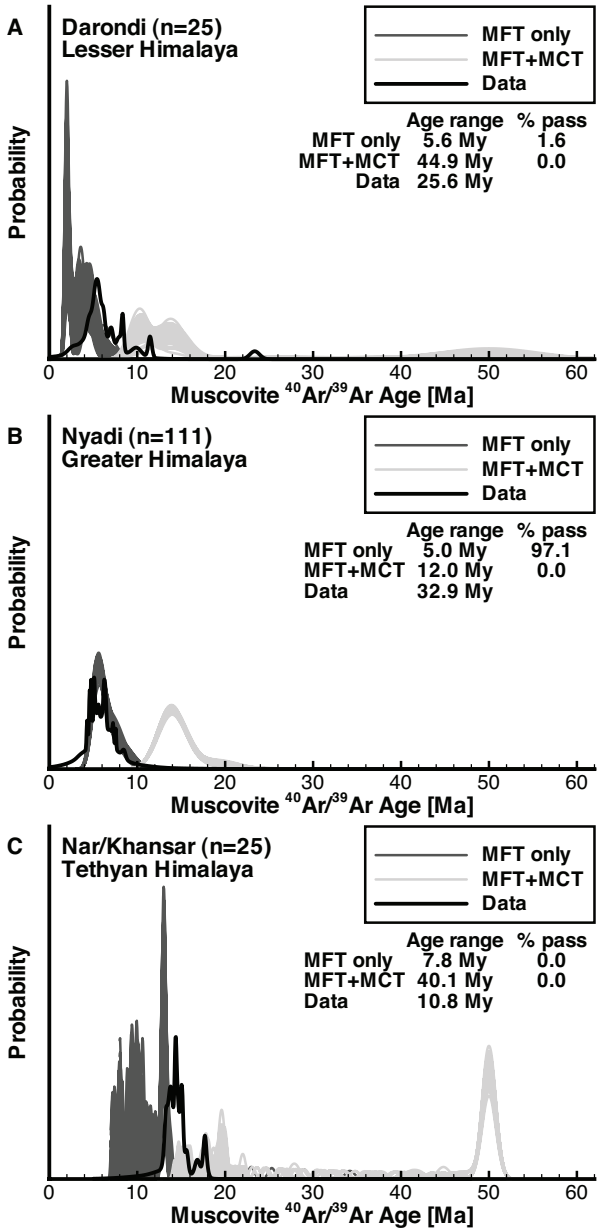

Figure 4.4: Observed and predicted MAr ages from tectonic models with and without out-of-sequence motion on the MCT. 100 predicted MAr PDFs from a Monte Carlo model are shown for models where the MFT is the only active fault from 3−0 Ma (dark gray) or the MFT and MCT are active over that time period (light gray). Predicted ages are shown with data from three catchments, draining primarily (A) the Lesser Himalaya (Darondi), (B) the Greater Himalaya (Nyadi) and (C) the Tethyan Himalaya (Nar/Khansar). n is the number of dated samples contributing to the age PDFs, the age range is the range of ages covered by 99% of the area under the PDFs and % pass is the percentage of predicted age PDFs that pass Kuiper's goodness-of-fit test. Abbreviations as in Figures 2 and 3.

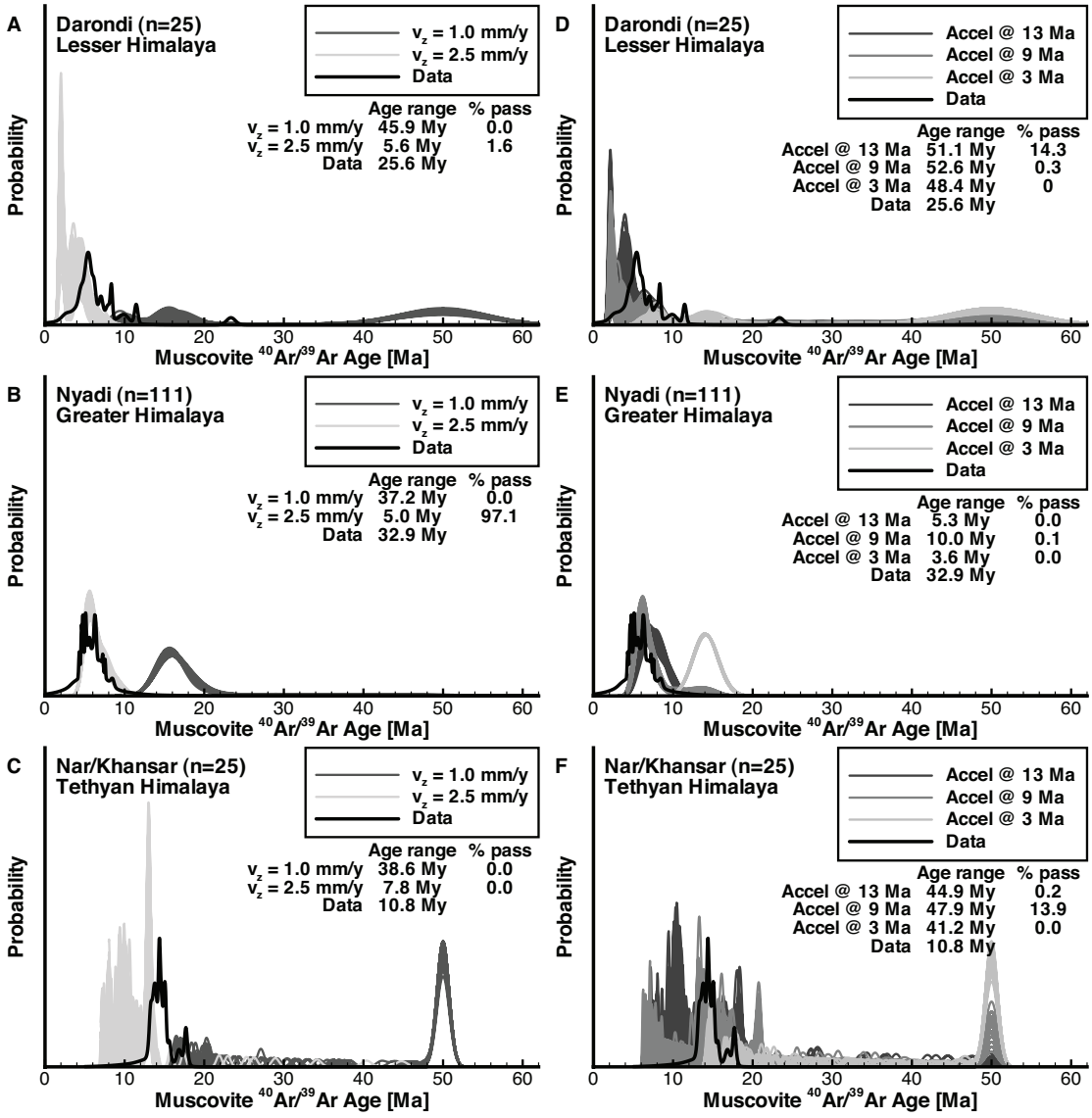

Figure 4.5: Observed and predicted MAr ages from models with overthrusting rates that produce variable maximum GHS denudation rates. 100 predicted MAr PDFs from a Monte Carlo model are shown for models where the maximum GHS denudation rate from 3−0 Ma ranges between 1.0−2.5 mm/y. (A-C) Time-invariant overthrusting rate models with maximum GHS denudation rates of either 1.0 mm/y (dark gray) or 2.5 mm/y (light gray). (D-F) Models where the overthrusting rate accelerates from producing a denudation rate of 1.0 mm/y to 2.5 mm/y at 13 Ma (dark gray), 9 Ma (medium gray) or 3 Ma (light gray). Predicted ages are shown with data from three catchments, draining primarily (A,D) the Lesser Himalaya (Darondi), (B,E) the Greater Himalaya (Nyadi) and (C,F) the Tethyan Himalaya (Nar/Khansar). The kinematic model with no out-of-sequence thrusting is used. n is the number of dated samples contributing to the age PDFs, the age range is the range of ages covered by 99% of the area under the PDFs and % pass is the percentage of predicted age PDFs that pass Kuiper's goodness-of-fit test. Abbreviations as in Figures 2 and 3.

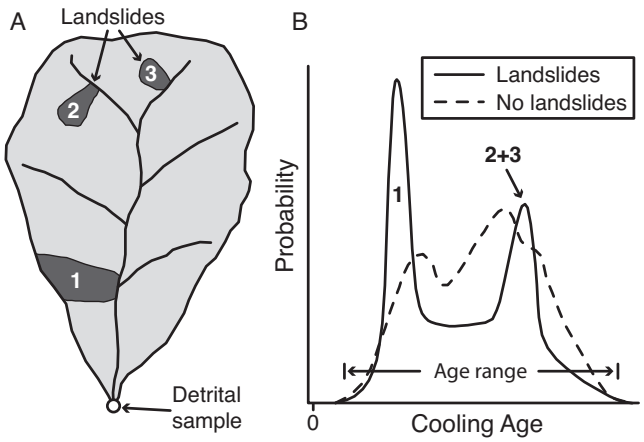

Figure 4.6: Schematic drainage basin showing the effect of bedrock landslides on detrital age PDFs. (A) Drainage basin with several bedrock landslides and a detrital thermochronometer sample location downstream of the slides. (B) Thermochronometer age PDFs for the basin with (solid line) and without (dashed line) bedrock landslides. Slide 1 occurs at low elevation and produces and abundance of young detrital ages while slides 2 and 3 occur at high elevation in the catchment producing an older age peak. Both PDFs have similar age ranges, defined as the range beneath 99% of the area under the PDF curves.

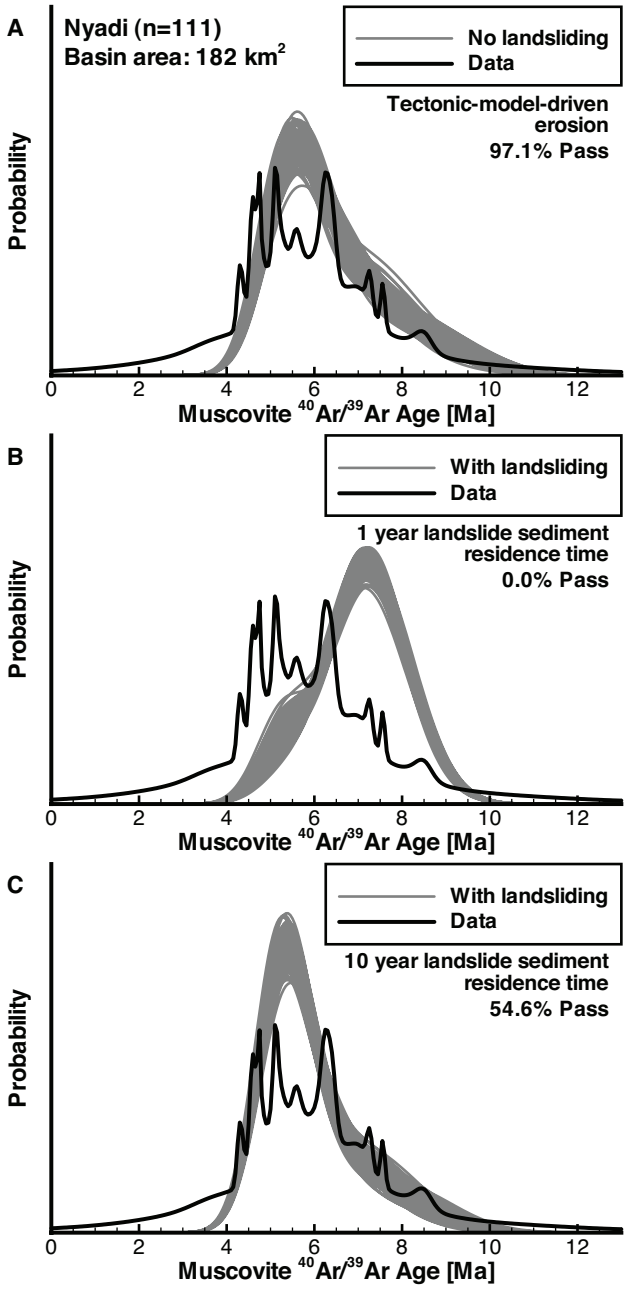

Figure 4.7: Observed and predicted MAr ages in the Nyadi catchment from models with and without landsliding. 100 predicted MAr PDFs from a Monte Carlo model are shown for models with (A) no landsliding, (B) one year of landslides with a one year landslide sediment residence time, and (C) one year of landslides with a ten-year residence time. Predicted ages are shown with data from the Nyadi catchment. The kinematic model with no out-of-sequence thrusting and a GHS denudation rate of 2.5 mm/y is used. n is the number of dated samples contributing to the age PDFs and % pass is the percentage of predicted age PDFs that pass Kuiper's goodness-of-fit test.

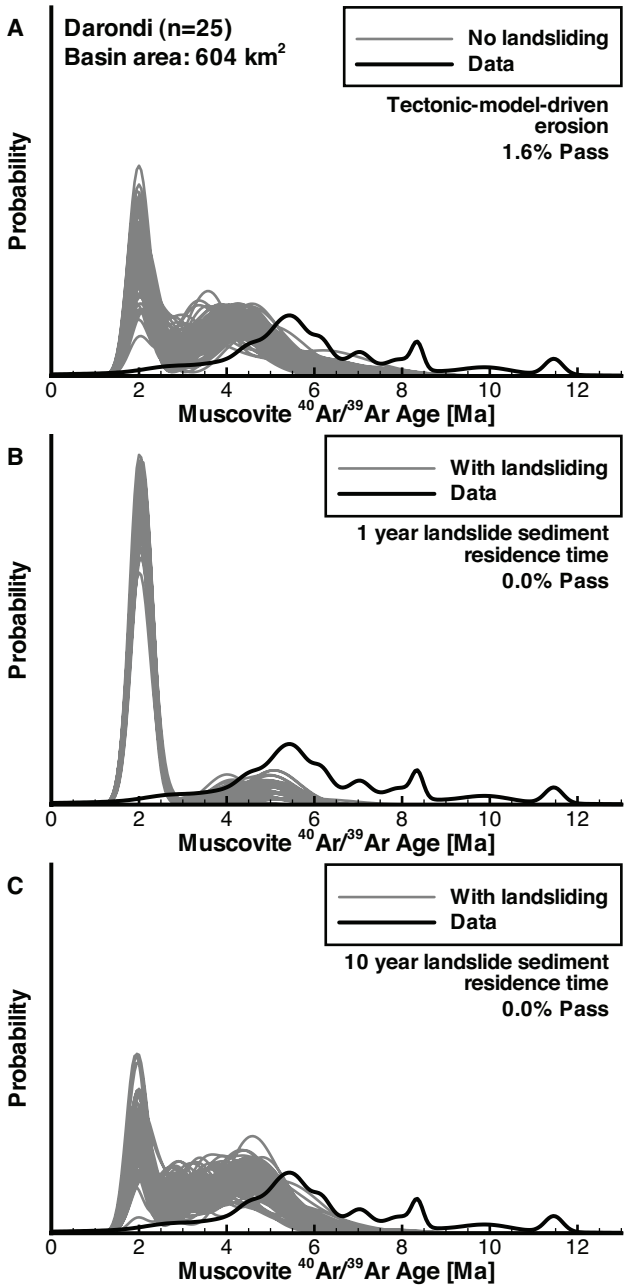

Figure 4.8: Observed and predicted MAr ages in the Darondi catchment from models with and without landsliding. 100 predicted MAr PDFs from a Monte Carlo model are shown for models with (A) no landsliding, (B) one year of landslides with a one-year landslide sediment residence time, and (C) one year of landslides with a ten-year residence time. Predicted ages are shown with data from the Darondi catchment. The kinematic model with no out-of-sequence thrusting and a GHS denudation rate of 2.5 mm/y is used. n is the number of dated samples contributing to the age PDFs and % pass is the percentage of predicted age PDFs that pass Kuiper's goodness-of-fit test.

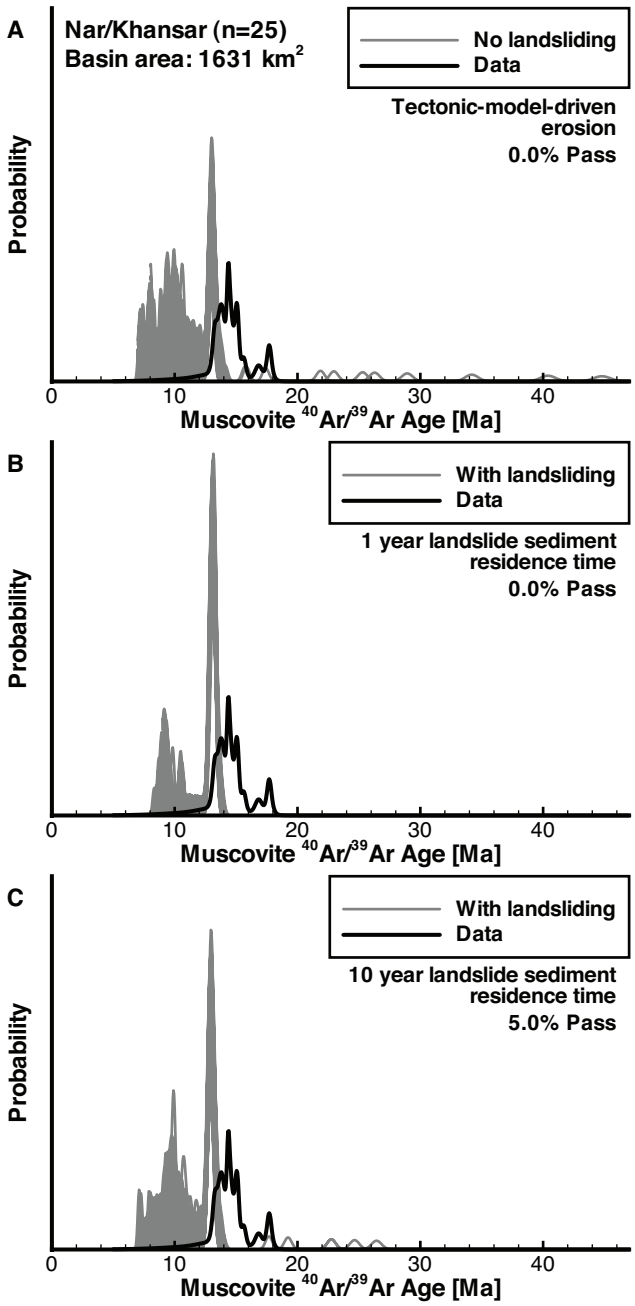

Figure 4.9: Observed and predicted MAr ages in the Nar/Khansar catchment from models with and without landsliding. 100 predicted MAr PDFs from a Monte Carlo model are shown for models with (A) no landsliding, (B) one year of landslides with a one-year landslide sediment residence time, and (C) one year of landslides with a ten-year residence time. Predicted ages are shown with data from the Nar/Khansar catchment. The kinematic model with no out-of-sequence thrusting and a GHS denudation rate of 2.5 mm/y is used. n is the number of dated samples contributing to the age PDFs and % pass is the percentage of predicted age PDFs that pass Kuiper's goodness-of-fit test.

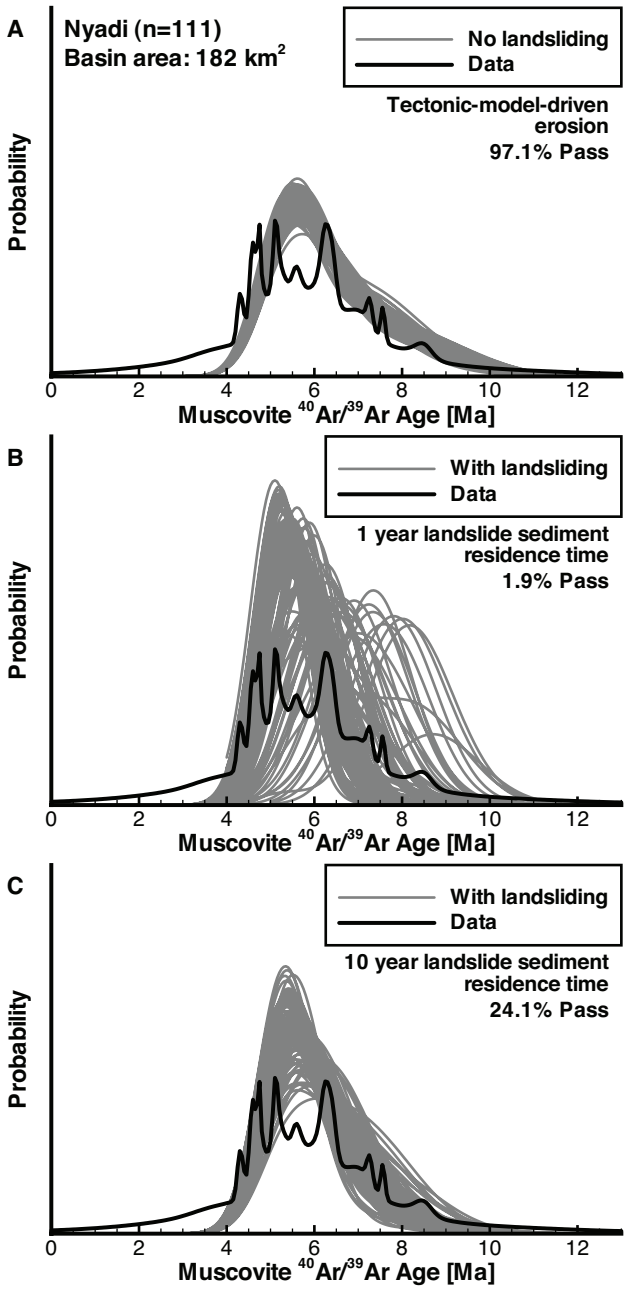

Figure 4.10: Observed and predicted MAr ages in the Nyadi catchment from models with and without landsliding over 100 years. 100 predicted MAr PDFs from a Monte Carlo model are shown for models with (A) no landsliding, (B) one hundred years of landslides with a one-year landslide sediment residence time, and (C) one hundred years of landslides with a ten-year residence time. Predicted ages are shown with data from the Nyadi catchment. The kinematic model with no out-of-sequence thrusting and a GHS denudation rate of 2.5 mm/y is used. n is the number of dated samples contributing to the age PDFs and % pass is the percentage of predicted age PDFs that pass Kuiper's goodness-of-fit test.

Bibliography

Amidon, W. H., Burbank, D. W. and Gehrels, G. E. Construction of detrital mineral populations: insights from mixing of U-Pb zircon ages in Himalayan rivers. *Basin Research*, 17(4):463–485, 2005.

Beaumont, C., Jamieson, R. A., Nguyen, M. H. and Lee, B. Himalayan tectonics explained by extrusion of a low-viscosity crustal channel coupled to focused surface denudation. *Nature*, 414(6865):738–742, 2001.

Bernet, M., van der Beek, P., Pik, R., Huyghe, P., Mugnier, J.-L., Labrin, E. and Szulc, A. Miocene to Recent exhumation of the central Himalaya determined from combined detrital zircon fission-track and U/Pb analysis of Siwalik sediments, western Nepal. *Basin Research*, 18(4):393–412, 2006. doi:10.1111/j.1365-2117.2006.00303.x.

Bettinelli, P., Avouac, J.-P., Flouzat, M., Jouanne, F., Bollinger, L., Willis, P. and Chitrakar, G. Plate Motion of India and Interseismic Strain in the Nepal Himalaya from GPS and DORIS Measurements. *Journal of Geodesy*, 80(8):567–589, 2006. doi:10.1007/s00190-006-0030-3.

Bilham, R., Larson, K. M., Freymueller, J. T., Jouanne, F., Le Fort, P., Leturmy, P., Mugnier, J. L., Gamond, J. F., Glot, J. P., Martinod, J., Chaudury, N. L., Chitrakar, G. R., Gautam, U. P., Koirala, B. P., Pandey, M. R., Ranabhat, R., Sapkota, S. N., Shrestha, P. L., Thakuri, M. C., Timilsina, U. R., Tiwari, D. R., Vidal, G., Vigny, C., Galy, A. and de Voogd, B. GPS measurements of present-day convergence across the Nepal Himalaya. *Nature*, 386(6620):61–64, 1997.

Blythe, A. E., Burbank, D. W., Carter, A., Schmidt, K. and Putkonen, J. Plio-

Quaternary exhumation history of the central Nepalese Himalaya: 1. Apatite and zircon fission-track and apatite [U-Th]/He analyses. *Tectonics*, 26, 2007. doi: 10.1029/2006TC001990.

Bollinger, L., Avouac, J., Beyssac, O., Catlos, E., Harrison, T., Grove, M., Goffé, B. and Sapkota, S. Thermal structure and exhumation history of the Lesser Himalaya in central Nepal. *Tectonics*, 23(5), 2004.

Braun, J. Pecube; a new finite-element code to solve the 3D heat transport equation including the effects of a time-varying, finite amplitude surface topography. *Computers & Geosciences*, 29(6):787–794, 2003.

Brewer, I. and Burbank, D. W. Thermal and kinematic modeling of bedrock and detrital cooling ages in the central Himalaya. *J. Geophys. Res.*, 111(B9):B09409, 2006.

Brewer, I. D., Burbank, D. W. and Hodges, K. V. Modelling detrital cooling-age populations; insights from two Himalayan catchments. *Basin Research*, 15(3):305–320, 2003.

Brewer, I. D., Burbank, D. W. and Hodges, K. V. Downstream development of a detrital cooling-age signal; insights from $^{40}Ar/^{39}Ar$ muscovite thermochronology in the Nepalese Himalaya. In Willett, S. D., Hovius, N., Brandon, M. T. and Fisher, D. M., editors, *Tectonics, Climate and Landscape Evolution*, volume 398 of *Penrose Conference Series*, pages 321–338. Geological Society of America, 2006.

Brown, L. D., Zhao, W., Nelson, K. D., Hauck, M., Alsdorf, D., Ross, A., Cogan, M., Clark, M., Liu, X. and Che, J. Bright spots, structure, and magmatism in southern Tibet from INDEPTH seismic reflection profiling. *Science*, 274(5293):1688–1690, 1996.

Brunel, M. Ductile thrusting in the Himalayas; shear sense criteria and stretching lineations. *Tectonics*, 5(2):247–265, 1986.

Burchfiel, B. C. and Royden, L. H. North-south extension within the convergent Himalayan region. *Geology*, 13(10):679–682, 1985.

Carrapa, B., Strecker, M. R. and Sobel, E. R. Cenozoic orogenic growth in the Central Andes: Evidence from sedimentary rock provenance and apatite fission track thermochronology in the FiambalBasin, southernmost Puna Plateau margin (NW Argentina). *Earth and Planetary Science Letters*, 247(1-2):82–100, 2006.

Catlos, E. J., Harrison, T. M., Kohn, M. J., Grove, M., Ryerson, F. J., Manning, C. E. and Upreti, B. N. Geochronologic and thermobarometric constraints on the evolution of the Main Central Thrust, central Nepal Himalaya. *Journal of Geophysical Research, B, Solid Earth and Planets*, 106(8):16,177–16,204, 2001.

DeCelles, P. G., Robinson, D. M., Quade, J., Ojha, T. P., Garzione, C. N., Copeland, P. and Upreti, B. N. Stratigraphy, structure, and tectonic evolution of the Himalayan fold-thrust belt in western Nepal. *Tectonics*, 20(4):487–509, 2001.

Farr, T. G., Rosen, P. A., Caro, E., Crippen, R., Duren, R., Hensley, S., Kobrick, M., Paller, M., Rodriguez, E., Roth, L., Seal, D., Shaffer, S., Shimada, J., Umland, J., Werner, M., Oskin, M., Burbank, D. and Alsdorf, D. The shuttle radar topography mission. *Reviews of Geophysics*, 45(2), 2007. ISSN 8755-1209. doi: 10.1029/2005RG000183.

Gansser, A. *Geology of the Himalayas*. Wiley Interscience, London, 1964.

Grujic, D., Casey, M., Davidson, C., Hollister, L. S., Kuendig, R., Pavlis, T. L. and

Schmid, S. M. Ductile extrusion of the Higher Himalayan Crystalline in Bhutan; evidence from quartz microfabrics. *Tectonophysics*, 260(1-3):21–43, 1996.

Hansen, F. D. and Carter, N. L. Creep of selected crustal rocks at 1000 MPa. *Eos, Transactions, American Geophysical Union*, 63(18):437, 1982.

Harris, N. Channel flow and the Himalayan-Tibetan orogen: a critical review. *Journal of the Geological Society, London*, 164(3):511–523, 2007.

Harrison, T. M., Ryerson, F. J., Le Fort, P., Yin, A., Lovera, O. M. and Catlos, E. J. A late Miocene-Pliocene origin for the central Himalayan inverted metamorphism. *Earth and Planetary Science Letters*, 146(1-2):E1–E7, 1997.

Herman, F., Braun, J. and Dunlap, W. J. Tectonomorphic scenarios in the Southern Alps of New Zealand. *Journal of Geophysical Research*, 112:no. B4, 25, 2007.

Hodges, K. V. Tectonics of the Himalaya and southern Tibet from two perspectives. *Geological Society of America Bulletin*, 112(3):324–350, 2000.

Hodges, K. V., Hurtado, J. M. and Whipple, K. X. Southward extrusion of Tibetan crust and its effect on Himalayan tectonics. *Tectonics*, 20(6):799–809, 2001.

Hodges, K. V., Parrish, R. R. and Searle, M. P. Tectonic evolution of the central Annapurna Range, Nepalese Himalayas. *Tectonics*, 15(6):1264–1291, 1996.

Hodges, K. V., Wobus, C. W., Ruhl, K., Schildgen, T. and Whipple, K. X. Quaternary deformation, river steepening, and heavy precipitation at the front of the Higher Himalayan ranges. *Earth and Planetary Science Letters*, 220:379–389, 2004.

Hovius, N., Stark, C. P. and Allen, P. A. Sediment flux from a mountain belt derived by landslide mapping. *Geology*, 25(3):231–234, 1997.

Huntington, K. W., Blythe, A. E. and Hodges, K. V. Climate change and Late Pliocene acceleration of erosion in the Himalaya. *Earth and Planetary Science Letters*, 252(1-2):107–118, 2006.

Huntington, K. W. and Hodges, K. V. A comparative study of detrital mineral and bedrock age-elevation methods of estimating erosion rates. *Journal of Geophysical Research, F, Earth Surface*, 111(F03011):doi:10.1029/2005JF000454, 2006.

Jessup, M. J., Law, R. D., Searle, M. P. and Hubbard, M. S. Structural evolution and vorticity of flow during extrusion and exhumation of the Greater Himalayan Slab, Mount Everest Massif, Tibet/Nepal: implications for orogen-scale flow partitioning. *Geological Society, London, Special Publications*, 268(1):379–413, 2006.

Jouanne, F., Mugnier, J. L., Gamond, J. F., Le Fort, P., Pandey, M. R., Bollinger, L., Flouzat, M. and Avouac, J. P. Current shortening across the Himalayas of Nepal. *Geophysical Journal International*, 157(1):1–14, 2004.

Larson, K. M., Buergmann, R., Bilham, R. and Freymueller, J. T. Kinematics of the India-Eurasia collision zone from GPS measurements. *Journal of Geophysical Research, B, Solid Earth and Planets*, 104(1):1077–1093, 1999.

Lavé, J. and Avouac, J. P. Active folding of fluvial terraces across the Siwaliks Hills, Himalayas of central Nepal. *Journal of Geophysical Research, B, Solid Earth and Planets*, 105(3):5735–5770, 2000.

Le Fort, P. Himalayas; the collided range; present knowledge of the continental arc. *American Journal of Science*, Vol. 275-A, Tectonics and mountain ranges:1–44, 1975.

Macfarlane, A. M., Hodges, K. V. and Lux, D. A structural analysis of the Main

Central Thrust zone, Langtang National Park, central Nepal Himalaya. *Geological Society of America Bulletin*, 104(11):1389–1402, 1992.

Meigs, A. J., Burbank, D. W. and Beck, R. A. Middle-late Miocene (¿10 Ma) formation of the Main Boundary Thrust in the western Himalaya. *Geology*, 23(5):423–426, 1995.

Pandey, M. R., Tandukar, R. P., Avouac, J. P., Lave, J. and Massot, J. P. Interseismic strain accumulation on the Himalayan crustal ramp (Nepal). *Geophysical Research Letters*, 22(7):751–754, 1995.

Pearson, O. N. and DeCelles, P. G. Structural geology and regional tectonic significance of the Ramgarh Thrust, Himalayan fold-thrust belt of Nepal. *Tectonics*, 24:no.4, 26, 2005.

Press, W. H., Teukolsky, S. A., Vetterling, W. T. and Flannery, B. P. *Numerical Recipes in C: The Art of Scientific Computing*. Cambridge University Press, 2 edition, 1992.

Reiners, P. W. Thermochronologic Approaches to Paleotopography. *Reviews in Mineralogy and Geochemistry*, 66(1):243–267, 2007.

Robinson, D. M., DeCelles, P. G., Garzione, C. N., Pearson, O. N., Harrison, T. M. and Catlos, E. J. Kinematic model for the Main Central Thrust in Nepal. *Geology*, 31(4):359–362, 2003.

Robinson, D. M., DeCelles, P. G., Patchett, P. J. and Garzione, C. N. The kinematic evolution of the Nepalese Himalaya interpreted from Nd isotopes. *Earth and Planetary Science Letters*, 192(4):507–521, 2001.

Roy, S. and Rao, R. U. M. Heat flow in the Indian Shield. *Journal of Geophysical Research, B, Solid Earth and Planets*, 105(11):25,587–25,604, 2000.

Ruhl, K. W. and Hodges, K. V. The use of detrital mineral cooling ages to evaluate steady state assumptions in active orogens; an example from the central Nepalese Himalaya. *Tectonics*, 24:no.4, 14, 2005.

Schelling, D. and Arita, K. Thrust tectonics, crustal shortening, and the structure of the far-eastern Nepal Himalaya. *Tectonics*, 10(5):851–862, 1991.

Searle, M. P. and Godin, L. The South Tibetan detachment and the Manaslu Leucogranite; a structural reinterpretation and restoration of the Annapurna-Manaslu Himalaya, Nepal. *Journal of Geology*, 111(5):505–523, 2003.

Searle, M. P., Law, R. D. and Jessup, M. J. Crustal structure, restoration and evolution of the Greater Himalaya in Nepal-South Tibet: implications for channel flow and ductile extrusion of the middle crust. *Geological Society, London, Special Publications*, 268(1):355–378, 2006.

Searle, Michael P., R. A. J. Thermal model for the Zanskar Himalaya. *Journal of Metamorphic Geology*, 7(1):127–134, 1989.

Seeber, L. and Gornitz, V. River profiles along the Himalayan Arc as indicators of active tectonics. *Tectonophysics*, 92(4):335–367, 1983.

Shroder, J. F. Slope failure and denudation in the western Himalaya. *Geomorphology*, 26(1-3):81–105, 1998.

Shroder, J. F. and Bishop, M. P. Mass movement in the Himalaya: new insights and research directions. *Geomorphology*, 26(1-3):13–35, 1998.

Sobel, E. R., Chen, J. and Heermance, R. V. Late Oligocene-Early Miocene initiation of shortening in the Southwestern Chinese Tian Shan: Implications for Neogene shortening rate variations. *Earth and Planetary Science Letters*, 247(1-2):70–81, 2006.

Stock, G. M., Ehlers, T. A. and Farley, K. A. Where does sediment come from? Quantifying catchment erosion with detrital apatite (U-Th)/He thermochronometry. *Geology*, 34(9):725–728, 2006.

Stock, J. D. and Montgomery, D. R. Estimating palaeorelief from detrital mineral age ranges. *Basin Research*, 8(3):317–327, 1996. doi:10.1046/j.1365-2117.1996.00177.x.

Suppe, J. Geometry and kinematics of fault-bend folding. *American Journal of Science*, 283(7):684–721, 1983.

Szulc, A. G., Najman, Y., Sinclair, H. D., Pringle, M., Bickle, M., Chapman, H., Garzanti, E., Ando, S., Huyghe, P., Mugnier, J.-L., Ojha, T. and DeCelles, P. Tectonic evolution of the Himalaya constrained by detrital ^{40}Ar-^{39}Ar, Sm-Nd and petrographic data from the Siwalik foreland basin succession, SW Nepal. *Basin Research*, 18(4):375–391, 2006. doi:10.1111/j.1365-2117.2006.00307.x.

Valdiya, K. S. The two intracrustal boundary thrusts of the Himalaya. *Tectonophysics*, 66(4):323–348, 1980.

van der Beek, P., Robert, X., Mugnier, J.-L., Bernet, M., Huyghe, P. and Labrin, E. Late Miocene - Recent exhumation of the central Himalaya and recycling in the foreland basin assessed by apatite fission-track thermochronology of Siwalik sediments, Nepal. *Basin Research*, 18(4):413–434, 2006. doi:10.1111/j.1365-2117.2006.00305.x.

Vermeesch, P. Quantitative geomorphology of the White Mountains (California) using detrital apatite fission track thermochronology. *Journal of Geophysical Research, F, Earth Surface*, 112(F3):F03004, 2007. doi:10.1029/2006JF000671.

Whipp, Jr., D. M. and Ehlers, T. A. Effects of exhumation kinematics and topographic evolution on detrital thermochronometer data. *Chapter 3 (this volume)*, 2008.

Whipp, Jr., D. M., Ehlers, T. A., Blythe, A. E., Huntington, K. W., Hodges, K. V. and Burbank, D. W. Plio-Quaternary exhumation history of the central Nepalese Himalaya: 2. Thermo-kinematic and thermochronometer age prediction model. *Tectonics*, 26, 2007. doi:10.1029/2006TC001991.

Wobus, C. W., Heimsath, A., Whipple, K. X. and Hodges, K. V. Active out-of-sequence thrust faulting in the central Nepalese Himalaya. *Nature*, 434:1008–1011, 2005.

Wobus, C. W., Hodges, K. V. and Whipple, K. X. Has focused denudation sustained active thrusting at the Himalayan topographic front? *Geology*, 31(20):861–864, 2003.

Zhao, W., Nelson, K. D., Che, J., Quo, J., Lu, D., Wu, C. and Liu, X. Deep seismic reflection evidence for continental underthrusting beneath southern Tibet. *Nature*, 366(6455):557–559, 1993. doi:10.1038/366557a0.

CHAPTER V

Influence of groundwater flow on thermochronometer-derived exhumation rates in the central Nepalese Himalaya

5.1 Abstract

Mountain topography creates variations in water-table elevation that drive groundwater flow. Consequently, advective heat transport by topography-driven fluid flow can modify the crustal thermal field and bias exhumation rates calculated from thermochronometer data. Although previous studies have considered the thermal effects of fluid flow, none has quantified the influence on thermochronometer ages. We use a steady-state three-dimensional coupled hydraulic thermokinematic finite-element model to simulate the influence of fluid flow on exhumation rates derived from thermochronometer data in the Nepalese Himalaya. Local hot springs suggest substantial heat transport by fluid flow and are adjacent to apatite fission-track samples. Model hydraulic conductivity controls the rate of fluid flow, and values characteristic of fractured rock ($\gg 10^{-9}$ m/s) yield a fluid advection-dominated thermal field. Hydraulic conductivity is estimated by minimizing the misfit between predicted and observed hot spring thermal power. The best-fit hydraulic conduc-

Official citation:
Whipp, D.M., Jr., and T.A. Ehlers, 2007, Influence of groundwater flow on thermochronometer-derived exhumation rates in the central Nepalese Himalaya: *Geology*, v. 35, p. 851-854, doi:10.1130/G23788A.1.

tivity value of $\sim 5 \times 10^{-7}$ m/s produces a fluid advection-dominated thermal field and older predicted apatite fission-track ages. To fit the observed age-elevation relationship, model-predicted ages require denudation rates that are ~5 mm/yr, ~200% higher than predictions from thermal models that do not simulate fluid flow. Thus, true exhumation rates can be substantially underestimated in orogenic systems where fluid advection is significant.

5.2 Introduction

Surface heat-flow studies suggest that advective heat transport by groundwater flow perturbs the background conductive thermal state of the crust (e.g., Van Orstrand, 1934). Mountain topography produces differences in hydraulic head (e.g., Hubbert, 1940), driving ground water flow that captures heat from the surrounding bedrock. The water then returns to the surface as warm springs within valleys and modifies the crustal thermal field (Figure 5.1). Previous two- and three-dimensional (2-D, 3-D) thermokinematic modeling studies have shown how denudation, surface topography, exhumation trajectory, and topographic evolution affect the subsurface thermal field and predicted mineral cooling ages (Stüwe et al., 1994; Mancktelow and Grasemann, 1997; Ehlers and Farley, 2003; Braun and van der Beek, 2004). Furthermore, 2-D coupled hydrologic-thermal models show modification of the crustal thermal field by topography-driven fluid flow (Smith and Chapman, 1983; Forster and Smith, 1989; Person and Garven, 1994). As noted by Ehlers (2005) and Dempster and Persano (2006), the influence of topography-driven fluid flow on thermochronometer data is seldom considered and poorly quantified.

This work complements previous studies by quantifying the thermal effect of fluid flow on the exhumation histories determined from low-temperature thermochronome-

ter data. We present results from a 3-D coupled hydrologic, thermal, and kinematic model used to predict mineral cooling ages as a function of advective and conductive heat transfer, topography, exhumation rate, and material properties. Predicted apatite fission-track (AFT) ages and hot spring thermal power are compared to observed values from the Marsyandi drainage in central Nepal (Evans et al., 2004; Blythe et al., 2007).

5.3 Nepalese Himalayan Geology, Fluid Flow and Cooling Ages

Indo-Tibetan convergence in the Nepalese Himalaya during late Miocene−Holocene time is thought to occur dominantly on two major thrusts, the Main Frontal thrust (MFT) and Main Central thrust (MCT) (e.g., Lavé and Avouac, 2000; Hodges et al., 2004), which separate lithostratigraphic units with different hydro-thermo-physical properties. Fractured igneous and upper amphibolite facies metamorphic rocks of the Greater Himalayan Sequence (GHS) are in the hanging wall of the MCT, structurally overlain by the sedimentary rocks of the Tibetan Sequence. Lower grade metasedimentary rocks of the Lesser Himalayan Sequence (LHS) are in the MCT footwall, and the crystalline Indian shield is subducted beneath the Himalaya (e.g., Gansser, 1964).

Evans et al. (2004) compiled a map of hot spring locations within the GHS and LHS in central Nepal, including four springs located within the Marsyandi River valley (Figure 5.2). They noted, however, that there may be many unmapped hot springs within the area, including the Nyadi River valley within our study area. They used a geochemical tracer (Ge concentrations) to calculate hot spring input to the Marsyandi River, finding a total hot spring discharge of 330 L/s, or 0.16% of the

Marsyandi River discharge [see Appendix B and Evans et al. (2004) for calculation details]. The high average spring temperature (∼51°C) reflects heat advected from the surrounding rock.

Mapped hot springs in the Marsyandi River valley are adjacent to AFT samples and may have affected their cooling history (Huntington et al., 2006; Blythe et al., 2007). AFT ages reflect the time since cooling below an effective closure temperature of ∼100−140°C for cooling rates of 2−100°C/Myr (e.g., Ketcham et al., 1999). This study focuses on a subset of nine samples along a vertical transect to Nagi Lek peak (Figure 5.2). AFT ages range from ca. 0.5 to 1.6 Ma over ∼3 km of elevation, and the steep slope of the data regression line reflects rapid exhumation. Previous thermokinematic models (without fluid flow) of Whipp et al. (2007), using the AFT data of Blythe et al. (2007), constrained the denudation rates in this region to 1.8−5.0 mm/yr over the past ∼3 Myr

5.4 Numerical Model

Thermochronometer data are sensitive to the thermal effects of faulting, denudation, topography, and groundwater flow (e.g., see review in Ehlers, 2005). To address these complexities, we use the 3-D coupled thermokinematic finite-element model of Whipp et al. (2007) with the addition of a coupled hydrologic model (see approach of Kohl et al., 2001). The model free parameters are the fault kinematics and hydraulic conductivity (K). The model domain is 84 × 140 × 50 km and large enough to prevent the boundary conditions from biasing the fluid flow and predicted ages. The upper surface is derived from a 250 m digital elevation model. The coupled hydraulic thermokinematic model generates a steady-state thermal solution for this crustal block. A steady-state calculation is used because previous studies have shown

that rapidly eroding regions will reach 90% of steady state at AFT closure depths in <5 Myr (e.g., Stüwe et al., 1994). Particles coincident with the sample locations are tracked through the model to produce time-temperature histories and predict AFT ages using a cooling-ratedependent age prediction algorithm. We conducted 50 simulations to explore the influence of K and fault kinematics on thermochronometer ages. Details on the numerical model and figures illustrating the model domain and fluid flow pathways can be found in Appendix B.

The thermokinematic model simulates erosional exhumation of material carried by the MFT and MCT. The MFT and MCT are active at overthrusting rates of 2−8 and 1−4 mm/yr, respectively, generating denudation rates of 1.3−5.0 mm/yr (Whipp et al., 2007). The remainder of the 20 mm/yr of Indo-Tibetan convergence is accommodated by subduction of the Indian shield (e.g., Larson et al., 1999). The model topography is in steady state, which is the simplest assumption because the AFT data are likely most sensitive to variations in the short-wavelength mountain-valley topography dictated by the river locations, thought to have followed similar paths for several million years (e.g., Gupta, 1997). Although relief may have changed, we have no clear data on relief changes.

Hydraulic conductivity is the free parameter in the hydrologic model and controls the rate of fluid flow. The water-table elevation drives fluid flow and is set to mimic topography as an approximation of the true water-table geometry. K decreases quasi-exponentially with depth from sequence-specific maxima, following the permeability trend observed in borehole measurements in crystalline rock. K is fixed at 10^{-12} m/s below the approximate brittle-ductile transition, as suggested by studies of geothermal data and metamorphic systems (Ingebritsen and Manning, 1999, and references therein). K is recalculated in each model time step to account

for pressure- and temperature-dependent fluid density, and temperature-dependent fluid viscosity (Phillips et al., 1981; Smith and Chapman, 1983). We recognize that smaller-scale variations in K may exist with lithology or in fault zones, and that localized areas with very high K may have significant thermal effects. However, we do not model this behavior because only some of the observed hot springs are coincident with mapped fault traces (Figure 5.2), spring locations vary over much shorter time scales than our cooling ages integrate, and the stress state and mineral precipitation in fault zones can both increase and decrease K (Hickman et al., 1995).

5.5 Results and Discussion

We focus on three important questions related to groundwater flow and thermochronometer ages. (1) What is the threshold K value above which fluid flow modifies thermochronometer ages beyond typical sample uncertainties? (2) How can hot spring thermal power measurements be used to quantify K? (3) How much does fluid flow influence interpreted exhumation rates relative to commonly used thermal models that ignore groundwater flow? We address each of these questions by presenting results for a subset of simulations. Note that our use of a steady-state thermal solution likely produces the maximum effect of groundwater flow.

First, we explored the range of K values in the GHS representative of fractured metamorphic rock to unfractured crystalline rock (10^{-4} and 10^{-12} m/s; Freeze and Cherry, 1979, p. 29). These simulations used a constant denudation rate of 2.5 mm/yr and K was the only model free parameter. K has a strong influence on the thermal field because increased downward fluid flow depresses the near-surface isotherms, counter acting the effects of erosional heat advection (Figure 5.3A). At K values of $\sim 10^{-12}$ m/s, erosional advection and heat conduction dominate advective

heat transport by fluid flow, whereas for K values of $\sim 5 \times 10^{-7}$ m/s, fluid-driven advection becomes the principal heat transfer process modifying the thermal field. A K value of $\sim 10^{-9}$ m/s marks the threshold value, above which fluid advection dominates, and below which erosional advection and conduction dominate the thermal field (see also Forster and Smith, 1989). A vertical temperature profile in the middle of the Nagi Lek ridge shows a temperature difference of ~ 75 °C at -10 km depth for high K values (Figure 5.3A); the difference decreases to <5 °C at -50 km depth. Thus, in models dominated by fluid-advective heat transfer, low-temperature thermochronometer samples would travel longer distances from their closure isotherms to the surface, generating older predicted ages (Figure 5.3B). For example, the predicted AFT ages in the fluid-advective models increase by ~ 1.8 Myr relative to the non-fluid-advective models. The fluid-advective-model-predicted ages also have a shallower slope on an age versus elevation plot and provide a poor fit to the observed AFT data.

Second, we compare the modeled and observed thermal power of fluids in the Marsyandi River catchment to determine the range of K values applicable to the study area. Thermal power provides a means for quantifying advective heat transport by groundwater flow. Thermal power of the Marsyandi hot springs is calculated following the method outlined by Ehlers and Chapman (1999). We use data collected from four hot springs in the Marsyandi River valley (Tables 2 and 6 of Evans et al., 2004). Evans et al. (2004) showed that Ge/Si ratios could be used to calculate hot spring flux in central Nepal with a simple end-member mixing equation. The total observed thermal power for the hot springs draining into the Marsyandi River is 61.4 ± 36.3 MW; the uncertainty reflects the standard deviation of Ge/Si in the measured springs. Predicted thermal power is calculated from fluids flowing out of

the upper model surface using three different sets of assumptions to quantify the range of thermal power (see Appendix B).

The resulting range of predicted thermal power output shows a strong positive correlation with K (Figure 5.4A). Only models with K values of $\sim 1-8 \times 10^{-7}$ m/s have sufficient fluid flow to generate the observed range of thermal power. Thus, advective heat transport by fluid flow may be the dominant heat transfer mechanism in this area. The fluid-advective model K value (5×10^{-7} m/s) is within the range constrained by the observed thermal power (dashed line in Figure 5.4A), suggesting that fluid-advective models should be used to determine denudation rates from the AFT data.

Third, we investigated the influence of groundwater flow on interpreted exhumation rates with a suite of simulations that fixed K at the fluid-advective value (5×10^{-7} m/s) while varying the denudation rate to fit the observed cooling ages (Figure 5.4B). Groundwater flow leads to an increase in the interpreted exhumation rate relative to rates determined from thermal models that do not include groundwater flow. For example, the best-fit non-fluid-advective-model-predicted ages presented in Figure 5.3B had a denudation rate of 2.5 mm/yr, but predicted ages from a fluid-advective model ($K = 5 \times 10^{-7}$ m/s) produce a poor fit to observed ages at that denudation rate (Figure 5.4B, upright triangles). However, increasing the denudation rate to 5.0 mm/yr produces a data fit that is as good as the non-fluid-advective model with a denudation rate of 2.5 mm/yr (cf. Figures 5.3B and 5.4B).

5.6 Conclusions

In this example from the central Nepalese Himalaya, the thermal-power-constrained hydraulic conductivity is high and shows that the denudation rate needed to fit the

observed AFT data must be ≥200% larger than that calculated from models that ignore the role of fluid flow. Note, however, that the magnitude of the effect of fluid flow may vary spatially depending on whether valleys or ridges are sampled. This example has extreme topographic relief, but the thermal effects of groundwater flow in other orogens with less relief and precipitation may still be substantial and should be considered (e.g., Saar and Manga, 2004). Furthermore, the downward flow of groundwater may counteract the topographic effects on effective closure isotherms and yield exhumation rates that are similar to those calculated from the slope of a linear regression through the data in an age-elevation plot. Unfortunately, this potential agreement would be mere coincidence because many of the underlying assumptions would be invalid, so it is advisable to utilize numerical models to quantify the dominant influences on the thermal field.

5.7 Acknowledgements

We thank Matt Evans, Louis Derry, and Ye Zhang for thoughtful discussions during the early stages of this study. Tim Dempster, Neil Mancktelow, and an anonymous reviewer provided constructive reviews. This study was supported by National Science Foundation grants EAR-9909647 and EAR-0409289 to Ehlers.

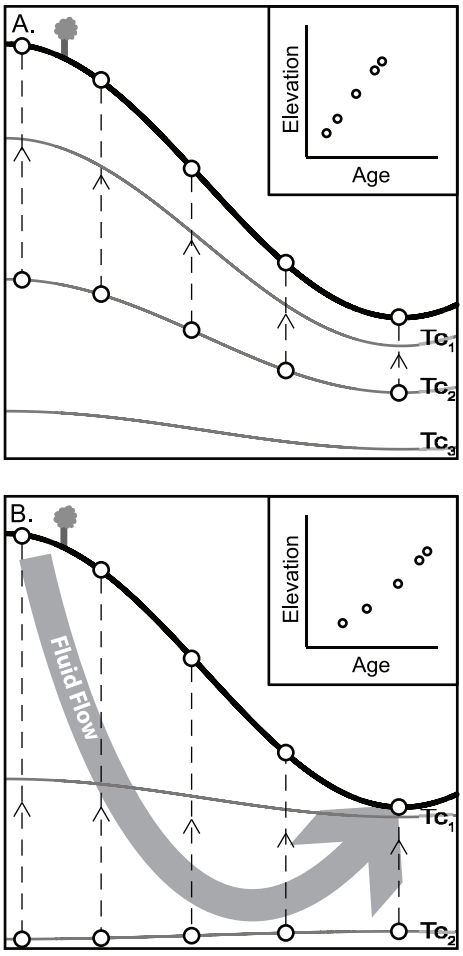

Figure 5.1: Schematic topographic cross sections showing thermal effects of topography and groundwater flow. Surface topography (thick black line) affects the position of isotherms (thin black lines) and the thermal history recorded in rock samples (white circles) cooling through closure temperatures $Tc_1 - Tc_3$. Insets show distribution of sample ages as function of elevation. A: Thermal field is dominated by erosional advection and heat conduction, and sample ages plot in a straight line on the inset plot. B: Gravity and lateral pressure gradients drive groundwater flow from high to low elevation, leading to heat transfer by fluid advection. This process perturbs closure temperature isotherms, and generates ages that are older and follow curved age-elevation trends.

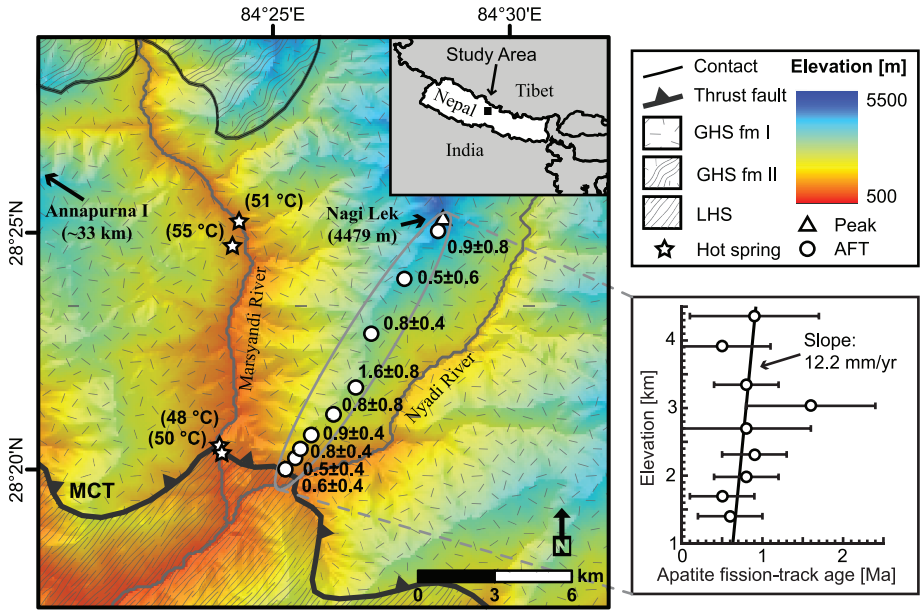

Figure 5.2: Shaded relief digital elevation model (DEM) of study region in central Nepal with thermochronometer samples, hot spring locations, and major lithostratigraphic units. Apatite fission-track samples (AFT, white circles) are located along Nagi Lek ridge, between Marsyandi and Nyadi Rivers, and adjacent to mapped hot spring locations (white stars). Note that the lack of mapped hot springs in the Nyadi River valley does not preclude their existence. Major thrust fault in the study area (MCT, Main Central thrust) separates Greater Himalayan sequence (GHS) from Lesser Himalayan sequence (LHS). GHS formation I is predominantly biotite-muscovite gneiss, formation II is mainly calc-silicate gneiss, and the map section of LHS is dominantly schists and phyllites. DEM is 250 m resolution resampled from 90 m U.S. Defense Mapping Agency data. Lithostratigraphic units and faults are from Searle and Godin (2003) and Colchen et al. (1986). Outer plot: sample ages with 2σ uncertainties as function of elevation with weighted regression line through the data.

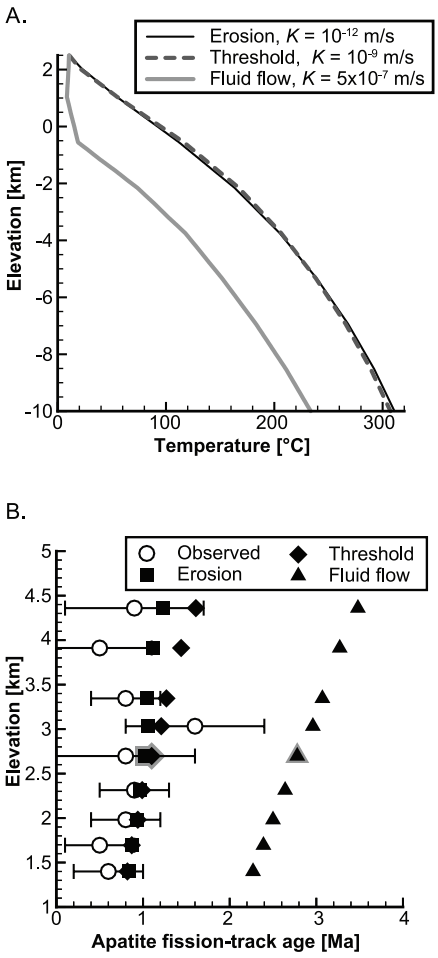

Figure 5.3: Influence of variable hydraulic conductivity (K) on geothermal gradients and thermochronometer ages from the Nagi Lek transect. A: Variation in model temperature as function of depth for models with K values that produce thermal fields dominated by erosional advection and conduction (erosion, black solid line) and fluid advection (fluid flow, gray solid line). Threshold geotherm (threshold, dashed gray line) is from a model thermal field that is neither non-fluid advective nor fluid advective. B: Apatite fission-track data with 2σ uncertainties (white circles) and predicted ages from non-fluid-advective (black squares), fluid-advective (black triangles), and threshold (black diamonds) models. Denudation rate is 2.5 mm/yr for all simulations. Symbols outlined in gray denote location of temperature-depth profiles shown in A. Shallow age-elevation trend and older ages in B, and depressed geothermal gradient in A from the fluid-advective model (black triangles, solid gray line), show the effect of groundwater flow.

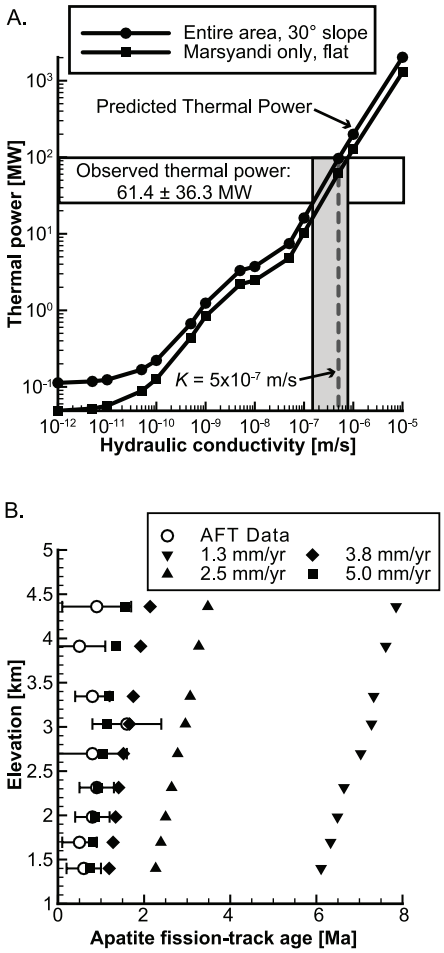

Figure 5.4: Influence of denudation rate and hydraulic conductivity (K) on thermal power and thermochronometer ages. A: Model-predicted thermal power at denudation rate of 2.5 mm/yr as function of K calculated from models using fluid fluxes from the entire model domain with assumed 30° hillslope angle (black line with black circles) or only Marsyandi River drainage basin and zero slope (black line with black squares). Calculation details are in Appendix B. The observed thermal power (white box) constrains the model K values; only models with K value within gray shaded box produce observed thermal power. B: Observed apatite fission-track (AFT) ages (white circles) with 2σ uncertainties and predicted ages for fluid-advective models that have denudation rates of 1.3 (black inverted triangles), 2.5 (black upright triangles), 3.8 (black diamonds), and 5.0 mm/yr (black squares). Rapid denudation rates are required for the fluid-advective model predicted ages to fit the data. Predicted AFT ages are from model with $K = 5 \times 10^{-7}$ m/s (dashed gray line in A).

Bibliography

Blythe, A. E., Burbank, D. W., Carter, A., Schmidt, K. and Putkonen, J. Plio-Quaternary exhumation history of the central Nepalese Himalaya: 1. Apatite and zircon fission-track and apatite [U-Th]/He analyses. *Tectonics*, 26, 2007. doi: 10.1029/2006TC001990.

Braun, J. and van der Beek, P. Evolution of passive margin escarpments; what can we learn from low-temperature thermochronology? *Journal of Geophysical Research*, 109(F4):F04009, 2004.

Colchen, M., Le Fort, P. and Pecher, A. *Recherches geologiques dans l'Himalaya du Nepal, Annapurna; Manaslu, Ganesh Himal; notice de la carte geologique au 1/200 000 ^{e} –Geological research in the Nepal Himalayas, Annapurna, Manaslu, Ganesh Himal; 1:20,000 geological map.* Cent. Natl. Rech. Sci., Paris, France (FRA), Poitiers, France (FRA), 1986.

Dempster, T. J. and Persano, C. Low-temperature thermochronology; resolving geotherm shapes or denudation histories? *Geology*, 34(2):73–76, 2006.

Ehlers, T. A. Crustal Thermal Processes and the Interpretation of Thermochronometer Data. *Reviews in Mineralogy and Geochemistry*, 58:315–350, 2005.

Ehlers, T. A. and Chapman, D. S. Normal fault thermal regimes; conductive and hydrothermal heat transfer surrounding the Wasatch Fault, Utah. *Tectonophysics*, 312(2-4):217–234, 1999.

Ehlers, T. A. and Farley, K. A. Apatite (U-Th)/He thermochronometry; methods and applications to problems in tectonic and surface processes. *Earth and Planetary Science Letters*, 206(1-2):1–14, 2003.

Evans, M. J., Derry, L. A. and France-Lanord, C. Geothermal fluxes of alkalinity in the Narayani river system of central Nepal. *Geochemistry, Geophysics, Geosystems - G (super 3)*, 5:no.8, 21, 2004.

Forster, C. B. and Smith, L. The influence of groundwater flow on thermal regimes in mountainous terrain; a model study. *Journal of Geophysical Research, B, Solid Earth and Planets*, 94(7):9439–9451, 1989.

Freeze, R. A. and Cherry, J. A. *Groundwater*. Prentice-Hall, Inc., Englewood Cliffs, NJ, 1979.

Gansser, A. *Geology of the Himalayas*. Wiley Interscience, London, 1964.

Gupta, S. Himalayan drainage patterns and the origin of fluvial megafans in the Ganges foreland basin. *Geology*, 25(1):11–14, 1997.

Hickman, S., Sibson, R. H. and Bruhn, R. Introduction to special section; Mechanical involvement of fluids in faulting. *Journal of Geophysical Research*, 100(B7):12,831–12,840, 1995.

Hodges, K. V., Wobus, C. W., Ruhl, K., Schildgen, T. and Whipple, K. X. Quaternary deformation, river steepening, and heavy precipitation at the front of the Higher Himalayan ranges. *Earth and Planetary Science Letters*, 220:379–389, 2004.

Hubbert, M. K. The theory of ground-water motion. *Journal of Geology*, 48(8, Part 1):785–944, 1940.

Huntington, K. W., Blythe, A. E. and Hodges, K. V. Climate change and Late Pliocene acceleration of erosion in the Himalaya. *Earth and Planetary Science Letters*, 252(1-2):107–118, 2006.

Ingebritsen, S. E. and Manning, C. E. Geological implications of a permeability-depth curve for the continental crust. *Geology*, 27(12):1107–1110, 1999.

Ketcham, R. A., Donelick, R. A. and Carlson, W. D. Variability of apatite fission-track annealing kinetics; III, Extrapolation to geological time scales. *American Mineralogist*, 84(9):1235–1255, 1999.

Kohl, T., Signorelli, S. and Rybach, L. Three-dimensional (3-D) thermal investigation below high Alpine topography. *Physics of the Earth and Planetary Interiors*, 126:195–210, 2001.

Larson, K. M., Buergmann, R., Bilham, R. and Freymueller, J. T. Kinematics of the India-Eurasia collision zone from GPS measurements. *Journal of Geophysical Research, B, Solid Earth and Planets*, 104(1):1077–1093, 1999.

Lavé, J. and Avouac, J. P. Active folding of fluvial terraces across the Siwaliks Hills, Himalayas of central Nepal. *Journal of Geophysical Research, B, Solid Earth and Planets*, 105(3):5735–5770, 2000.

Mancktelow, N. S. and Grasemann, B. Time-dependent effects of heat advection and topography on cooling histories during erosion. *Tectonophysics*, 270(3-4):167–195, 1997.

Person, M. and Garven, G. A sensitivity study of the driving forces on fluid flow during continental-rift basin evolution. *Geological Society of America Bulletin*, 106(4):461–475, 1994.

Phillips, S., Igbene, A., Fair, J., Ozbek, H. and Tavan, M. A Technical Databook for Geothermal Energy Utilitzation. Technical Report LBL-12810, Lawrence Berkeley Laboratory, USA, 1981.

Saar, M. O. and Manga, M. Depth dependence of permeability in the Oregon Cascades inferred from hydrogeologic, thermal, seismic, and magmatic modeling constraints. *Journal of Geophysical Research, B, Solid Earth and Planets*, 109:no.4, 19, 2004.

Searle, M. P. and Godin, L. The South Tibetan detachment and the Manaslu Leucogranite; a structural reinterpretation and restoration of the Annapurna-Manaslu Himalaya, Nepal. *Journal of Geology*, 111(5):505–523, 2003.

Smith, L. and Chapman, D. S. On the thermal effects of groundwater flow - 1. Regional scale systems. *Journal of Geophysical Research*, 88(B1):593–608, 1983.

Stüwe, K., White, L. and Brown, R. The influence of eroding topography on steady-state isotherms; application to fission track analysis. *Earth and Planetary Science Letters*, 124(1-4):63–74, 1994.

Van Orstrand, C. E. Temperature gradients. In Wrather, W. and Lahee, P., editors, *Problems in Petroleum Geology*, page 1073. The American association of petroleum geologists, Tulsa, OK, 1934.

Whipp, Jr., D. M., Ehlers, T. A., Blythe, A. E., Huntington, K. W., Hodges, K. V. and Burbank, D. W. Plio-Quaternary exhumation history of the central Nepalese Himalaya: 2. Thermo-kinematic and thermochronometer age prediction model. *Tectonics*, 26, 2007. doi:10.1029/2006TC001991.

CHAPTER VI

Summary and conclusions

6.1 Results summary

This dissertation aims to quantify how tectonic, thermal and surface processes affect exhumation histories generated from bedrock and detrital thermochronometer data. The following sections summarize the major results of each chapter, return to answer the major motivating questions from the introductory chapter (chapter 1) and provide general conclusions from this work.

6.1.1 Chapter 2 results

The aim of chapter two was to quantify the rates and spatial variations in exhumation in the Nepalese Himalaya using a 3-D thermokinematic numerical model and bedrock apatite fission-track (AFT) dataset from Blythe et al. (2007). Results suggest: (1) The kinematics of rock exhumation dominate the effects of other thermal influences, such as rock material properties and heat flux into the base of the crust. (2) The range of exhumation rates calculated from thermochronometer age-elevation relationships based on 1-D interpretations of the thermal field ($-2.6 - 12.2$ mm/y) can be decreased by >200% by using 3-D models (1.8−5.0 mm/y). (3) AFT data do not have a significant sensitivity to differences in the faulting history in the Nepalese Himalaya. (4) Sensitivity to faulting history in the Himalaya would in-

crease for larger differences in rock exhumation pathway, slower exhumation rates or thermochronometers that are sensitive to higher temperatures (e.g., muscovite $^{40}Ar/^{39}Ar$). (5) Spatial variations in the model exhumation rate were observed, suggesting that this model does not incorporate certain influences that could affect the predicted AFT ages, such as unmapped small-scale faults, topographic relief change or groundwater flow.

6.1.2 Chapter 3 results

The goal of chapter three was to investigate the sensitivity of detrital apatite (U-Th)/He (AHe), zicron fission-track (ZFT), and muscovite $^{40}Ar/^{39}Ar$ (MAr) thermochronometers to changes in exhumation kinematics and topographic evolution. Model results show: (1) Exhumation rates calculated using 1-D assumptions about the thermal field can be overestimated by >300% and ∼90% for the AHe and MAr thermochronometers, respectively, relative to 3-D models. (2) Because of a shorter response time, low-temperature thermochronometers are preferable for addressing recent changes in rock exhumation histories, whereas higher-temperature systems can address changes earlier in a regional exhumation history. (3) The influence of other thermal parameters and processes is again dominated by the rate of exhumation for low-temperature thermochronometers. (4) The kinematics of exhumation have a strong effect on predicted age distributions, and higher-temperature systems show the greatest sensitivity to the exhumation kinematics. (5) In general, detrital thermochronometers show little sensitivity to changes in topographic relief at exhumation rates above ∼1 mm/y. (6) Temporal records of basin exhumation preserved in basin sediments are predicted to have high sensitivity and rapid responses to changes in exhumation rate, while topographic evolution produces little change in the age distributions.

6.1.3 Chapter 4 results

Chapter four used a coupled tectonic, thermal and age prediction model to explore the effects of faulting and bedrock landslides on detrital MAr data from the Nepalese Himalaya. Preliminary results are: (1) Variations in exhumation rate and faulting history do not provide a good fit to the observed MAr distributions, suggesting that (2) river channel sediment samples may be affected by non-uniform sediment generation by surface processes such as bedrock landsliding, or the tectonic model parameter space was not large enough. (3) At short sediment residence times ($\sim$1 year), bedrock landsliding can shift both the peak age and age range of detrital thermochronometer data, potentially leading to errors in calculated exhumation rates if sediment is assumed to be contributed from the entire drainage basin area. (4) Although peak ages and age ranges are quite variable at short sediment residence times, increased sediment residence time or sediment samples from preserved basin sediments can potentially provide a better record of basin-wide exhumation. (5) To account for possible undersampling of the basin area, by processes such as bedrock landsliding, when possible, it is best to collect detrital thermochronometer samples in regions with available bedrock thermochronometer datasets.

6.1.4 Chapter 5 results

The aim of chapter five was to explore the potential impact of groundwater circulation on exhumation rates calculated from AFT data in the Nepalese Himalaya. Results show: (1) At hydraulic conductivity (K) values typical of fractured igneous or metamorphic rock, groundwater flow is the dominant heat transfer process in the upper crust, heavily modifying the thermal field. (2) Measured hot spring thermal power values, the energy used to heat hot spring fluids, can be used to constrain

the average rock hydraulic conductivity. (3) The high K values suggested by measured hot spring thermal power in central Nepal show that the crustal thermal field should be modified by groundwater flow. Using an appropriate value for K, this study finds that failure to account for the effects of groundwater flow could lead to underestimation of true exhumation rates by $\geq$200%.

6.2 Responses to motivating questions

Responses to the motivating questions on exhumation in active orogens from chapter 1 are listed below.

(1) What are the dominant thermal processes affecting thermochronometer ages?

The dominant thermal processes influencing thermochronometer ages vary with the effective closure temperature. Low-temperature thermochronometers, such as AHe and AFT, are most sensitive to their exhumation rate in regions where significant groundwater circulation is not present. Where bedrock is fractured and K is high, groundwater flow occurs at high rates, decreasing the sensitivity of low-temperature thermochronometers to the exhumation rate. Sensitivity to differences in fault kinematics was not observed in bedrock AFT ages, however, detrital MAr age distributions show strong sensitivity to faulting history. In both cases, significant sensitivity to thermophysical material properties, basal heat flux and evolution of surface topography was not observed because the thermal field was dominated by advection from rapid exhumation rates.

(2) Which thermochronometer systems and sampling approaches are best suited for use in tectonic versus surface process studies?

Higher-temperature thermochronometers, such as MAr and ZFT, have sensitivity to differences in faulting history. These thermochronometer systems integrate

their cooling history over larger temporal and spatial distances than low-temperature systems, leading to increased differences in cooling history, even with fairly small differences in tectonic transport direction (i.e., fault geometry). Low-temperature systems are more sensitive to the overall exhumation rate, with little sensitivity to faulting histories that are not vastly different. However, certain surface processes, such as bedrock landsliding, can impact detrital age distributions in both high- and low-temperature thermochronomters. The reason for this is that grain-ages are effectively contributed from point sources within a given drainage basin, rather than sampling the entire basin area. Thus, input of ages from individual landslide events could generate basin age distributions that do not reflect the age range and distribution of surface ages. Notably, this surface process sensitivity to bedrock landslides would likely be undetectable in bedrock thermochronometer samples, even for low-temperature thermochronometers. Overall, this suggests that detrital and low-temperature bedrock thermochronometers are best used for determining exhumation rates resulting from surface processes, while higher-temperature thermochronometers are a better tool for investigating tectonic problems.

(3) How large is the difference in exhumation rates calculated from a 1-D versus a 3-D thermal field?

Using 1-D assumptions about the thermal field ignores the role of several important thermal influences. The most obvious is the lack of consideration for the influence of topography, which warps crustal isotherms to mimic a damped version of the surface topography. The net result of this is a potential overestimation of true exhumation rates when using 1-D assumptions. For bedrock AFT data in Nepal, it was observed that exhumation rates were overestimated by >200% compared to 3-D models without the effect of groundwater flow. Furthermore, a comparison of

3-D model input denudation rates and those calculated from predicted detrital AHe and MAr distribution age ranges shows denudation rate overestimates of >300% and ∼90%, respectively, at exhumation rates typical of active convergent orogens. Models that include the effects of groundwater flow suggest that these overestimates may be lower, decreasing to ∼200% for bedrock AFT data. Regardless, results show potential for overestimation of exhumation rates from 1-D methods and suggest that such techniques should be utilized with caution.

(4) What is the potential impact of non-uniform sediment supply by processes like bedrock landsliding on detrital thermochronometer age distributions?

Preliminary model results show that bedrock landsliding can strongly skew detrital age distributions towards the ages sampled by the slides, particularly in regions with short sediment residence times. For sediment residence times of ∼1 year, peak ages of predicted MAr age distributions from one tributary catchment to the Marsyandi River differed by ∼40%. If detrital sediment samples are derived from landslides, rather than sampling the entire basin area, data interpretation with models that assume age contribution from the entire basin could be erroneous. This problem is less of a concern in the well-mixed sediment in foreland basins, but should be considered by studies using modern river sands in landslide-dominated regions.

(5) How much does groundwater circulation affect exhumation rates calculations?

In regions with fractured bedrock, groundwater circulation is an important influence on the thermal field and thermochronometer ages. Model calculations show estimated exhumation rates can be >200% lower in models that do not consider the effects of groundwater flow. In regions where the bulk bedrock hydraulic conductivity is lower, the effects of groundwater would decrease. This suggests that future studies should consider the distribution, flow rates and temperatures (i.e., thermal

power) of springs in their study region.

6.3 Conclusions

In spite of the challenges of data interpretation, thermochronology remains a powerful tool for quantifying rock exhumation over millions of years. Much of the presented work focused on the power of 3-D thermokinematic and age prediction modeling for improving existing exhumation history calculations from thermochronometer datasets. However, there are numerous free parameters and uncertainties that may limit these models. Constraints on measurable model parameters such as rock thermophysical properties, and comparison of model and observed surface heat flow can limit uncertainty, but even complex 3-D model results are still a simplification of an extremely complicated natural system. That said, model results should be viewed as estimates of true exhumation rates that have some uncertainty. I explored a number of potential factors that influence the thermal field and by determining the dominant influences, the hope is that those parameters can be constrained to minimize uncertainty in model results.

The 3-D models used in this dissertation offer an excellent method for improving thermochronometer dataset interpretation, but can be prohibitively complex for many potential users. Basic data interpretation using simple 1-D numerical models can overestimate exhumation rates of a given region, but these models are still useful for providing a general range of exhumation rates. In particular, the combination of 1-D models and higher temperatures (e.g., MAr) thermochronometer datasets from regions with slightly slower exhumation rates or less tectonic complexity should provide good estimates of exumation rates. Furthermore, in regions with pervasive groundwater circulation, the potential for overestimation of exhumation rates can de-

crease as groundwater flow can damp the thermal field perturbation from the overlying topography. In general, I strongly recommend continued use of both bedrock and detrital thermochronology with consideration of the potential impacts of the tectonic and surface processes addressed in this dissertation. In particular, I would not argue that applications of low-temperature (e.g., AHe, AFT) thermochronometer data should be avoided, but rather that the potential to overestimate exhumation rates and the interpretational limitations with 1-D techniques should be acknowledged.

The 3-D thermal modeling software presented in this dissertation is cutting-edge technology and represents some of the most powerful programs available for solving the problems I addressed. However, there is still room for improvement and growth in the interpretation of thermochronometer data with numerical models. For example, the thermokinematic numerical models I used were limited by two restrictive assumptions: (1) The kinematic field for a given tectonic setting is known and (2) other than scaling of topographic relief, the surface topography does not evolve with time. In the kinematic models for the Nepalese Himalaya, we used available geologic cross-sections and maps to design the geometry. There is unfortunately little constraint on the subsurface geometry of the structure in this region. This means that there could be problems with the kinematic model that could influence data interpretation. As an alternative, thermomechanical models that consider the dynamics of orogen formation may offer insight that is not easily found using purely kinematic models. Furthermore, the combination of thermomechanical models with surface process models that dictate the temporal evolution of topography is a very powerful method of investigating thermochronometer datasets in areas with little constraint on the tectonic history, structural geometry and topographic evolution. Although these models also have potential issues, such as difficulty in recreating the

present-day topography of a region and additional free parameters, they can avoid some of the limits of thermokinematic modeling and offer great promise for further understanding both thermochronometer data and orogen geodynamic processes.

Bibliography

Blythe, A. E., Burbank, D. W., Carter, A., Schmidt, K. and Putkonen, J. Plio-Quaternary exhumation history of the central Nepalese Himalaya: 1. Apatite and zircon fission-track and apatite [U-Th]/He analyses. *Tectonics*, 26, 2007. doi: 10.1029/2006TC001990.

APPENDICES

APPENDIX A

Thermal Property Measurements

Thermal conductivity was measured on 11 samples from Formations I and II in the GHS from central Nepal (Table A.1) (see Hodges (2000) for a description of the GHS formations). The measurements were made by P. Galanis and C. Williams at the U.S. Geological Survey office in Menlo Park, California, using the technique outlined by Sass et al. (1984). Samples were measured both parallel and perpendicular to the dominant foliation and a significant anisotropy was observed.

Radiogenic heat-producing element concentrations were measured on 7 of the 11 samples from the GHS (Table A). Samples were analyzed for the K, Th, and U via gamma ray spectrometry by J. Kaste and A. Heimsath at Dartmouth College in Hanover, New Hampshire. Potassium values were determined by measuring the ^{40}K emission at 1461 keV, and assuming a ^{40}K abundance of 0.01177% and ^{40}K branching ratio (e.g., gamma yield) of 10.7%. Thorium concentrations were determined by measuring the ^{228}Ac gamma ($T_{1/2}$ = ~6 hr) at 911 keV, assuming a gamma yield of 28.7% and secular equilibrium between it and ^{232}Th. ^{238}U was determined by measuring the ^{234}Th decay emission (direct daughter of ^{238}U, $T_{1/2}$ = 24 d) at 63.3 keV. ^{235}U was calculated by assuming a ^{235}U/^{238}U abundance of 0.72% (J. Kaste, personal communication, 2006). Radiogenic heat production was calculated using

an equation modified from Birch (1954),

$$A = 0.01\rho(9.69(^{238}\mathrm{U} + ^{235}\mathrm{U}) + 2.65\mathrm{Th} + 3.58\mathrm{K}) \tag{A.1}$$

where A is the volumetric heat production in $\mathrm{mW/m^3}$, ρ is the average rock density in $\mathrm{g/cm^3}$, K is the potassium concentration in percent, and ^{238}U, ^{235}U, and Th are the uranium and thorium concentrations in parts per million. An average rock density of 2.8 $\mathrm{g/cm^3}$ was assumed in calculating A for Table A.

Table A.1: GHS Thermal Conductivity Measurements

Sample	Formation	Lithology	Foliation-Parallel Whole Rock Conductivity, W/m K	Foliation-Perpendicular Whole Rock Conductivity, W/m K	Foliation
NP001	I	biotite-muscovite gneiss	5.0		F_1
NP002	I	biotite-muscovite gneiss	4.0		F_1
NP003	I	biotite-muscovite gneiss	4.7	2.3	F_2
NP004	I	biotite-muscovite gneiss	4.0	2.9	F_1
NP005	I	biotite-muscovite gneiss	3.2	3.0	F_1
NP006	I	biotite-muscovite gneiss	4.3		F_1
NP007	I	biotite-muscovite gneiss	3.6	2.6	F_1
NP008	I	biotite-muscovite gneiss	3.9	2.3	F_1
	I	biotite-muscovite gneiss		3.8	F_1
NP009	II	banded calc-silicate gneiss	2.4	2.0	F_1
NP010	II	banded calc-silicate gneiss	3.2		F_1
	II	banded calc-silicate gneiss	3.2		F_1
NP011	II	banded calc-silicate gneiss	4.4	2.6	F_2

Table A.2: GHS Radiogenic Heat Production Measurements

Sample	Formation	Lithology	K, %	^{235}U, ppm	^{238}U, ppm	^{232}Th, ppm	A, μW/m^3
NP002	I	biotite-muscovite gneiss	3.26	0.016	2.161	14.893	2.0
NP004	I	biotite-muscovite gneiss	1.03	0.012	1.599	7.379	1.1
NP005	I	biotite-muscovite gneiss	3.92	0.033	4.608	18.229	3.0
NP007	I	biotite-muscovite gneiss	2.10	0.017	2.287	12.228	1.7
NP009	II	banded calc-silicate gneiss	3.34	0.024	3.269	15.259	2.4
NP009	II	banded calc-silicate gneiss	3.06	0.017	2.388	11.692	1.8
NP009	II	banded calc-silicate gneiss	4.37	0.020	2.737	17.095	2.4

Bibliography

Bilham, R., Larson, K. M., Freymueller, J. T., Jouanne, F., Le Fort, P., Leturmy, P., Mugnier, J. L., Gamond, J. F., Glot, J. P., Martinod, J., Chaudury, N. L., Chitrakar, G. R., Gautam, U. P., Koirala, B. P., Pandey, M. R., Ranabhat, R., Sapkota, S. N., Shrestha, P. L., Thakuri, M. C., Timilsina, U. R., Tiwari, D. R., Vidal, G., Vigny, C., Galy, A. and de Voogd, B. GPS measurements of present-day convergence across the Nepal Himalaya. *Nature*, 386(6620):61–64, 1997.

Birch, A. F. Heat from radioactivity. In Faul, H., editor, *Nuclear Geology*, pages 148–175. Wiley, New York, 1954.

Brooks, A. and Hughes, T. Streamline Upwind / Petrov-Galerkin formulations for convective dominated flows with particular emphasis on the incompressible Navier-Stokes Equations. *Computer Methods in Applied Mechanics and Engineering*, 32:199–259, 1982.

Ehlers, T. A. and Chapman, D. S. Normal fault thermal regimes; conductive and hydrothermal heat transfer surrounding the Wasatch Fault, Utah. *Tectonophysics*, 312(2-4):217–234, 1999.

Ehlers, T. A., Willett, S., Armstrong, P. A. and Chapman, D. S. Exhumation of the Central Wasatch Mountains, Utah: 2. Thermo-kinematics of exhumation and thermochronometer interpretation. *Journal of Geophysical Research*, 108(B3):2173, 2003.

Evans, M. J., Derry, L. A. and France-Lanord, C. Geothermal fluxes of alkalinity in the Narayani river system of central Nepal. *Geochemistry, Geophysics, Geosystems - G (super 3)*, 5:no.8, 21, 2004.

Hodges, K. V. Tectonics of the Himalaya and southern Tibet from two perspectives. *Geological Society of America Bulletin*, 112(3):324–350, 2000.

Ingebritsen, S. E. and Manning, C. E. Geological implications of a permeability-depth curve for the continental crust. *Geology*, 27(12):1107–1110, 1999.

Kohl, T. and Hopkirk, R. J. "FRACTure" a simulation code for forced fluid flow and transport in fractured, porous rock. *Geothermics*, 24(3):333–343, 1995.

Larson, K. M., Buergmann, R., Bilham, R. and Freymueller, J. T. Kinematics of the India-Eurasia collision zone from GPS measurements. *Journal of Geophysical Research, B, Solid Earth and Planets*, 104(1):1077–1093, 1999.

Laslett, G. M., Green, P. F., Duddy, I. R. and Gleadow, A. J. W. Thermal annealing of fission tracks in apatite. *Chemical Geology; Isotope Geoscience Section*, 65(1):1–13, 1987.

Phillips, S., Igbene, A., Fair, J., Ozbek, H. and Tavan, M. A Technical Databook for Geothermal Energy Utilitzation. Technical Report LBL-12810, Lawrence Berkeley Laboratory, USA, 1981.

Putnam, S. N. and Chapman, D. S. A geothermal climate change observatory; first year results from Emigrant Pass in Northwest Utah. *Journal of Geophysical Research, B, Solid Earth and Planets*, 101(10):21,877–21,890, 1996.

Sass, J. H., Kennelly, J. P., J., Smith, E. P. and Wendt, W. E. Laboratory line-source methods for the measurement of thermal conductivity of rocks near room temperature. Technical Report 84-91, United States Geological Survey, 1984.

Sauty, J. P., Gringarten, A. C., Menjoz, A. and Landel, P. A. Sensible energy storage in aquifers; 1, Theoretical study. *Water Resources Research*, 18(2):245–252, 1982.

Smith, L. and Chapman, D. S. On the thermal effects of groundwater flow - 1. Regional scale systems. *Journal of Geophysical Research*, 88(B1):593–608, 1983.

Whipp, Jr., D. M., Ehlers, T. A., Blythe, A. E., Huntington, K. W., Hodges, K. V. and Burbank, D. W. Plio-Quaternary exhumation history of the central Nepalese Himalaya: 2. Thermo-kinematic and thermochronometer age prediction model. *Tectonics*, 26, 2007. doi:10.1029/2006TC001991.

Williams, C. F. and Narasimhan, T. N. Hydrogeologic constraints on heat flow along the San Andreas Fault; a testing of hypotheses. *Earth and Planetary Science Letters*, 92(2):131–143, 1989.

APPENDIX B

Numerical model setup, thermal power calculations and additional model analyses

B.1 Numerical model setup

B.1.1 Thermal model

The thermal field for the central Nepal study region is calculated using a modified version of the 3-D finite-element code of FRACTure (Kohl and Hopkirk, 1995), similar to that implemented by Whipp et al. (2007). We briefly summarize here the governing equations used in the FRACTure program. The thermal field in a porous media results from diffusion and advection of heat. If the solid (rock) and the fluid phase are considered separately, they are connected via a heat transfer coefficient. The thermal energy equation for the fluid phase is given by

$$[\rho c_p]_f \cdot \frac{dT_f}{dt} + [\rho c_p]_f \cdot \mathbf{v} \cdot \nabla T_f - \nabla \cdot (K \cdot \nabla T_f) + h \cdot (T_f - T_s) + Q = 0, \tag{B.1}$$

where T_f is the temperature of the fluid, T_s the temperature of the solid phase, $[\rho c_p]_f$ the thermal capacity of the fluid (J/m^3 K), $\mathbf{v}$ the Darcy velocity, K the thermal conductivity of the fluid (W/m K), h the heat transfer coefficient (W/m K) and Q heat sources. If no solid movements are considered the energy equation of the solid phase can be expressed by

$$[\rho c_p]_s \cdot \frac{dT_s}{dt} - \nabla \cdot (\Lambda_s \cdot \nabla T_s) + h(T_s - T_f) + Q = 0, \tag{B.2}$$

where $[\rho c_p]_s$ is the thermal capacity of the rock (J/m^3 K) and Λ_s is the rock thermal conductivity tensor.

For heat transfer in porous media it can be assumed that the heat transfer coefficient is sufficiently large so that $T_f = T_s$ is valid. Given this, the thermal energy equation describing the temperature distribution in a saturated porous medium is given by Sauty et al. (1982)

$$\langle \rho c_p \rangle \cdot \frac{\partial T}{\partial t} = \nabla \cdot (\langle \Lambda \rangle \cdot \nabla T) - [\rho c_p]_f \cdot \mathbf{v} \cdot \nabla T - Q, \tag{B.3}$$

where ρc_p is the averaged fluid-solid thermal capacity, Λ the averaged fluid-solid thermal conductivity tensor and $[\rho c_p]_f$ the thermal capacity of the fluid. For our application to the Himalaya, the steady-state form of Equation (B.3) was used.

The previous equations are solved using a Galerkin finite element scheme with implicit time stepping. For all of the models, the thermal calculation is run until a thermal steady state is reached. The upper surface of the model is a 250 m digital elevation model (DEM) of an 84 $\times$ 140 km area surrounding the Marsyandi River valley and the model extends to 50 km below sea level (Figure B.1). The top surface model has a fixed temperature boundary condition with a temperature of 28°C at 0 m elevation and the temperature decreases 7°C/km elevation increase. The base of the model has a constant flux boundary condition of 35 mW/m^2 and the other faces of the model have a zero flux boundary. Elements in Lesser Himalayan Sequence (LHS) and Indian Shield (IS) in the model have assigned radiogenic heat production values of 0.8 μW/m^3. The Greater Himalayan Sequence (GHS) elements have a heat production value of 1.9 μW/m^3 and the Tibetan Sequence (TS) have a prescribed heat production of 0.5 μW/m^3. The entire model domain uses a thermal conductivity value of 2.5 W/m K. Thermal and hydrologic model parameters used in our simulations are summarized in Table B.1.

B.1.2 Tectonic (kinematic) model

The kinematic model prescribes a velocity field for elements within the model that reflects transport of material parallel to the active faults in the model domain. Fault motion is partitioned between underthrusting (subduction) of the Indian Shield and overthrusting on the Main Frontal Thrust (MFT) and Main Central Thrust (MCT). The model allows for convergence to occur solely across the MFT (Figure B.1b) or across the MFT and MCT (Figure B.1c). The fault geometry is described in detail by Whipp et al. (2007). The horizontal convergence rate between India and Tibet is fixed at 20 mm/yr in the model, consistent with present-day geodetic measurements (Bilham et al., 1997; Larson et al., 1999). For models without slip on the MCT, 7 mm/yr of convergence is accommodated by the MFT with the remaining 13 mm/yr occurring by subduction. For the majority of the models with the MCT active, 4 mm/yr of convergence is accommodated by the MFT, 2 mm/yr by the MCT and 12 mm/yr by subduction. Because the model geometry does not change with time, both of these kinematic scenarios generate vertical exhumation (erosion) rates of $\sim$2.5 mm/yr. For the models where the kinematics are varied, the MFT and MCT are active at convergence rates of $2-8$ mm/yr and $1-4$ mm/yr, respectively, generating erosion rates of $1.3-5.0$ mm/yr.

B.1.3 Hydrologic model

In addition to modeling 3-D thermal processes, the finite element code FRACTure can simulate coupled hydraulic-thermal systems. The hydrologic model utilized in this study simulates the large-scale flow of a fluid (water) driven by pressure gradients resulting from variations in the water table elevation due to topography (Figure B.2). The primary effect in the upper crust is flow from ridges into adjacent valleys (Fig-

ure B.2b). The other major circulation pattern is the flow from the Tibetan Plateau down toward the Indian foreland (Figure B.2c). The superposition of both flows generates the observed thermal disturbance.

The surface boundary condition has the water table elevation set to mimic topography as an approximation of the true water table geometry. All other sides of the model have a zero flux boundary. The fluid in the model is set to behave like water with a temperature-dependent viscosity following the approaches of Smith and Chapman (1983) and pressure and temperature-dependent density (Phillips et al., 1981). Because heat transfer in the model is often dominated by fluid advection, streamline upwinding is used to stabilize the solution following the approach of Brooks and Hughes (1982). Other model parameters are summarized in Table B.1.

The primary variable in the hydrologic model, the hydraulic conductivity (K), is specified for each lithologic unit and varied across a range of values measured in different rock types (Table B.1). The hydraulic conductivity decreases following an exponential function from the surface of the model to a minimum value at a depth of -7 km (Equation (B.4)). This depth is the approximate depth of the brittle-ductile transition in the models, a depth below which rock permeability is thought to decrease to a low, constant value (Ingebritsen and Manning, 1999; Williams and Narasimhan, 1989). K is assigned across 1 km intervals from the mean elevation of $\sim$3 km down to the constant value at -7 km. Elements above the mean elevation have a constant value of the maximum K for the given lithology. The general equation used for K at depth is given by

$$\log_{10}(K) = (-n/d) \times z + \log_{10}(K_{max}), \tag{B.4}$$

where n is the number of orders of magnitude between the highest K value and the impermeable value, d is the thickness of the unit above the brittle-ductile transition

(10 km), z is the elevation of the depth interval relative to the mean elevation and K_{max} is the maximum K value for the lithology. The range of K values for the different lithologic units is listed in Table B.1.

Following the same approach of Whipp et al. (2007), thermochronometer ages are calculated using predicted cooling histories for model points coincident with the AFT sample locations. Cooling histories were generated by tracking the temperature of samples from the surface back to different depths in the thermal model. Predicted AFT ages were calculated using the Laslett et al. (1987) kinetic annealing algorithm as implemented by Ehlers et al. (2003). Although other (multi-)kinetic models have been proposed, the data used in this study have no compositional data available, and cooled extremely fast, and therefore do not warrant use of a multi-kinetic model.

Muscovite $^{40}Ar/^{39}Ar$ ages were predicted in the following appendix from the sample cooling histories, but the kinetics of argon diffusion in muscovite are not understood in sufficient detail such that an forward age prediction model can be developed. Because of this, we report the predicted ages as the time since the rock cooled below 350°C. We regard this estimated closure temperature as a minimum estimate and use it only for illustrative purposes of how a higher temperature thermochronometer responds to different kinematic scenarios.

B.2 Thermal power calculations

The thermal power of the hot springs in the Marsyandi River valley provides a means for quantifying advective heat transport by groundwater flow. The observed thermal power is calculated using data collected from four hot springs in the Marsyandi River valley (Evans et al., 2004). Evans et al. (2004) showed that the hot springs in central Nepal were enriched in Ge, compared to the river water and

thus Ge/Si ratios could be used to calculate the hot spring water input using a simple end-member mixing equation (Equation (1) of Evans et al., 2004). The mixing equation is

$$F_W^{HS} = \frac{[Si]_{trib}}{[Si]_{HS}} \times \frac{\left(\frac{Ge}{Si}\right)_R - \left(\frac{Ge}{Si}\right)_{trib}}{\left(\frac{Ge}{Si}\right)_{HS} - \left(\frac{Ge}{Si}\right)_R}, \tag{B.5}$$

where F_W^{HS} is the fraction of river discharge attributed to hot spring input, $[Si]_{trib}$ is the concentration of Si in surface waters unaffected by hot spring input, $[Si]_{HS}$ is the hot spring Si concentration, $(Ge/Si)_R$, $(Ge/Si)_{trib}$ and $(Ge/Si)_{HS}$ are the Ge/Si ratios of the river down stream of the springs, unaffected surface waters and hot springs, respectively. The $[Si]_{HS}$, $(Ge/Si)_{HS}$ and other values dependent on them differ from the published values due to the inclusion of an additional sample. Unless otherwise noted, all other values are taken from Evans et al. (2004) and summarized in Table B.3. The equation used to calculate thermal power is the same as that used by Ehlers and Chapman (1999),

$$P = \frac{\partial m}{\partial t} c(T_w - T_g), \tag{B.6}$$

where P is the thermal power, $\partial m/\partial t$ is the mass flow rate, c is the fluid specific heat and $T_w - T_g$ is the temperature difference between the hot spring water and the ground. The mass flow rate ($\partial m/\partial t$) is calculated as the product of F_W^{HS}, the river volume flux and density of water. The average temperature of the observed springs is used for the spring water temperature (T_w). For the average ground temperature (T_g), the average air temperature is first calculated at the average elevation of the Marsyandi River basin. The average elevation is used because the groundwater in the Marsyandi River valley is likely infiltrating from all points within the basin and in equilibrium with the air temperatures. The average elevation calculated from a 250 m DEM is 3442 m. Using a sea level temperature of 28°C and an atmospheric lapse rate

of 7°C/km, the average air temperature is 3.9°C at 3442 m elevation. The calculated ground temperature at that elevation is 2.5°C warmer, to estimate the influence of excess solar insolation (Putnam and Chapman, 1996). The total observed thermal power of the Marsyandi River valley hot springs is 61.4 ± 36.3 MW, where the uncertainty reflects the standard deviation of $(Ge/Si)_{HS}$.

Thermal power is also calculated for each simulation to compare to the observed value and constrain the range of K values. Equation (B.6) is again used to calculate the thermal power. In the finite element model, only elements at the top surface with positive velocity z-components contribute to the thermal power. The temperature gradient $(T_w - T_g)$ is the thermal gradient across the element in the models. The mass flow rate $(\partial m/\partial t)$ is the product of the flow velocity, area of the upper surface of the element and the fluid density. The element upper surface area is based on the 700 m x-y spacing of nodes in the model. To place bounds on the range of model thermal powers, it is calculated three different ways for each model: (1) All surface elements in the model contribute and are assumed to be flat lying, (2) all surface elements contribute and are assumed to be dipping at 30° and (3) only elements within the Marsyandi River basin contribute and are assumed to be flat lying. Scenario (2) provides an upper bound for the thermal power calculations because it includes some elements outside of the Marsyandi River basin and uses a dip angle of 30° for the element surface area, which is higher than the average hillslope angle calculated from a 250 m DEM (∼24°). Scenario (3) is likely to be an underestimate because it only includes elements within the Marsyandi River basin and assumes they are flat lying, underestimating the true surface area.

B.3 Additional model analyses

In addition to the Nagi Lek transect, three other transects within the Marsyandi drainage basin were analyzed: The Tal (A), Syange South (B) and Jagat (C) transects (Figure B.3; Whipp et al., 2007). Similar to the Nagi Lek transect, the kinematic model used here has the Main Central Thrust (MCT) and the Main Frontal Thrust (MFT) active, producing an erosion rate of ∼2.5 mm/yr. The erosion-dominated models have a hydraulic conductivity (K) value of 10^{-12} m/s, the threshold models have $K = 10^{-9}$ m/s and $K = 10^{-7}$ m/s in the fluid-advection-dominated models. In addition to AFT cooling ages, muscovite $^{40}Ar/^{39}Ar$ ages are predicted to characterize the effects of the free parameters on a higher-temperature system (Closure temperature, Tc = ∼350°C), but the predicted $^{40}Ar/^{39}Ar$ ages are not compared to any data. All three transects show similar trends to those observed in the Nagi Lek transect; ages predicted from the fluid-advective models are older and follow a more gradual age-elevation slope than those predicted from the erosion-dominated or threshold models.

The predicted ages for the additional transects may be similar to the Nagi Lek predicted ages, but there are some subtle differences. Samples in the Tal transect range in age from 0.3 to 0.9 Ma over ∼1700 m of elevation (A in Figure B.3). As noted by Whipp et al. (2007), the samples on this transect require a higher model erosion rate to fit the data (3.3−5.0 mm/yr), so even the erosion-dominated predicted ages are older than the observed ages (Figure B.4a). The erosion-dominated and threshold model predicted AFT ages are similar irrespective of sample elevation in this transect, but the threshold model predicted ages are slightly younger than those from the erosion-dominated model. The fluid-advective model predicted AFT ages are ∼1 My

older and follow an age-elevation trend very similar to that of the erosion-dominated model predicted ages. The predicted $^{40}Ar/^{39}Ar$ ages from the erosion-dominated and threshold models are nearly identical, while the fluid-advective model ages are ∼0.9 My older (Figure B.4d). The $^{40}Ar/^{39}Ar$ ages predicted from the fluid-advective model also have a steeper age-elevation trend than those from the other two models. The AFT ages predicted from the Syange South samples follow a trend much like that of the Tal predicted AFT ages; all of the predicted AFT ages follow a similar age-elevation trend, the erosion-dominated and threshold model predicted ages are very similar and the fluid-advective ages are older by ∼1 Ma (Figure B.4b). For Syange South, however, the predicted $^{40}Ar/^{39}Ar$ ages also all follow a similar age-elevation trend (Figure B.4e). The predicted AFT ages from the Jagat transect are much like those of the Nagi Lek transect; the high elevation threshold model ages fall off the trend of the erosion-dominated ages and the fluid-advective ages are significantly older with a shallower age-elevation trend (Figure B.4c). The predicted $^{40}Ar/^{39}Ar$ ages all follow similar age-elevation trends with fluid-advective model predicted ages that are ∼1 Ma older than the erosion-dominated and threshold model predicted ages (Figure B.4f).

Table B.1: Numerical model parameters

Property/Parameter	Input value
General model	
Model time step	10^5 yr
Horizontal node spacing	700 m
Average vertical node spacing	∼1500 m
Model domain (x,y,z)	84 x 140 x 50 km
Thermal model†	
GHS heat production	1.9 μW/m^3
LHS/IS heat production	0.8 μW/m^3
TS heat production	0.5 μW/m^3
Thermal conductivity	2.5 W/m K
Rock specific heat	800 J/kg K
Rock density	2750 kg/m^3
Surface temperature	28 - (7 × z) °C
Basal heat flow	35 mW/m^2
Kinematic model†	
India-Tibet convergence rate	20 mm/yr
MFT overthrusting rate	2−8 mm/yr
MCT overthrusting rate	1−4 mm/yr
Hydrologic model	
GHS hydraulic conductivity§,#	$10^{-4} - 10^{-12}$ m/s
LHS hydraulic conductivity§,#	$5 \times 10^{-7} - 10^{-12}$ m/s
TS hydraulic conductivity§,#	$10^{-10} - 10^{-12}$ m/s
IS hydraulic conductivity§,#	10^{-12} m/s
Hydraulic conductivity below B/D#,††	10^{-12} m/s
Porosity	10%
Specific storage§§	10^{-10} m^{-1}
Fluid specific heat##	4200 J/kg K
Fluid density##	1000 kg/m^3

Note: † See Whipp et al., 2007 for parameter sources.
§ Freeze and Cherry, 1979, p. 29, 37.
# Ingebritsen and Manning, 1999 and references therein.
†† B/D = Brittle-ductile transition
§§ Typical value, see Fetter, 1988, p. 106.
Average value from Lide, 1990, p. **6-**8.

Table B.2: Thermal Power Values

Parameter	Value
Spring temperature*	51 °C
Average surface elevation†	3442 m
Calculated air temperature	3.9 °C
Calculated ground temperature	6.4 °C
Fluid-ground ΔT	44.6 °
$Si^{\S}_{trib}$	155 μmol/kg
Si^{*}_{HS}	1371 μmol/kg
$(Ge/Si)^{\S}_{R}$	2.2 μmol/mol
$(Ge/Si)^{\S}_{trib}$	0.7 μmol/mol
$(Ge/Si)^{*,\#}_{HS}$	109.03 μmol/mol
HS Fraction*	0.1587%
River flux§	210 m^3/s
Volume flux*	330 L/s; 0.33 m^3/s
Water density	988.063 kg/m^3
Mass flow rate*	329.32 kg/s
Specific heat	4183 J/kg K
Thermal power	61.4 ± 36.3 MW

Note: * Recalculated from data of Evans et al. (2004).
† Calculated from 250 m DEM (see text).
§ Value from Evans et al. (2004).
# Si weighted average.

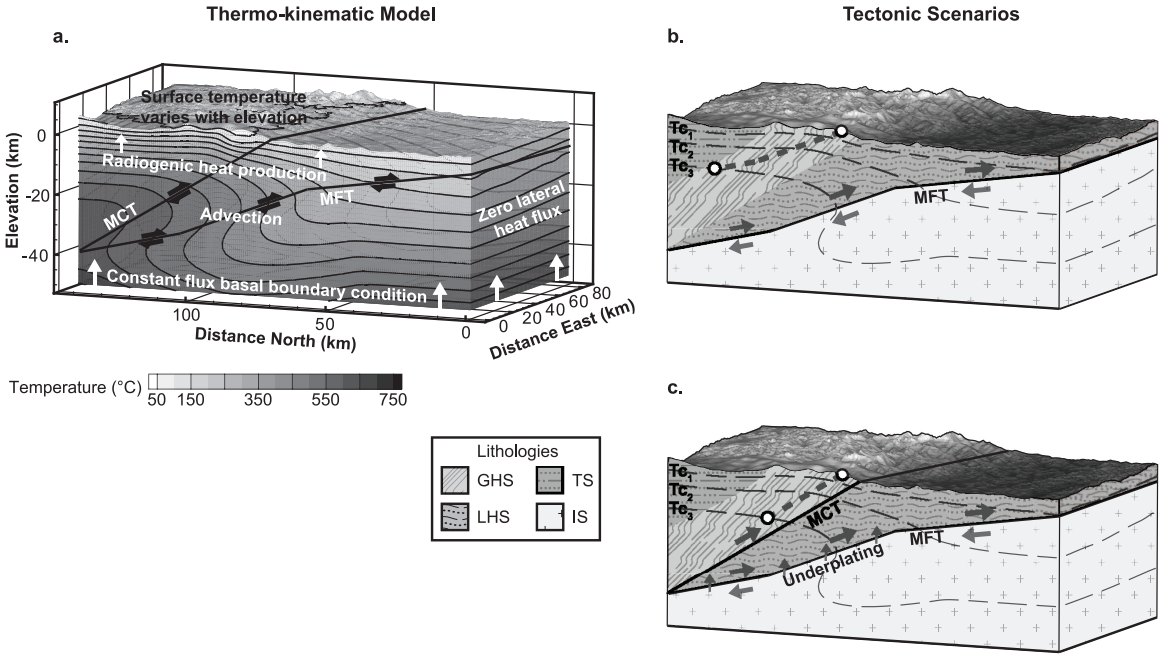

Figure B.1: 3-D block diagram of the thermokinematic model and tectonic scenarios. (a) Example conductive thermokinematic model illustrating the boundary conditions and thermal model components. The kinematic model has the Main Frontal Thrust (MFT) and Main Central Thrust (MCT) active (thick lines). Contoured temperatures (thin lines) show significant perturbation to the subsurface thermal field from the kinematic model and other thermal influences. (b) 3-D schematic block diagram for the tectonic scenario where slip occurs only on the MFT (arrows show sense of motion on fault). The exhumation pathway (thick dashed line) parallels the fault and transports rock through closure temperatures ($Tc_1 - Tc_3$) for several isotopic systems (thin dashed lines). This example exhumation pathway is for a thermochronometer sample sensitive to closure temperatures $Tc_1 - Tc_3$ (white circles). (c) Tectonic scenario where slip is partitioned between the MCT and MFT. In this scenario, sample exhumation parallels the MCT and material is transferred into the overriding wedge via underplating (small vertical arrows).

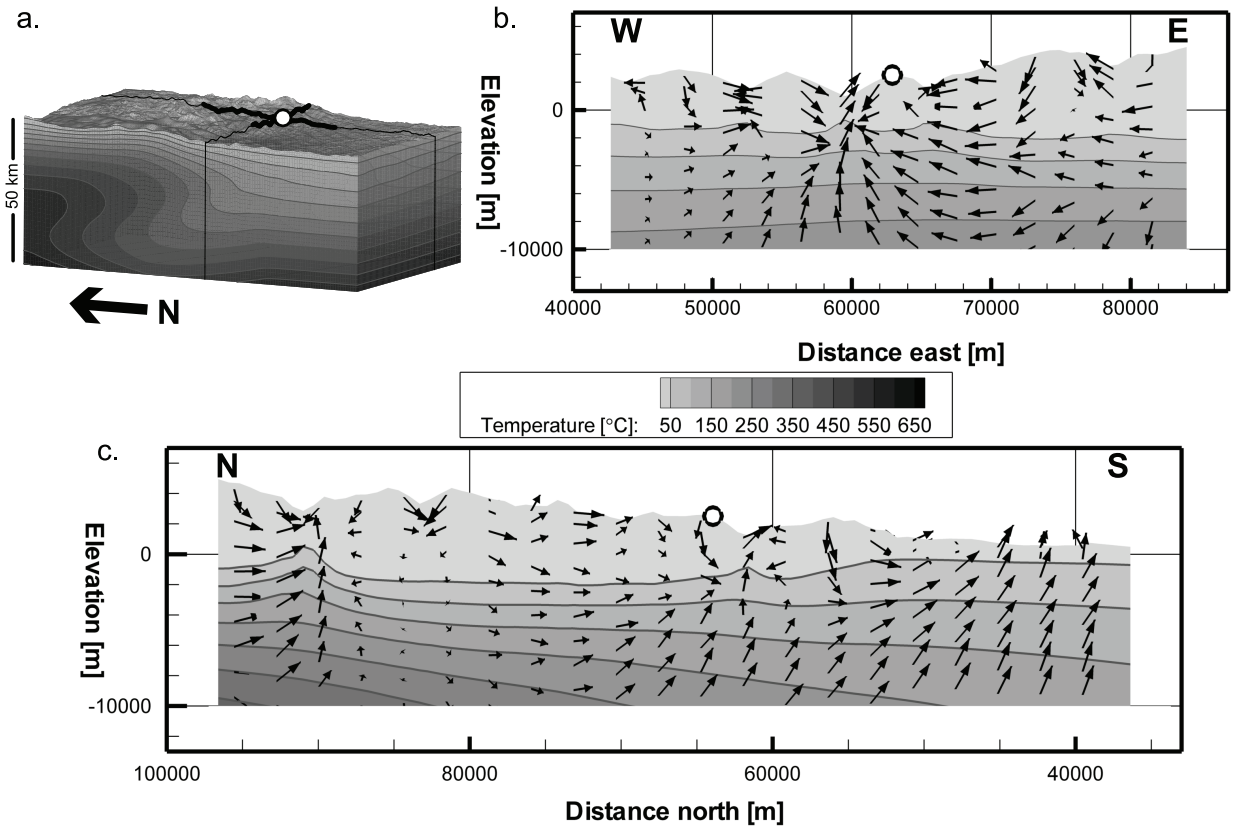

Figure B.2: Vertical slices extracted from a fluid-advective thermokinematic model illustrating groundwater flow pathways. (a) 50 km thick thermokinematic model block with extracted slice locations (heavy black lines) and Nagi Lek data transect location (white circle). (b) West to east vertical slice through model to -10 km depth with schematic flow vectors and data transect location (white circle). Vectors illustrate fluid flow patterns affected by short wavelength topography, but the vector lengths have no meaning. (c) North to south slice through model with flow vectors and data transect location. Longer wavelength topography drives a broader circulation pattern with flow down from the Tibetan Plateau toward the Indian foreland. Downward fluid flow depresses the thermal gradient and upward flow compresses it, as shown by the near-surface isotherms.

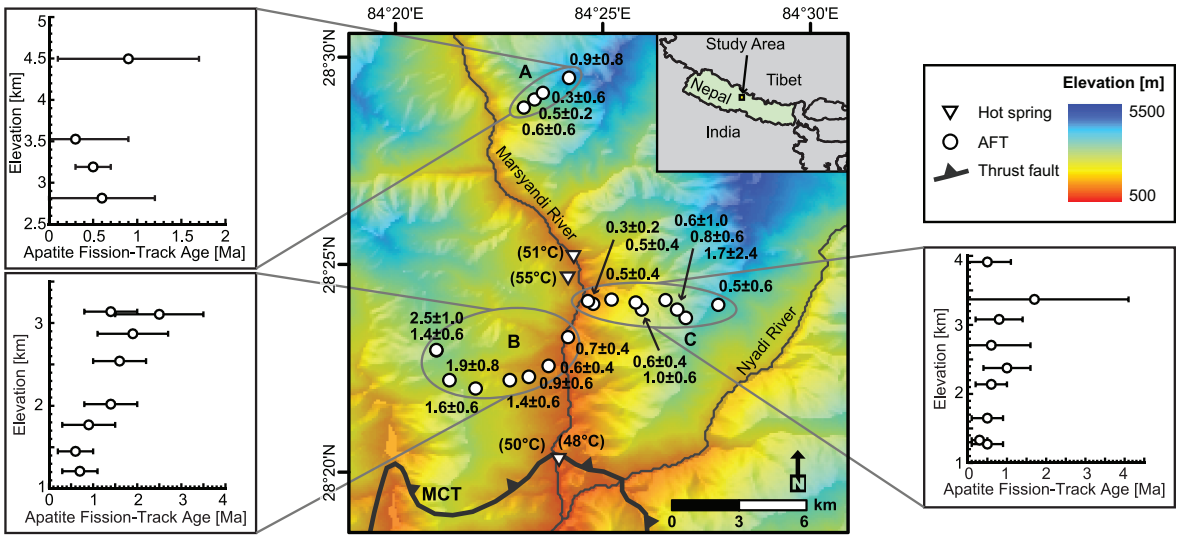

Figure B.3: Shaded relief digital elevation model of the study region in central Nepal. Apatite fission-track samples (white circles) were collected along three transects: Tal (A), Syange South (B) and Jagat (C). Mapped hot spring locations (white inverted triangles) along the Marsyandi River (dark gray line) are shown along with the major thrust fault in the study area (MCT = Main Central Thrust). The outer plots show the sample ages with 2σ uncertainties as a function of sample elevation.

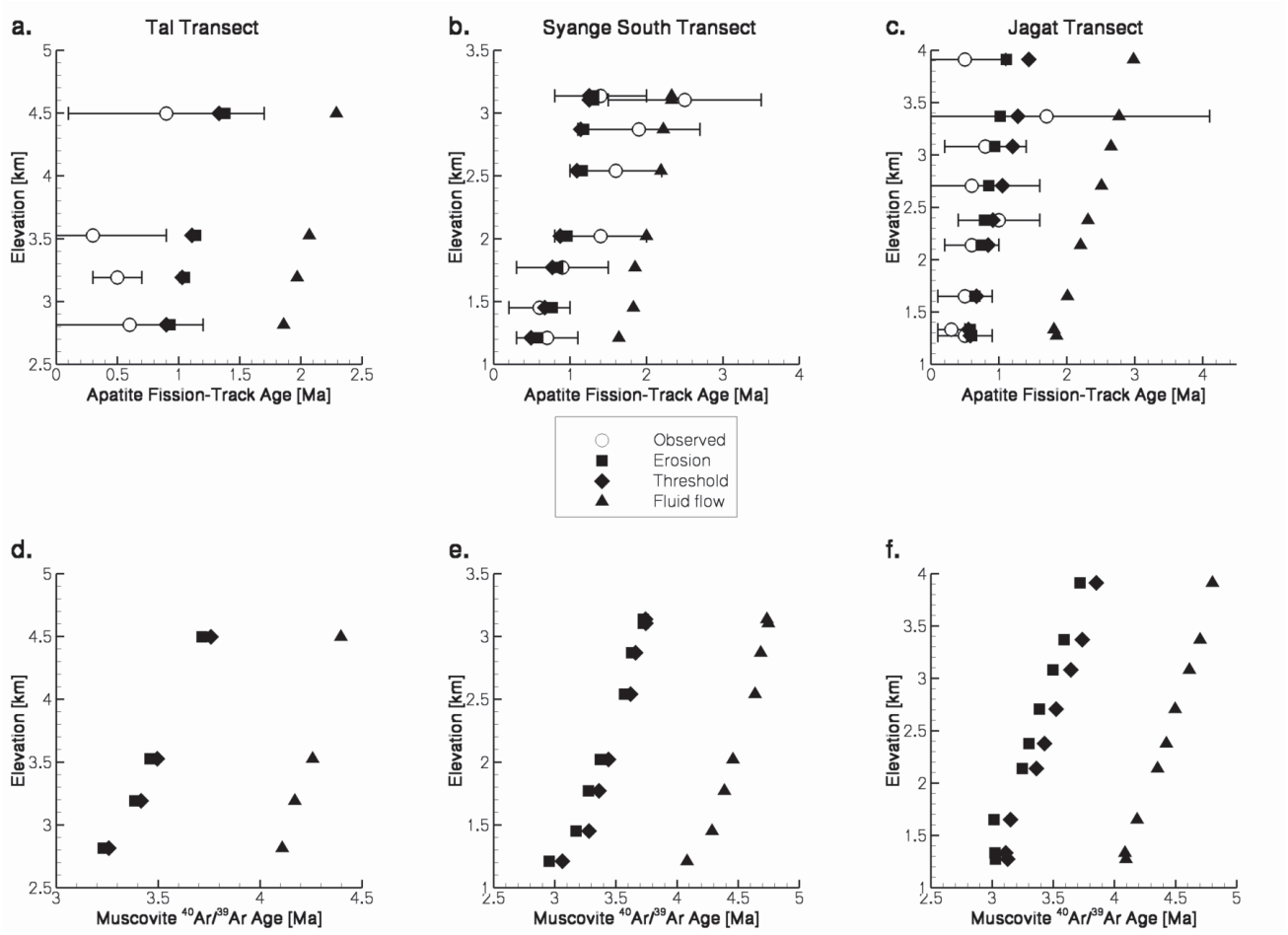

Figure B.4: Predicted and observed apatite fission-track (AFT) and muscovite $^{40}Ar/^{39}Ar$ ages for the Tal (a,d), Syange South (b,e) and Jagat (c,f) transects. (a-c) AFT data shown with 2σ uncertainties (white circles) and predicted ages from models that have hydraulic conductivity (K) values that produce erosion-dominated (black squares) and fluid-advection-dominated (black triangles) thermal fields. The threshold predicted ages (black diamonds) are from a model with a thermal field that is neither erosion nor fluid-advection dominated. The older ages of the fluid-advection-dominated model (black triangles) show the effect of substantial groundwater flow on the predicted ages. (d-f) Predicted muscovite $^{40}Ar/^{39}Ar$ ages for erosion-dominated (black squares), threshold (black diamonds) and fluid-advective (black triangles) models. Again, topography-driven fluid flow produces older ages in the fluid-advective models (black triangles).

Bibliography

Bilham, R., Larson, K. M., Freymueller, J. T., Jouanne, F., Le Fort, P., Leturmy, P., Mugnier, J. L., Gamond, J. F., Glot, J. P., Martinod, J., Chaudury, N. L., Chitrakar, G. R., Gautam, U. P., Koirala, B. P., Pandey, M. R., Ranabhat, R., Sapkota, S. N., Shrestha, P. L., Thakuri, M. C., Timilsina, U. R., Tiwari, D. R., Vidal, G., Vigny, C., Galy, A. and de Voogd, B. GPS measurements of present-day convergence across the Nepal Himalaya. *Nature*, 386(6620):61–64, 1997.

Birch, A. F. Heat from radioactivity. In Faul, H., editor, *Nuclear Geology*, pages 148–175. Wiley, New York, 1954.

Brooks, A. and Hughes, T. Streamline Upwind / Petrov-Galerkin formulations for convective dominated flows with particular emphasis on the incompressible Navier-Stokes Equations. *Computer Methods in Applied Mechanics and Engineering*, 32:199–259, 1982.

Ehlers, T. A. and Chapman, D. S. Normal fault thermal regimes; conductive and hydrothermal heat transfer surrounding the Wasatch Fault, Utah. *Tectonophysics*, 312(2-4):217–234, 1999.

Ehlers, T. A., Willett, S., Armstrong, P. A. and Chapman, D. S. Exhumation of the Central Wasatch Mountains, Utah: 2. Thermo-kinematics of exhumation and thermochronometer interpretation. *Journal of Geophysical Research*, 108(B3):2173, 2003.

Evans, M. J., Derry, L. A. and France-Lanord, C. Geothermal fluxes of alkalinity in the Narayani river system of central Nepal. *Geochemistry, Geophysics, Geosystems - G (super 3)*, 5:no.8, 21, 2004.

Hodges, K. V. Tectonics of the Himalaya and southern Tibet from two perspectives. *Geological Society of America Bulletin*, 112(3):324–350, 2000.

Ingebritsen, S. E. and Manning, C. E. Geological implications of a permeability-depth curve for the continental crust. *Geology*, 27(12):1107–1110, 1999.

Kohl, T. and Hopkirk, R. J. "FRACTure" a simulation code for forced fluid flow and transport in fractured, porous rock. *Geothermics*, 24(3):333–343, 1995.

Larson, K. M., Buergmann, R., Bilham, R. and Freymueller, J. T. Kinematics of the India-Eurasia collision zone from GPS measurements. *Journal of Geophysical Research, B, Solid Earth and Planets*, 104(1):1077–1093, 1999.

Laslett, G. M., Green, P. F., Duddy, I. R. and Gleadow, A. J. W. Thermal annealing of fission tracks in apatite. *Chemical Geology; Isotope Geoscience Section*, 65(1):1–13, 1987.

Phillips, S., Igbene, A., Fair, J., Ozbek, H. and Tavan, M. A Technical Databook for Geothermal Energy Utilitzation. Technical Report LBL-12810, Lawrence Berkeley Laboratory, USA, 1981.

Putnam, S. N. and Chapman, D. S. A geothermal climate change observatory; first year results from Emigrant Pass in Northwest Utah. *Journal of Geophysical Research, B, Solid Earth and Planets*, 101(10):21,877–21,890, 1996.

Sass, J. H., Kennelly, J. P., J., Smith, E. P. and Wendt, W. E. Laboratory line-source methods for the measurement of thermal conductivity of rocks near room temperature. Technical Report 84-91, United States Geological Survey, 1984.

Sauty, J. P., Gringarten, A. C., Menjoz, A. and Landel, P. A. Sensible energy storage in aquifers; 1, Theoretical study. *Water Resources Research*, 18(2):245–252, 1982.

Smith, L. and Chapman, D. S. On the thermal effects of groundwater flow - 1. Regional scale systems. *Journal of Geophysical Research*, 88(B1):593–608, 1983.

Whipp, Jr., D. M., Ehlers, T. A., Blythe, A. E., Huntington, K. W., Hodges, K. V. and Burbank, D. W. Plio-Quaternary exhumation history of the central Nepalese Himalaya: 2. Thermo-kinematic and thermochronometer age prediction model. *Tectonics*, 26, 2007. doi:10.1029/2006TC001991.

Williams, C. F. and Narasimhan, T. N. Hydrogeologic constraints on heat flow along the San Andreas Fault; a testing of hypotheses. *Earth and Planetary Science Letters*, 92(2):131–143, 1989.